Theoretical, Computational, and Experimental Studies of a Metamaterial-Enhanced Resistive Wall Amplifier

By
Raymond Tyler Rowe

A dissertation submitted in partial fulfillment of
the requirements for the degree of

Doctor of Philosophy
(Electrical Engineering)

at the
UNIVERSITY OF WISCONSIN-MADISON
2017

Date of final oral examination: April 13, 2017
The dissertation is approved by the following members of the Final Oral Committee:
John H. Booske, Professor, Electrical and Computer Engineering
Nader Behdad, Associate Professor, Electrical and Computer Engineering
Carter Armstrong, Adjunct Professor, Electrical and Computer Engineering
David Anderson, Professor, Electrical and Computer Engineering
Jan Egedal, Professor, Physics

To Haley, for all of your support

Acknowledgements

First and foremost, I need to acknowledge my beautiful wife, Haley, for all of her support throughout this work. Thank you, Haley. Secondly, I would like to sincerely thank and acknowledge my advisors Prof. John H. Booske and Prof. Nader Behdad. Thank you both for supporting me in this work, always challenging me to think outside of the box and maintain focus on the larger picture. I will always be indebted to you for your mentorship. Thank you to the other members of my preliminary and defense committee: Prof. David Anderson, Dr. Carter Armstrong, and Prof. Jan Egedal. I greatly appreciate the time, encouragement, and critical feedback you have provided me.

To my lab mates, especially, Dr. Matthew Kirley, Dr. Ryan Jacobs, Dr. Chien-Hao Liu, Dr. Amin Momeni, Paul Carrigan, Konstantinos Mavrakakis, Patrick Forbes, Ting-Yen Shih, Kasra Ghaemi, Daniel Enderich, and Wyatt Rufener, thank you all for your friendship. In addition to being great friends and classmates, you all were great lab mates. This project would not have been successful without the brainstorming, teamwork, helping me with simulation and experimental issues, and encouragement. Thank you also to the undergraduates who have helped me on my project along the way, including Tristan Steiner, Patrick Forbes, and Kevin Houck.

I also would like to thank Peter Marhdall, for helping me configure ICEPIC and the diagnosis of numerical Cherenkov radiation problem I had in my simulations, and Jason Hummelt, for discussing the methods he used to overcome CST's relativistic electron beam limitations.

To the staff of the ECE department, thank you all for your assistance, especially, Allysa Greiber, Kathy Hall, Dwight Redders, and Lori Burrows. I sincerely appreciate how anytime I had a question, needed help, or had to schedule meetings, you all put me to the top of your priority list.

I have undoubtedly left someone off this list of people who I owe a thank you too. If you helped me in any way during the time I worked on this research, I sincerely thank you.

Finally, I would also like to thank the numerous funding sources of my research, including the Air Force Office of Scientific Research under Award Nos. FA9550-11-1-0050, FA9550-09-1-0086, and FA9550-09-1-0086, the National Science Foundation under NSF Award No. ECCS-1101146, the Office of Naval Research under ONR Award N00014-15-1-2207, several graduate fellowships from the Directed Energy Professional Society, the Duane H and Dorothy M Bluemke Professorship fund, and the Vilas Distinguished Achievement Professorship fund.

Contents

List of Figures

List of Abbreviations

- **3D** – three dimensional
- **ac** – alternating current
- **AFRL** – Air Force Research Laboratory
- **BW** – backwards
- **BWO** – backwards wave oscillator
- **CAD** – computer-aided design
- **CST –** Computer Simulation Technology
- **Cu** – Copper
- **dc** – direct current
- **DNG** – double-negative
- **DPS** – double-positive
- **EM -** electromagnetic
- **ENG –** epsilon negative
- **FDTD** – finite difference time domain
- **FFT** – fast Fourier transform
- **FIT** – finite integration technique
- **HPM** – high power microwave
- **HV** – high voltage
- **I-V** – current to voltage relationship
- **ICEPIC –** improved concurrent electromagnetic particle-in-cell
- **MERWA** – metamaterial enhanced resistive wall amplifier
- **MNG** – mu-negative
- **MTM -** metamaterial
- **MVED** – microwave vacuum electron device
- **MW** – megawatt
- **NCR** – numerical Cherenkov radiation
- **OHFC** – oxygen free high conductivity
- **PEC** – perfect electric conductor
- **PIC** – particle-in-cell
- **PMC** – perfect magnetic conductor
- **PML** – perfectly matched layer
- **RF** – radio frequency
- **RMS** – root mean square
- **RWA** – resistive wall amplifier
- **SCL** – space charge limited
- **SMA** – subminiature version A, coaxial RF connector

- **SS** – stainless steel
- **TD** – time domain
- **TLM** – transmission line matrix
- **TM** – transverse magnetic
- **TWT** – traveling wave tube
- **UHV** – ultra high vacuum
- **VED** – vacuum electron device
- **VNA** – vector network analyzer

Abstract

Vacuum electron devices (VEDs) continue to be the most cost effective and efficient devices for high power microwave (HPM) technology. Medicine, electronic warfare and electronic countermeasures, satellite communication, and scientific research are all specific applications that continue to depend on HPMs. In addition to cost effectiveness and efficiency, VEDs can provide larger bandwidth, higher output powers, and higher operating frequencies than many solid state alternatives. VEDs also continue to be unique sources of Megawatt (MW) level HPMs for electronic warfare, scientific, and medical applications.

This project focuses on a specific VED, the resistive wall amplifier (RWA). The RWA passes a velocity-modulated electron beam near a resistive surface to amplify electromagnetic signals. It was originally introduced in 1950 and received limited further theoretical and experimental investigation [1-11]. Birdsall and Whinnery demonstrated that if the admittance of the RWA's wall was resistive or resistive-inductive (as seen by the electron beam), the device would support a growing space charge wave and produce gain [1]. However, when constructing a practical device a dielectric substrate is necessary to support the resistive medium. The addition of a dielectric introduces a capacitive component to the wall's admittance (less inductive), reducing the device's performance.

This work investigates how metamaterials (MTMs) can improve the RWA performance. MTMs are composite structures engineered to have electromagnetic (EM) properties that are not readily available in nature (e.g., negative permittivity and/or permeability). The metamaterial enhanced

resistive wall amplifier (MERWA) was theoretically, computationally, and experimentally investigated in this work.

The analytic theory investigation revealed how the addition of an epsilon negative (ENG) medium liner could make the wall's admittance more inductive and enhance the gain-bandwidth product of a RWA. We then examined how a periodic, inductively-meandered, metal wire array could be used as an ENG MTM medium for the MERWA. Finally, we developed and analyzed a relativistic analytic theory MERWA model. The computational portion of the MERWA investigations included electromagnetic (EM) and particle-in-cell (PIC) studies of the ENG-medium-lined RWA and the inductively-meandered, metal-wire-array, MTM-lined MERWA realization. The computational simulation results agreed well with the analytic theory predictions. Finally, the experimental investigation of the MERWA included design, fabrication, assembly and measurements of inductively-meandered, metal-wire-array MTM-lined waveguide circuits as well as vacuum "hot test" experiments with an electron beam were conducted. The experimental measurement results verified the predicted EM properties of the inductively-meandered wire array MERWA circuit, confirmed the presence of a simulation-predicted oscillation instability, demonstrated the successful suppression of the oscillation, and provided preliminary characterization of the amplification properties.

Chapter I: Motivation and Project Tasks

1.1 Problem Statement

Through a combination of theory, simulation, and experimental investigation we examine a novel vacuum electron device, the metamaterial-enhanced resistive wall amplifier (MERWA). The MERWA uses metamaterials (MTMs) with negative permittivity response to greatly improve the performance of a traditional resistive wall amplifier. We examine, through theory and simulation, both a lower power (10 kW) MERWA as well as a relativistic high power (50 MW) MERWA to determine their capabilities as wideband amplifiers. We further study the lower power version by constructing and testing a prototype device to demonstrate amplification.

1.2 Novelty of Work

The MERWA has the capability to be a high gain wideband amplifier that has previously not been investigated. Through a combination of theory, simulation, and experiments, this work will demonstrate the capability of the MERWA to outperform most commercially available devices. As a result of our investigation of the MERWA, we have revealed some properties of the MERWA that can degrade its performance and investigated methods to overcome them. Finally, our investigation of a relativistic high power MERWA will provide the foundation of an entirely new type of high power amplifiers.

1.3 Motivation

Vacuum electron devices continue to be the most cost effective and efficient devices for high power microwave (HPM) technology in a variety of applications. Medicine, electronic warfare and electronic countermeasures, satellite communication, and scientific research are all specific applications that continue to depend on HPMs and their supporting technology. In addition to

cost effectiveness and efficiency, vacuum electron devices can also often provide larger bandwidth, higher output powers, and higher operating frequencies than many solid state alternatives.

In addition, vacuum electron devices remain to be one of the only sources of Megawatt (MW) level HPM currently used for electronic warfare, scientific, and medical purposes. Currently, most commercially available MW level HPM devices are oscillators. However, an increased availability of HPM amplifiers would lead to enhanced electronic warfare and countermeasure systems. There continues to be an unfilled need for broadband, efficient, HPM amplifiers. The MERWA [11] investigated in this work may be a viable option to fill the need for HPM amplifiers.

1.4 Specific Project Tasks

The overall task of this project is to investigate the viability of a MERWA. Investigation of the MERWA for the purpose of this research project will be divided into five specific tasks. This report consists of a thorough discussion of each of the five tasks. The five tasks include:

Task 1: Theoretically Investigate MERWA Concept

To initially test the viability of the MERWA concept, Task 1 consisted of a thorough investigation of the original resistive wall amplifier and how the integration of MTMs can enhance the device's performance. Task 1 consisted of a full theoretical analysis of the MERWA device in addition to some initial particle-in-cell (PIC) simulations.

Task 2: Backwards Wave Oscillation Suppression in MERWA

During the investigation of Task 1 it was discovered that as a consequence of using MTMs in the MERWA, a possibility of oscillation behavior arises. Task 2 investigated this oscillation to determine its source and methods to suppress the oscillation without substantially reducing the MERWA gain.

Task 3: Practical Implementation of MERWA

Task 3 focused on techniques to create a practically implementable MERWA. For initial investigation in Tasks 1 and 2, the MTMs were assumed to be bulk dielectric materials. Task 3 determined a structure that exhibits the desired electromagnetic properties but also had physical properties that allow for use in the MERWA.

Task 4: Relativistic HPM MERWA

A large need exists also for HPM or MW level amplifier devices. Task 4 investigated the performance of a HPM MERWA. To achieve HPM performance the electron beam of the device will have a relativistic velocity. Therefore, Task 4 focused on the device operation under relativistic beam conditions. An investigation of the device performance with a relativistic beam provided insight into the capabilities of an HPM MERWA. The investigation of a relativistic MERWA in Task 4 consisted of a theoretical investigation and particle-in-cell simulations. A theoretical investigation was necessary as the analytic equations used to predict MERWA performance needed to be modified to incorporate relativistic beam conditions.

Task 5: Experimental Testing of MERWA Prototype

Task 5 focused on the experimental testing of a prototype MERWA. The experimental testing of the MERWA prototype consisted of the electromagnetic ‘cold test’ measurements along with electron beam interaction or ‘hot test’ measurements. The cold tests consisted of constructing a practical MTM that was similar to the structure investigated in Task 3 and measuring the electromagnetic response. The constructed MTM was then used in a vacuum chamber system in conjunction with a thermionic electron source (to generate an electron pencil beam) to conduct the hot test. For the hot test measurements, diagnostics were added to the MERWA structure to measure the performance of the system and these measurements were used to calculate the device’s gain rate and examine oscillation behavior. This task included the configuration of the vacuum chamber system, electron cathode and electron beam optics, electromagnetics for beam confinement, high voltage pulsed power supply system, design and construction of a system to velocity modulate the electron beam, an electron beam collector, and the diagnostics to measure RF signals.

1.5 Organization of the Dissertation

This dissertation is organized into eight chapters. Chapters one and two discuss the motivation, background, and specific project tasks of the MERWA and this project. Chapters three through seven discuss the details of each of the five tasks outlined above. Chapter eight discusses the future work of this research project. In addition to these eight chapters, there is a section at the end of the dissertations outlining the journal and conference publications of the author. Finally, three appendices are included, which thoroughly discuss some of the mathematical derivations of the equations used in the earlier chapters.

Chapter II: Background

2.1 VEDs (VEDs)

The basic principal of VED operation is using the potential or kinetic energy of particles (usually electrons) to amplify or generate an electromagnetic signal. The particles that are used to generate an electromagnetic signal travel in a vacuum space and do not suffer from conduction losses that are typically seen in solid state alternatives. The absence of conduction losses allows for much higher currents. Fig. 1 presents a pictorial representation of a basic vacuum electron amplifier [12]. In this device, an electron beam is emitted from a cathode and travels from left to right. The electron beam travels through some type of interaction circuit where the electrons of the beam interact with an electromagnetic wave traveling on the interaction circuit. As the electrons interact with the electromagnetic wave, they give a small portion of their kinetic or potential (depending on the specific device) energy to the electromagnetic wave causing amplification. A focusing magnet is placed around the interaction circuit to provide a static magnetic field for beam confinement. Near the end of the interaction circuit the amplified electromagnetic signal is coupled out of the device and the electron beam is collected. Since the collector surface is the only place where electrons strike a surface, this is the only location of heat.

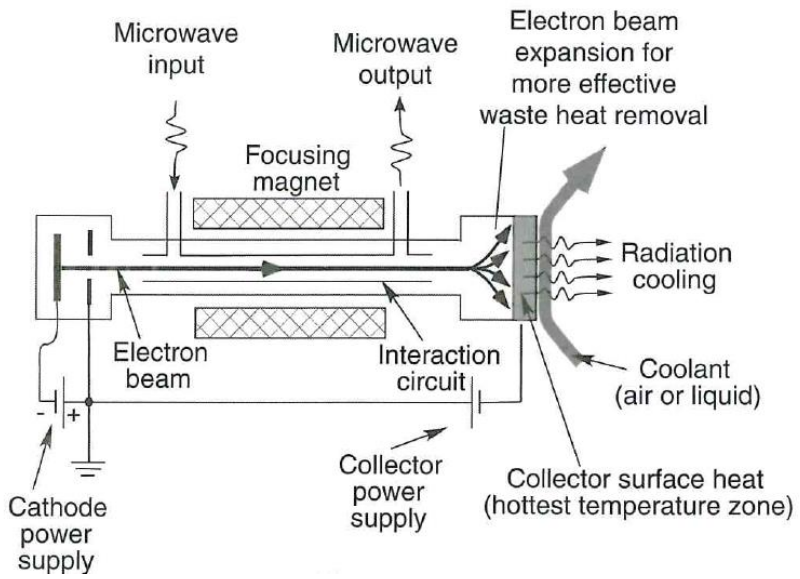

Fig. 1: Illustrative graph indicating the basics of a VED [12]. Used with permission © 2005 by the Institute of Electrical and Electronics Engineers, Inc.

While VEDs are no longer used in many consumer products except for microwave ovens, they continue to thrive in a variety of fields. VEDs currently have applications in medicine, military, scientific research, and communications. A variety of different VEDs have been theorized and successfully implemented as microwave amplifiers and sources [13-15] and continue to prevail as the most efficient cost-effective devices for HPM applications. Some specific examples include TWTs for satellite communication, klystrons for radar, gyrotrons for plasma heating, etc. Outside of a few specific cases, VEDs are the common methods for electromagnetic amplification and oscillation when high power (>1kW) and high frequency (>100 GHz). However, most currently available HPM sources and amplifiers are limited in instantaneous bandwidth (klystrons, crossed-field amplifiers or coupled cavity traveling wave tubes) [13, 14]. In addition, most commercially available multi-megawatt-level sources are oscillator devices when a strong need for amplifiers exists. There continues to be a lack of efficient, high gain, broadband amplifiers for HPM applications. Fig. 2 presents an illustrative graph presenting

commercially available VED devices along with commercially available solid state devices on a frequency versus output power plot [12]. It is possible to observe in Fig. 2 that for high output power and high frequency of operation VEDs are the best, and often only, device to use. This work focused on a lower frequency device (1-3 GHz) high power (>10 kW) device.

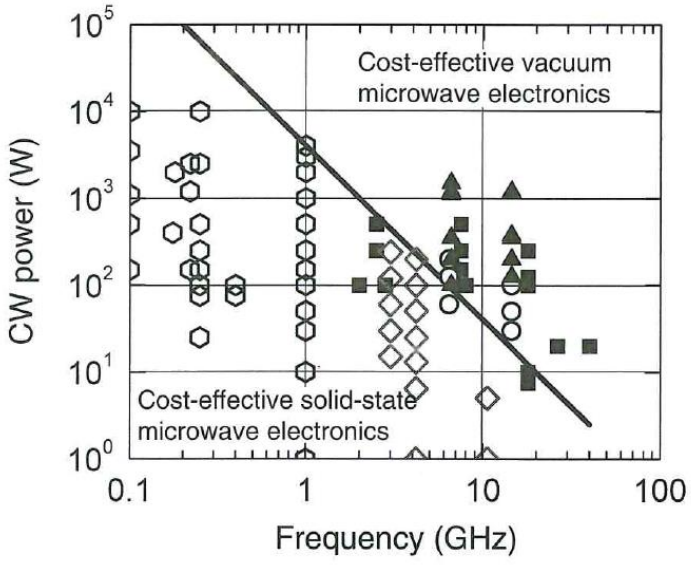

Fig. 2: Illustrative graph indicating various commercially available solid state devices and their VED counterparts. Solid symbols indicate VEDs while open symbols represent solid state devices [12]. Used with permission © 2005 by the Institute of Electrical and Electronics Engineers, Inc.

2.2 Resistive Wall Amplifiers

The resistive wall amplifier (RWA) is a VED where an electron beam is passed near a wall with conductive losses to amplify a microwave signal. Passing the electron beam near a resistive medium induces charges in the wall and the space charge forces associated with the wall charges act on the electron stream causing electron bunches to form as the electron beam propagates. This bunching of the electron beam results in an exponential growth of the ac component of the electron beam current along the direction of the beam flow [1, 2].

Fig. 3 shows the physical configuration of a traditional RWA. The RWA was initially presented as the 'Easitron' in 1950 by L. R. Walker at the Electron Tube Conference [1]. Later, it was discussed in a publication by Pierce in 1951 [16] and later thoroughly investigated both theoretically and experimentally by Birdsall, et. al, in 1953 [1, 2]. Since the original device presentation, the physics of the RWA have been investigated by a number of different groups [3-8]. However, only a few actual device designs have been examined [9, 10, 17] and only one experimentally tested [2].

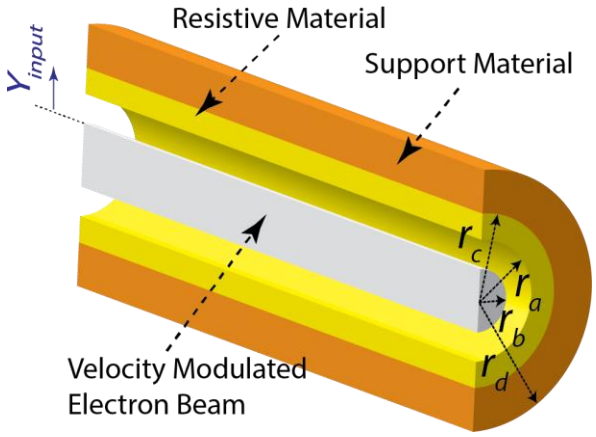

Fig. 3: Cross sectional view of the RWA. The RWA consists of a cylindrical vacuum drift tube, where the electron beam travels, which is surrounded by a resistive material and a dielectric support material.

Pierce's work showed that if the wall surrounding the electron beam had an inductive or resistive admittance (as seen by the beam), a growing and decaying space charge wave would exist on a one dimensional beam [16]. Based upon Pierce's work, Birdsall, et al., derived a three-dimensional theoretical investigation of the RWA for arbitrary wall admittances [1].

In their arbitrary wall admittance investigation, Birdsall, et al., showed that if the wall admittance at the edge of the beam was capacitive or if it exhibited an infinite or zero conductance, a growing wave would not exist; rather, two unattenuated space charge waves would exist, as typically seen in klystron devices [16]. However, if the wall admittance was resistive, resistive-inductive, or purely inductive, the two space charge waves would each exhibit gain. One wave would be exponentially attenuated (negative gain) while the second wave would have exponential growth (positive gain). A purely resistive wall admittance would yield moderate gain, a resistive-inductive admittance would yield greater gain, and a purely inductive admittance could exhibit high to even theoretically infinite gain. This infinite gain occurs when the frequency and wave number satisfy the cold-tube dispersion relation of the lossless circuit, in which case Pierce's classical 3-wave TWT theory may be applied to evaluate the spatial amplification for this synchronous interaction. The RWA structure does not allow for the propagation of waves in the absence of the electron beam. This fundamentally differentiates the RWA from a traveling wave device, such as a traveling wave tube. By not allowing for the propagation of waves in the absence of the electron beam, the structure is inherently cutoff to EM waves (at frequencies where RWA gain exists). This makes this amplifier inherently immune to oscillation.

To calculate the performance of the device, the same procedure as developed by Birdsall, et al., was used for this work [1]. The method is briefly reviewed here, but is discussed in more detail in [1]. The gain is calculated by equating the admittance of the beam at the beam edge to the admittance of the wall surrounding the electron beam. It is assumed that the electric field of the electron beam is symmetric around the axis; therefore, equating the tangential fields across the

beam and wall interface only requires that the radial admittances be equal. The stream admittance is calculated by solving Maxwell's equations using small signal theory. Using this procedure, the radial admittance of the electron beam is

$$Y_{beam} = -\frac{H_\phi}{E_z} = \frac{j\omega\varepsilon_0}{\psi^2}\frac{T\,\mathrm{J}_1(Tr)}{\mathrm{J}_0(Tr)}, \qquad (1)$$

where

$$T^2 = (\beta^2 - k_0^2)\left[\frac{\beta_p^2}{(\beta-\beta_e)^2} - 1\right], \qquad (2)$$

$$\psi^2 = \beta^2 - k_0^2, \qquad (3)$$

$$\beta_e = \omega/u_0, \qquad (4)$$

$$\beta_p = \frac{\omega_p}{u_0}, \qquad (5)$$

$$u_0 = (-2\eta V_0)^{1/2}, \qquad (6)$$

and

$$\omega_p = \left(\frac{\eta i_0}{\varepsilon_0 u_0}\right)^{1/2}. \qquad (7)$$

β is the phase constant in the assumed solution form of $e^{j(\omega t-\beta z)}$, k_0 is the free space wave number, J_1 and J_0 are Bessel's function of order 1 and zero, β_e is the wave number of the electron beam, β_p is the plasma wave number, ω_p is the plasma frequency of the electron beam, η is the electron charge to mass ratio ($-1.76x10^{11}$), u_0 is the dc velocity of the beam, V_0 is the beam voltage, i_0 is the dc current density of the electron beam, and ε_0 is the permittivity of free space.

The admittance of the wall is calculated using cutoff transmission line equations in cylindrical coordinates. The beam's admittance is then evaluated at the edge of the beam ($r = b$) using (1) and set equal to the admittance of the wall:

$$Y_{beam}(b) = Y_{wall} = \frac{j\omega\varepsilon_0}{\psi^2}\frac{T\mathrm{J}_1(Tb)}{\mathrm{J}_0(Tb)}. \qquad (8)$$

Equation (8) can be rearranged to form the transcendental equation:

$$Tb\frac{\mathrm{J}_1(Tb)}{\mathrm{J}_0(Tb)} = \frac{(\psi b)^2}{j\omega\varepsilon_0 b}Y_{wall}. \qquad (9)$$

If it is assumed that the stream admittance is a slowly varying function of β, that the β of interest is near the β value of the electron beam, β_e, and that β is much greater than k_0 (electron beam is non-relativistic), (2) reduces to

$$T^2 = \left(\beta_e{}^2\right)\left[\frac{\beta_p^2}{(\beta - \beta_e)^2} - 1\right]. \qquad (10)$$

Using (10), (9) forms a transcendental equation that can be solved for the complex wave number, β, of the space charge wave. The real part of β relates to the phase velocity of the wave and the imaginary part of β relates to the gain/attenuation of the wave. To solve the transcendental equation, Birdsall developed a set of contour maps that were used in sequence to compute the solution [1]. In this work, a numerical method similar to the bisection method was used to iteratively minimize the residual of the transcendental equation. In the bisection method, the function is evaluated at the midpoint of an interval that is known to contain a zero. The method then determines if the zero exists to the left or right of the midpoint and then uses the midpoint as a new boundary, cutting the interval by half. This bisection of the interval is then repeated until the algorithm converges to the zero [18]. The use of a numerical method to solve the equation

improves the accuracy of the calculations and allows for many calculations to be performed in a relatively short period of time.

To illustrate the gain rate calculation in an RWA, we consider an example device with tunnel radius of 10 mm, beam voltage of 10 kV, and a beam current of 1 A. A resistive material with a conductivity of σ and a thickness of 0.1 mm is assumed to cover the interior surface of a dielectric support layer with an inner diameter of 20.2 mm and a thickness of 5 mm (see Fig. 3). The dielectric constant of this support material is 1 (free space). In this example, the beam voltage is kept low to ensure that the non-relativistic assumptions made in the theory remain valid. Fig. 4 shows the gain rate of this device as a function of the conductivity σ of the resistive material for different values of the fill factor F which is defined as

$$\mathrm{F} = \frac{r_b^2}{r_a^2}, \qquad (11)$$

where r_b is the beam radius and r_a is the inner radius of the resistive medium. Different fill factors were obtained by modifying the inner radius of the resistive medium (maintaining the electron beam's current density).

It can be observed from the results shown in Fig. 4 that this device shows small gain rate values. These limited gain rate values are primarily caused by the fact that the admittance seen at the edge of the beam (Y_{in} in Fig. 3) is resistive-capacitive, in this example. As described in [1], such resistive-capacitive admittances do not offer optimum conditions for achieving high gain rate values. The capacitive nature of the admittance seen at the edge of the beam is exacerbated as the dielectric constant of the dielectric support layer increases and as the beam filling factor

decreases. The latter can be observed from the results shown in Fig. 4 where it can be observed that as the beam filling factor is decreased from 100% to 50%, the highest achievable gain rate reduces significantly from 9 dB/m to 1.8 dB/m. The gain rate is presented as per meter of the axial length of the device. To demonstrate how the dielectric constant of the dielectric support layer affects the gain rate of an RWA, the gain rate of the same amplifier is calculated for various dielectric constant values of the dielectric support layer and the results are presented in Fig. 5.

The calculated results in Fig. 4 and Fig. 5 show that a conventional RWA achieves its highest gain rate when the beam filling factor is 100% (i.e., the electron beam occupies the entire volume within the drift tube) and the dielectric constant of the dielectric support layer is 1 (i.e., the resistive material is suspended in air). Since both of these conditions are naturally impractical to achieve, only moderate gain rate values have been experimentally achieved from conventional RWAs in the past [2].

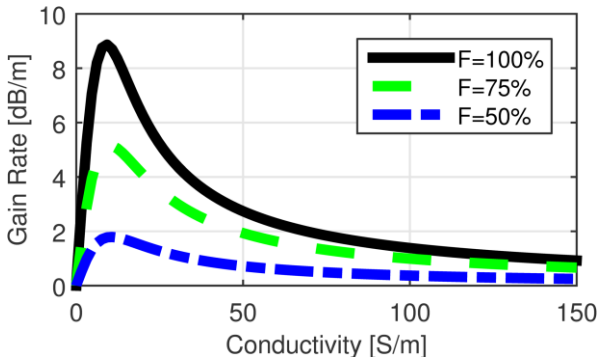

Fig. 4: Gain of the RWA (per meter of axial length of the device) versus the conductivity of the resistive material for three different fill factors (F) of 50%, 75%, and 100%. The fill factor was modified by changing the inner radius of the resistive medium from 1.41 cm, 1.15 cm, and 1 cm, respectively. The support medium for the resistive layer is free space (ε_r=1) and the electron beam has a radius of 1 cm. The figures were calculated assuming a resistive layer thickness of 0.1 mm, a support medium thickness of 5 mm, and a frequency of operation of 2 GHz.

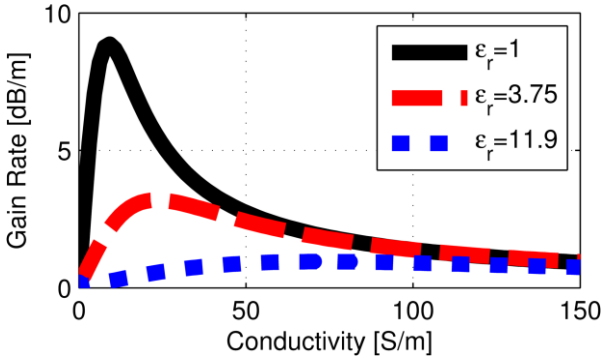

Fig. 5: Gain of the RWA (per meter of axial length of the device) versus the conductivity of the resistive material for three different support materials of air (ε_r=1), glass (ε_r=3.75), and silicon (ε_r=11.9). These figures were calculated assuming a resistive layer thickness of 0.1 mm, a support medium thickness of 5 mm, a 100% fill factor, and a frequency of operation of 2 GHz.

2.3 Metamaterials

Metamaterials (MTMs) are composite structures constructed of sub-wavelength components that produce electromagnetic characteristics that either do not occur in natural materials (e.g. negative index of refraction) or are not readily achievable at certain frequencies of interest (e.g. negative permittivity at microwave frequencies). The use of MTMs has had a very large interest over the last two decades. Their use has been investigated in countless applications across almost all frequencies from sound wave suppression to optical applications. Types of MTMs include epsilon-negative (ENG), mu-negative (MNG), and double-negative (DNG) materials. Fig. 6 presents a graphical interpretation of the various MTM types. The four types of MTMs are discussed in further detail below.

DPS materials are the materials most commonly encountered where both the permittivity and permeability have positive values. Traditional dielectric materials fit into this category of DPS materials. An ENG material is one which has a negative permittivity and a positive permeability. Plasmas are one of the most common sources of ENG response. A plasma exhibits an ENG response when the frequency of the electromagnetic wave interacting with the plasma has a frequency that is less than the plasma frequency. The most common description of this behavior is through the Drude description of a plasma where the relative permittivity if a plasma is:

$$\varepsilon_r = 1 - \frac{\omega_p^2}{\omega(\omega + j\omega_c)}; \qquad (12)$$

where ε_r is the relative permittivity of the dielectric, ω_p is the plasma frequency of the Drude dispersion model, ω_c is the collision frequency of the Drude dispersion model, and ω is the frequency of operation of the device. Opposite of an ENG material, a MNG material exhibits a negative permeability response and positive permittivity. Gyrotropic magnetic materials are one of the natural sources of MNG type materials. DNG materials are a category where both the permittivity and permeability have a negative value. These DNG materials are not found in natural materials, but can be realized through a combination of ENG and MNG materials. In a DNG material, the phase velocity and group velocity of an electromagnetic wave have opposite signs. Therefore, it appears that the phase is advancing as it travels.

For this work we are primarily focused on the investigation of ENG materials. The use of ENG materials is based upon the desired ‘inductive-resistive’ wall admittance. It will be shown in subsequent chapters that an ENG material provides the correct material properties to provide an inductive wall admittance. The use of ENG materials is discussed in more detail in Chapter III.

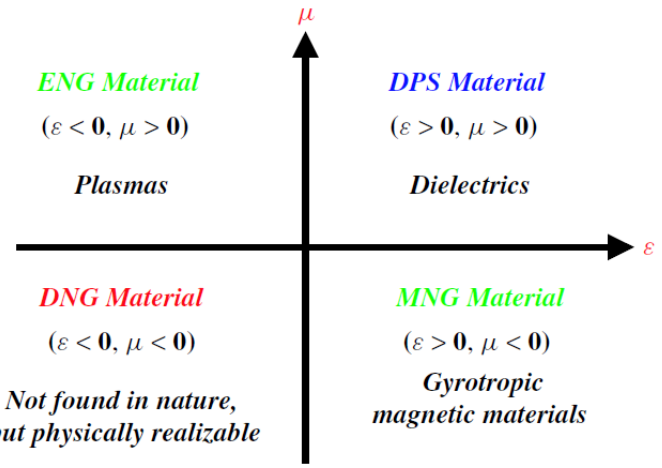

Fig. 6: Graphical representation of the various MTM distinctions [19]. Used with permission © 2006 by the Institute of Electrical and Electronics Engineers, Inc.

2.3 Current Usage of MTMs in VEDs

The topic of MTMs has been a heavily investigated area for the last couple decades. Unsurprisingly, several research groups have investigated how the introduction of MTMs can increase the performance of various VEDs. The investigation of MTMs in VEDs have included traveling wave tubes [20-24] and Cerenkov-like masers [25-27], as well as basic investigations of the coupling between electron beams and MTM structures [28, 29]. In addition, various groups have investigated MNG and DNG MTM designs to achieve backward wave interaction for use in oscillators [30, 31]. While many of these devices have shown promising uses of MTMs in VEDs most of these devices have focused on oscillators, traveling wave type devices, or backward wave structures. Our work is one of the only investigations of using MTMs in a non-traveling wave type device where the electromagnetic energy is amplified through the growth of space charge waves. In addition to developing a novel VED, our work will provide information

useful to future researchers on the interaction of MTM structures with charged particle beams and the HPM capabilities of some MTM structures.

Chapter III: Theoretically Investigate MERWA Concept

Task 1 consisted of theoretically investigating the MERWA concept through both analytic theory and simulation. The results of Task 1 have been published in the IEEE Transactions on Plasma Science (© 2015 IEEE. Reprinted, with permission, from T. Rowe, J. H. Booske, and N. Behdad, Metamaterial-Enhanced Resistive Wall Amplifiers: Theory and Particle-In-Cell Simulations, IEEE Transactions on Plasma Science, Dec. 2015). A summary of these results is presented here.

3.1 Theoretical Study

As part of the theoretical study two possible methods that can be used to implement a MERWA are presented. In the first technique, the dielectric support layer of the conventional RWA shown in Fig. 3 is replaced with a lossless epsilon-negative MTM layer as shown Fig. 7. When a negative permittivity wall liner is present, the radial admittance, as seen by the beam, becomes inductive rather than the capacitive radial admittance encountered in the traditional RWA. While this is a highly idealized operational scenario, examination of this structure allows for a direct comparison of the performance of the MERWA with that of the conventional RWA examined in Chapter II. Specifically, by examining the two-layer heterogeneous structure shown in Fig. 7, it is possible to demonstrate that using ENG MTMs can address both of the major limitations of conventional RWAs: (1) the need to use low dielectric constant materials and (2) the need to have high beam filling factors. Subsequently, a more practical technique to implement MERWAs will be presented in which the electron beam is propagated through a tunnel lined with a single, uniform lossy ENG MTM shell. The theoretical analysis will demonstrate that this structure,

which is much easier to realize in practice, is also able to address the major issues of conventional RWAs and offer large gain values over a broad bandwidth.

3.1a A MERWA using a lossless ENG MTM support medium and a resistive layer

Fig. 7 shows the cross sectional view of the RWA shown in Fig. 3 where the dielectric support medium is replaced with a lossless ENG MTM layer. The gain rate of this device, calculated using the procedure discussed in Section II, for various dielectric constant values of the ENG layer, are presented in Fig. 8. As the permittivity of the MTM support layer is decreased from the relative permittivity of one to a relative permittivity of zero and even negative permittivity values, the gain rate of the device greatly increases. However, if the permittivity is made more negative than -0.5 the gain rate reduces. The negative permittivity value that provides the maximum gain rate is a specific value for this scenario. For any given set of operating parameters (beam power, beam size, MTM layer thickness, etc.), a negative permittivity value can be found that maximizes the gain rate of the device.

As observed, extremely high gain rate values exceeding 100 dB/m (1 dB/cm) can be obtained by using ENG MTM layers as the support medium of the resistive layer in an RWA. However, this design has the drawback that it requires coating a thin resistive material layer on the interior surface of the MTM shell, which could be difficult to construct in practice. In addition, all physically-realizable ENG MTM shells have some degree of loss. Therefore, in the next sub-section we examine a more practical implementation technique for MERWAs.

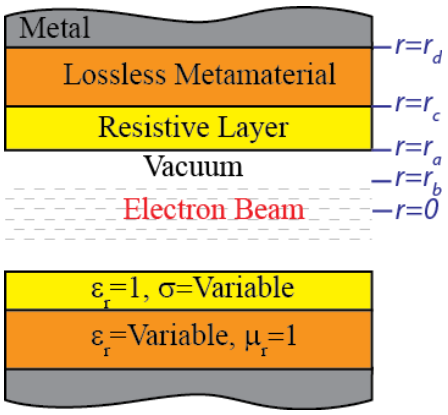

Fig. 7: Cross-sectional view of a MERWA that uses an ENG MTM as the support material for the resistive layer. The resistive material has a relative permittivity and permeability equal to one, but exhibits non-zero conductivity. The MTM support material is lossless and exhibits the permeability of free space, but has a relative permittivity not equal to one.

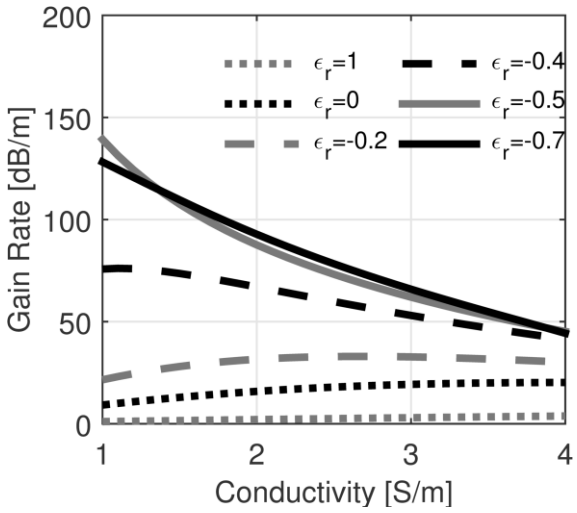

Fig. 8: Gain of the MERWA shown in Fig. 7 versus the conductivity of the resistive medium for different relative permittivity values of the MTM support material. Observe that for a low-loss resistive layer, the gain of the device can be very high if negative permittivity support materials are used. The figures were calculated assuming a beam radius of 0.87 cm, a wall radius of 1 cm (75% fill factor), resistive thickness of 0.1 mm, a support medium thickness of 5 mm, and a frequency of operation of 2 GHz.

3.1b A MERWA using a lossy ENG MTM

An alternative to using a lossless ENG MTM as only the support material for a thin resistive layer is to use a thick lossy MTM layer. This lossy MTM layer functions as both the resistive medium as well as the support medium. A cross-sectional view of this structure is shown in Fig. 9. Using the procedure described in Chapter II, we calculated the gain rate of such a device where the beam radius was 0.87 cm, the inner radius of the lossy MTM was 1 cm, the MTM layer was 5 mm thick, and the device operated at 2 GHz. Fig. 10 shows the gain rate of the single layer MERWA versus conductivity for different permittivity values of the lossy MTM layer. Similar to the 2-layer MERWA, the maximum gain rate of the device increases with a more negative permittivity value until a specific permittivity value is reached. If the permittivity is made more negative than this specific value, -0.5 in this example, the gain rate of the device decreases.

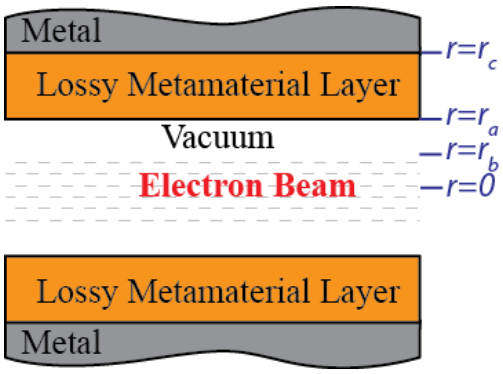

Fig. 9 : Cross-sectional view of a MERWA that uses a lossy ENG MTM as both the resistive medium and support medium in a single integrated layer. The relative permittivity of the MTM layer is negative and contains a non-zero conductance.

Fig. 11 shows the calculated gain rate of this device for various beam fill factors using a MTM shell with a relative permittivity value of -0.62. The gain rate is presented as a function of the

conductivity of the MTM layer. As can be observed, the MERWA using a lossy MTM layer provides very high gain rate values (greater than 150 dB/m) for a wide range of conductivity values. This insensitivity of the gain rate to the exact conductivity value of the lossy MTM layer is extremely beneficial since precisely controlling the conductivity of the MTM layer is difficult in a practical implementation of an ENG structure. Fig. 11 also shows that the gain rate of the structure decreases as the beam filling factor decreases. This, however, is not expected to be a serious limitation in this MERWA for two reasons. First, even though the peak gain rate value decreases with decreasing the beam filling factor, extremely high gain rate values can still be obtained. Moreover, the dielectric constant of the ENG layer used in this example was optimized to achieve the desired gain rate value for the beam fill factor of 100%. For a beam fill factor less than 100%, the dielectric constant of the MTM layer can be changed to recover the desired gain rate value. It should be noted that the gain rates presented throughout this article are not the only factor determining total gain from a device. Additional factors such as input-output coupling, launching loss, saturation, etc. must all be incorporated to determine a device's actual gain.

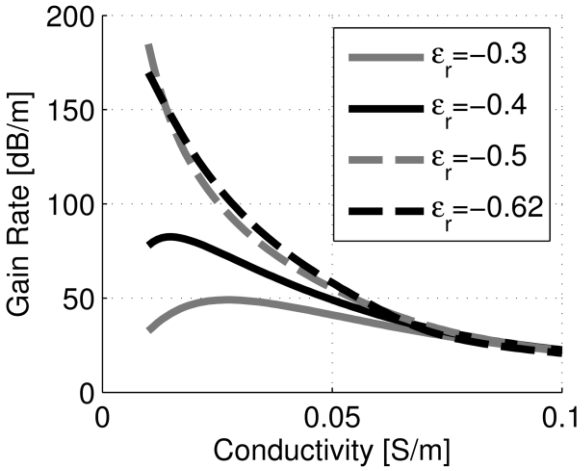

Fig. 10: Gain of the MERWA shown in Fig. 6 versus the conductivity of the resistive medium for different relative permittivity values of the MTM. Observe that the maximum gain value increases by making the permittivity of the MTM more negative up to a maximum gain when the permittivity is -0.5. If the permittivity is made more negative than -0.5 the maximum gain decreases. The figures were calculated assuming a beam radius of 0.87 cm, a wall radius of 1 cm (75% fill factor), MTM thickness of 5 mm, and a frequency of operation of 2 GHz.

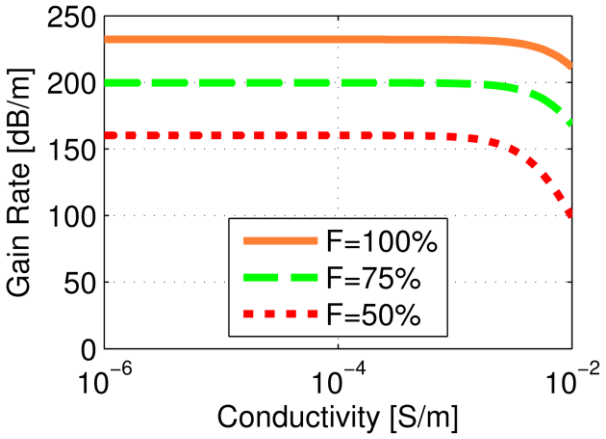

Fig. 11: Gain of the structure shown in Fig. 9 versus the conductivity of the MTM layer for beam fill factors (F) of 50%, 75%, and 100%. To obtain different fill factors the beam radius was held constant (0.87 cm) and the inner radius of the MTM was equal to 1.23 cm, 1 cm, and 0.87 cm, respectively.

To examine the bandwidth of this device, its gain rate was calculated as a function of frequency. To calculate the gain rate versus frequency, the MTM shell was assumed to be a homogeneous dielectric with a Drude-type dispersion. Using a dielectric with a Drude dispersion model emulates a dielectric with a negative permittivity when the plasma frequency of the Drude model is greater than the frequency of operation. The use of a Drude dispersion model for the dielectric material is reasonable because numerous ENG MTM layers have been demonstrated in various experiments to exhibit this behavior [32-34]. The relative permittivity that the MTM shell exhibits can be calculated using

$$\varepsilon_r = 1 - \frac{\omega_p^2}{\omega(\omega + j\omega_c)}; \qquad (13)$$

where ε_r is the relative permittivity of the dielectric, ω_p is the plasma frequency of the Drude dispersion model, ω_c is the collision frequency of the Drude dispersion model, and ω is the frequency of operation of the device. Consistent with the analytic model derived in Section I, the frequency of operation, ω, arises from the assumption that the fields will be time-harmonic with a complex exponential dependence on time in the form of $e^{j\omega t}$. For the MERWA, the negative permittivity associated with the plasma frequency exceeding the operating frequency results in an inductive radial wall admittance.

Fig. 12 shows the calculated gain rate over the frequency range of 1.5 to 2.5 GHz using a MTM with a lossy Drude dispersion model. The parameters of the Drude model used in these calculations are provided in the caption of Fig. 12. The calculated gain rate is very high at the center frequency with moderate gain rates near the band edges. If additional loss is added to the MTM layer (by increasing the collision frequency) the maximum gain rate decreases but the gain rate of the device becomes more uniform across the displayed frequency range. Alternatively, if the collision frequency of the MTM layer is decreased, the maximum gain rate increases, but the bandwidth is decreased. In the example provided, the gain rate exceeds 40 dB/m over the 25% fractional bandwidth of 1.75 – 2.25 GHz. For this particular case with very high peak gain rate, the -3 dB bandwidth is approximately 38 MHz, but this can be increased by decreasing the peak gain rate using a lossier ENG layer.

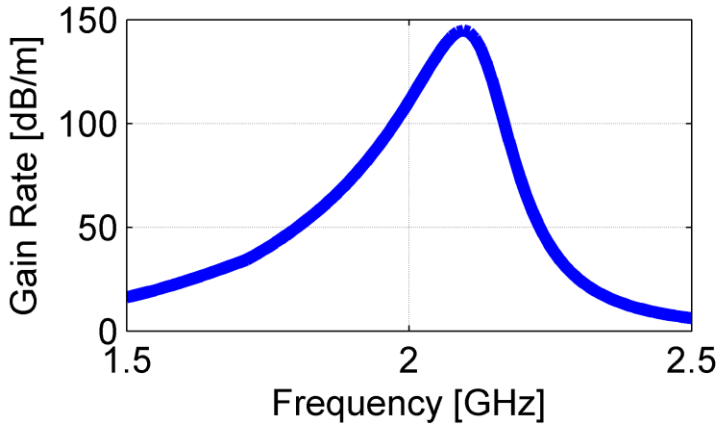

Fig. 12: Gain of the structure shown in Fig. 9 versus the frequency of operation of the device. These calculations assumed a beam radius of 0.87 cm, a wall radius of 1 cm (75% fill factor), and a MTM layer thickness of 5 mm. The MTM layer has a Drude dispersion where the plasma frequency is equal to 2.63 GHz and a collision frequency of $2 \cdot \pi \cdot 0.2$ GHz.

3.2 Particle-In-Cell Simulation Study

To test the theoretical calculations presented in the previous section, the PIC software CST Particle Studio [35] was used to simulate a MERWA. The MERWA model was constructed to simulate a device that is similar to that shown in Fig. 9. However, for convenience, the cross section of the simulated device was made to be square-shaped instead of circular. By using a square cross section the number of mesh cells for the PIC simulation was significantly decreased thereby reducing the simulation time. The model consists of a vacuum drift tube, where the beam travels, surrounded by a lossy MTM shell. A pictorial representation of the simulation model can be seen in Fig. 13. In Fig. 13 a vacuum region is surrounded by a lossy ENG shell (MTM). The medium surrounding the MTM shell is a perfect electric conductor (PEC). Fig. 13 also shows vacuum space in the model that forms a resonant cavity.

A 10 kV, 1 A, circular DC electron beam is passed from right-to-left through a rectangular resonant cavity, operating in the fundamental mode, to velocity modulate the electron beam. The modulated electron beam then travels through the vacuum region surrounded by the MTM shell. A large static magnetic field, sufficient to suppress radial electron motion, is applied along the axial direction of the device.

Similar to the calculations for Fig. 9, the MTM shell in the PIC model was simulated as a homogenous dielectric with a Drude dispersion model. The plasma frequency of the Drude dispersion model was selected to be 2.63 GHz with a collision frequency of $2 \cdot \pi \cdot 0.2$ GHz. The vacuum space of the drift tube has a cross section of 2 cm by 2 cm, the beam has a radius of 0.87 cm, and the MTM layer thickness is 5 mm. The length of the MTM shell is 57.5 cm and it is surrounded by PEC. At the axial end of the drift tube is a perfectly matched layer (PML) which is configured to have a small enough reflection (-150 dB) to ensure that regenerative oscillations do not occur. In addition, the collision frequency of the Drude liner is made large enough to suppress an absolute (backwards wave) oscillation instability that can arise in a lossless Drude-lined RWAs. The model was simulated for 75 ns and particle velocity versus position was plotted at the end of the simulation time. A summary of all of the PIC simulation parameters are reviewed in Table 1.

Table 1: Simulation Parameters

Simulation Parameter	Symbol	Value
Frequency of Operation	ω	$2\pi \times 2$ GHz
Drude Plasma Frequency	ω_p	$2\pi \times 2.63$ GHz
Drude Collision Frequency	ω_c	$2\pi \times 0.2$ GHz
Simulation Time	t_{run}	75 ns
Time Step	t_{step}	0.9 ps
Number of Particles	N_{part}	10^5
Beam DC Voltage	V_0	10 kV
Beam DC Current	I_0	1 A
Beam Radius	r_b	0.87 cm
Drift Tube Radius	r_a	1 cm
MTM Thickness		5 mm
PIC Grid Spacing		0.5 – 1.27 mm^3

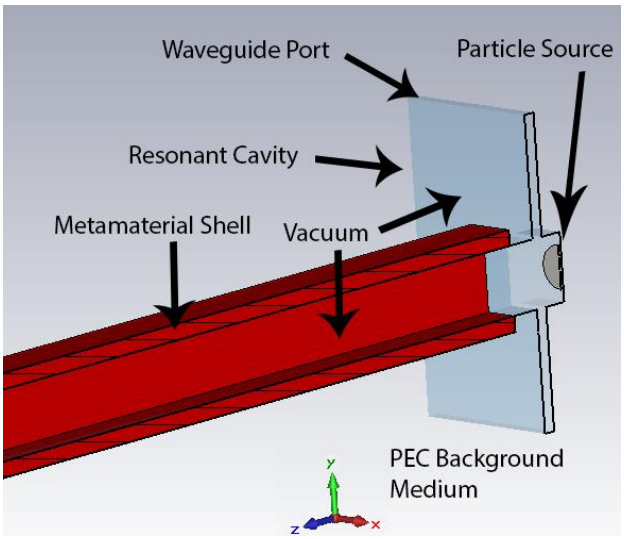

Fig. 13: A cross sectional view of the PIC simulation model of the RWA. In this image the background medium is PEC, the red material is the MTM liner, and the resonant cavity and interior of the MTM liner are vacuum. The electron beam is emitted from a PEC surface on the right side of the image and travels axially through the drift tube from right to left. To velocity modulate the beam, the beam travels through a rectangular resonant cavity which is operated in the fundamental mode to apply an axial electric field to the electron beam, causing velocity modulation.

The particle velocities versus position at the end of the simulation are plotted in Fig. 14. The results in Fig. 14b were obtained with the simulation model described above, while the results in

Fig. 14a were obtained by replacing the MTM with PEC. The comparison of the two phase space plots in Fig. 14 shows that the addition of the ENG MTM is responsible for the emergence of an exponentially growing space charge wave.

The gain rate of the MERWA was estimated by measuring the ac component of the velocity modulation, shown in Fig. 14, at two points along the axis of the device. The two points where the velocity modulation was measured were selected at locations where the modulation was undergoing exponential growth to provide a measurement of the gain rate of the system. Therefore, the first location where the ac velocity modulation was measured at an axial location where the velocity begins to see exponential growth and the second axial location was selected to be before the device reaches saturation. Using the phase space plot, the estimated gain rate of the PIC simulation is 75 dB/m. This value is lower than the theory-predicted value, 110 dB/m, shown in Fig. 12. It is also possible to see in Fig. 14b that a point exists where the velocity modulation of the beam begins to saturate. This saturation is an over bunching of the electron beam, a behavior of the system operating outside of the small signal regime.

Although the gain rate estimated from the PIC simulations is smaller than the theoretically predicted value, the simulation verifies that the MERWA yields an exponentially growing space charge wave with much higher growth rates than expected from conventional, capacitive-impedance RWAs. Further investigation will be necessary to determine the specific reasons why the simulation and theory do not produce identical results. Two possible sources for the lower gain rate seen in the simulation compared to theory can be envisioned. First, the PIC simulations use a MTM shell with a square cross section whereas the theoretical analysis assumes a MTM

shell with a circular cross section. Secondly, at the expense of drastically increasing the simulation times of the structure, the parameters of the numerical simulation models (e.g., the grid size, number of particles, etc.) can be increased to produce a more accurate representation of the MERWA.

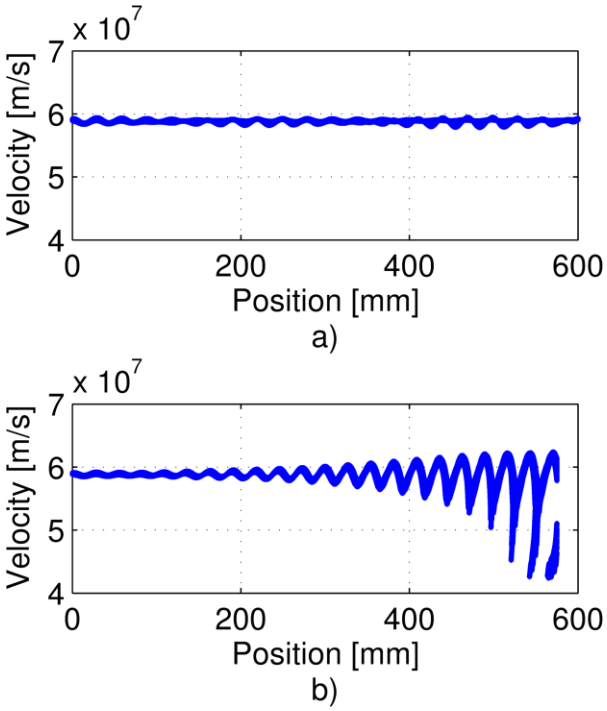

Fig. 14: Velocity phase space of the MERWA a) without a MTM shell and b) with a MTM shell. The growth of the alternating component of the velocity modulation in (b) is a clear indicator that a growing space charge wave exists.

Chapter IV: Backwards Wave Oscillation Suppression in MERWA

As discussed in the Chapter II, one of the major advantages of using a RWA is an inherent suppression of backward waves and immunity to oscillation instabilities. This inherent suppression of the backward wave is because the electron drift tube dimensions are selected such that the structure is cutoff to all transverse magnetic (TM) EM waves. In addition, for the MERWA, we have demonstrated that by using ENG materials as a liner in the drift tube we can greatly enhance device performance. However, in the presented MERWA configuration, where an ENG MTM liner is used along the drift tube, a new hybrid TM mode EM wave emerges that has a passband below the cutoff frequency of the unlined drift tube [36].

This task focused on developing a thorough understanding of this new TM EM wave and determined methods to suppress this wave. To investigate this EM mode we began by calculating and simulating the dispersion diagram of the EM wave. We then examined the interaction of the electron beam with this EM wave by modifying the theoretical model presented by Birdsall and Whinnery [5] to solve a third order system instead of the second order system they presented. The third order system arises because when the EM wave is present, the frequency and wave number of the electron beam can satisfy the cold-tube dispersion relation of the MTM lined waveguide, in which case Pierce's classical 3-wave TWT theory may be applied to evaluate the spatial amplification for this synchronous interaction [37] (synchronous interaction means beam velocity equals slow wave circuit velocity). This task focused on the investigation of a parallel plate configuration of the MERWA. Fig. 15 shows a pictorial representation of the planar, or

parallel plate configuration of the MERWA. In this configuration, the infinite dimension is y, and the electron sheet beam travels along the z-axis. The parallel configuration was selected to simplify the mathematics and is a closer representation of the practical device that will be built for experimental testing, discussed in more detail in the next chapter. Finally, we then used the calculated Pierce theory to determine the gain of the traveling wave and proposed four different suppression methods, discussing the benefits and drawbacks of each methods.

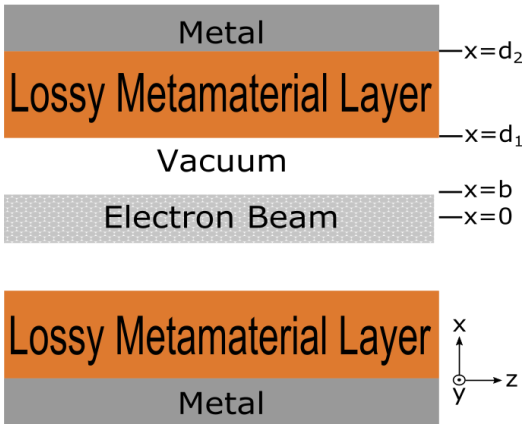

Fig. 15: Configuration of a parallel plate MERWA where the beam travels along the z direction. Both the beam and the waveguide are infinite in the y direction. The lossy MTM liner has a thickness of $s = d_2 - d_1$ and is assumed to be a homogeneous dielectric with a Drude dispersion. The plasma frequency of the Drude medium is ω_p. The sheet beam has a thickness of 2b.

4.1 Dispersion of the EM Mode

Before examining the Pierce theory of the synchronous wave interaction, it was first important to fully understand the new EM mode, particularly the dispersion of this mode. The dispersion is necessary to determine the cold circuit wave velocity, u_{cc}, which is necessary for the Pierce theory. The existence of the new EM mode that is introduced when the drift tube is lined by an ENG material wave was initially hinted at by Birdsall and Whinnery [1] where they stated that if the wall of the structure has a purely inductive impedance, it is possible to have wave

propagation in the absence of the electron beam. Similarly, in the MERWA, the passband of this new mode occurs when the boundary conditions of the structure are such that the wall has an 'inductive' admittance (Y_{wall} in the previous section is imaginary and less than zero). Another way of understanding this below cutoff EM wave is to view this behavior through a transmission line perspective, from the axis of the device outward. Because the cross section of the device is very small, the radial admittance of the structure from the wall inward is capacitive (vacuum space that is less than a quarter wavelength). From the wall outward, when a less than quarter wavelength thick ENG liner is present, the wall can exhibit a purely inductive wall impedance. When the inward capacitance and outward inductance form a 'resonant' system, an EM wave can propagate.

To examine the new EM wave we have evaluated the cold circuit dispersion using CST and compared that to the analytic dispersion. Because the wave is below the cutoff of the unlined structure, simulation becomes slightly difficult, but two methods to simulate the structure will be presented here. To solve the dispersion of an anisotropic Drude lined parallel plate waveguide it is necessary to solve the equation presented in [28]

$$1 - \left(\frac{\varepsilon_0 \beta_{x,2}}{\varepsilon_{z,2} \beta_{x,1}}\right) \tan\left(d_1 \beta_{x,1}\right) \tan\left((d_2 - d_1)\beta_{x,2}\right). \qquad (14)$$

In (14) the x-direction wavenumber in the vacuum space (region 1) is

$$\beta_{x,1}^2 = \left(\frac{\omega^2}{\mathrm{c}^2} - \beta_z^2\right), \qquad (15)$$

and in the liner (region 2) is

$$\beta_{x,2}^2 = \frac{\varepsilon_{z,2}}{\varepsilon_{x,1}}\left(\omega^2 \varepsilon_{x,2}\mu_{y,2} - \beta_z^2\right), \qquad (16)$$

where $\varepsilon_{x,2}$, $\varepsilon_{z,2}$, and $\mu_{y,2}$ are the x-directed permittivity, z- directed permittivity, and y- directed permeability of the liner, respectively. In addition, c is the speed of light in free space, ε_0 is the permittivity of free space, and d_1 and d_2 are defined in Fig. 15. Fig. 16 shows the dispersion of a parallel plate MERWA configuration where the Drude liner is isotropic and has a plasma frequency of 3 GHz.

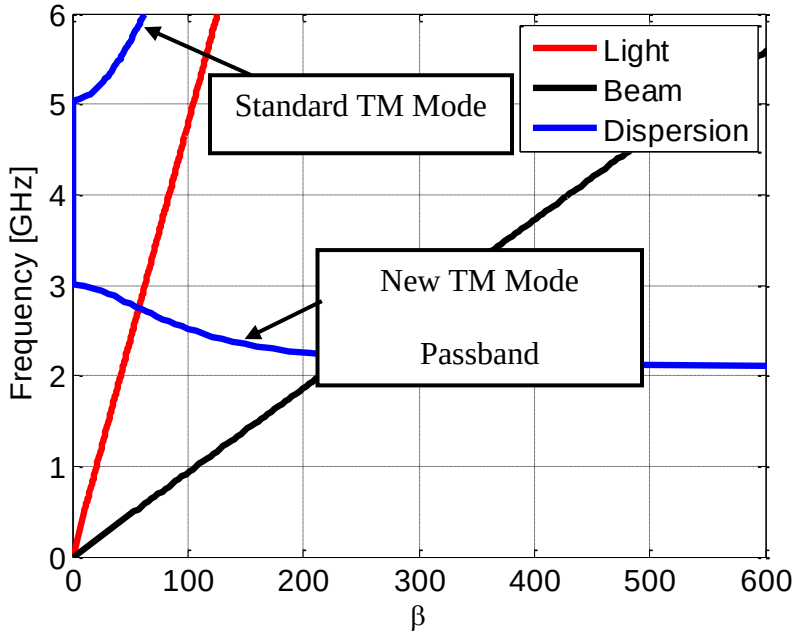

Fig. 16: Dispersion of the lowest order TM Mode of parallel plate waveguide lined with homogenous, isotropic Drude-type liners. The structure for these calculations had the following dimensions: d_1 = 10 mm, d_2 = 15 mm, and b = 8.7 mm, with reference to Fig. 15. The Drude-type liner had a plasma frequency of was 3 GHz and the collision frequency was 0.

Simulating the dispersion of a structure that contains a dispersive material can be slightly difficult. Two methods were used in this work to calculate the dispersion of this structure: 1) an eigenmode solver with an iterative method and 2) a time domain (TD) analysis.

The dispersion diagram can be calculated using an eigenmode simulation with periodic boundary conditions [38, 39]. A variation in the phase shift of a periodic boundary condition is equivalent to varying the wavenumber of the simulation ($\beta = \phi d$) where ϕ is the phase shift and d is the spacing between the periodic boundaries. Fig. 17 shows the unit cell model used to calculate the eigenmode frequencies. One problem exists with calculating the dispersion in this way. Since this is an eigenmode calculation, the solver must first determine the permittivity of the material before solving the eigenmode. If a material in the structure is dispersive, like an ENG material, one can only know the permittivity of the material if the frequency is known. Since the eigenmode calculation is trying to determine the frequency it is possible to see that there is a problem with this method.

One way to correct the eigenmode method, which is what we have done for this work, is to use an iterative method approach. The iterative method used the following steps: 1) we started with an assumed solution (frequency) to evaluate the material's permittivity and used this to calculate the eigenmode solution, 2) we then used the new eigenmode solution to re-evaluate the permittivity of the dispersive material, 3) re-calculate the eigenmode frequency and repeated the process. This iterative method was repeated for each desired wavenumber point on the dispersion curve. Alternatively, for each point on the dispersion curve, one can set frequency at which the dispersive material is evaluated and then vary the phase shift between the periodic boundaries (vary the wavenumber) using the iterative method to converge to a valid solution. Each of these two methods (fix the phase shift and vary frequency vs fixing the frequency and varying the phase shift) have different advantages for various shaped dispersion curves. For the dispersion

curves presented in this work, the frequency has been held constant and then the phase shift varied to converge to a solution for a given point on the dispersion curve.

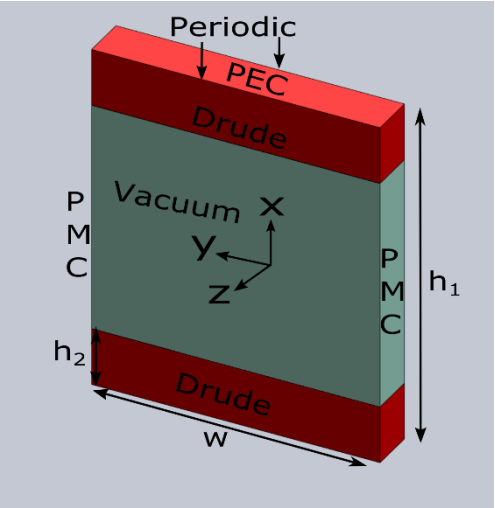

Fig. 17: Eigenmode model of the Drude lined planar structure used to calculate the dispersion. To model a parallel plate configuration the boundaries at $y_{min,max}$ were configured to be perfect magnetic conductors, the boundaries at $x_{min,max}$ were perfect electric conductor, and the boundaries at $z_{min,max}$ were periodic. The Drude liner had a permeability of free space and a permittivity that followed the Drude model with a plasma frequency of 3 GHz and collision frequency of 1 Hz. The overall height of the structure, h_1, was 30 mm and a width, w, was 25 mm. The period of the structure was 4 mm.

In a TD analysis it is difficult to couple the energy into the 'cutoff' structure. To accomplish this, two larger waveguide structures were added to the ends of the MTM lined structure. By using larger waveguides at either end it was possible to assign ports to the ends of the larger waveguides to couple energy into the system. Using this method provided a slight problem because of the large change in wave impedance between the larger waveguides and the smaller lined waveguide. The large difference in impedance resulted in a Fabry-Perot type behavior inside of the lined waveguide. Nevertheless, it was possible to calculate the dispersion by using an electric field monitor in the structure for a specific frequency and then measure the wavelength (wavenumber) from the electric field plot. Fig. 18 shows the CST TD simulation model that was used to calculate the dispersion of this system.

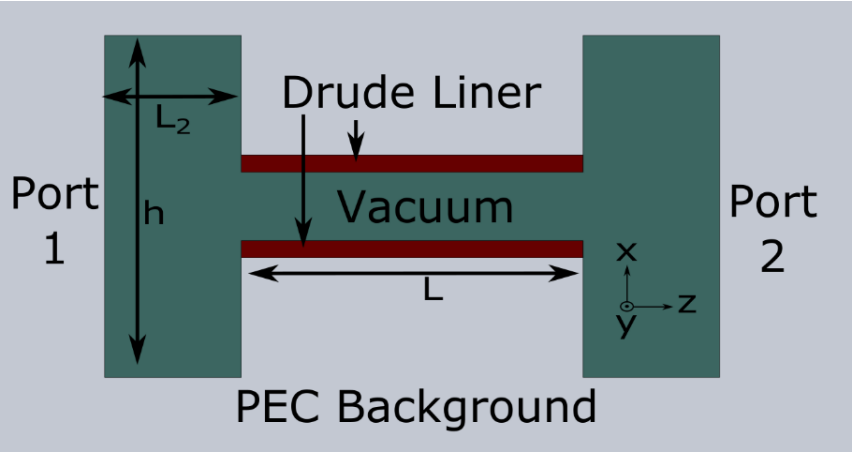

Fig. 18: Time domain simulation of an infinite parallel plate waveguide with an isotropic Drude liner. To model an infinite parallel plate configuration, the boundaries at $y_{max,min}$ were perfect magnetic conductors. The ports at either end of the device were configured as waveguide ports and the S-parameters were measured. The lined portion of the structure had the same height and width and material properties as the eigenmode structure shown in Fig. 17. The other dimensions of the structure were: $L = 150\ mm, L_2 = 100\ mm,$ and $h = 160\ mm$.

Fig. 19 presents the analytic dispersion of the planar configuration of the device along with the results of the eigenmode and TD simulations discussed above. The TD simulations have a much lower accuracy because they require the user to measure the wavelength of the electric or magnetic field along the length of the device, which inherently will have some user error; however, the TD simulations required much less simulation time because an iterative method was not required. On the other hand, the eigenmode simulations, which did require more time because of the iterative method, were much more accurate and could also calculate many more points along the dispersion curve. The number of points that could be calculated using the TD method are limited to wavelengths where the length of the lined waveguide section is equal to an integer number of half wavelengths, due to the Fabry-Perot behavior. Nevertheless, both of these methods are able to compute the expected dispersion of this structure.

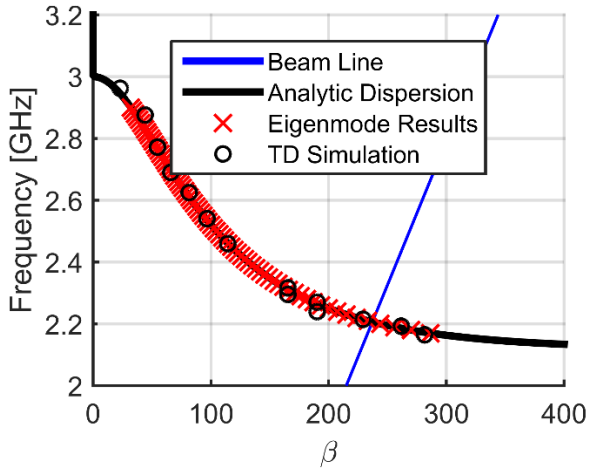

Fig. 19: Analytical dispersion of an infinite parallel plate waveguide with an isotropic Drude liner compared to the results obtained from CST using both and eigenmode and TD simulation.

4.2a Pierce Theory

The EM wave, which has a negative group velocity, can couple to the electron beam. The coupling between the EM wave and the electron beam can be observed on a dispersion curve when the beam line and EM dispersion line cross. An example of an EM mode that can interact with an electron beam is shown in Fig. 19. In Fig. 19, the beam line crosses the dispersion line at approximately 2.2 GHz allowing for the potential of coupling between the electron beam and the EM wave. Knowing the dispersion of the structure, it was possible to calculate the gain of the backwards EM mode. The theory on backward wave interaction is based upon the work completed by Pierce [37]. Pierce demonstrated that two equations can be used to solve for the one-dimensional space charge wave numbers: 1) the electronic equation and 2) the circuit equation. The electronic equation relates the ‘current’ and ‘electric field’ of the electron beam, while the circuit equation relates the current flow and electric field in the slow wave structure. The second equation is called the circuit equation because Pierce uses a transmission line equivalent circuit model to determine the current and electric field ratio of the traveling EM

wave. Since the currents in the slow wave structure are related to the currents in the beam, we can combine these two equations to determine the propagation constants of the space charge wave. The basic theory and equations have been summarized here for clarity.

The first equation is the electronic equation, which is derived by a solution of Maxwell's equations and the continuity equation. The derivation of this equation is not included here, but can be found in numerous works [37, 40, 41]. The electronic equation is

$$i_1 = -\frac{je\beta_e\rho_0}{u_0(\Gamma - j\beta_e)^2}E_1, \qquad (17)$$

where Γ is the propagation constant of the wave solutions, β_e is the wave number of the electron beam, u_0 is the electron beam velocity, ρ_0 is the space charge density of the electron beam, e is the charge of an electron, i_1 is the ac variation of the beam's current, and E_1 is the ac component of the electric field. We can re-write this equation in terms of a beam current and voltage as

$$i_1 = \frac{j\beta_e I_0}{2V_0(\Gamma - j\beta_e)^2}E_1, \qquad (18)$$

where I_0 and V_0 are the DC beam current and voltage, respectively. In Eqns. (17) and (18), the ac quantities ω and Γ are assumed to vary as

$$e^{j\omega t - \Gamma z}. \qquad (19)$$

The second equation is the circuit equation. The circuit equation is based on Pierce's derivation that demonstrates that the RF circuit (the wave guide and liner for the MERWA) can be described as a transmission line with an effective capacitance and inductance per unit length, resulting in a medium with an effective impedance and propagation constant. In Pierce's work he

applied this principle using a transmission line with series inductors and parallel inductors (similar to a traditional transmission line). However, in this work we were interested in a backwards EM wave. It can be shown that when the backwards EM wave is of interest, which has a negative group velocity, the circuit equation presented by Pierce is modified by a change of sign in the circuit equation [41]. This change in the sign of the circuit equation is equivalent to a switch of the inductor and capacitor locations in the equivalent circuit model of the transmission line. Therefore, the circuit equation for the backwards wave neglecting space charge effects is [41]:

$$E_1 = \frac{+\Gamma^2 \Gamma_0 K_0}{(\Gamma^2 - \Gamma_0^2)} i_1 \qquad (20)$$

where Γ_0 the propagation constant of the cold circuit wave, Γ is the propagation constant of the space charge wave, and K_0 is the Pierce interaction impedance, discussed below.

Eqns. (17) and (20) (circuit and electronic equation), were combined to arrive at the final equation which was used to solve for the propagation constants Γ:

$$1 = \left[\frac{\Gamma^2 \Gamma_0 K_0}{\Gamma^2 - \Gamma_0^2}\right]\left[\frac{j\beta_e I_0}{2V_0(\Gamma - j\beta_e)^2}\right]. \qquad (21)$$

To solve this equation, Γ_0 was taken from the dispersion diagram. In addition, we needed to calculate K_0 which will be discussed in more detail below. The solution of (21) is valid for a system that assumes that the space charge is negligible. In the case of the MERWA, the space charge is not negligible so the circuit equation must be modified to account for the space charge. The next section will discuss how the equation can be modified.

4.2b Pierce Theory with the Addition of Space Charge

To account for space charge effects we have to change E_1 of the circuit equation, (20), to be

$$E_1 = E_{1c} + R_{sc}E_{1s} \qquad (22)$$

where E_{1c} represents the electric field due to the EM circuit wave, i.e. the circuit equation derived in the previous section,

$$E_{1c} = \frac{\Gamma^2\Gamma_0 K_0}{(\Gamma^2 - \Gamma_0^2)}\, i_1, \qquad (23)$$

R_{sc} is the space charge reduction factor, and E_{1s} is the electric field due to the local space charge. E_{1s} can be derived from Poisson's equation

$$\frac{\partial E_{1s}}{\partial z} = \frac{\rho_1}{\varepsilon_0}, \qquad (24)$$

where ρ_1 is the first order ac component of the electron beams space charge density. In addition to Poisson's equation we need the continuity equation,

$$\frac{\partial i_1}{\partial z} = -j\omega\rho_1. \qquad (25)$$

Equations (24) and (25) can be re-written to obtain (using Fourier time harmonic analysis, and assuming variation with $e^{-\Gamma z}$)

$$-\Gamma E_{1s} = \frac{\rho_1}{\varepsilon_0}, \qquad (26)$$

and

$$-\Gamma i_1 = -j\omega\rho_1. \qquad (27)$$

We then combined (26) and (27) to

$$E_{1s} = j\frac{i_1}{\omega\varepsilon_0}. \qquad (28)$$

Using (28) with E_{1c}, (23), the total electric field, E_1 can be written as

$$E_1 = \left[\frac{\Gamma^2\Gamma_0 K_0}{(\Gamma^2 - \Gamma_0^2)} + j\frac{R_{sc}}{\omega\varepsilon_0}\right] i_1, \qquad (29)$$

which is the new circuit equation that includes the effect of space charge forces. This 'new' circuit equation was then combined along with the electronic equation, (17), the final transcendental equation is now

$$1 = \left[\frac{\Gamma^2\Gamma_0 K_0}{(\Gamma^2 - \Gamma_0^2)} + j\frac{R_{sc}}{\omega\varepsilon_0}\right] \frac{j\beta_e I_0}{2V_0(\Gamma - j\beta_e)^2}, \qquad (30)$$

which can be rewritten using a change of variables to the form

$$1 = \left[\frac{\Gamma^2\Gamma_0 K_0}{\Gamma^2 - \Gamma_0^2}\right]\left[\frac{j\beta_e}{(\Gamma - j\beta_e)^2 + \beta_q^2}\frac{I_0}{2V_0}\right], \qquad (31)$$

where

$$\beta_q = \beta_e\frac{\sqrt{4QC^3}}{1 + \sqrt{4QC^3}}, \qquad (32)$$

C is the Pierce Parameter, discussed more below, and Q is the Pierce space charge parameter.

This transcendental equation is a fourth order equation for the propagation constants, Γ. To reduce the order of the problem (from fourth to third) and to solve this equation we can make some assumptions. First, we assume that for interaction to occur, the EM wave propagation constant must be close to that of the beam, i.e.

$$\Gamma_0 = j\beta_e + jh, \tag{33}$$

where

$$h = b\beta_e C, \tag{34}$$

$$C^3 = \frac{K_0 I_0}{4V_0}, \tag{35}$$

$$K_0(r) = \frac{|E_z(r)|^2}{2\beta_p^2 P_z}, \tag{36}$$

$$b = \frac{u_0 - u_{cc}}{C u_{cc}}, \tag{37}$$

and u_{cc} is the cold circuit wave propagation speed.

We also assume, under small signal approximations, that the presence of the electrons has only a small effect on the propagation constant, therefore

$$\Gamma = j\beta_e - \xi, \tag{38}$$

where

$$\xi = \delta\beta_e C. \tag{39}$$

This small signal assumption of Γ is what reduced the fourth order problem to a third order one. The solution that it ignores is a EM solution that travels in the direction opposite the direction we are investigating (the ignored solution is a forward EM wave).

Assuming ξ and h are small, we can reduce the original transcendental equation to

$$\delta^2 = \frac{1}{b - j\delta} - 4QC, \tag{40}$$

where

$$\beta_q = \beta_e \frac{\sqrt{4QC^3}}{1+\sqrt{4QC^3}}. \qquad (41)$$

We can re-write the cubic equation in the standard polynomial form:

$$\delta^3 + jb\delta^2 + 4QC\delta + j(4bQC - 1) = 0. \qquad (42)$$

To solve (42), we need b and $4QC$. The calculation of these parameters as well as the interaction impedance are discussed in the next section.

4.3 Calculating Interaction Impedance

The interaction impedance is the ratio of the axial electric field squared to that of the power traveling through the cross section of the device. The interaction impedance for a given radial location is equal to

$$K_{int}(r) = \frac{|E_z(r)|^2}{2\beta^2(\omega)P_z}, \qquad (43)$$

where P_z is the Poynting power and β is the wavenumber of the EM wave. Fig. 20 presents the analytically calculated interaction impedance for the structure discussed in Fig. 17. The equations used to solve this analytically for the parallel plate structure are discussed in Appendix 1. The CST simulation results presented in Fig. 20 use the same equations as the analytical result, but instead of using the analytic electric field the simulations result used the eigenmode electric and magnetic fields to calculate P_z and subsequently K_{int}. The results presented in Fig. 20 are the 'on-axis' interaction impedance, where the axial electric field at $r = 0$ is used to compute the interaction impedance, i.e. $K_{int}(r = 0)$. This interaction impedance is a simpler

calculation but is less accurate than the 'beam averaged' interaction impedance used in some other works where the electric field is averaged over the entire cross section of the electron beam, and that averaged electric field is used to calculate the interaction impedance.

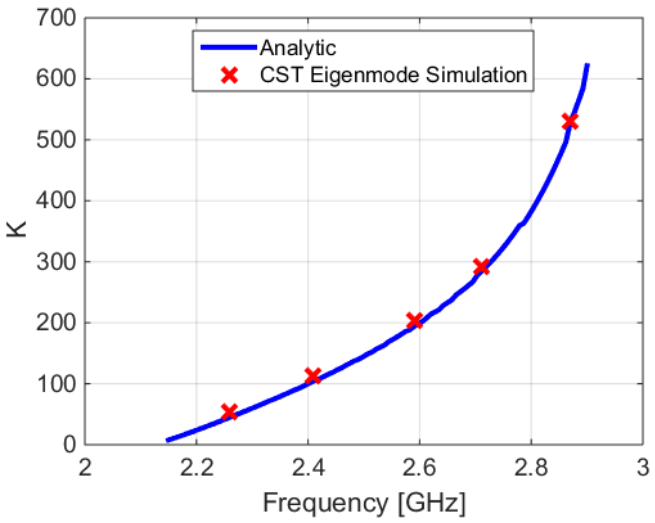

Fig. 20: Calculated on-axis interaction impedance of the structure discussed in Fig. 17. The eigenmode simulations results used the electric and magnetic fields calculated by the simulation to determine the time-averaged power and to calculate the interaction impedance.

Using the calculated interaction impedance we calculated the Pierce parameter, C, using (35) with a beam that had a voltage of 10 kV and carried 1 A of current. Fig. 21 presents the calculated Pierce parameter versus frequency.

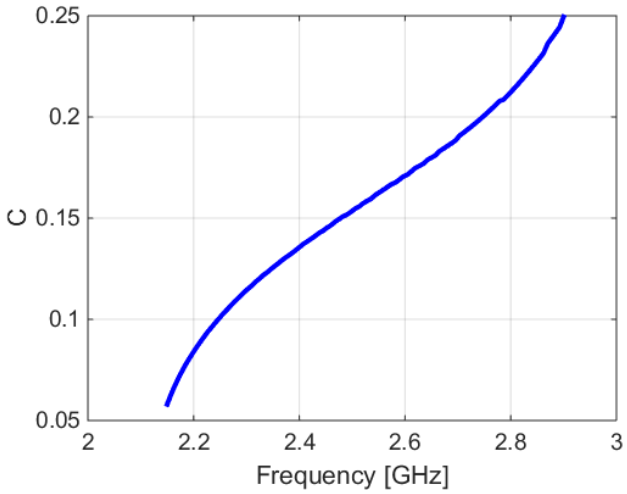

Fig. 21: Pierce parameter, (35), of the MERWA configuration discussed in Fig. 17. The beam was assumed to have a voltage of 10 kV and carry 1 A of current.

We then used the calculated dispersion of the structure, shown in Fig. 16, along with the calculated Pierce parameter in Fig. 21, to determine *b* using (37). The calculated *b* value is presented versus frequency in Fig. 22.

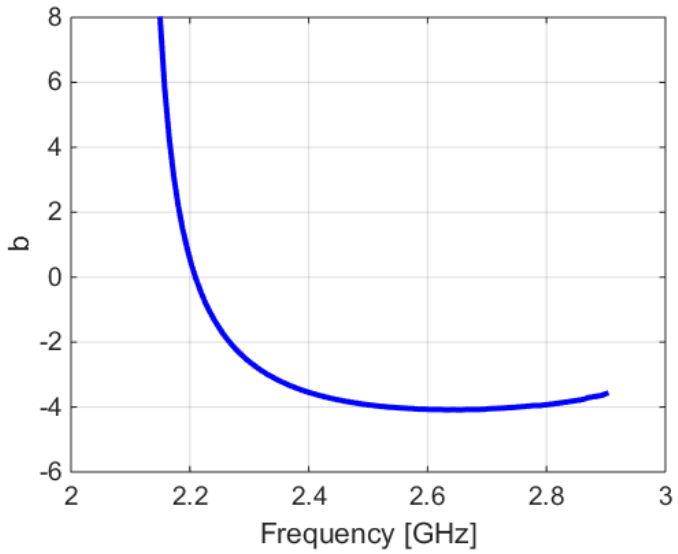

Fig. 22: Analytic calculation of the *b* value of (37) for the MERWA configuration discussed in Fig. 17. To calculate the *b* value it was assumed that the beam voltage was 10 kV and the current was 1A.

Using b from Fig. 22, along with the Pierce parameter of Fig. 21, the three complex wave numbers can be calculated using (42). Fig. 23 presents the real and imaginary parts of the complex wave numbers versus frequency assuming a moderate Q value of 0.1. A more accurate determination of Q will be necessary for accurate results, but the Q of 0.1 was used for initial estimation of the gain.

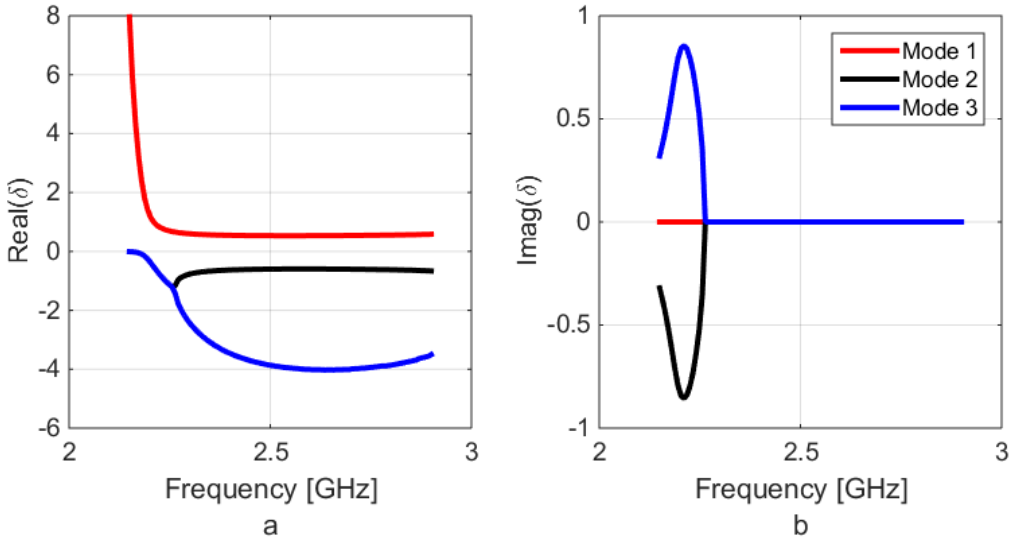

Fig. 23: Real a) and imaginary b) part of the three complex wave numbers from (42) using the b values of Fig. 22 and the Pierce parameters shown in Fig. 21. For these calculations Q was assumed to be 0.1.

4.4 Calculating Backwards Wave Gain

Using the solutions for δ, we obtain three complex propagation constants ($\Gamma_n = j\beta_e - \beta_e C\delta_n$). The fourth root is the ignored forward wave. The specific method used to solve the gain of the backwards wave was based upon the work presented in [41], and is summarized here for clarity.

To calculate the backwards wave gain it was necessary to determine the total electric field as a function of axial position, z, and evaluate the change in the electric field at two different positions in z (input and output). To create an equation of the total electric field we needed to enforce boundary conditions. We selected the initial conditions to be when the velocity and current modulation both equal zero, at the end of the device ($z = 0$), and that the sum of the fields of the three waves equals E_0 at $z = 0$. The end of the device is defined as $z = 0$ to simply the mathematics as we are evaluating a backwards wave that 'starts' at the end of the device. The boundary conditions can be mathematically described as:

1) The velocity modulation boundary condition:

$$\sum_{\nu=1}^{3} \frac{\Gamma_\nu - j\beta_e}{(\Gamma_\nu - j\beta_e)^2 + \beta_q^2} = 0 \qquad (44)$$

2) The current modulation boundary condition:

$$\sum_{\nu=1}^{3} \frac{1}{(\Gamma_\nu - j\beta_e)^2 + \beta_q^2} = 0 \qquad (45)$$

3) The field summation boundary condition:

$$\sum_{\nu=1}^{3} E_\nu(z = 0) = E(0) \qquad (46)$$

We then applied these three boundary condtions to determine the electric field of each mode (E_1, E_2, E_3) at $z = 0$. To find the electric field at an arbitrary z, the coefficients E_1, E_2, E_3, were multiplied by the corresponding propagation constants ($\Gamma_1, \Gamma_2, \Gamma_3$). The resulting equation for the electric field at an arbitrary point z is

$$E(z) = E_0\left[\frac{(\Gamma_1 - j\beta_e)^2 + \beta_q^2}{(\Gamma_1 - \Gamma_2)(\Gamma_1 - \Gamma_3)}e^{-\Gamma_1 z} + \frac{(\Gamma_2 - j\beta_e)^2 + \beta_q^2}{(\Gamma_2 - \Gamma_1)(\Gamma_2 - \Gamma_3)}e^{-\Gamma_2 z} + \frac{(\Gamma_3 - j\beta_e)^2 + \beta_q^2}{(\Gamma_3 - \Gamma_2)(\Gamma_3 - \Gamma_1)}e^{-\Gamma_3 z}\right]. \quad (47)$$

We then evaluated (47) at $z = L$, and made some variable substitutions to arrive at:

$$E(z = L) = E(0)e^{-j\beta_e L}\left[\frac{\delta_1^2 + 4QC}{(\delta_1 - \delta_2)(\delta_1 - \delta_3)}e^{\beta_e CL\delta_1} + \frac{\delta_2^2 + 4QC}{(\delta_2 - \delta_1)(\delta_2 - \delta_3)}e^{\beta_e CL\delta_2} + \frac{\delta_3^2 + 4QC}{(\delta_3 - \delta_2)(\delta_3 - \delta_1)}e^{\beta_e CL\delta_3}\right]. \quad (48)$$

Using knowledge of the electric field value at two special locations, the gain of the backwards wave is

$$G = \left|\frac{E(0)}{E(L)}\right|^2, \quad (49)$$

or

$$G = \left|e^{-j\beta_e L}\left[\frac{\delta_1^2 + 4QC}{(\delta_1 - \delta_2)(\delta_1 - \delta_3)}e^{\beta_e CL\delta_1} + \frac{\delta_2^2 + 4QC}{(\delta_2 - \delta_1)(\delta_2 - \delta_3)}e^{\beta_e CL\delta_2} + \frac{\delta_3^2 + 4QC}{(\delta_3 - \delta_2)(\delta_3 - \delta_1)}e^{\beta_e CL\delta_3}\right]\right|^{-2} \quad (50)$$

Fig. 24 presents the calculated gain using (50), as a function of frequency. The gain was calculated using the parameters of the device described in Fig. 16 and the calculated Pierce parameter, b value, and propagation constants presented in Fig. 21, Fig. 22, and Fig. 23,

respectively. Fig. 24 shows that the gain of the backwards wave is strongly dependent upon the frequency of the wave and has a peak gain at a frequency near the intersection point of the dispersion curve and the beam line. For optimal MERWA performance, it will be best to operate the device at a frequency not equal to where the peak gain occurs as the backward wave gain can interfere with MERWA gain. Further, the very high peak of the backward wave gain suggests an instability point where the device may oscillate even if operated at a different frequency. To prevent this oscillation it is desirable to reduce this peak gain, which can be done by one of the suppression methods discussed in the next section.

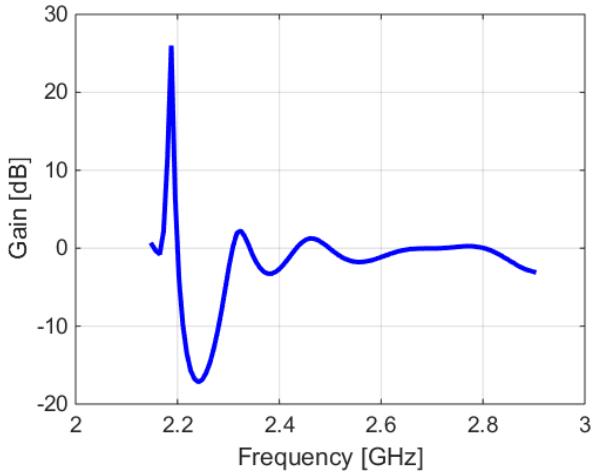

Fig. 24: The gain of a backwards EM mode versus frequency for a device with the parameters discussed in Fig. 23. For this calculation we assumed a device with a length of 10 cm.

4.5 Suppression Techniques of Backwards Wave

Based upon the calculated gain of the backwards wave, we can predict if an oscillation will arise (the gain peaks at high gain rates). With knowledge of backwards wave oscillation, it was necessary to implement some method to suppress the backwards EM wave to prevent oscillation;

however, it was also important to note that the suppression of the backwards wave may affect other device performance objectives. The performance objectives of a device often include overall gain, stability of backward wave oscillation suppression, efficiency, and bandwidth. To an engineer, the overall performance of the device will be a combination of one or more of the device objectives, depending on the end application. Ideally, the suppression of this backwards EM wave will ensure that oscillation does not occur, but still allow for large gain resistive wall amplification.

Traveling wave tubes (TWTs) often also have problems of backward wave oscillations being excited. In TWTs, there are various methods to suppress backwards wave interaction typically at the cost of some other properties of the device. Some of these methods include:

- Using intentional structure loss to damp the backwards EM wave at the cost of reduced gain [40]
- Introducing a slow change in the pitch of the slow wave structure to achieve a 'velocity tapering' effect which increases the devices efficiency and bandwidth [40] at the cost of reduced peak gain
- Introducing lossy severs in the device to increase stability against oscillation but at the cost of reduced gain [40]
- The introduction of subwavelength intentional randomization of spatial circuit features can also suppress the backwards wave at a small cost of reduced gain [42]

Our preliminary investigation of the TM mode in the MERWA demonstrate that these same options are available for this device. Therefore, we have proposed four methods to suppress the gain and oscillation of the backwards wave mode: 1) adding distributed lossy material to the ENG liner, 2) shortening the drift tube to be shorter than the minimum oscillation length, 3) adding discrete loss or severs to damp EM wave propagation, and 4) intentional randomization of the MTM.

Each of these suppression methods have benefits and drawbacks. Overall, the suppression of the backwards wave gain usually comes at the cost of peak device gain and may or may not affect the bandwidth of the device. Therefore, to select the best suppression technique it is necessary to investigate each of the mentioned techniques and how they affect all of the device parameters (peak gain, bandwidth, stability, etc.). The investigation of all four of the mentioned suppression techniques to determine the optimal method would be a tremendous task and is outside the scope of this work. For this work, we have elected to focus on investigating the distributed loss suppression technique and examining the effects on device performance. However, all four of these suppression methods are discussed in this section.

The distributed loss method was selected for a variety of reasons; however, the most important reason we have elected to investigate this method is because it is one of the simplest methods to experimentally replicate.

4.5a: Distributed Loss

Distributed loss is arguably one of the simplest methods to suppress backwards wave gain. In TWTs, distributed loss is incorporated by constructing the slow wave circuit of the device with materials that have moderate loss at the frequency of operation. In the MERWA, the distributed loss method was implemented by adding loss to the MTM liner structure. The distributed loss technique was implemented in the results discussed in Task 1 where the collision frequency of the Drude material liner was increased to suppress the oscillation behavior. In a practical device, we implemented a distributed loss by adding lossy materials to the liner area, including colloidal graphite in addition to using materials of small to moderate loss to construct the individual elements of the MTM structure, which are discussed in more detail in Chapter VII. The use of

distributed loss may not be the best method to suppress backwards wave gain because it may or may not reduce the forward wave gain, but it was the easiest method initially experimentally implement.

4.5b: Shortened Drift Tube

It is also possible to shorten the length of the device to help suppress the oscillation of the backwards wave. The basis of this suppression method is based on the fact that the gain of the backwards wave is strongly dependent on the length of the device. The calculation of the backwards gain can be computed using (50) and varying the length of the device, L. Fig. 25 presents the gain of the backwards mode versus the length. It is possible to see in Fig. 25 that the gain of the backwards wave is strongly dependent on the device length and has a very large gain at a specific length. In fact, we can define the peak point as the minimum oscillation length [41]. If the device is made longer than this minimum oscillation length then it will have an absolute instability and an oscillation will develop because some portion of the device with be the ‘length’ at which oscillation will occur. Therefore, if the length of the device is kept sufficiently below the minimum oscillation length, it is possible to suppress the backwards wave gain while still realizing forward gain.

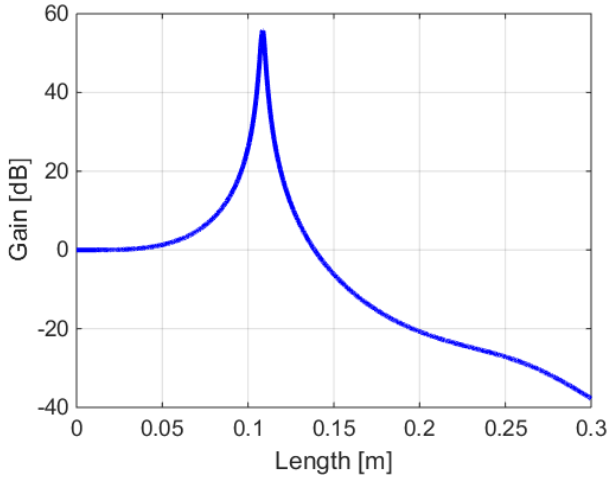

Fig. 25: The gain of a backwards EM mode versus axial length for a device using the same parameters as those discussed in Fig. 24 but by varying the length L and keeping the frequency constant at 2.19 GHz ($b = 1.5$).

In addition, this use of minimum lengths may also be beneficial for a proposed research topic of the future which would be a very broadband MERWA. This very wideband MERWA is constructed by varying the plasma frequency of the liner along the length of the device, as depicted by Fig. 26. By using different MTM 'sections' along the device each section will amplify signals over a given frequency band and each section will be kept below the minimum oscillation length to prevent device oscillation. In this configuration, the 'length' of the device corresponds to the length of each individual section because the passband is a function of the plasma frequency and is therefore different for each section preventing propagation along the entire device.

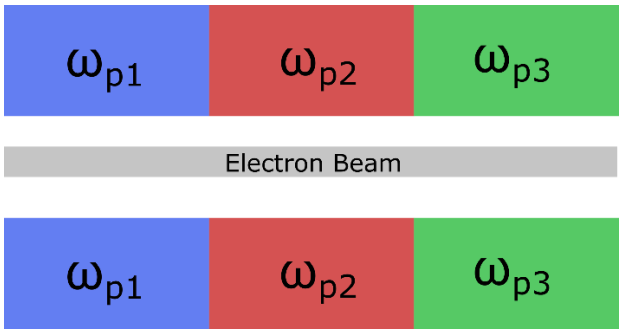

Fig. 26: Pictorial representation of a very broadband MERWA. By modifying the plasma frequency of individual sections the frequncy band that is amplfiied is different for each section allowing for a more wide band response while also preventing oscillation as each section has a different passband.

4.5c: Adding Discrete Loss Elements

Another method of suppressing backwards wave gain is by adding lossy blocks to the MTM. Fig. 27 presents one method of introducing lossy blocks, where we have introduced graphite blocks to discrete locations in the Drude liner. The purpose of the graphite blocks is two-fold: 1) by placing a lossy material at discrete locations in the MTM liner the losses of the material can damp the EM wave and 2) if the height of the graphite blocks is a significant portion of the Drude liner they can also prevent the flow of the EM mode as a majority of the energy of the new EM travels in the liner. One drawback of this method is it can introduce resonant modes where EM energy can travel back and forth between the graphite blocks creating additional problems.

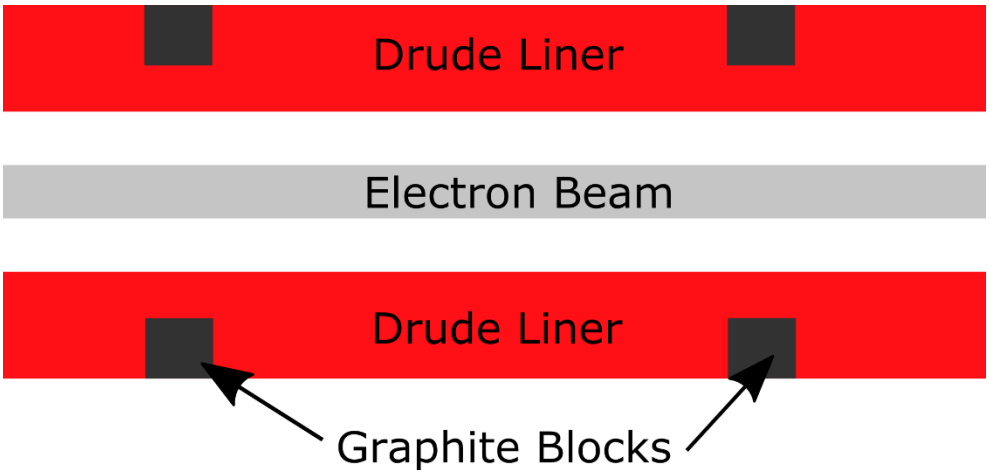

Fig. 27: The addition of graphite blocks to the MTM structure adds loss to help absorb some of the EM energy of the traveling wave. If the height of the blocks are made large enough to be a sufficient portion of the Drude liner's height the EM mode can be significantly damped as a majority of the EM energy travels in the liner.

4.5d: Intentional Randomization of MTM Elements

The fourth method we have proposed to help suppress the backwards wave gain is by creating an intentional randomization of the MTM liner structure. This method is inspired by the work of Sengele, et al., where he investigated how random fabrication errors of a TWT's slow wave structure suppressed backwards wave gain at the cost of bandwidth, with only a slight reduction in overall fundamental forward wave gain [43].

In the next chapter we discuss how to realize a MTM structure to use as the liner for the MERWA structure. We will demonstrate that the MTM structure can be created through a periodic arrangement of periodic elements. Therefore, this suppression method would be implemented in the MERWA by intentionally varying the dimensions of the individual MTM elements. If we intentionally change random elements of the MTM structure, the MTM will not appear as a continuous 'Drude' like medium but will actually appear as a Drude medium that has a varying plasma frequency. By randomly changing the emulated plasma frequency of the liner,

the phase velocity of the EM mode is varied resulting in a reduced backwards wave interaction. The randomized material effects are also anticipated to have a more wideband type behavior similar to the concept discussed in Fig. 26; however, the different ‘gain sections’ will not be discrete sections but rather a distributed effect.

Chapter V: Implementation of Planar MERWA using Periodically Spaced Inductive Meandered Lines

Task 3 consisted of determining a realizable MTM that could be used in an MERWA. To simplify this task we examined a planar configuration of the MERWA device. The results of Task 3 have been published in the IEEE Transactions on Plasma Science (© 2016 IEEE. Reprinted, with permission, from T. Rowe, N. Behdad, and J. H. Booske, Metamaterial-Enhanced Resistive Wall Amplifier Design Using Periodically Spaced Inductive Meandered Lines, IEEE Transactions on Plasma Science, Oct. 2016). A summary of these results is presented here.

In previous tasks, a homogenous dielectric with a Drude dispersion was used to emulate the ENG MTM. In task 3 we focused on creating a practical implementation of the MTM liner that exhibits ENG behavior at our frequency of interest. To simplify the problem of creating a practical MTM some initial work was conducted to determine the modification of the theoretical model for both a planar and anisotropic MTM liner. This section will discuss these theoretical models and how they led to a practical MTM design.

5.1 Practical Anisotropic MTM Liners

For simplicity, in this work, we reduced the three dimensional (cylindrical) problem investigated in previous work to an infinitely wide parallel plate, two dimensional situation. This simplification reduced the complexity of the theoretical model and more importantly, it significantly reduced the simulation time of the MTM structures in both full wave EM and PIC

simulations. Fig. 28 presents a pictorial representation of the parallel plate MERWA, where the structure is infinite in the y-direction.

Although an unlined parallel plate waveguide does allow for propagation of a TEM wave at all frequencies, the TEM waves are not of concern because they cannot couple to the electron beam effectively. However, the transverse magnetic (TM) modes that the parallel plate waveguide supports have a longitudinal electric field component that can couple to the electron beam. The cutoff frequencies of these TM modes, however, are inversely proportional to the separation between the two plates. In this study, the parallel plate spacing was set so that the cutoff frequency was at least a factor of two greater than the operating frequency.

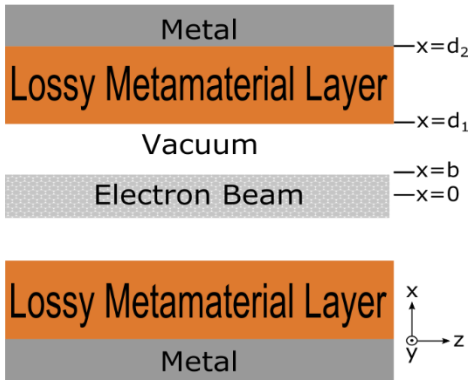

Fig. 28: Pictorial representation of the parallel plate MERWA configuration. In this configuration, the mediums are infinite in the y-dimension and an infinitely wide electron beam travels along the z-direction. The electron sheet beam has a width of $2b$ and the anisotropic MTM liner has a thickness of $d_2 - d_1$. For this work $d_2 = 15\ mm$, $d_1 = 10\ mm$, and $b = 8.7\ mm$.

An MERWA in a planar configuration has plane symmetry, and the equation used to determine the space charge wave numbers was

$$Tb\tan(Tb) = (\psi b)^2 Y_{wall}/j\omega\varepsilon_0 b. \qquad (51)$$

Equation (1) is presented in [1], where

$$T^2 = (\beta^2 - k_0^2)\left[\frac{\beta_p^2}{(\beta - \beta_e)^2} - 1\right], \quad (52)$$

$$\psi^2 = \beta^2 - k_0^2, \quad (53)$$

$$\beta_e = \omega/u_0, \quad (54)$$

$$\beta_p = \frac{\omega_p}{u_0}, \quad (55)$$

$$v_0 = (-2\eta V_0)^{1/2}, \quad (56)$$

and

$$\omega_{p,beam} = \left(\frac{\eta i_0}{\varepsilon_0 u_0}\right)^{1/2}. \quad (57)$$

β is the phase constant in the assumed solution form of $e^{j(\omega t - \beta z)}$, k_0 is the free space wave number, β_e is the wave number of the electron beam, β_p is the plasma wave number, $\omega_{p,beam}$ is the plasma frequency of the electron beam, η is the electron charge to mass ratio ($-1.76x10^{11}$), u_0 is the dc velocity of the beam, V_0 is the beam voltage, i_0 is the dc current density of the electron beam, and ε_0 is the permittivity of free space. Y_{wall} is the admittance of the wall as seen by the electron beam and is discussed in more detail in Appendix 2.

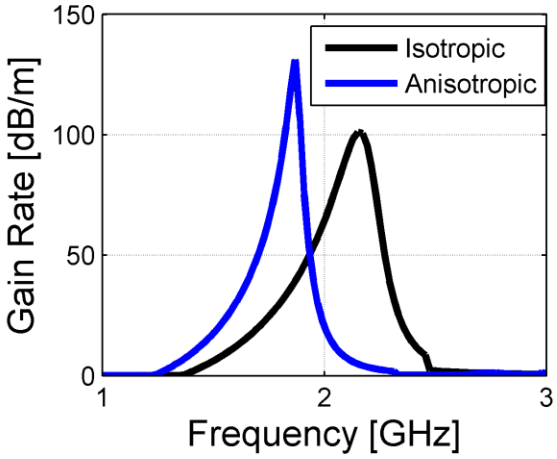

Fig. 29: Theoretical gain of a planar MERWA with an isotropic and anisotropic liner. For these calculations, the beam voltage was 10 kV and had a current of 1 A, d_1 = 10 mm, d_2 = 15 mm, and b = 8.7 mm, from Fig. 28. For both cases the plasma frequency of the liner was 3 GHz and the collision frequency was 0.2 GHz. The isotropic liner used the permittivity of (13) for both the x and z direction relative permittivity. The anisotropic liner had a permittivity of free space in the z direction and permittivity of (13) for the x direction.

For the MERWA configuration it was desired that the lossy MTM liner exhibit epsilon negative (ENG) properties where the permittivity is negative but the permeability is positive. One method to represent ENG materials is to use a Drude dispersion model. Using the Drude dispersion model, the relative permittivity that the MTM shell exhibits can be calculated using

$$\varepsilon_r = 1 - \frac{\omega_{p,Drude}^2}{\omega(\omega + j\omega_c)}; \qquad (58)$$

where ε_r is the relative permittivity of the dielectric, ω_p is the plasma frequency of the Drude dispersion model, ω_c is the collision frequency of the Drude dispersion model, and ω is the frequency of operation. The permittivity of the liner is used to determine Y_{wall}, the admittance of the wall as seen by the electron beam (Appendix 2).

Previous work focused on solving Eqs. (51)-(58) with an isotropic liner. However, because many MTM structures exhibit anisotropic dielectric properties, we examined how this anisotropy changes the gain of the MERWA. We examined various combinations of the anisotropy and

found that for the structure to support a growing space charge wave it is necessary for the liner to have a negative permittivity in the x-direction. The permittivity of the liner in the z-direction does not have to be negative.

It is then possible to solve (51)- (58) and the equations in Appendix 2 for the situation when the liner is an isotropic ENG liner ($\varepsilon_x = \varepsilon_z = \varepsilon_r$) and compare that to when the liner is anisotropic, with a negative permittivity in only the x direction ($\varepsilon_x = \varepsilon_r; \varepsilon_z = \varepsilon_0$). Fig. 29 shows the gain rate of this device with the two different liners. The anisotropic liner has a narrower bandwidth of operation but an increased peak gain rate.

Having established that only a negative permittivity in the x-direction is necessary for large gain, we examined possible MTM structures that provide x-directed ENG properties and also conform to the physical dimensions of the liner structure. We examined a wire grid loaded with lumped elements and a meander line element structure.

5.2a Wire Grid with Lumped Elements

Wire grid structures have been shown, both theoretically and experimentally, to approximate a Drude dispersion model at wavelengths much longer than the wire spacing [32, 34]. In the planar MERWA configuration, we desired a MTM layer with an ENG response in the x-direction. A corresponding anisotropic wire "grid" would be a periodic array of vertical wire segments, aligned along the x-axis and periodically spaced along the y and z dimensions, as illustrated in Fig. 30.

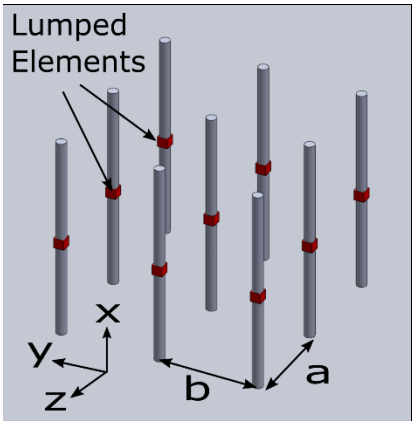

Fig. 30: Two dimensional array of loaded parallel wires that is known to provide Drude type dispersion and may be a practical MTM structure for an experimental MERWA device. The red squares represent periodically loaded lumped element components. The addition of lumped element inductors reduces the emulated plasma frequency of the structure.

One of the practical challenges of a wire grid-based (or wire array-based) MERWA is satisfying the competing requirements of the wire spacing. On the one hand, a MTM (continuous-medium-like) response is only achieved for wires spacing much less than the wavelength of the wave. In an RWA, the disturbance to be amplified is a beam density perturbation, for which the wavelength is approximately

$$\lambda_e = 2\pi u_0/\omega, \qquad (59)$$

where u_0 is the velocity of the electron beam. Therefore, we need the wire spacing to be significantly smaller than λ_e, i.e., $a/\lambda_e \ll 1$. In particular, to approximate a continuous Drude-like medium dispersion, the wire elements in a MTM array need to be spaced less than or equal to approximately one-tenth of a wavelength [32]. On the other hand, for large MERWA gain, it can be shown that the effective plasma frequency of the MTM liner, $\omega_{p,eff}$, needs to be close to, but slightly greater than, the operating frequency of the device. This results in a permittivity that is negative but near zero, i.e., $\omega_{p,eff}/\omega \approx 1.5 - 4$. From results in [32], one can calculate

$$\frac{\omega_{p,eff}}{\omega} = \frac{c_0}{v_0}\frac{\sqrt{2\pi}}{\sqrt{\ln(a/r)}}\left[\frac{a}{\lambda_e}\right]^{-1} \sim \frac{c_0}{v_0}\frac{1}{(a/\lambda_e)}, \quad (60)$$

where c_0 is the speed of light, a is the spacing between wires, and r is the wire radius. From (60), we see that $\omega_{p,eff}/\omega$ scales inversely with a/λ_e and depends on the magnitude of the normalized velocity, u_0/c_0. For a non-relativistic beam, the MTM requirement of $a/\lambda_e \ll 1$ can cause $\omega_{p,eff}/\omega \gg 1$, resulting in weak gain. Fig. 31 illustrates this issue by displaying curves for $\omega_{p,eff}/\omega$ versus a/λ_e for a non-relativistic (10 keV, $u_0/c_0 = 0.19$), mildly relativistic (100 keV, $u_0/c_0 = 0.55$), and highly relativistic (100 MeV, $u_0/c_0 \approx 1$) configuration. From Fig. 31, we can see that for the nonrelativistic and mildly relativistic electron beam examples ($u_0 = c_0/5, c_0/2$), keeping $a/\lambda_e \leq 0.1$ results in overly large values of $\omega_{p,eff}/\omega$. Knowing that lower voltage (mildly relativistic) electron beam HPM VED designs provide advantages for the power supply design requirements, we conclude that it would be advantageous to identify a method to decrease the wire array (or grid) $\omega_{p,eff}$ without increasing the wire spacing *a*.

Smith, et al., demonstrated that it is possible to lower the effective plasma frequency of the wire grid (array) structure, while maintaining a given wire spacing, if small loops are added to the wire, effectively increasing the inductance of the wires [44]. Tretyakov performed a more thorough investigation of this topic by adding a lumped LC element to the wire grid structure and deriving an analytical effective permittivity [45]. Fig. 30 shows a pictorial representation of what a periodically loaded wire grid structure might look like for uniaxial anisotropic ENG behavior.

To evaluate the effective permittivity of the MTM containing wires with lumped elements, Tretyakov assumed a spacing of the lumped element significantly smaller than the wire spacing,

which permits representing the lumped elements as a uniformly distributed impedances per unit length of the wire [45]. Specifically, if the lumped elements are parallel LC circuit loads the effective permittivity can be described as [45]

$$\varepsilon(\omega) = \varepsilon_0 \left(1 - \frac{2\pi/(\varepsilon_0 \mu_0 \omega^2 ab)}{X}\right), \qquad (61)$$

where

$$X = \log \frac{b}{2\pi r_0} + \frac{2\pi L/\mu_0}{1 - \omega^2 LC} + \sum_{n=1}^{\infty} \left(\frac{\coth\left(\pi n a/b\right) - 1}{n} \right) + \frac{\pi a}{6b}, \qquad (62)$$

where L and C are the inductance and capacitance of the lumped element, ω is the frequency, μ_0 and ε_0 are the permeability and permittivity of free space, a and b are the wire spacing in the z and y directions, respectively, and $r_0$is the radius of an individual wire. Fig. 31 presents the effective normalized effective plasma frequency versus normalized wire spacing for two additional grid configurations (dashed lines). Each of these curves corresponds to the effective plasma frequency of a wire grid with lumped element inductance added to each wire (inductance values are specified in the figure caption). The results displayed in Fig. 31 confirm that increasing the inductance of the wire elements allow one to realize an adequately low effective plasma frequency while maintaining an adequately small element spacing, even for non-relativistic electron beams.

We have followed on the work of Smith, et al., and Tretyakov but instead of using loops (which require an axial ‘depth’ to the wire element) or lumped elements (which requires laborious construction and questionable vacuum compatibility), we have implemented a meander line

element to increase the effective inductance of the wire grid structure and reduce the effective plasma frequency.

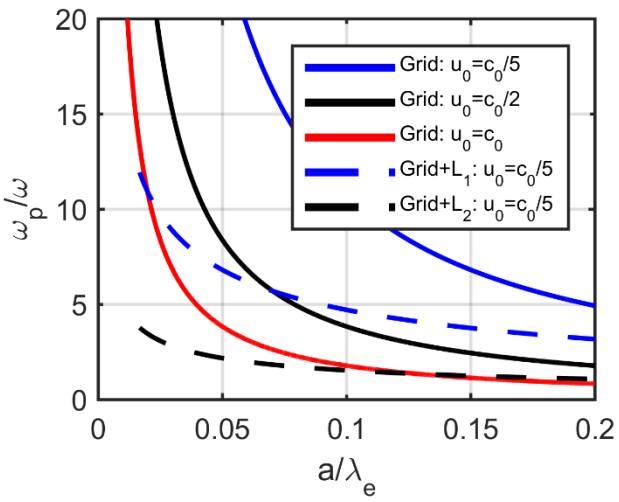

Fig. 31: The ratio of the emulated plasma frequency of the liner to the operating frequency of the device for various wire grid spacing, a. The wire grid spacing is divided by the wavelength of the electron beam, λ_e, for three different beam velocities of $c_0/5$, $c_0/2$, and c_0. The solid curves demonstrate the emulated frequency of a standard wire grid. The dotted lines represent grids that are periodically loaded with lumped element inductors, specifically L_1 = 10nH and L_2 = 100 nH.

5.2b Meander Line Elements

To achieve a negative permittivity in the x-direction using a meander line circuit, the meander should sit in the x-y plane with its ends at different x-values. Fig. 32 shows an example meander line structure. To our knowledge, an accurate, closed form equation for the inductance and capacitance of a meander line circuit is not known. Therefore, numerous eigenmode and full wave simulations were conducted to determine the appropriate meander line dimensions necessary to replicate the results of the wire array with lumped elements.

While a meander line structure may not be the ultimate choice for a MW level high power amplifier, it provides us with a practical realization for experimental and computational study of an MERWA. Additional work outside the scope of this investigation will be necessary to determine the power handling limits of this design and compare it to other ENG implementations.

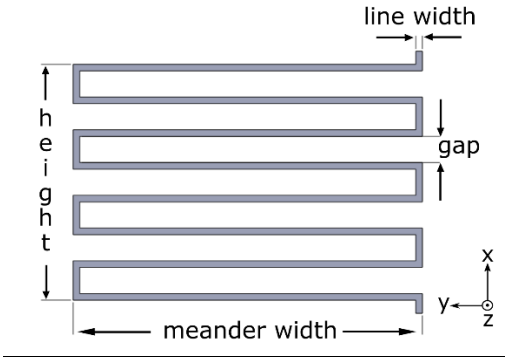

Fig. 32: Single meander element of a practical MTM used to emulate a low frequency Drude medium. The final configuration used had a meander width of 15 mm, a line width of 0.15 mm, a gap of 0.6 mm, an overall height of 5 mm, and a thickness into the page of 0.1 mm. The meander path is constructed of PEC.

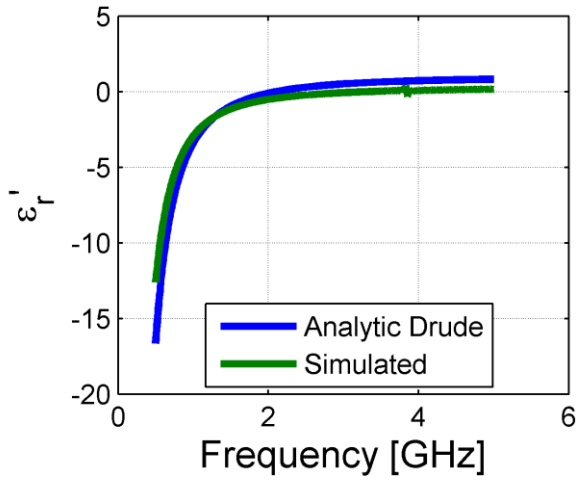

Fig. 33: Real part of the analytic permittivity of an analytic Drude dispersion model with ω_p = 2.1 GHz and $\omega_c = 0$ compared to the extracted effective permittivity of the simulated infinitely periodic meander line structure. The unit cell contained the meander element described in Fig. 32 and was 5 mm by 25 mm by 4 mm, for the x, y, and z directions, respectively.

To determine the effective permittivity of the meander-line-based MTM, we used the computational method developed by Smith, et al., where the S-parameters of a unit cell of the MTM are simulated and then used to calculate the medium's effective permittivity [46]. The specifics of the method used to convert the S-parameters to the permittivity are not included here. However, the basic procedure uses the reflection and transmission coefficients (S-parameters) of the unit cell and coverts those to an effective refractive index (n) and impedance (z). The index of refraction and impedance can then be used to compute the effective permittivity using the equation [46]

$$\varepsilon_{eff}(\omega) = n(\omega)/z(\omega). \qquad (63)$$

Fig. 33 presents the extracted real part of the effective permittivity of the computationally-modeled meander line structure shown in Fig. 32 compared to the effective permittivity predicted by the analytic Drude dispersion model of Eq. (58), with $\omega_p = 2.1\ GHz$ and $\omega_c = 1\ Hz$. For the illustrative results shown in Fig. 6, the width of the meander element was 15 mm, the line width of the meander was 0.15 mm, the gap in the meander path was 0.6 mm, and the meander lines had a periodicity into the z-dimension of 4 mm and a 25 mm period in the y-dimension.

Our meander-line wire array configuration will have an anisotropic response. The effective permittivity presented in Fig. 33 will only be valid for the direction of the applied electric field used in the characterization simulations. In this case, the applied electric field was vertical (x-oriented), to the structure shown in Fig. 32. Therefore, when this meander is placed in the planar configuration shown in Fig. 28, the meander line elements will only introduce a negative permittivity in the x-direction, ε_x.

5.3 Dispersion of Parallel Plate Waveguide Loaded With Practical MTM

In a traditional RWA, the beam tunnel size is selected such that the tunnel is cutoff to transverse magnetic (TM) EM waves to prevent traveling waves that can interfere with the resistive wall amplification mechanism. In this work, we desired to add an ENG liner to the beam tunnel structure to greatly enhance gain. However, when an ENG liner is introduced to a waveguide, as discussed in this work, a new EM mode arises. This mode has a passband that is below the cutoff frequency of the unlined waveguide [36]. The presence of this EM wave is undesired as it can introduce traveling waves in the structure that can inhibit or interfere with the resistive wall amplification mechanism. In addition, the phase velocity of this below-cutoff EM wave is negative, which can give rise to backward wave oscillation. Losses must be introduced into the structure to ensure that the EM wave is sufficiently damped to prevent device oscillation.

However, we used the presence of this EM wave to characterize the EM behavior of the meander line implementation of the ENG liner. Specifically, we compared the analytic dispersion curve of a parallel plate waveguide with an anisotropic ENG layer to the eigenmode simulation results of the configuration with the meander line elements. These simulations provide confirmation that the meander line elements are properly emulating a finite thickness ENG structure, whereas the simulation results of the previous section assumed a three dimensional infinite structure.

To solve the dispersion of an anisotropic Drude lined parallel plate waveguide it is necessary to solve the equation presented in [28]

$$1 - \left(\frac{\varepsilon_0 \beta_{x,2}}{\varepsilon_{z,2} \beta_{x,1}}\right) \tan\left(d_1 \beta_{x,1}\right) \tan\left((d_2 - d_1)\beta_{x,2}\right). \qquad (64)$$

In (14) the x-direction wavenumber in the vacuum space is

$$\beta_{x,1}^2 = \left(\frac{\omega^2}{c_0^2} - \beta_z^2\right), \qquad (65)$$

and in the liner is

$$\beta_{x,2}^2 = \frac{\varepsilon_{z,2}}{\varepsilon_{x,2}}\left(\omega^2 \varepsilon_{x,2} \mu_{y,2} - \beta_z^2\right), \qquad (66)$$

where $\varepsilon_{x,2}$, $\varepsilon_{z,2}$, and $\mu_{y,2}$ are the x-direction permittivity, z-direction permittivity, and y-direction permeability of the liner, respectively. In addition, c_0 is the speed of light in free space, ε_0 is the permittivity of free space, and d_1 and d_2 are defined in Fig. 28.

Using the meander line elements to create the physically-realizable MTM gives rise to a negative permittivity response in the x direction, but a free space permittivity in the axial direction ($\varepsilon_x = ENG, \varepsilon_z = \varepsilon_0$). To measure the meander line's response in the parallel plate configuration, an eigenmode simulation was used to calculate the dispersion which was compared to the analytic dispersion. Fig. 34 presents the eigenmode model that was used to measure the structure's dispersion. In the eigenmode model, the front and back surfaces are periodic boundary conditions where the phase shift is varied. The top and bottom boundaries are perfect electric conductor (PEC) surfaces and the left and right boundaries are perfect magnetic conductor (PMC) boundaries used to model an infinite parallel plate configuration. The meander elements are constructed of PEC and have a finite thickness. The period of the eigenmode structure is 4 mm and the other model dimensions are presented with Fig. 17.

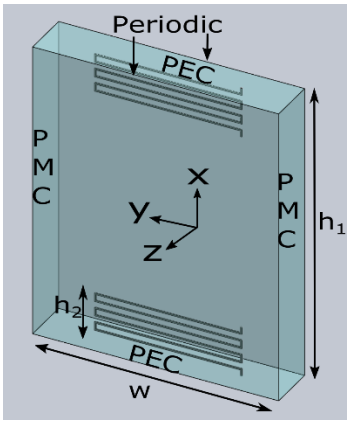

Fig. 34: Single period of the MTM structure used for an eigenmode simulation to calculate the dispersion. The meander line elements are 15 mm wide, have a z-direction finite thickness of 0.1 mm, the line width is 0.15 mm, the wire gap is 0.6 mm, the height of each meander, h_2, is 5 mm, the overall height of the structure, h_1, is 30 mm and a width, w, of 25 mm. The period of the structure was 4 mm.

Fig. 35 presents the simulated dispersion of the structure shown in Fig. 17 and compares it to the dispersion diagram obtained by theoretical analysis of a parallel plate waveguide lined with an anisotropic Drude medium (labeled Analytic Drude 1). Fig. 35 also presents the light line and the dispersion line of a 20 kV beam for reference. These simulations provide confirmation that the meander line elements are properly emulating a finite thickness ENG structure. Note that both the ENG and meander based liners exhibit the propagating hybrid TM mode, share the same effective plasma frequency and similar (negative group velocity) dispersion over a small range of wavenumber, β. Further, the electric field profiles of the meander and ENG based structures were compared and found to be very similar.

Fig. 35 also presents an additional analytic solution, Analytic Drude 2. This second analytic solution was solved by keeping all other parameters of the calculation constant but modifying the thickness of the MTM Drude slabs on both the top and bottom of the drift tube. For the solution presented as Drude 2, we have reduced the Drude thickness from 5 mm to 2.5 mm and increased

d_1 to keep the overall height, $2d_2$, constant. The agreement between the Drude 2 analytic solution and the meander element solution is much better as can be seen from the figure. These results indicate that the meander line elements, which have a finite thickness h_2 in Fig. 17, appear to electromagnetically emulate a thinner plasma layer than the height h_2. We have investigated various meander heights and found that this trend appeared consistent, where the dispersion curve had much better agreement with an analytic solution that assumes a Drude slab that was thinner than h_2.

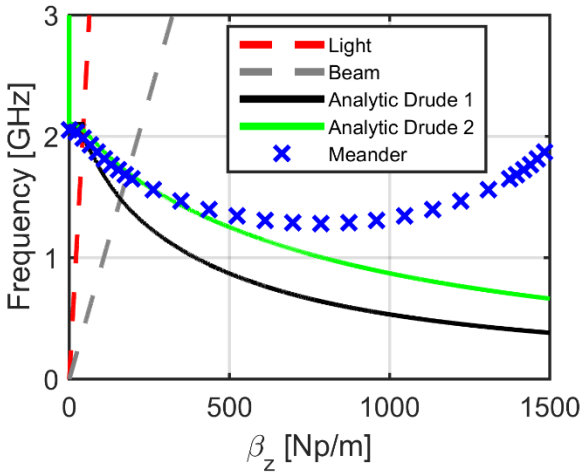

Fig. 35: Dispersion of the parallel plate ENG lined structure simulated using an eigenmode simulation of CST and compared to two analytic solutions of (14) using (58) where $\omega_p = 2.1\ GHz$ and $\omega_c = 1$ for $\varepsilon_{x,2}$, the permittivity of free space for $\varepsilon_{z,2}$, the permeability of free space for $\mu_{y,2}$. For the analytic solution of Drude 1, d_1 = 1 cm, and d_2 = 1.5 cm, and for Drude 2, d_1 = 1 cm, and d_2 = 1.25 cm.

We can further investigate this behavior, where the meander elements appear to emulate a thinner Drude liner, by examining the current flow on the meander line elements. Fig. 36 shows the current flow on the top meander element of the simulation presented in Fig. 17. The current flow observed on the meander along the bottom of the waveguide is very similar, but a mirror image. It is possible to see in Fig. 36 that the current flow on the lower two meanders of the

meander line is much smaller than the current flow on the remaining portion of the structure. The small current means that the lower meanders do not have a large EM effect on the overall system. Therefore, the 5 mm tall meander appears to electromagnetically have a shorter effective height. This shorter effective height demonstrates why the dispersion of this structure agrees well with a thinner Drude liner.

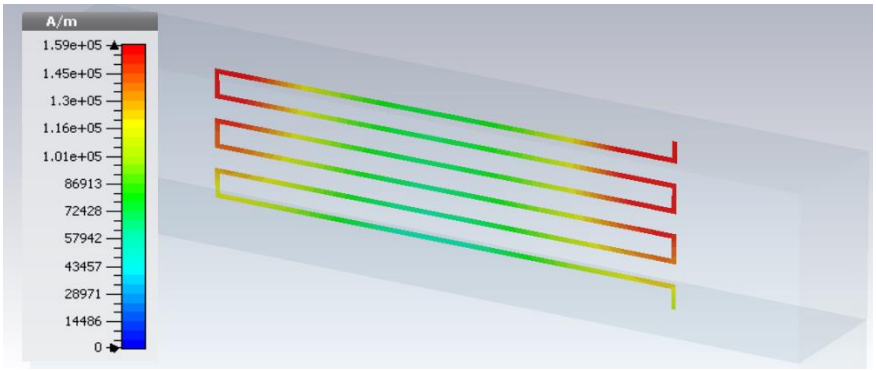

Fig. 36: Surface current on the top meander element of Fig. 17, calculated by the CST eigenmode solver. The color map of the surface current ranges from 0 to 1.59 x 10^5 A/m. The surface current in the bottom two turns of the meander (farthest from the PEC wall) is much smaller than the rest of the meander. This same behavior can be observed in the bottom meander of Fig. 17.

5.4 Meander Line Implementation of MTM PIC Simulations

CST Particle Studio [35] was used to conduct PIC simulations of the parallel plate configuration of the MERWA. The MERWA model was constructed to simulate a device similar to the design shown in Fig. 28, but the lossy MTM liner has been replaced with a periodic arrangement of the MTM configuration presented in Fig. 17. Fig. 37 shows the CST model of the parallel plate MERWA. To simulate an infinitely-wide, parallel plate configuration, we applied PMC boundary conditions to the y_{min} and y_{max} boundaries.

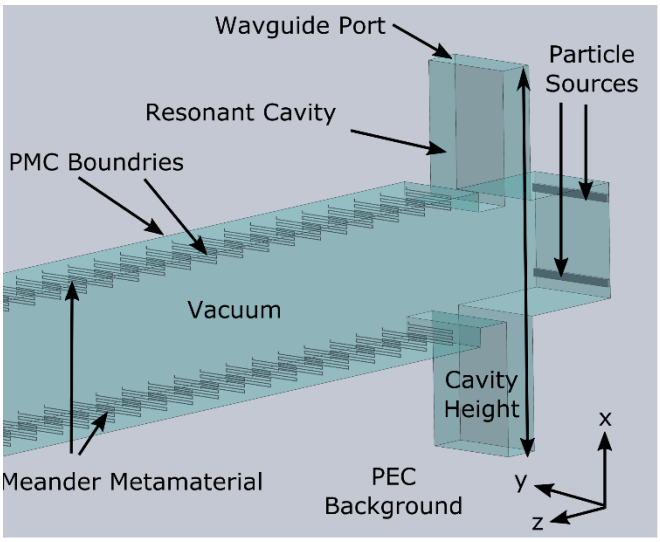

Fig. 37: Practical Parallel Plate MERWA model constructed in CST Particle Studio. The physically-realizable implementation of the MTM used the meander line elements, embedded in a lossy material. Two separate particle sources were used to generate two separate 2 mm thick sheet beams. The electron beams are passed through a resonant cavity to cause velocity modulation before being injected into the drift tube of the MERWA device.

Instead of using a single sheet beam, as presented in the theoretical analysis, two separate thinner sheet beams were used, as shown in Fig. 37. One sheet beam passed slightly below the top MTM structure while the second sheet beam passed slightly above the bottom MTM structure. Two sheet beams were used for two purposes. First, using a smaller beam that travels near the surface of the MTM liner, rather than a sheet beam that fills the entire drift tube space, is a closer representation of what our future experimental configuration is anticipated to be. Secondly, the EM TM mode has an axial electric field along the center of the waveguide. Therefore, by placing the electron beam off axis it is more difficult to excite the EM TM mode that can lead to backwards wave instability

Each sheet beam had a potential of 20 kV, a thickness of 2 mm, a current density of 2 A/cm^2, and was injected from the right end of Fig. 37 in the z-direction. To velocity modulate the electron beam, the beam was passed through a short but infinitely wide cavity. The cavity had a conducting wall (PEC) on the bottom surface and was excited from the top surface with an EM

port. The port was configured to operate in the fundamental (E_z) mode and the cavity height was selected to focus an axial (E_z) field at the center of the electron beam. The height of the cavity was varied with the operating frequency to ensure a maximum electric field occurred at the center of the electron beam. A strong 1 T static magnetic field was imposed along the axis of the beam to limit electron motion to the z direction.

To more effectively cause the velocity modulation, two transparent PEC sheets were added to the simulation at the two z positions where the resonant cavity intersects the drift tube. These PEC sheets were 100% transparent to the electron beam but electrically crossed the drift tube opening in the cavity to allow for the fundamental electric mode to be excited. These transparent surfaces would be similar to using a wire mesh structure which the beam was passed through.

Using Fig. 28 as a reference for the dimension labels, the PIC model used the following dimensions: d_1 = 1 cm, d_2 = 1.5 cm, and b = 9 mm. The thinner sheet beams were each 2 mm thick and were placed with the top surface of the beam at b. The width of the simulation, w, is 25 mm and the length of the MTM shell is 1 m. At the axial end of the structure a PML is used to absorb EM energy and is configured to prevent regenerative oscillation.

To introduce loss to the simulation, a background loss was added to the MTM liner (only in the area of the meander elements, i.e. $d_1 < x < d_2$). This background loss was simulated by changing the host medium of the meander line structure to a ‘lossy air’ where the permeability and real permittivity are equal to that of free space but the conductivity is non-zero. It is expected

that practical implementations of this background loss will be implemented through the use of lossy graphite blocks, increasing the loss of meander elements, or the use of colloidal graphite.

The model was simulated for 75 ns and the particle velocity versus position was evaluated to measure the gain rate of the system. The gain rate was measured by evaluating the exponential growth of the AC component of the particle velocity before beam saturation, as described in [11].

In addition to using two separate electron sheet beams, we have also demonstrated that the meander based MTM liner does not behave exactly like a Drude liner of the same thickness. Therefore, to provide an accurate analytic case to compare to, it was not appropriate to use the theoretical description used in Fig. 29 where the sheet beam filled most of the drift tube and the Drude model was the full 5 mm thick. Therefore, the analytic result had to be calculated for a 'modified' configuration of the device, shown in Fig. 38. In the modified theoretical model we have assumed that the MTM liner had a Drude-type response for the x-directed permittivity, $\omega_p = 2.05\ GHz$ and $\omega_c = 1\ Hz$. In addition, to account for the background loss we have added, the x-directed permittivity also includes an added loss component where $\sigma = 0.05$ (i.e. $\varepsilon_x = \epsilon_0\varepsilon_r - j\,\sigma/\omega\,, \varepsilon_r$ from (58)). The z-direction permittivity was equal to free space plus the loss term (i.e. $\varepsilon_z = \varepsilon_0 - j\,\sigma/\omega$). The liner had a thickness of 2.5 mm. The thickness of the liner and the values selected for the permittivity were taken from the best fit of the dispersion diagram, Fig. 35. To account for the shortened effective height of the meander elements the theoretical model used a larger gap between the electron beam and the Drude liner than the gap between the beam and the meander elements in simulation (i.e. $g_1 = 1\ mm, g_2 = 3.5\ mm$). Finally, the

modified theoretical configuration used an electron beam that was on-axis and axis-symmetric, but had the same current density and thickness as the beam in simulation. Moving the beam to on-axis is an estimation of the simulated hollow beam configuration and allowed for the theoretical model presented in Section II to be used. Fig. 39 shows the calculated gain rate of the PIC simulation for various frequencies with a comparison to the analytical result. The analytic curve presented in the results is produced by calculating (51)-(58) and using the structure in Fig. 38.

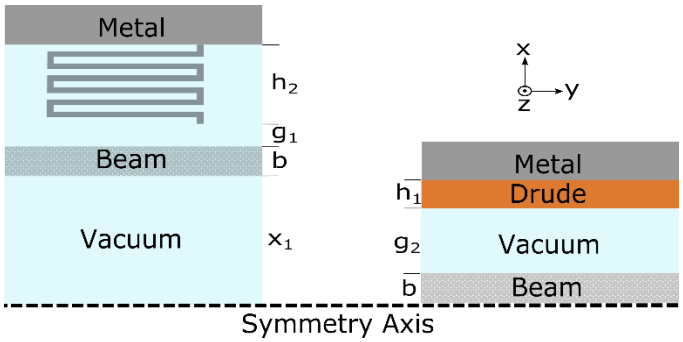

Fig. 38: The configuration of the simulation (left) compared to the configuration used for theoretical comparison (right). In the simulation, $h_2 = 5\,mm$, $g_1 = 1\,mm$, $b = 2\,mm$, and $x_1 = 7\,mm$. In the theoretical configuration, $h_1 = 2.5\,mm$, $g_2 = 3.5\,mm$, and $b = 2\,mm$. The theoretical configuration used a thinner liner along with a larger vacuum gap between the beam and liner to compensate for the effective height of the meander elements. In addition, the theoretical configuration used an on-axis beam to compare to the two sheet beams of the simulation. Both models used electron beams with identical current density.

The results presented in Fig. 39 demonstrate good general agreement between the PIC results and the modified theoretical configuration. The PIC gain rates are within approximately 3 dB of the analytical curve. In these simulations we have used a liner loss that is greater than necessary to ensure stability. The gain rate could be increased if the loss of the liner is decreased. However, if the loss of the liner is decreased by too much, the backwards wave instability will arise. In addition, it is also possible to increase the current density of the electron beam to increase the gain rate.

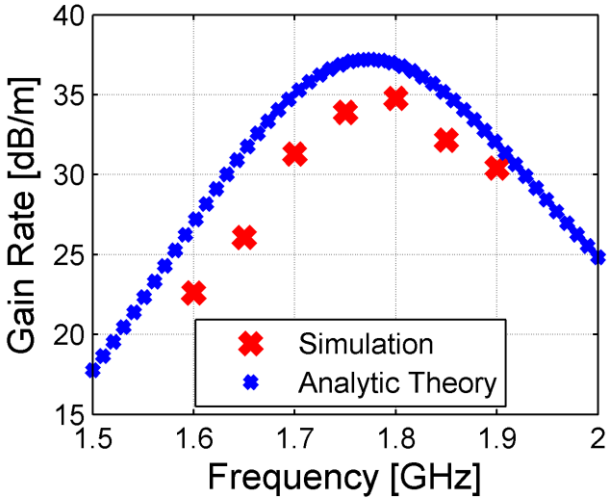

Fig. 39: Gain rate calculated by measuring the growth of the AC component of the electron beam's velocity modulation from the simulations conducted in CST using the model shown in Fig. 37. The simulated gain rates are compared to the theoretical gain rate of the configuration discussed in Fig. 38.

In Fig. 39, the gain rates are lower than those shown in Fig. 29 because of the reduced effective liner height. The gain rate should increase if a taller meander (larger h_2 in Fig. 17) were used to emulate a thicker Drude layer. Therefore, by using taller meander elements to emulate a 5 mm Drude liner (approximately 8 mm tall meander elements) it should be possible to realize gain rates closer to those presented in Fig. 29. Nevertheless, the results presented in Fig. 39 clearly demonstrate that this structure is capable of supporting MTM-enhanced resistive wall gain.

Chapter VI: Relativistic HPM MERWA

In Task 4 we examined the performance of the MERWA under relativistic beam conditions. A MERWA that uses a relativistic electron beam is of interest as it will provide the capabilities of MW power level performance. MW level amplifiers are very desirable devices in the electronic warfare and electronic countermeasures markets. This chapter examines the modifications that must be made to the analytic theory examined in Chapters I, II, and III to account for relativistic particle effects. In addition, we calculated the expected performance of a relativistic test case using the updated theory and compare the results to a PIC simulation result. A subset of the results discussed in this chapter were presented at the 2016 International Conference on Plasma Science.

6.1 Theoretical Analysis

The first step in investigating a relativistic MERWA was to study the modifications necessary to the current theoretical model derived by Birdsall and Whinnery [1] and discussed in Chapter I. Part of Birdsall and Whinnery's theoretical work made assumptions that the device was non-relativistic to simplify the calculations. The calculations for the performance of a relativistic RWA are nearly identical to those presented in Chapter I, but a few equations must be modified to account for the relativistic particle velocities. The modifications required to the original theory primarily consisted of adding the relativistic correction to the equations involving particle motion and removing the assumption that the beam is significantly slower than the speed of light. Derivation of the gain equation is presented here to demonstrate the addition of the relativistic correction factor.

To calculate the gain of a relativistic MERWA we begin with three equations: the continuity of charge equation,

$$\nabla \cdot \boldsymbol{i} + \frac{\partial \rho}{\partial t} = 0, \tag{67}$$

the convection current equation,

$$\boldsymbol{i} = \boldsymbol{u}\rho,$$

and the force equation,

$$\frac{d(\gamma \boldsymbol{u})}{dt} = \eta \boldsymbol{E}, \tag{68}$$

where $\boldsymbol{i}$ is the current density vector, ρ is the charge density, $\boldsymbol{u}$ is the particle velocity vector, η is the electron charge to mass ratio and γ is the relativistic correction factor, explained below. The continuity of charge and convection current equations are unmodified from the non-relativistic case. The force equation now includes the relativistic correction factor

$$\gamma^2 = \left(1 - \frac{u^2}{c^2}\right)^{-1}, \tag{69}$$

where c is the speed of light and u is the particle's velocity.

We begin the analytic analysis by examining the force equation. First, we perform the product and chain rules on the partial derivative and re-arrange the terms of the equation resulting in the simplified force equation

$$\frac{d\boldsymbol{u}}{dt} = \frac{\eta \boldsymbol{E}}{\gamma^3}. \tag{70}$$

We can then assume a small signal theory with

$$\boldsymbol{u} = \boldsymbol{u_0} + \boldsymbol{u_1}, \tag{71}$$

and

$$\rho = (\rho_0 + \rho_1), \tag{72}$$

where terms with a subscript of zero are constant terms and a subscript of one denotes a first order, time- or space-varying perturbation term. Using the small signal theory assumptions, we can re-write the force equation:

$$\frac{d(\boldsymbol{u_0} + \boldsymbol{u_1})}{dt} = \frac{\eta \boldsymbol{E}}{\gamma^3}. \tag{73}$$

Since the particle is moving, and assuming only z-direction motion, chain rule can be applied as:

$$\begin{aligned} \frac{d(\boldsymbol{u_0} + \boldsymbol{u_1})}{dt} &= \frac{\partial(\boldsymbol{u_0} + \boldsymbol{u_1})}{\partial t} + (\boldsymbol{u_0} + \boldsymbol{u_1})\frac{\partial(\boldsymbol{u_0} + \boldsymbol{u_1})}{\partial z} \\ &= \frac{\partial \boldsymbol{u_1}}{\partial t} + u_0\frac{\partial u_1}{\partial z} + \frac{\partial u_0}{\partial t} + (\boldsymbol{u_0} + \boldsymbol{u_1})\frac{\partial \boldsymbol{u_0}}{\partial z} + \boldsymbol{u_1}\frac{\partial u_1}{\partial z}. \end{aligned} \tag{74}$$

Setting derivatives of constant, zero order components to zero

$$\frac{d(\boldsymbol{u_0} + \boldsymbol{u_1})}{dt} = \frac{\partial \boldsymbol{u_1}}{\partial t} + u_0\frac{\partial u_1}{\partial z} + \boldsymbol{u_1}\frac{\partial u_1}{\partial z}, \tag{75}$$

and removing the 2nd order components

$$\frac{\partial(\boldsymbol{u_0} + \boldsymbol{u_1})}{\partial t} \approx \frac{\partial \boldsymbol{u_1}}{\partial t} + u_0\frac{\partial u_1}{\partial z}, \tag{76}$$

reduces the force equation to

$$\frac{\partial \boldsymbol{u_1}}{\partial t} + u_0\frac{\partial u_1}{\partial z} = \frac{\eta \boldsymbol{E}}{\gamma^3}. \tag{77}$$

The continuity of charge and convection current equations can also be reduced using small signal theory. In addition, using the assumption that only the z-direction motion is the dominant factor the continuity of charge becomes

$$\frac{\partial \boldsymbol{i_1}}{\partial z} = -\frac{\partial \rho}{\partial t}, \tag{78}$$

and the first order components of the convection current become

$$\boldsymbol{i_1} = \rho_1 \boldsymbol{u_0} + \boldsymbol{u_1}\rho_0. \tag{79}$$

Assuming space and time harmonics, the three above equations can then be combined to define the first order components [40] of the charge density

$$\rho_1 = -j\frac{k\,\beta_p^2 \epsilon_0 \boldsymbol{E}}{\gamma^3\,(\beta_e - \beta)^2}, \tag{80}$$

and current density

$$i_1 = \frac{-\beta_p^2}{\gamma^3\,(\beta_e - \beta)^2}(j\omega\epsilon_0 \boldsymbol{E}). \tag{81}$$

Where all variables of the equations are defined in Chapter III. These expressions for the current and particle density perturbations can then be input to the wave equation, which is not modified due to relativistic particle conditions. The wave equation is given by

$$\nabla^2 \boldsymbol{E} - \mu_0\epsilon_0\frac{\partial^2 \boldsymbol{E}}{\partial t^2} = \frac{1}{\epsilon_0}\nabla\rho + \mu_0\frac{\partial \boldsymbol{i}}{\partial t}, \tag{82}$$

where $\boldsymbol{E}$ is the electric field vector, μ_0 and ε_0 are the permeability and permittivity of free space, ρ is the electron density, and $\boldsymbol{i}$ is the current density vector. The wave equation is simplified, in a cylindrical coordinate system, to just examine the z-directed electric field to be

$$\nabla_{r,\phi}^2 E_z + \frac{\partial^2 E_z}{\partial z^2} - \mu_0 \epsilon_0 \frac{\partial^2 E_z}{\partial t^2} = \frac{1}{\epsilon_0} \nabla \rho_z + \mu_0 \frac{\partial i_z}{\partial t}. \qquad (83)$$

Again, assuming $\rho = \rho_0 + \rho_1, i_z = i_0 + i_1$, and time- and space-harmonic variation in ρ_1, i_1, and E_z, the wave equation can be transformed into

$$\nabla_{\perp}^2 E_z - \beta^2 E_z + \mu_0 \epsilon_0 \omega^2 E_z = \frac{-j\beta}{\epsilon_0} \rho_1 + j\omega\mu_0 i_1, \qquad (84)$$

where $\nabla_{\perp}^2$ is the Laplacian in the variables transverse to $\hat{z}$, ω is the temporal frequency, and β is the spatial wavenumber along $\hat{z}$. The first order current and charge density expressions are then substituted into the wave equation to produce:

$$\nabla_{\perp}^2 E_z + (\omega^2 \mu_0 \epsilon_0 - \beta^2) E_z = \frac{-j\beta}{\epsilon_0} \left(-j \frac{k\, \beta_p^2 \epsilon_0 \boldsymbol{E}}{\gamma^3\, (\beta_e - \beta)^2} \right) + j\omega\mu_0 \left(\frac{-\beta_p^2}{\gamma^3 (\beta_e - \beta)^2} (j\omega\epsilon_0 \boldsymbol{E}) \right),$$

which can be rearranged to form [1]:

$$\nabla_{\perp}^2 E_z + (\beta^2 - k_0^2) \left[\frac{\beta_p^2}{\gamma^3 (\beta - \beta_e)^2} - 1 \right] E_z = 0, \qquad (85)$$

which is in the form of the Helmholtz Equation, where

$$\beta_p = \frac{\omega_p}{u_0} = \left[\frac{\eta i_0}{\epsilon_0 u_0^3} \right]^{\frac{1}{2}}, \qquad (86)$$

$$\beta_e = \frac{\omega}{u_0}, \qquad (87)$$

$$k_0 = \frac{\omega}{c}, \qquad (88)$$

$$\eta = -1.76x10^{11}. \qquad (89)$$

The Helmholtz equation is then used to determine the gain of the MERWA. For the relativistic scenario, we have once again assumed a planar configuration, identical to the configuration in Fig. 28 in Chapter V, where the axial direction is z and the transverse directions are x and y. This specifies the equation to be

$$\nabla_{x,y}^2 E_z + (\beta^2 - k_0^2)\left[\frac{\beta_p^2}{\gamma^3(\beta - \beta_e)^2} - 1\right]E_z = 0. \qquad (90)$$

Further, we assume a transverse-z magnetic mode (TM^z, where $H_z = 0$) and therefore the fields have no variation in y-direction reducing the wave equation for this problem to its final form

$$\nabla_x^2 E_z + T^2 E_z = 0, \qquad (91)$$

where

$$T^2 = (\beta^2 - k_o^2)\left[\frac{\beta_p^2}{\gamma^3(\beta - \beta_e)^2} - 1\right]. \qquad (92)$$

This simplified version of the wave equation for a planar configuration has solutions of the form:

$$E_z = A\cos(Tx) + B\sin(Tx). \qquad (93)$$

To solve for the coefficients of the fields we can use vector potentials. Since the wave is a TM^z mode, the electric fields are of the form [47]:

$$E_z = -j\frac{1}{\omega\mu\epsilon}(-\beta_z^2 + k_0^2)A_z \qquad (94)$$

where

$$A_z = \frac{j\omega\mu\epsilon}{k_0^2 - \beta_z^2}E_z. \qquad (95)$$

In addition, the magnetic fields of the structure must be of the form [47]

$$H_y = -\frac{1}{\mu}\frac{\partial A_z}{\partial x}. \tag{96}$$

Using the vector potential we can rewrite the magnetic field to be

$$H_y = -\frac{1}{\mu}\frac{\partial A_z}{\partial x} = -\frac{1}{\mu}\frac{\partial}{\partial x}\left(\frac{j\omega\mu\epsilon}{k_0^2-\beta_z^2}E_z\right), \tag{97}$$

and using the assumed form of the axial electric field

$$H_y = \frac{j\omega\epsilon}{k_0^2-\beta_z^2}(A\,T\sin(Tx) - B\,T\,cos(Tx)). \tag{98}$$

Now, we assume the problem is symmetric about $x = 0$, therefore

$$H_y(0) = \frac{j\omega\epsilon}{k_0^2-\beta_z^2}(A\,T\sin(0) - B\,T\cos(0)) = 0, \tag{99}$$

requiring $B = 0$,

$$H_y = \frac{j\omega\epsilon}{k_0^2-\beta_z^2}(A\,T\sin(Tx)), \tag{100}$$

and

$$E_z = A\cos(Tx). \tag{101}$$

Using the defined electric and magnetic fields we can now determine the admittance at the edge of the beam ($x = b$) to be

$$Y_{beam} = -\frac{H_y(b)}{E_z(b)}, \tag{102}$$

or

$$Y_{beam} = \frac{j\omega\epsilon b}{(\psi b)^2} Tb \tan(Tb), \tag{103}$$

which is the same solution as found in the low energy analysis provided Birdsall [1] except with the difference that T is now

$$T^2 = (\beta^2 - k_o^2)\left[\frac{\beta_p^2}{\gamma^3(\beta - \beta_e)^2} - 1\right] \tag{104}$$

and

$$\psi^2 = \beta_z^2 - k_0^2. \tag{105}$$

Finally, to then calculate the gain of the device, we then solve the problem identical to the previous analysis where we equate this beam admittance to the admittance of the wall, as seen by the beam. The admittance of the wall is unmodified by the relativistic correction factor and can still be solved through the use of cutoff transmission line equations.

6.2 Analytic Calculation of a Relativistic Scenario

To confirm the relativistic corrections made to the theory, we examined a scenario very similar to the low energy planar configuration examined in Chapter II, but with increases in both the electron beam voltage and current. The new relativistic theory was then compared to the old 'low energy' theory.

The parameters that were originally desired for the relativistic device were to use an arbitrarily chosen 500 kV, 500 A electron beam in the same physical configuration as the Drude lined planar device of Chapter II. Before calculating the expected gain of the device it was necessary to ensure that our selected beam properties (current and velocity) are appropriate for the physical dimensions of our structure, two properties must be verified. First, one must ensure that the large current is not space charge limited in the conducting tube. Secondly, one must verify the magnetic field required to confine the electron beam is a reasonably achievable value. The equations for these two constraints are derived in Appendix 3 and calculated below for the 500 kV, 500 A beam.

6.2.1 Space Charge Limited Current in a Conducting Tube

The first constraint to check is that the current of the electron beam is not limited by the space charge created potential depression at the center of the electron beam. If we assume a beam with a 50 % fill factor, $r_b = 0.5r_w$, we can calculate the limiting current using the equation from Appendix 3

$$I_{max} = [1 + 2\ln(2)](32.4 \times 10^{-6})\Phi_b^{3/2}. \qquad (106)$$

Using (106) it can be determined that for a 50% fill factor 500 keV beam, the limiting current is 27.33 kA. This limit is orders of magnitude greater than our anticipated beam current indicating that our tube size is sufficient for an electron beam of this voltage and current.

6.2.2 Brillion Field Requirement

The second requirement we must verify is that the magnetic field required to confine the beam is realistic. From Appendix 3, is it shown that the Brillioun field requirement is approximately

$$B_B \approx 0.83 \times 10^{-3} \left(\frac{I^{1/2}}{r_b \, \gamma^2 \, V^{1/4}} \right) \; [Tesla]. \qquad (107)$$

For the 500 kV, 500 A electron beam, the Brillouin field requirement is approximately 20.5 mT. This field requirement is reduced from the 80.2 mT field that would have been the requirement if the relativistic correction factor had not been taken into account. A 20.5 mT field is an easily achievable magnetic field using permanent- or electro-magnets [48]; therefore, the magnetic field is not prohibitive for the chosen beam parameters.

6.2.3 Expected Gain of Relativistic Device using the Updated Equations

Based upon our verified calculations that the 500 kV and 500 A beam were realistic, we were able to calculate the expected gain of the device. Fig. 40 presents a comparison of the low energy theory presented in Chapter I with the new relativistic high energy theory discussed here. It is possible to see in Fig. 40 that when the relativistic corrections are taken into account the maximum gain rate of the device substantially increases while the bandwidth decreases. This change in the peak gain and band width are due to the addition of the relativistic correction factor.

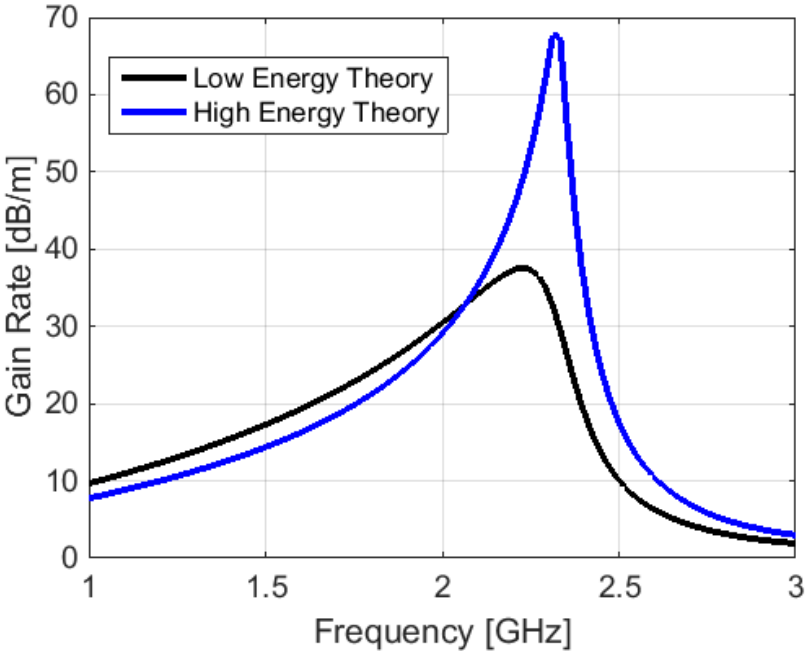

Fig. 40: Calculated MERWA gain using the original theory presented in Chapter III and the updated relativistic or high energy theory.

6.3 Relativistic HPM Particle-In-Cell Simulations

To verify the theoretical model, PIC simulations were conducted using relativistic conditions. To perform the PIC simulations, it was necessary to first resolve an issue with CST Particle Studio. CST Particle Studio had some numerical instabilities that arose when relativistic beams were used; specifically, numerical Cherenkov radiation excited RF waves that would not exist in an actual device. Therefore, as part of this work we investigated methods to avoid the numerical Cherenkov radiation to allow for the use of CST to model the relativistic HPM MERWA. Specifically, we found that higher mesh density and deliberate randomization of the mesh cell size reduced the instability. The specifics of this method along with the simulation results are presented in this section.

For relativistic MERWA simulation, a parallel plate configuration of the device was used, identical to the configuration discussed in Chapter V. The parallel plate model that was used is shown in Fig. 41. In this model, the y-boundaries are set as PMC boundary conditions to create the parallel plate configuration. The red portion of the model is the ENG medium with a Drude dispersion, the vacuum material has a wire grid outlining, and the background is PEC. The electron beam is emitted from the particle source and travels left to right at a relativistic velocity. The electron beam is velocity modulated through the use of a short-ended parallel plate waveguide that is fed by a port at the top of the model. For demonstration purposes this model was run with model properties outlined in Table 2.

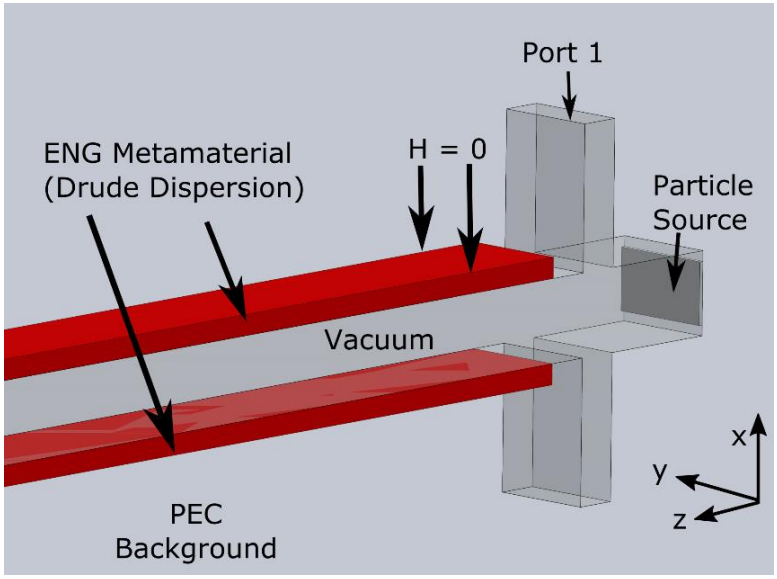

Fig. 41: Relativistic parallel plate MERWA model used with CST Particle Studio where the red material represents the ENG liner. The electron sheet beam is emitted from the particle source and travels left to right

Table 2: Relativistic Simulation Model Parameters

Parameter	Value
Axial Length	0.6 m
Simulation Time	100 nS
Drude Medium Plasma Frequency	2.64 GHz
Drude Medium Collision Frequency	1.8 GHz
Drude Medium Liner Thickness (x-directed)	5 mm
Beam Potential	500 kV
Relativistic Correction Factor	1.978
Beam Velocity	2.588×10^6 m/s
Beam Current	500 A
Beam Thickness (x-directed)	17.4 mm
Simulation Width (y-directed)	10 mm

Using the simulation parameters presented in Table 2 we found that the simulation was unstable and often producing unrealistic results. Initially, we believed that the instability was a result of the very large current exciting the backwards wave instability. However, after closer examination we found that the simulation was not stable even in the absence of the metamaterial liner (just the electron beam traveling through a PEC tube was unstable). Therefore, it was determined that the instability that we were observing was not an instability of the device we were using, but rather was an instability of the CST PIC software. To demonstrate the instability that was happening, the beam current was substantially lowered (to 10 A) and the phase space plots were examined.

Phase space plots of the electron beam at the various times in the simulation are shown in Fig. 42. In Fig. 42 (a) we can see that the electron beam is traveling through the axial length of the device and there is a clear amount of velocity modulation present (with a wavelength of approximately 160 mm). As the simulation progresses from Fig. 42 (a) to Fig. 42 (b) and (c) something appears to be happening to the beam near the end of the tube. Further, Fig. 42 (d) and (e) show that whatever is happening traveling from the end of the device back toward the beam source and is completely swamping the velocity modulation signal.

In addition, if you look very closely at the oscillation that begins on Fig. 42 (b), it appears that the oscillation has a short wavelength. Fig. 42 (b) is plotted again in Fig. 43 (a) with a zoomed in examination of the phase space plot in Fig. 43 (b). In the zoomed in plot of Fig. 43 (b), there is a very clear short wavelength present on the beam. It was unclear why a ‘higher’ frequency signal appeared to be excited.

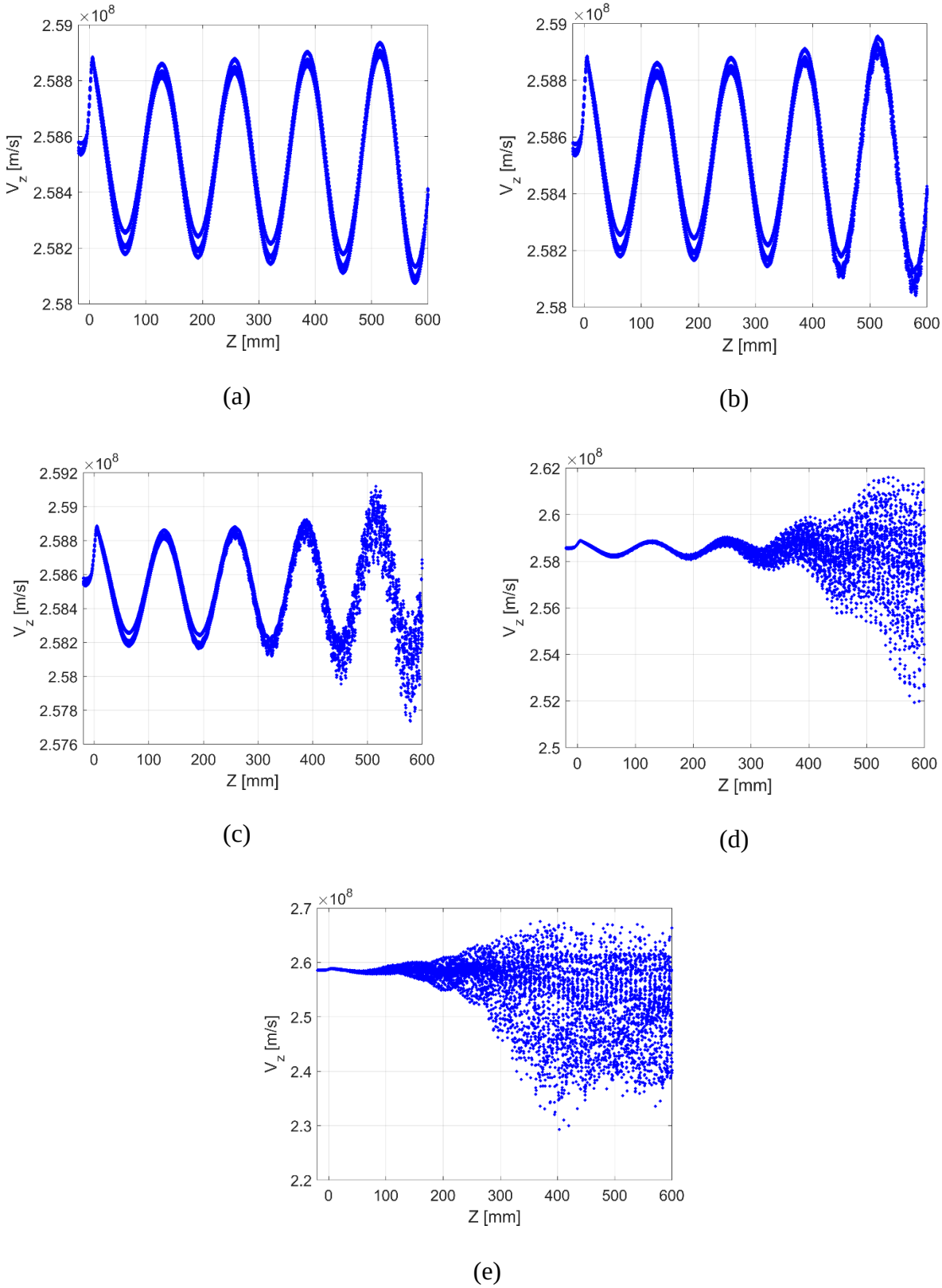

Fig. 42: Phase space of relativistic simulation showing the growth of a short wavelength signal at different times: (a) 10 nS, (b) 23 nS, (c) 30 nS, (d) 37 nS, and (e) 45 nS

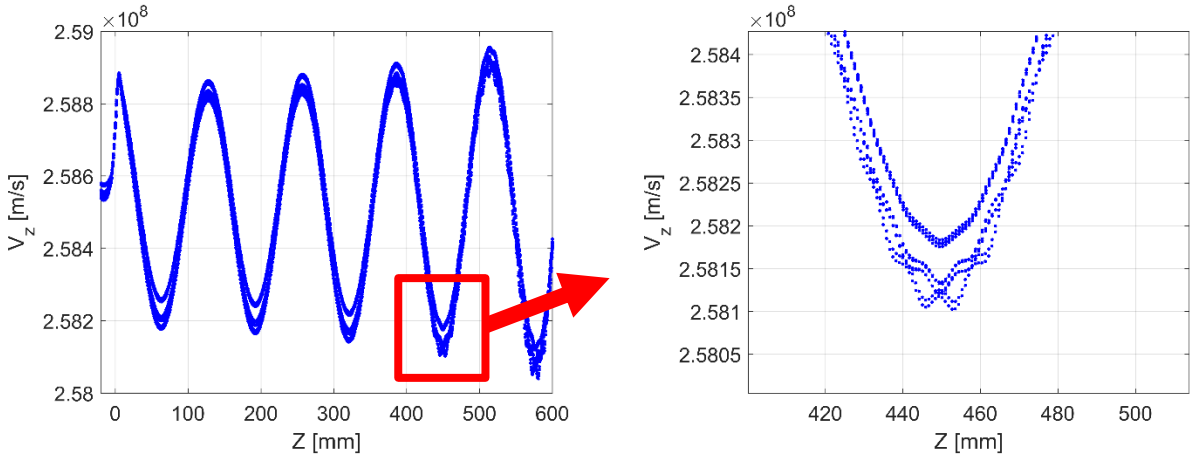

(a) (b)

Fig. 43 (a) Repeat version of Fig. 42 (b) showing the location of the zoomed in plot (b) comes from. In (b) we can see the rise of a clear oscillation wavelength.

The first guess to correcting the issue would be to assume that there is a problem with the Courant condition [49]. The Courant condition is a limiting value of the partial differential equations that can be used to ensure stability. In PIC simulations, the Courant condition is used to calculate the maximum time step to ensure that electrons do not cross more than one mesh cell in a single time step. The Courant condition can be defined as

$$C = \frac{u_x \Delta t}{\Delta x} + \frac{u_y \Delta t}{\Delta y} + \frac{u_z \Delta t}{\Delta z}, \tag{108}$$

where u_x, u_y, and u_z are the magnitude of wave velocities in the x, y, and z directions, respectively, Δt is the time step length, and $\Delta x, \Delta y$, and Δz are the smallest mesh length in the x, y, and z directions, respectively. Since the beam is primarily traveling in the axial direction, the Courant number can reduced to

$$C = \frac{u_z \Delta t}{\Delta z} \leq C_{max}, \tag{109}$$

where C_{max} is the maximum Courant number used in the simulation (usually set to 1). The maximum Courant number is used by the simulation to determine the time step. To determine the time step, the PIC simulation examines the mesh that has been created, it then determines the smallest mesh dimension in all three directions. Then, based upon the smallest mesh dimension in the simulation and the maximum Courant number that is set, the algorithm determines how small the time step must be to meet the Courant condition. To examine if the Courant condition is the culprit of the oscillation we conducted two additional simulations of the structure with 1) an increase in the axial mesh density and 2) a decrease in the simulation time step.

A simulation identical to that of Fig. 43 was run again but with the mesh density, along the axial direction, substantially increased. The phase space results of the increased mesh density simulation are presented in presented in Fig. 44. Comparing Fig. 44 to Fig. 42(a) and Fig. 42(b) we notice two things. First, the instability is still present and is actually worse with the smaller grid. Second, the apparent wavelength of the oscillation that was observed in Fig. 42 does not appear to be present in Fig. 44 (b). This indicates that an increase in the mesh density did not help to reduce the oscillation behavior of the relativistic beam. In addition to increasing the mesh density, we attempted to suppress the oscillation by reducing the time step of the simulation. A reduction in the time step can be achieved by reducing the maximum Courant number allowed in the simulation. Several simulations were run with various reduced Courant numbers and no change in the results was observed.

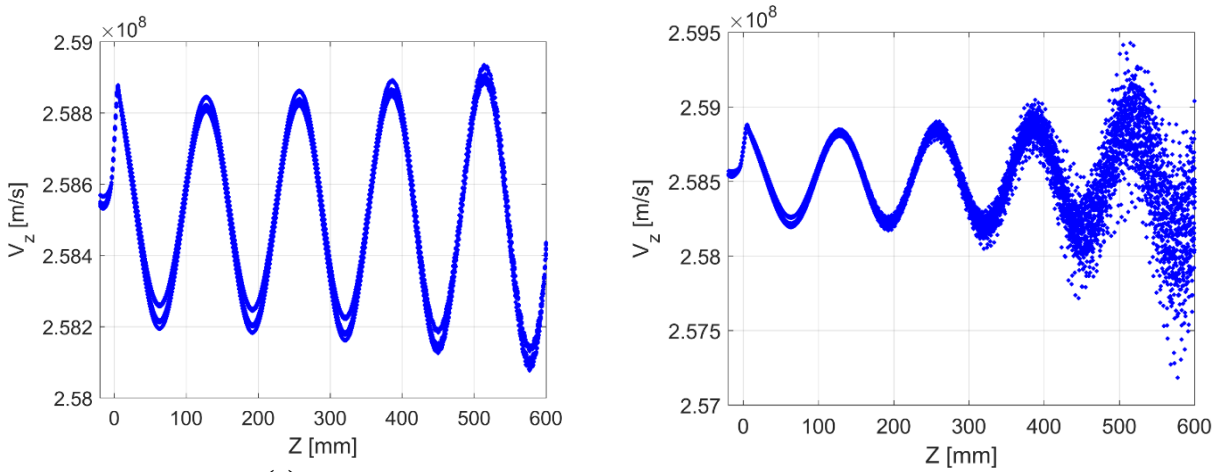

Fig. 44: Phase space at (a) 16 nS and (b) 23 nS of relativistic simulation identical to Fig. 42 but the mesh density along the axial direction is substantially increased.

Since a reduction in the simulations time step and increase in the mesh density did not resolve the instability, we still believed that there was an error in the CST algorithms for relativistic particles. However, we found that other researchers have had success with relativistic high power devices in CST, in particular [30], where a 500 kV, 80 A beam is used. In a combination of discussions with Jason Hummelt of Massachusetts Institute of Technology (MIT) and Peter Mardahl of Air Force Research Laboratory (AFRL) we discovered that the problem we were experiencing was numerical Cherenkov radiation (NCR) [50].

Cherenkov radiation is the phenomena where electromagnetic radiation occurs if a particle travels in a medium faster than the phase velocity of that medium [51]. Numerical Cherenkov radiation is the production of an electromagnetic wave due to a particle traveling faster than the phase velocity of vacuum as defined by the numerical dispersion of the simulation [49, 50]. Since finite difference time domain (FDTD) simulations exhibit some level of numerical dispersion based upon the size of the mesh cells, Cherenkov radiation can be excited if the beam

travels faster than the ‘numerical’ speed of light. The change in behavior examined in Fig. 44 (b) actually reaffirms the numerical Cherenkov diagnosis. In numerical Cherenkov radiation, the wavelength of the excited oscillation is on the order of the mesh size. By increasing the mesh density we decreased the wavelength of the oscillation. Therefore, in Fig. 44 (b) the wavelength of the instability has not gone away but has actually just decreased, as it shifted the numerical Cherenkov radiation to a higher frequency, making it difficult to distinguish in the figure [52].

Some codes have methods to help eliminate the numerical instability; specifically, the improved concurrent electromagnetic particle-in-cell (ICEPIC) software package developed by AFRL [53, 54]. ICEPIC software uses a filter technique where they filter out oscillation behavior that is around the frequency where it would occur [52]. In addition, some previous research has discussed the possibility of using a non-uniform mesh to help disrupt the generation of the oscillation [52]. Since we were not able to modify the source code of CST to implement any type of filtering techniques we attempted to spoil the oscillation behavior by creating a non-uniform grid and keeping a small mesh density. While CST cannot simply implement a non-uniform mesh (uniform meshes are usually desired for easier convergence) we were able to implement a method to force the simulation to generate a non-uniform grid. To create a non-uniform grid we used a feature of CST where the mesh will automatically align with the edges of PEC blocks. Using the scripting capabilities of CST we add a discrete number of PEC blocks to the model that are outside of the simulation domain (i.e. they are placed in the PEC background of the simulation). By using a scripting language we were able to arbitrarily place a specified number of PEC blocks along the length of the device each with a different size and spacing between

adjacent blocks. This forced the mesh to vary along the length of the device. The purpose of the PEC blocks are to force CST to place mesh cells that align with the edges of the blocks.

Fig. 45 (a) shows the CST model along with the blocks placed along the length of the device. The grey blocks are made of PEC, while the light blue blocks are inside of a vacuum region of the device and therefore made to be vacuum. Fig. 45 (b) shows the grid that is generated by CST when the blocks are present. It can be seen in Fig. 45 (b) that the grid snaps to the edges of the blocks (red dots indicate points where the algorithm has forced the mesh to align with a geometrical feature) and that the grid is clearly non-uniform along the axial length. While this has been very successful for us in suppressing numerical Cherenkov radiation, as will be shown below, one should note that some issues could arise from using this method. In particular, two concerns should be taken into consideration for future models, even though they did not appear to create problems for us. First, the blocks must be made with a reasonable axial length. If the length of the blocks is made too small, the time step required to meet the Courant condition becomes smaller, greatly increasing simulation time. Second, it is necessary to be aware of the variation of the axial length of the cells. If the variation in cell size becomes too dramatic (greater than 10:1 for adjacent cells) the standard FDTD algorithm is known to have convergence issues; however, CST may have ‘behind-the-scenes’ algorithms implemented to help overcome the convergence issues of non-uniform grids.

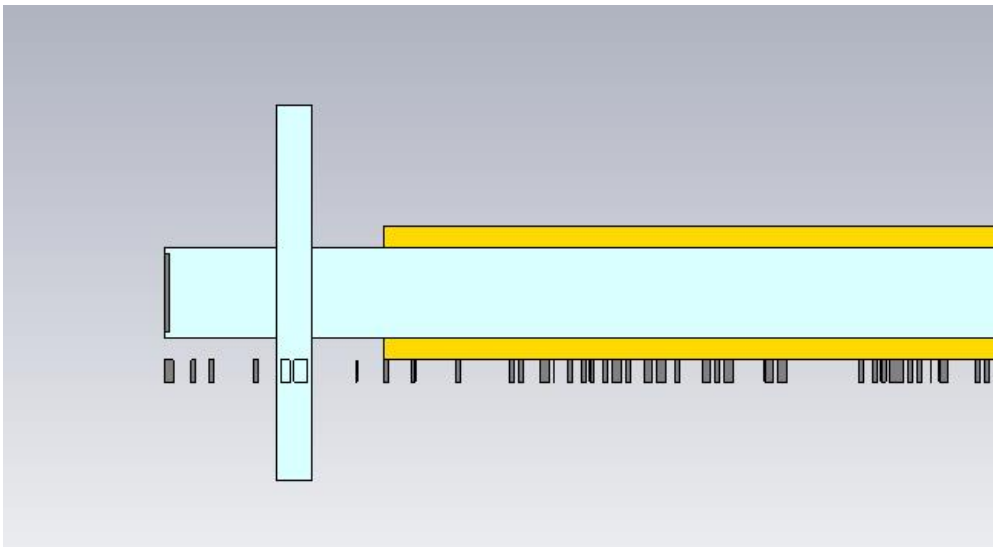

(a)

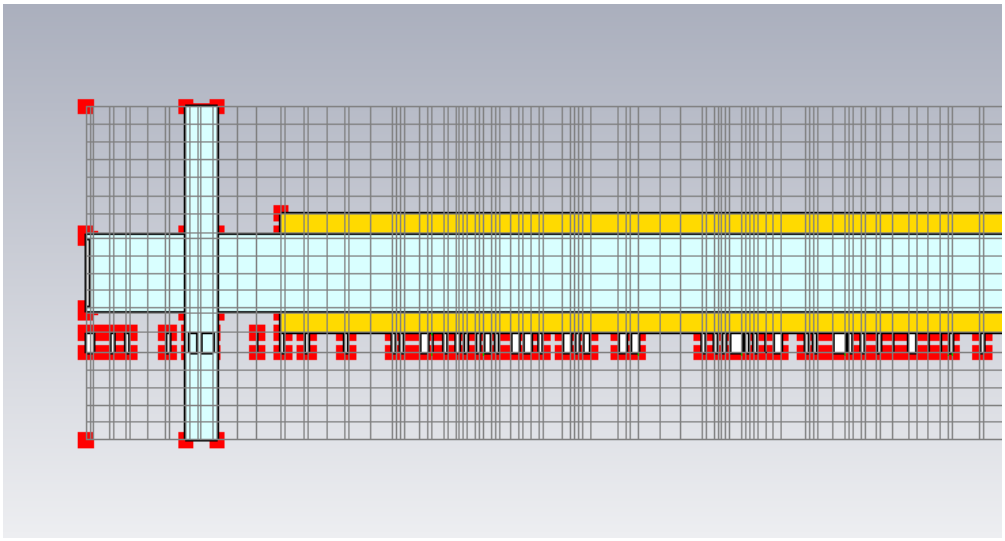

(b)

Fig. 45: Relativistic MERWA model with PEC blocks added to randomize the size of the mesh elements

This randomization method introduces an engineering tradeoff. More grid cells can result in a better suppression of the Cherenkov radiation but at the cost of simulation time. Through trial and error we were able to determine the number of PEC blocks that would provide adequate suppression of the numerical Cherenkov radiation with reasonable simulation times. Fig. 46

presents the phase space at the end (100 nS) of the relativistic MERWA simulation when the mesh has been randomized. Even at the time of 100 nS, no visible Cherenkov radiation has been excited.

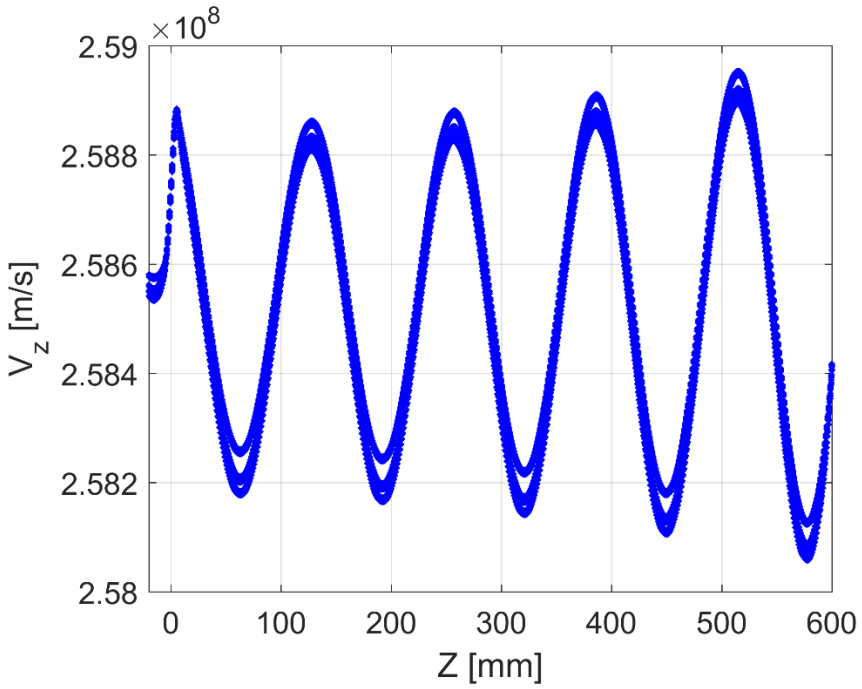

Fig. 46: Relativistic MERWA model with PEC blocks added to randomize the size of the mesh elements (100nS)

When we discovered the NCR issue, we discussed this with the developers of CST. While the engineers were unable to provide immediate solutions, CST now provides information about the Cherenkov instability issue in newer versions of CST, starting with CST 2016. In particular, in the help documentation of CST 2016 two mitigation methods are suggested. First, as previously mentioned in this report, CST suggests an increase in the mesh refinement along the direction of maximum particle velocity. The second method they suggest is to use a dispersive material to damp the oscillation. This method is very similar to the suppression method used by ICEPIC and

discussed above. In CST's implementation they suggest the use of a material with a dispersion property of:

$$\varepsilon_r(\omega) = \varepsilon_\infty + (1-\varepsilon_\infty)\left((1-r)\frac{\omega_R}{\omega_R + j\omega} + r\frac{\omega_0^2}{\omega_0^2 + j\omega\delta - \omega^2}\right), \qquad (110)$$

to fill the region where the particle travels (instead of vacuum). The dispersion that they suggest is a 'Lorentz-like' dispersion model. The idea of their method is to set the resonant frequency of the medium to be approximately equal to the numerical Cherenkov frequency (which can easily be estimated using a new built-in macro) to create large absorption for waves with frequencies near the Cherenkov frequency. Future work may look at the incorporation of this lossy material to our simulations, but at the current time the use of grid randomization has successfully mitigated the instability issues.

Using the randomization method we re-simulated the relativistic MERWA. Fig. 47 presents the results of the PIC simulations compared to the analytic result. Similar to previously discussed PIC results, the gain rate presented in Fig. 47 was calculated by measuring the exponential growth of the ac component of the electron beam's velocity modulation. The simulation results agree very well with the analytic results in Fig. 47. Fig. 47 presents a verification of the relativistic analytic theory as the simulation agrees much better with the high energy curve of Fig. 40 than the low energy curve.

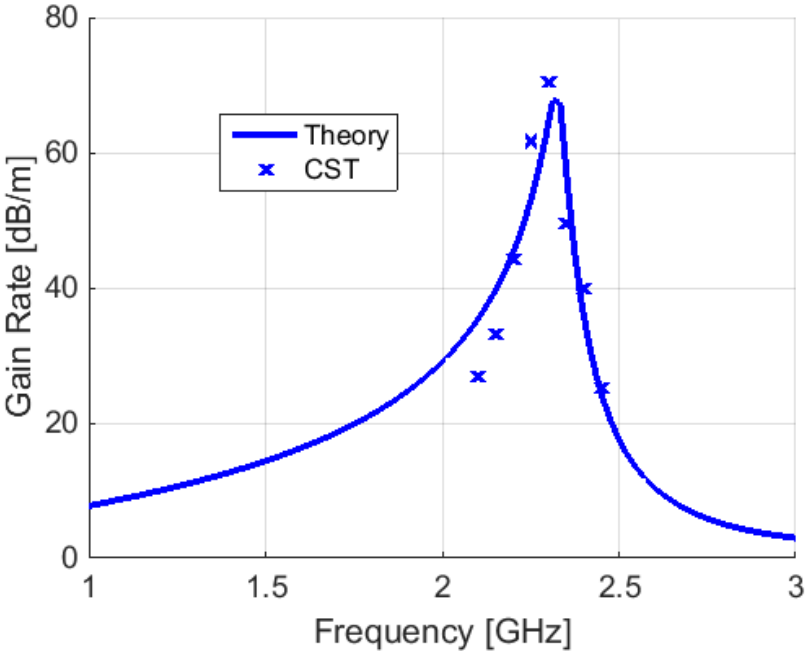

Fig. 47: Relativistic MERWA PIC simulation gain vs. analytic model

Chapter VII: Experimental Testing of MERWA Prototype

Task 5 of this work experimentally investigated a MERWA prototype. The experimental MERWA prototype was not intended to be a relativistic device, but rather a scaled, lower power, device with a beam voltage of 10 kV and beam current of 300 mA. The specifications of the MERWA prototype were selected as they are within the current capabilities of the vacuum electronics laboratory at the University of Wisconsin – Madison. The experimental research provided a verification of the theoretical work and provided insight to the overall capabilities of a MERWA. Portions of this work have been submitted to the IEEE Transactions on Plasma Science, the 2017 International Vacuum Electronics Conference, and the 2017 International Conference on Plasma Science.

The experimental work of this dissertation, task 5, incorporated all of the steps necessary to construct an experimental device and perform initial experiments. The vacuum chamber configuration, high voltage power supply system, electron gun construction, magnetic field configuration, testing of the cathode, cold tests of the metamaterial structure, and hot tests the MERWA device were all completed as part of this research. Task 5 is broken down into five primary steps for this report: 1) analytic description and model of the rectangular waveguide lined with an anisotropic metamaterial, 2) metamaterial design and construction, 3) cold (no electron beam) testing of the metamaterial structure, 4) configuration of the hot (with electron beam) test experiment, and 5) hot test results. Details of all five of these steps are outlined below.

7.1 Analytic Model of Rectangular Waveguide with Metamaterial Liner

This section develops the analytic model for the EM fundamental hybrid transverse magnetic (EH) mode that arises in a rectangular waveguide with an anisotropic ENG liner on one side, as shown in Fig. 48. A structure with a liner on only one side was investigated for simplicity of construction and ease of converting to a structure that can be used for future studies on metamaterial-enhanced resistive wall amplifiers. Further, we found that the liner only needed to provide an ENG response to electric fields parallel to the short side of the waveguide (y-directed) to allow for wave propagation. The derivation of the dispersion relation for the EH mode, detailed below, is based upon the theoretical analysis of [55] and [56].

In this analysis, we assumed the MTM liner was anisotropic, only having a non-unity relative permittivity in the y-direction. An anisotropic liner was investigated as only a y-directed negative permittivity is required for wave propagation and is much simpler to construct than an isotropic MTM. In addition, we assumed the material was non-magnetic, so the liner had the properties:

$$\varepsilon_{liner} = \begin{bmatrix} \varepsilon_0 & 0 & 0 \\ 0 & \varepsilon_{yy} & 0 \\ 0 & 0 & \varepsilon_0 \end{bmatrix} \text{ and } \mu_{liner} = \begin{bmatrix} \mu_0 & 0 & 0 \\ 0 & \mu_0 & 0 \\ 0 & 0 & \mu_0 \end{bmatrix}, \qquad (111)$$

where ε_{yy} is given by the dispersion of the MTM and ε_0 and μ_0 are the permittivity and permeability of free space, respectively.

Assuming that the y-directed electric field has the form

$$E_y(x, y, z, t) = E_y(y)e^{-j(\omega t - k_x x - k_z z)}, \qquad (112)$$

along with the properties of the liner, the resulting Helmholtz wave equation for the EH mode ($H_y = 0$) is

$$\frac{\partial^2 E_y}{\partial y^2} + \left(\frac{\omega^2}{c^2} - \frac{\epsilon_0}{\epsilon_{yy}} k_x^2 - \frac{\epsilon_0}{\epsilon_{yy}} k_z^2\right) E_y = 0, \qquad (113)$$

k_x and k_z are the x and z-directed wavenumbers, respectively. Using the Helmholtz equation, along with the $E_{||} = 0$ boundary conditions at the four metal boundary walls and continuity of the y-directed electric flux density ($D_y = \varepsilon_{yy} E_y$) at the interface of vacuum and the liner relation, the resulting dispersion relationship is

$$k_{y1} \tan\big(k_{y1}(d-b)\big) = k_{y2} \tan\big(k_{y2} d\big). \qquad (114)$$

where k_{y1} and k_{y2} are the y-directed wave numbers in region 1, vacuum, and region 2, the liner. The wave numbers are given by:

$$k_{y1}^2 = (\omega^2 c^2 - k_x^2 - k_z^2) \qquad (115)$$

and

$$k_{y2}^2 = \left(\omega^2 c^2 - \frac{\epsilon_0}{\epsilon_{yy}} (k_x^2 + k_z^2)\right). \qquad (116)$$

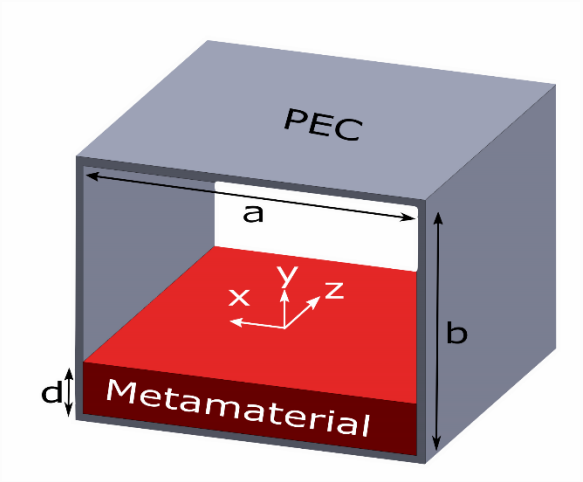

Fig. 48: Waveguide structure of interest with a metamaterial liner along the bottom portion of the waveguide that exhibits an ENG response in the y-direction.

To demonstrate the expected dispersion of this mode in the structure shown in Fig. 48, the analytic dispersion was calculated using (114) for a MTM with a Drude dispersion model,

$$\varepsilon_{yy} = \varepsilon_0 \left(1 - \frac{\omega_p^2}{\omega(\omega + j\omega_c)}\right), \qquad (117)$$

where ω_p and ω_c are the effective plasma and collision frequencies of the medium, respectively. Illustrative results are shown as the black solid line in Fig. 49 for $a = 25\ mm$, $b = 30\ mm$, $d = 5\ mm$, $\omega_p = 2\pi \times 3.5 \times 10^9\ [rad/sec]$ and $\omega_c = 0\ Hz$ (no loss). In Fig. 49, the EH mode of the analytic Drude medium liner scenario, propagates below 2.5 GHz while for the unlined waveguide there is no propagation below its cutoff frequency of 5 GHz.

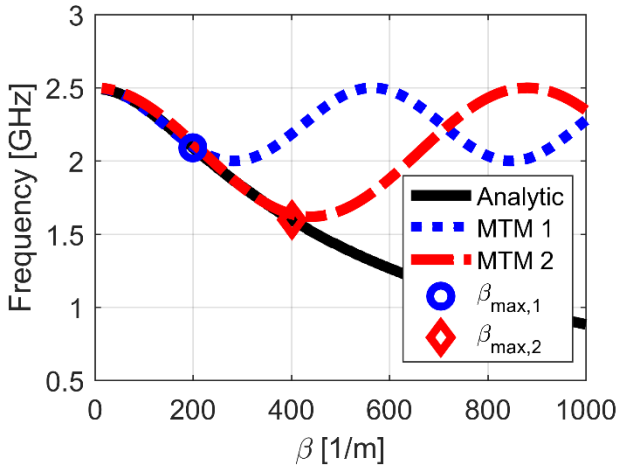

Fig. 49: Analytic dispersion of the lowest order EH mode for the structure shown in Fig. 48. In this analytic calculation $a = 25\ mm$, $b = 30\ mm$, $d = 5\ mm$, and the metamaterial used a Drude dispersion model with $\omega_p = 2\pi \times 3.5 \times 10^9\ [rad/s]$ and $\omega_c = 0\ [rad/s]$. The two additional curves (MTM 1 and MTM 2) are example curves used to demonstrate the effect of metamaterial periodicity and are described, along with the two β_{max} points, in the next section.

Since the previous work [57] only demonstrated the ENG properties of the meandered line MTM for a parallel plate configuration it was important to ensure these properties also existed when added to a rectangular waveguide. To verify that the meander line elements emulate a MTM

medium as the liner of a waveguide, eigenmode simulations were conducted using the structure shown in Fig. 50. This illustrative example is very similar to the structure examined in [57] but uses a perfect electric conductor (PEC) walled waveguide instead of an infinitely wide simulation. For this example, referring to Fig. 50, we used a waveguide width, a = 25 mm, waveguide height, b = 30 mm, a period of 4 mm, a meander width of 15 mm, a gap of 0.6 mm, and a line width of 0.15 mm. All four walls of the waveguide were assumed to be PEC as well as the meander line. To simulate the dispersion of the waveguide with meander line elements along the bottom, simulations were performed using a quasi-periodic measurement technique [38, 39] with CST's eigenmode solver [35].

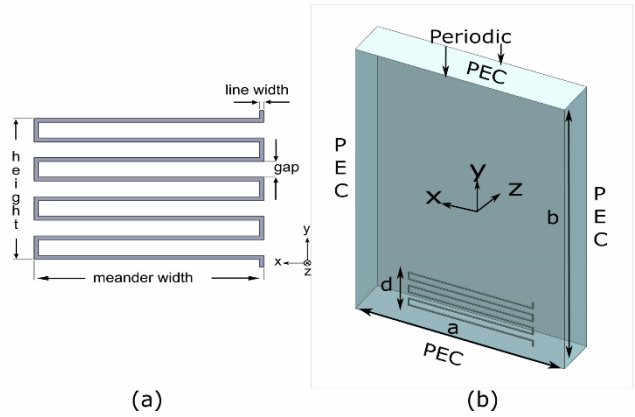

Fig. 50: (a) Pictorial representation of the meandered line element labeling the relevant dimensions. (b) Illustration of the model used to calculate the dispersion of the structure with a meander line based metamaterial liner.

Using the simulated dispersion of the structure, shown in Fig. 51(a), it was possible to extract/calculate the effective permittivity that the liner must have had to exhibit the measured dispersion using (114) with an assumed liner height. Evaluating the currents on the meander element as well as the y-directed electric field allowed determining the 'effective' height of the ENG liner. The extracted effective permittivity values of this structure are shown in Fig. 51(b).

After calculating, the extracted permittivity of the liner we fitted the results to known permittivity models using the method of least squares.

Using the least squares fitting analysis, we found that the effective permittivity of the liner, shown in Fig. 51(b), can be approximated by a Drude-Lorentz model. This was expected for several reasons. First, if the meander was infinitely long and continuous, the MTM structure would exhibit a Drude like response [44]. However, when the meander has edges (non-infinite meander) the effective permittivity has been demonstrated to be more similar to a Drude-Lorentz model [58, 59] as the finite length meander element has a resonant frequency. The equation of the Drude-Lorentz model is

$$\varepsilon_{yy} = \varepsilon_0 \left(1 - \frac{\omega_p^2 - \omega_0^2}{\omega^2 - \omega_0^2 + j\omega\omega_c}\right), \qquad (118)$$

where ω_p is the plasma frequency, ω_0 is the resonant frequency, and ω_c is the collision frequency. For the analysis in this paper we have neglected the losses of the MTM and therefore assumed that the collision frequency is zero. For the structure shown in Fig. 50, we found that the fitted Drude-Lorentz model that had the best agreement had an $\omega_p = 2\pi \times 2.42 \times 10^9\ [rad/s]$ and $\omega_0 = 2\pi \times 1.22 \times 10^9\ [rad/s]$. The permittivity of a Drude-Lorentz model with these parameters is presented in Fig. 51(b), labeled as 'Fit'.

It should be expected that the effective medium extraction will only work for small beta values (to remain consistent with the MTM assumption of $p \ll \lambda_z/10$). If it was desired to know the bottom of the passband ($p\beta_Z = \pi$) one can evaluate the resonant frequency of the meander element.

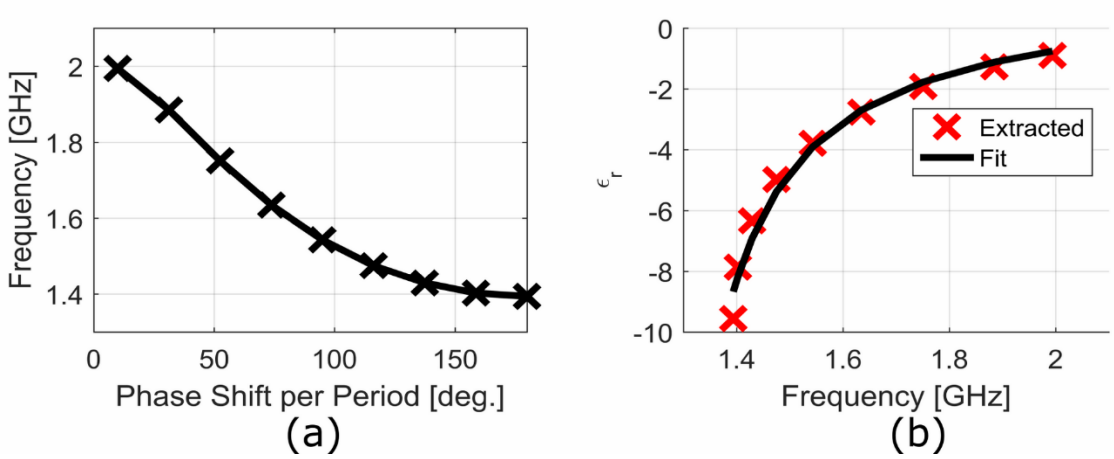

Fig. 51: a) Simulated dispersion of the structure shown in Fig. 50 (a) using CST's eigenmode solver. b) Effective permittivity of the metamaterial liner ($\varepsilon_r = \varepsilon_{yy}/\varepsilon_0$) extracted using the results of a) and an assumed height of 4.85 mm. The fit permittivity was found to fit (118) with $\omega_p = 2\pi \times 2.42\ GHz, and\ \omega_0 = 2\pi \times 1.22\ GHz$.

7.2 Experimental Metamaterial Design and Construction

This section discusses the fabrication of practical meander elements and the assembly of the MTM structure. We also address how the meander elements can be designed to modify the passband frequency. For this work we chose two different meander designs to provide the desired ENG response at L-band frequencies. The two meander designs were chosen to have very different passbands in order to demonstrate the flexibility of the design and to help verify theory.

7.2.1 Meander Element Designs

The two meander designs used in this work are presented in Fig. 28 and will be referred to as meander sets A and B for the remainder of this dissertation. In each of these meander designs, the unit element consisted of two meanders side-by-side instead of a single meander as shown in Fig. 50(b). For the experimental configuration, we desired to use a waveguide structure with a larger width (we choose the waveguide width to be 44 mm (1.73") for simple construction,

discussed in more detail below) which was wide enough to accommodate two side-by-side meanders. Though we used a rectangular waveguide, the fabrication method could easily be extended to circular waveguides.

In the meander elements, two individually meandered lines were placed next to each other and the resulting structure has nearly the same pass band as a structure containing only one of the meandered line with the same dimensions. Instead of using two side-by-side meanders, a single meander element could be used in the center of the wide waveguide, but the fields would not be uniform across the waveguide width. Alternatively, if the meander was made wider to cover a larger portion of the waveguide width, the inductance added by the meander would be too large, shifting the passband of the structure.

In addition to using two meanders, the meander elements that were constructed have a shorting bar between the side-by-side meanders. This shorting bar was added for structural stability as we feared that the relatively thin elements would not be able to keep upright. The addition of this shorting bar does shift the passband of the dispersion, as we are affecting the overall inductance of the meanders, but simulations allowed us to take this into account.

In meander set A, the meanders were 10 mm wide, separated by a 10 mm gap, and a height of 5 mm. Meander set B consisted of two 15 mm wide meanders separated by 5 mm, and a height of 7 mm. Referring to Fig. 50 (a), both meanders designs used a wire width of 0.15 mm, a gap between meander lines of 0.6 mm, a wire thickness (into the page) of 0.125 mm, and were constructed of copper. Below the meanders, a rectangular portion of metal was added to help

with the assembly process labeled as the alignment block and will be discussed in the next section.

As stated, the two meander designs were selected to provide very different effective permittivity and demonstrate the flexibility of this design. It is worth noting these meander designs can be altered to adjust the passbands and dispersion characteristics as desired. Specifically, increasing the meander width or the number of rungs increases inductance and lowers the plasma frequency [58, 59]. In addition, increasing the period between elements along the axis of the waveguide will lead to a decreased plasma frequency, however, one should remember that this will also raise the bottom of the passband due to the requirement that $p < \lambda/10$ as described in the previous section.

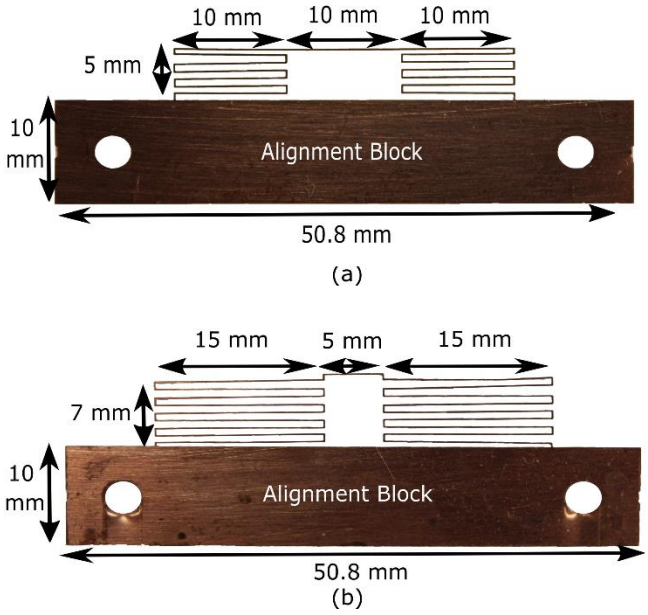

Fig. 52: Single meander elements for a) meander set A and b) meander set B, both constructed of copper. Meander set A uses a meander design with two 10 mm wide meander elements, a 10 mm space between them, and a height of 5 mm. Meander set B has two 15 mm wide meanders, a separation between them of 5 mm, and a meander height of 7 mm. The lower portion of the meander element structures, rectangular section with two holes, is only used for MTM assembly, discussed below.

The meander elements were constructed using a chemical etching process which allows for considerable flexibility for designing elements. In addition, this method allows for intricate designs to be developed as long as feature sizes are amenable to the chemical etching process (smallest feature sizes are approximately equal to material thickness, 0.125 mm). While we chose to use meander line elements, this technique could alternatively be used for other unit cell designs, such as loops or spirals, which may provide superior benefits; however, the investigation of alternative structures is outside the scope of this work.

7.2.2 Periodic Structure Design and Assembly

To create a periodic structure and set the periodicity, 4 mm (0.157”) stainless steel spacers were placed between each one of the meander line elements and aligned with the alignment blocks on the meander elements. These spacers were constructed using a laser cutting process. Stainless steel was used as it was cost effective and our analysis demonstrated they provided no disadvantage to copper. Using spacers in this configuration allowed for a simple method to set the periodicity of the structure by choosing the thickness of the sheet the spacers were cut from. The MTM was assembled, as shown in Fig. 53, by alternating the placement of meander and spacer elements and inserting long stainless steel threaded rods to hold the entire structure together.

A piece of aluminum U-channel, 1” x 2”, with a thickness of 0.13” was used to act as the remaining three sides of the rectangular waveguide, resulting in an interior cross section of 1.74” x 0.87”. To facilitate easy modeling of the structure, by avoiding issues that could arise from improperly matched end openings, the ends of the cold test structure were terminated with metal plates to give the effect of a PEC boundary. Fig. 54 shows the complete structure, minus a metal

end cap, which contains the MTM assembled structure, an aluminum top plate, and a monopole probe used for measurement.

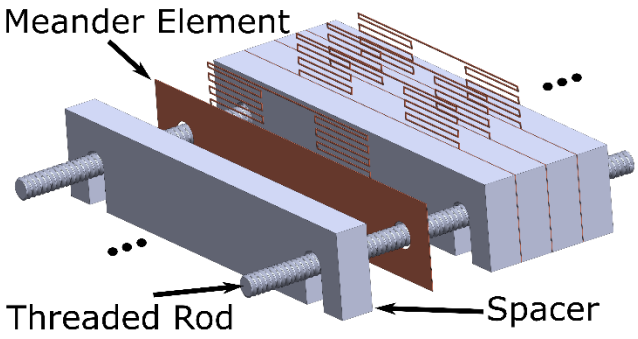

Fig. 53: Exploded view of the MTM periodic structure. The periodic structure consists of alternating meander and spacer elements. Two threaded rods are then used to hold the MTM structure together. This picture does not show the two metal plates that are placed at each end of the structure to act as end caps nor does it show the top and side walls of the waveguide.

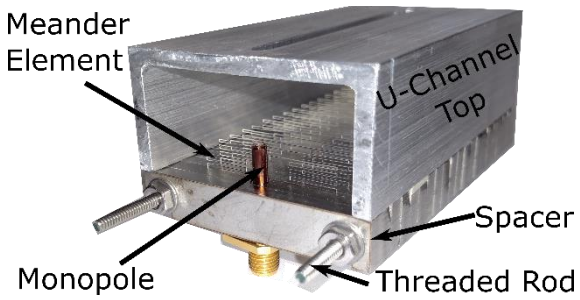

Fig. 54: Assembled MTM periodic structure included a top. This picture does not show the metal plate that is placed at the end of the structure to act as an end cap.

7.3 Cold Test of Practical Metamaterial

Two cold test experiments were performed to measure the performance of the meandered-line element MTM design and verify that the meanders are correctly exhibiting the desired ENG permittivity. These experiments were: 1) wave transmission (S-parameter measurement) and 2) dispersion measurement. Both of these methods, as well as their simulation counterparts, are discussed here along with the results.

7.3.1 Experiment 1: Transmission Measurement

Initial experiments using a vector network analyzer were conducted to measure the transmission of the EM passband. Measurement of the structure's transmission properties allowed for measurement of the EM passband as well as a quantitative measurement of the loss in the system.

The experimental structure contained 21 meanders and 22 4 mm spacers and is shown in Fig. 54. Electrically-small monopole antennas were inserted through the second to last spacer (between two adjacent meander elements) at each end and used as input and output coupling ports into the structure. These monopole antennas were flange mounted SMA connectors where the dielectric sheath of the center conductor has been removed. The design of these monopole antennas were not optimized for matching between the monopole and the structure. As a result, the magnitude of the measured transmission is relatively low in some of the experiments. The use of the monopole antennas is not intended to be a method to inject energy, if these structures were used for wave propagation, but provided a very simple method for us to inject energy, measure a frequency response, and compare to simulation. The overall experimental setup for the transmission measurement is shown in Fig. 54 and Fig. 55.

The simulation of the transmission measurement used the time domain solver in CST [35]. The entire structure was modeled as closely as possible to the experimental device, including modeling the SMA jacks as input and output ports. The time domain calculations implemented a hexahedral grid system which required many fewer mesh cells to properly mesh the meander line elements. The meanders were modeled as a lossy metal (good conductor approximation) with the

conductivity of copper ($5.96 \times 10^7\ S/m$) while the waveguide walls were simulated as aluminum ($3.56 \times 10^7\ S/m$).

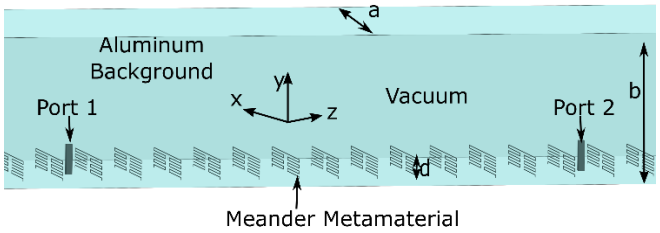

Fig. 55: CAD drawing of the MTM periodic structure assembly structure used to perform the transmission experiments. A vacuum (free space) region is surrounded by aluminum ($\sigma = 3.56e7$) and has a width, a, and height, b. The meander line elements are periodically spaced with period p and have a height of d. Two PEC monopoles are placed between meander elements at each end of the structure. The monopole antennas are fed with discrete ports at the bottom of the monopole; the monopoles are labeled as port 1 and port 2.

The simulation and experimental results of the transmission measurement are shown in Fig. 56, where the simulation matches the experiment well. In Fig. 56 there are two important properties of the curves to note. First, within the passband of the structure a series of ‘peaks’ occur. These peaks are due to a Fabry-Perot resonance that occurs because we choose to end the waveguide structure with metal endcaps. The number of peaks that is present in the passband is related to the number of elements used in the periodic structure, with more elements resulting in more peaks. Second, a frequency shift in the passband of the structure is present between meander set A and B. The frequency shift between the two meander sets is due to the different meander dimensions Meander set B uses 15 mm wide meanders versus the 10 mm wide design in set A. The wider meanders present in set B create a larger inductance on the periodic wire elements causing a lower effective plasma frequency. This lower effective plasma frequency results in a permittivity that is near zero and negative at a lower frequency resulting in a lower frequency passband.

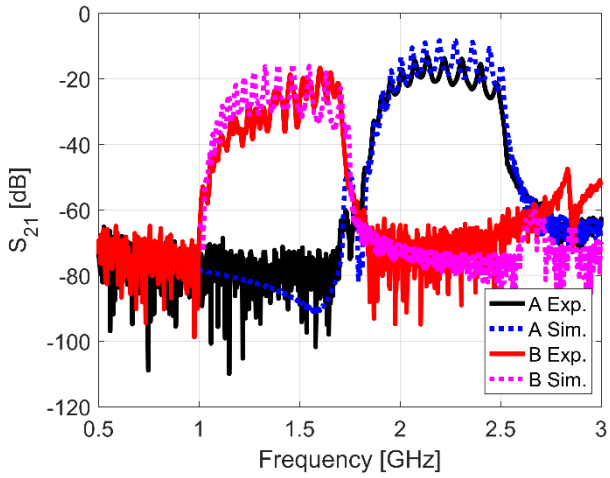

Fig. 56: Measured transmission between two monopoles configured in the cold test assembly shown in Fig. 54 with meander set A and B compared to the simulated response. The simulation results were obtained from CST using the model shown in Fig. 55.

The small discrepancies between the simulations and the experiments are attributed to the slight variation in meander dimensions in the manufactured elements where the simulation assumed perfect meander elements. In addition, the poor matching between the monopole antenna and the periodic structure is the reason that the magnitude of the transmission is variable over the two structures.

7.3.2 Experiment 2: Dispersion Simulation and Measurement

Simulations of the structure's dispersion were identical to the description of the dispersion measurement in Chapter 3, using CST's eigenmode solver. Since the meander material affects the propagation characteristics of our structure, losses were included by modeling the meander material as a lossy metal (good conductor approximation) and meshing the surface of the meander using a tetrahedral mesh.

To experimentally verify the desired effects of an ENG liner and validate simulation results, we measured the dispersion relationship of each of the two periodic structures, Set A and Set B. Our methodology was similar to that of [60], which will be explained briefly here. For each frequency of interest, a movable measurement probe was swept along the length of the structure using a precision linear motion system and the electric field was sampled at discrete intervals along the length of the waveguide. An illustration of the experimental dispersion setup can be seen in Fig. 3 of [60] for further information. In this setup, a power splitter is used to provide an input to the test structure and a reference to a mixer at the scope input. The input signal develops a phase shift as it travels the distance from the input probe to the moveable measurement probe. The output signal from the measurement probe is mixed with the reference signal provided by the power splitter. This mixing of two phase-shifted signals with the same frequency produces a DC term, which contains the phase shift information. To extract the phase shift information, a 4 GHz digital oscilloscope was used to take the time average of the signal. A spatial FFT of the measured phase shift values yields the propagation constants for that frequency.

Since the phase resolution of a spatial FFT is determined by the length of the structure, a 12 inch long test structure was constructed, though the measurement range was limited to 9.4 inches by the length of the linear motion system. With a MTM period of 4.1 mm and an overall length of 9.4 inches allowed for a phase resolution of the spatial FFT to be 4.5°. Our experiment varied from the one shown in [60] in two ways: 1) the monopoles presented in the cold test assembly in Fig. 55 were used to input a signal to the dispersion experiment and b) an aluminum plate was placed at the end of the waveguide instead of a matched waveguide.

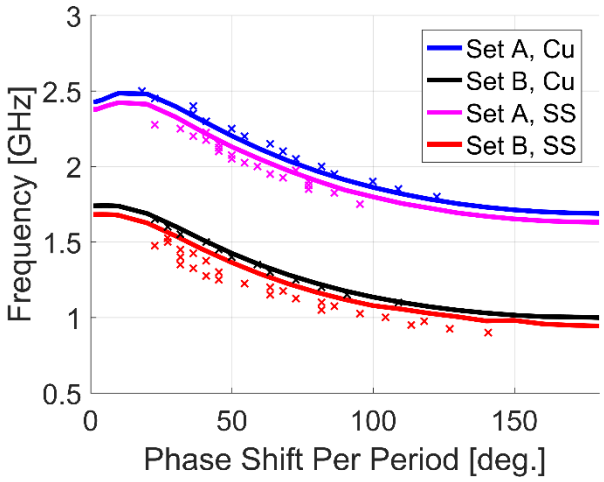

Fig. 57: Measured dispersion of copper (Cu) meander based MTM compared to simulation results obtained with an eigenmode method for set A (blue) and set B (black). The pink and red curves are the dispersion for a structure constructed with stainless steel (SS) meander sets and is discussed in section 0.

The results from both the dispersion simulation and experiment are plotted in Fig. 57. The simulation results are plotted as a solid line while the experiment results are x's. Data in blue represents copper meander set A while black data represents copper meander set B (labeled Set A, Cu and Set B, Cu, respectively). Two additional data sets are included in the figure and are discussed in the next section. By looking at the plot, one can quickly draw 2 conclusions: 1) The simulation and experimental data agree well, and 2) A large frequency shift occurs from meander set A to meander Set B as a result of the different dimensions of the MTM elements.

Similar to the example case in Section 7.1, we then used the simulated dispersion points to extract what the permittivity of the liner would have to be. The extracted permittivity values for each meander set, as well as the fit to a model are shown in Fig. 58. Similar to the single meander case, the constructed meanders very closely resembled a Drude-Lorentz permittivity model. For meander set A, the Drude-Lorentz model that had the closest match with the extracted permittivity had an $\omega_p = 2\pi \times 3.01\ GHz$ and $\omega_0 = 2\pi \times 1.43\ GHz$. For meander set

B, the fit Drude-Lorentz model had the properties $\omega_p = 2\pi \times 2.27\ GHz$ and $\omega_0 = 2\pi \times 0.84\ GHz$.

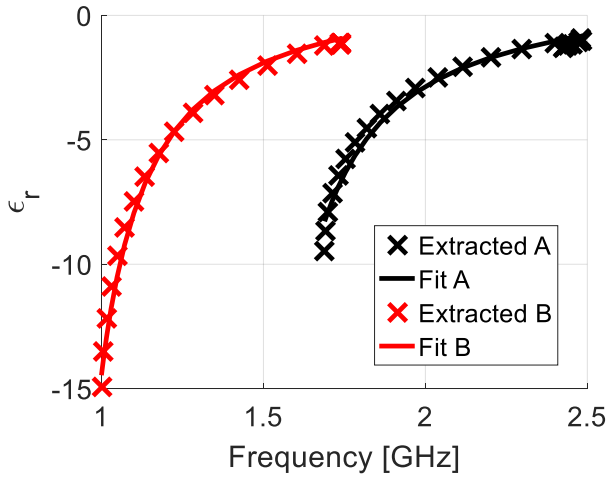

Fig. 58: Effective permittivity of the meander sets extracted using the method described in Section Chapter VII. with the dispersion curves in Fig. 57. The extracted effective permittivity was then fit to a Drude-Lorentz model for each meander set. For meander set A the fit parameters were $\omega_p = 2\pi \times 3.01\ GHz, \omega_0 = 2\pi \times 1.43\ GHz$, and for meander set B the fit Drude-Lorentz model has the properties $\omega_p = 2\pi \times 2.27\ GHz, \omega_0 = 2\pi \times 0.84\ GHz$.

7.3.3 Lossy Metal Implementation

Last, we explored how the meander material impacts transmission and dispersion by repeating the measurements with stainless steel meanders instead of copper meanders. Since we used a chemical etching process to fabricate the meander elements, it was very straightforward to construct the elements out of a different material, adding an additional benefit to the flexible chemical etching process. Through the experimental analysis of our stainless steel meander elements, we found that the choice of material used for the meander can have a large effect the transmission of the EM wave.

Analyzing the effects of metal choice can be understood by incorporating losses into the work of [32] as done by Maslovski, et al. [61]. While the work of [61] focused on a wire array, the same concepts can be applied to the meandered line array. Increasing the losses of the meander metal increases the resistance and self-inductance of the meander wire. The resulting increase in inductance shifts the effective plasma frequency of the MTM down while the additional resistance increases the losses.

Fig. 57 presents the measured dispersion of the stainless steel (SS) meander sets, labeled Set A, SS and Set B, SS. The dispersion of the stainless steel based MTM is very similar to the copper based MTM but is slightly shifted down in frequency for both meander sets. This small shift is consistent with the theory of wire loss presented in [61]. However, it can also be noticed that the experimental dispersion measurements of the stainless steel structure do not agree with simulation as well as the copper structures. The less accurate agreement between the simulation and experiment is due to a simulation meshing issue. As a result of the lower conductivity of the stainless steel meanders, the skin depth increases. The meander elements that were constructed were made of 0.1 mm thick stainless steel which is approximately equal to 10 skin depths. When a metal thickness is on the order of ~10 skin depths the meshing required for convergence is very high. Therefore, the slight discrepancy is explained by computational memory limitations of our simulation computer. Adaptive meshing was used to refine the mesh to the practical limits of our simulation computer's capabilities (64 GB RAM). Further increasing the mesh density would have the effect of slightly lowering the frequency of the simulated dispersion curve. While further increasing the mesh density is beyond the capabilities of our simulation computer,

analyzing the convergence as far as practical shows that we are likely within a few tens of MHz of the fully converged solution, which agrees with the experimental results.

Fig. 59 presents the transmission measurement of the two meander sets when they are stainless steel elements. By comparing the results of Fig. 59 with Fig. 56 we see to major differences: 1) a major reduction in the transmission level with only a slight shift in the frequency, and 2) the absence of the peaks in the passband of Fig. 56.

The conductivity of the meanders drastically affects the amount of power transmitted. This can be seen by comparing the levels of the S_{21} measurements in the passband between the copper structure in Fig. 56 (approximately -20 dB) and the stainless steel structure in Fig. 59 (approximately -30 to -40 dB). In addition, as a result of this electromagnetic dampening this also causes a reduction in the peaks in the passband of the structure as the Fabry-Perot resonance is also damped.

Again, as a consequence of the thin meander compared to a skin depth, there is less accurate agreement between the simulation and experiment due to simulation meshing. When simulating the dispersion of the structure, it is only necessary to model a single unit cell. Therefore, as described above, close agreement between simulation and experiment was achievable for the dispersion of the stainless steel structure by refining the mesh as much as practically possible. To simulate the transmission measurements, approximately twenty unit cells of the structure must be modeled. For the copper based structure, this poses no issues because a good conductor approximation can be used in the finite integration technique (FIT) algorithm. For the stainless steel structure, where the thickness of the element is only approximately 10 skin depths thick

(violating the good conductor assumption) one must have a very fine mesh inside of the metal material. A very fine mesh inside of the stainless steel is simply not practical as it would require more than 20 million mesh cells. To overcome this meshing constraint, we implemented a transmission line matrix (TLM) algorithm for the stainless steel structure. The TLM algorithm is known to have better modeling of thin elements by using a moderate mesh inside of the metal materials instead of the very fine mesh required by a FIT algorithm. As seen in Fig. 59, this yields good enough agreement to validate our theoretical understanding of the structure's electromagnetic properties. Further perfect agreement would have required a prohibitively expensive grid and simulation and that cost was not warranted merely to illustrate the reason for the small residual discrepancy. The CST model with stainless steel meanders had approximately 5M to 10M mesh cells and took about 4 hours to complete on the dual Xeon processor computer available to us for this research.

Though it usually would not be desirable to have a system that had a damped electromagnetic wave, this investigation of using the less conductive stainless steel did provide further verification that the meander structure emulates an ENG liner. In addition, some specific applications, such as a resistive wall amplifier [11], could benefit from a structure that provides some dampening. In the resistive wall amplifier, it is desirable to have the ENG properties but have the EM wave damped. The ENG properties provide improvement in device performance, but if the EM wave is not damped its presence may interact with the electron beam and can excite instabilities.

Decreasing the conductivity of the material had a small effect on the frequency range of the system but drastically modified the system's attenuation. Therefore, since the frequency shift in the results is minimal, the MTM can be designed by selecting the meander dimensions to create the desired passband and then select a metal with the appropriate conductivity to obtain the required power absorption coefficient.

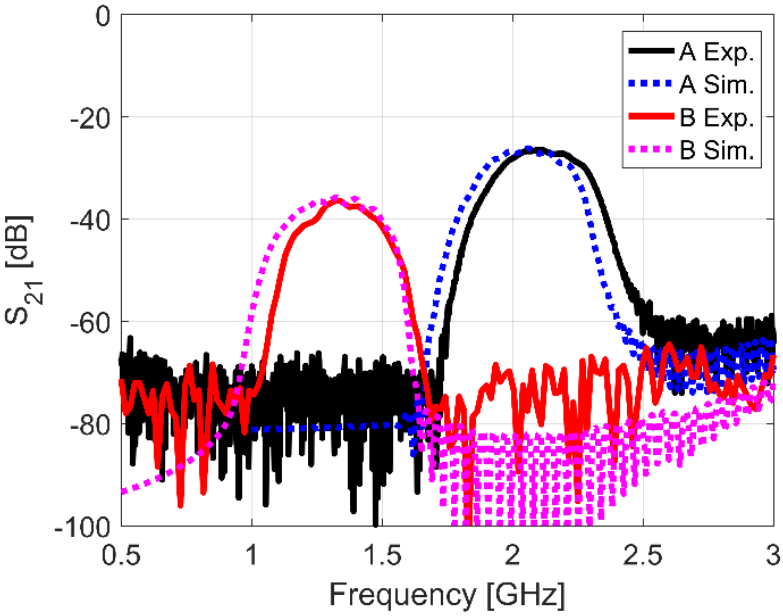

Fig. 59: Simulation and measurement results of the transmission measurement of the metamaterial constructed with stainless steel meander elements.

7.3.4 Lossy Paint Addition

To further damp the backward EM wave, a layer of lossy graphite was added to the bottom wall of the waveguide along with the meander elements. The layer of lossy graphite was implemented by using a graphite paint (Aquadag), discussed in more detail below. It was not practical to paint the entire MTM surface, which functioned as the bottom wall of the wave guide, so we implemented a MTM where the periodic spacer elements, between the individual meanders

elements, were coated with a lossy graphite layer. This lossy graphite layer is shown in a pictorial representation in Fig. 60.

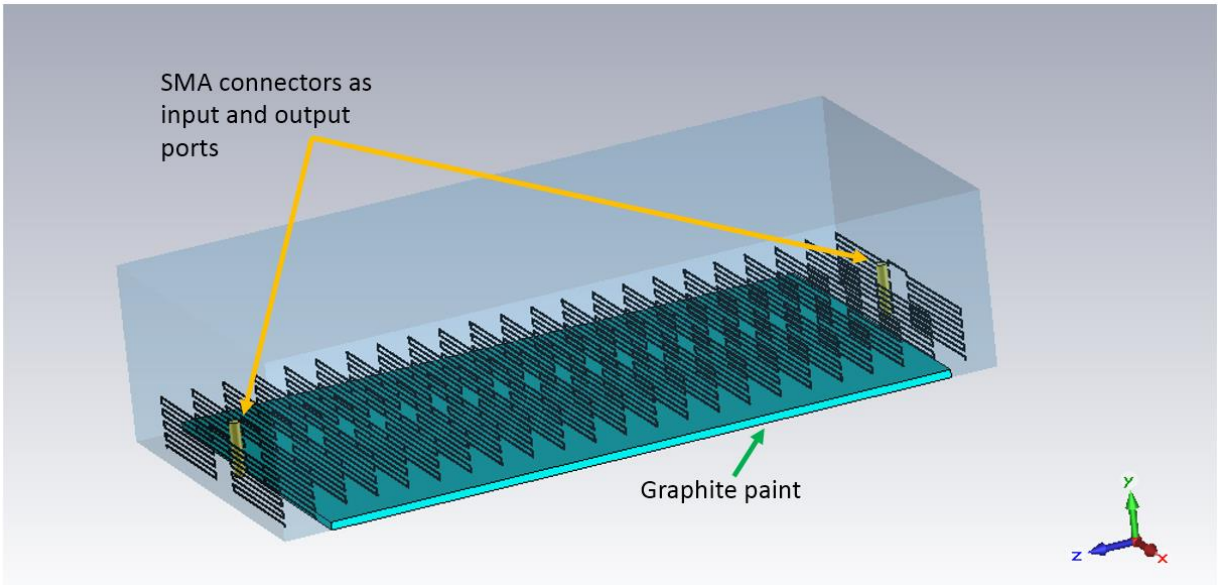

Fig. 60: Pictorial representation of a short section of rectangular waveguide with the meanders on the bottom surface of the waveguide and a graphite paint liner covering the bottom wall of the waveguide

The graphite paint was a water-based colloidal graphite. The graphite paint used for this project had the trademark name of Aquadag E (or simply Aquadag) from Ladd Research [62]. The electrical characteristics of the graphite paint (as a dry coating) can be varied by adjusting the ratio of concentrate to diluent, the method of application, the resulting dry thickness, and the type and degree of heat treatment. Typical resistance values of the dry coating on a glass substrate are presented in Table 3.

Table 3: Methods of application and resulting surface resistance of Aquadag E.

Application Method	**Thickness (Dry)**	**Cure Cycle**	**Resistance**
Dip 1:3	1.0 mil	5 minutes @ 302°F (150°C)	30 ohms/sq
Spray 1:5	0.5 mil	Preheat surface 212°F (100°C)	150 ohms/sq
Brush 1:1	0.3 mil	Air dry	1000 ohms/sq

In a waveguide liner, a coating of graphite paint on one surface acts as a sheet resistance. The sheet resistance is not only a function of the conductivity but also the thickness of the layer. For this application, we used simulations to determine that a lossy material thickness of approximately 0.5 mm thick was needed to significantly damp the EM wave. We attempted to create this relatively thick layer but several difficulties arose; in particular, we found that the paint had adhesion problems. We attempted to create the thick layer using two different methods: 1) painting several applications of thinner layers and 2) pouring the paint into a thick mold and allowing it to dry as a thick layer. When we attempted to paint several thinner layers we found that beyond the first layer, subsequent layers would not adhere to the lower layer. In addition, when adding a second layer, the paint would often reduce the adhesion of the first layer from the surface. Creating a thick layer of liquid in a mold resulted in a medium that would crack while drying and flake off of the surface. We attempted these application methods using a variety of techniques (droppers, paint brushes, etc.) and under several temperature conditions but did not find any methods that were successful.

To overcome the adhesion problems, we implemented a method of alternating the colloidal graphite between layers of Kapton tape. This method was extremely effective. By using alternating paint and Kapton, each layer of paint had a material that it could adhere to. The Kapton tape adhered to the graphite layer by tightly wrapping the Kapton around the edges of the spacer element. Fig. 61 presents a single spacer element where five alternating layers of Kapton tape and graphite paint have been applied. It is possible to see in Fig. 61 that the Kapton tape wraps around the entire spacer element. It was necessary to wrap the tape completely around the spacer on every layer as the tape did not adhere to the graphite paint, so by wrapping it around it would maintain its position. Further, it is possible to see on the top surface of the spacer that there is a small divot in the tape layer in the center. This was done for the same purpose as wrapping the tape around the edges. We intentionally left an approximately 3 mm section at the center of the top surface that was not painted, allowing the tape to stick to the surface on which the paint is applied.

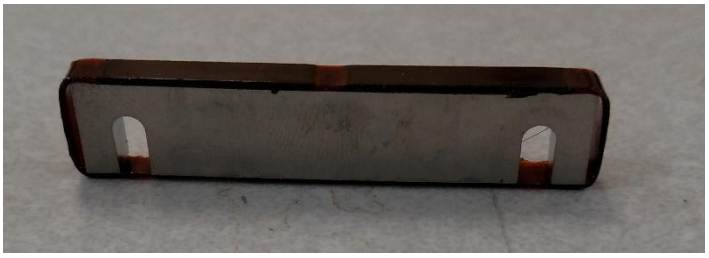

Fig. 61: A spacer element with five alternating layers of Kapton tape and graphite paint.

We were able to achieve a consistent paint layer thickness by using a specific amount of colloidal graphite on each spacer. To determine the paint thickness, we created several test structures with known paint volumes applied and measured the thickness. Using a profilometery

measurement, we determined that each layer of paint was approximately 50 μm thick separated by the tape thickness of 89 μm (0.0035 in thick tape).

The full sheet thickness was created by the following process:

1) Use metal threaded rods to hold ~10 to 20 spacer elements adjacent to each other;
2) Apply an initial layer of Kapton tape to the spacer elements;
3) Add a 3 mm wide strip of Kapton tape along the sides and center of the spacers (these Kapton strips act as barriers to the liquid paint that was applied keeping it in place as it dries);
4) Mix the colloidal graphite in a 1:1 mix with distilled water;
5) Measure out 1 droplet per spacer element from a 3 mL plastic transfer pipette;
6) Use a liquid dropper to apply the paint to the surface using the tip of the dropper to overcome surface tension and coat the entire surface;
7) Let the liquid dry for several hours;
8) Repeat for four layers of paint, resulting in five layers of Kapton tape;
9) After the final layer of Kapton tape is applied, use a very sharp knife to cut through the layer of Kapton tape and separate the individual spacer elements.

The painted meander elements can then be re-assembled in a MTM assembly with meander elements. Fig. 62 shows a short constructed MTM section using the painted spacer elements.

Fig. 62: Short section of assembled MTM structure using SS meander elements and painted spacers.

After constructing the painted MTM assembly, we tested the transmission properties discussed in section 7.3.1 . We conducted the transmission measurement using an MTM with no painted spacers, with half of the spacers coated with paint, and with all of the spacers coated in paint. The MTM structure was created using the SS meander set B. Fig. 63 presents the transmission results of the painted structures and can be compared to the results in Fig. 59. It is shown in Fig. 63 that the presence of the painted spacers using, five alternating layers of paint and tape, substantially damped the EM wave by over 20 dB.

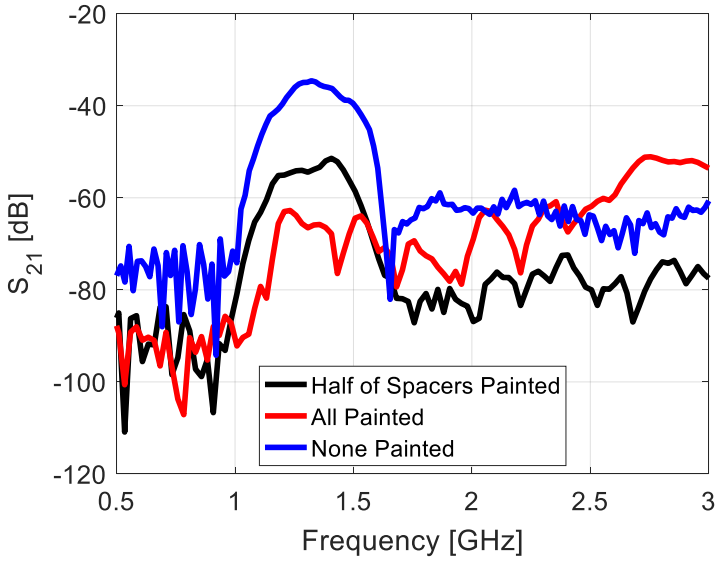

Fig. 63: Transmission measurement of the SS-based MTM set B with the introduction of the graphite painted spacer elements

7.3.5 Cold Test Conclusions

This section demonstrates that a periodic arrangement of inductive meander lines can be used as a practical MTM implementation that exhibits a Drude-Lorentz type permittivity. When placed along the bottom of a rectangular waveguide, this MTM implementation was demonstrated to

successfully emulate an ENG liner through both transmission and dispersion measurements that agree well with simulation. In addition, this work investigated how the material choice affects the performance of this MTM implementation by demonstrating that using less conductive metals does not have a large effect on the structure's dispersion but significantly increases the absorption.

The solderless, all metal structure design allows for vacuum compatibility while fabrication methods used in this work offer a flexible method to design reduced size waveguides. The meander elements discussed in this work can be designed as needed to shift the passband by adjusting the meander width, meander height, and periodic element spacing. The chemical etching process used to fabricate the meander elements can also be extended to other unit cell designs as needed while the overall waveguide construction can easily be extended to circular waveguides. This manufacturing process also allows for easily changing the material used for the meander elements, which could be beneficial for applications where the EM wave is damped without removing the ENG properties. In addition, we examined the use of stainless steel meanders, instead of copper, and the introduction of graphite painted layers to significantly reduce the propagation of the EM mode.

7.4 Experimental Hot Tests

Finally, the constructed MERWA was ‘hot tested’ with an electron beam. The hot tests of the prototype MERWA were all conducted using a vacuum chamber configuration at UW-Madison. In addition to the actual experiments, this task also included all of the necessary setup steps to perform the experiments including the assembly of the vacuum chamber, electromagnets for beam confinement, design and construction of the electron gun, and construction of a velocity modulation structure. All of the work completed to setup the system for the hot test experiments as well as the hot test results are discussed in this section.

7.4.1 Vacuum Chamber Configuration

The vacuum chamber used for this work is constructed of 4” stainless steel pipe connected with 6” conflat flanges and is shown in Fig. 64. The vacuum chamber is approximately 1.5 m long from left to right and features multiple locations for mounting necessary feedthroughs. At the left end of the chamber, a 4-axis positioner is used to hold the cathode and anode, inside of the vacuum chamber, and for beam alignment. A close up image of the positioner is shown in Fig. 65. The electron beam travels from left to right in the chamber shown in Fig. 64. In addition to providing physical position control, the positioner has been equipped with both high voltage and low voltage electrical feedthroughs to power the cathode and anode. The right end of the camber incorporates a conflat flange that is incorporated with a water cooled copper plate which is used for collection of the electron beam. The electrical design of the electron gun and collector systems are discussed in subsequent sections of this report. The vacuum chamber is also wrapped with heating tape. The heating tape allows for increasing the surface temperature of the chamber to above 100 C, allowing for the evaporation of water to increase vacuum.

Vacuum is obtained using a combination of three pumps, a diaphragm roughing pump (760 Torr to 2 Torr), turbomolecular pump (10 Torr to <0.1 mTorr), and an ion pump (< 0.1 mTorr). To measure the vacuum, two vacuum gauges are employed, a Convectron gauge to measure pressures between 1 mTorr and 1000 Torr and an ion gauge to measure pressures below 1 mTorr. The base pressure of the chamber is approximately 5 nTorr. The ion gauge is configured to have a set point at the maximum operating pressure of the system (10^{-7} Torr) and implements a relay system to disable the operation of the cathode if the pressure exceeds this set point.

Fig. 64: Vacuum chamber setup used for all experimental hot tests discussed in this dissertation. The vacuum chamber is a 4" cylindrical tube encompassed by large electromagnets. The electron pencil beam used for the experimental tests travels from left to right in this configuration.

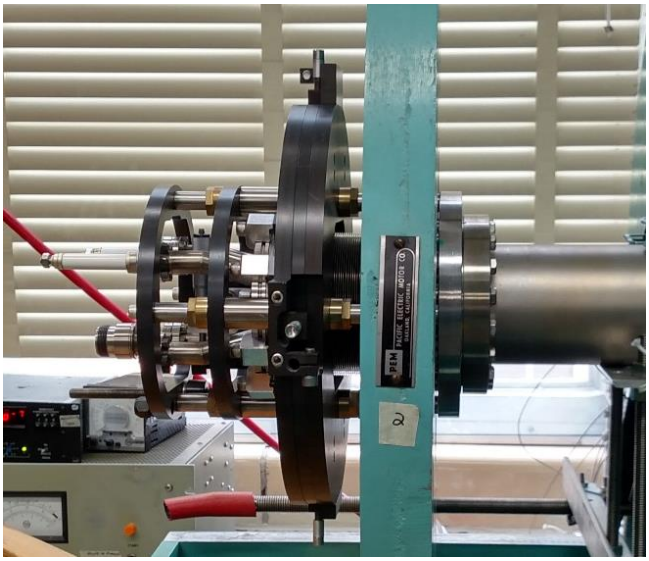

Fig. 65: Close up image of the 4-axis positioner used to hold and align the electron beam.

The large green rings, seen in Fig. 64, that encompass the vacuum chamber are water cooled electromagnets. The electromagnets are used to produce a uniform axial magnetic field along the center of the vacuum chamber. The axial magnetic field is required to keep the pencil beam from expanding. The design, power requirements, and achievable magnetic field are discussed in the next section.

7.4.2 Magnetics Design

As mentioned previously, it was desired to use a pencil electron beam with this experiment. Cylindrical electron beams naturally want to expand radially due to space charge forces. If a background axial magnetic field is present, an inward force is created to contain the electron beam in a pencil shape. To provide the beam confinement, a set of electromagnets are used. The seven electromagnets used in this work are shown in their final configuration in Fig. 64. The final configuration of the magnets was used to provide an axial magnetic field along the length of the vacuum chamber. When this project was started, the magnets had unknown properties (number of turns, resistance, etc.). Therefore, it was necessary to measure the properties and

performance of the magnets and compare the results to analytic theory. Several simple test cases were performed to determine the properties of the magnets. That procedure is discussed here along with the maximum field that we achieved and used for hot tests.

To determine the axial field that can be created by each of the electromagnets it was necessary to determine the number and dimensions of each wire turn inside of the coil. In addition, the number of wire turns and dimensions can be used to calculate the length of the wire and resulting resistance to help determine power supply requirements. To find the length of the magnet wire, in each coil, we first examined the construction of the magnets. Through physical examination we were able to determine that the magnets are constructed of 18 radial turns of wire and have 4 stacks, of the 18 turns, in the axial direction. Based upon the measured 6.75 in. coil section shown in Fig. 66 and the known number of 18 turns, the magnet wire can be determined to be 0.375 in. square. The length of continuous magnet wire can then be estimated by calculating a summation of 18 circle circumferences with diameters starting at 12 in. and increasing by 0.375 in. This results in a complete wire length of approximately 143 ft. (43.6 m) of wire, per stack of the magnet. The length of wire per stack is then multiplied by the 4 stacks per magnet, assumed to be in series, to a total of length approximately 572 ft. (174.3 m). Assuming the wire cross section of approximately 0.375 in. X 0.375 in. (9.525 mm) and a copper wire material, the expected DC resistance of the magnet wire can be calculated be 0.0359 Ohms.

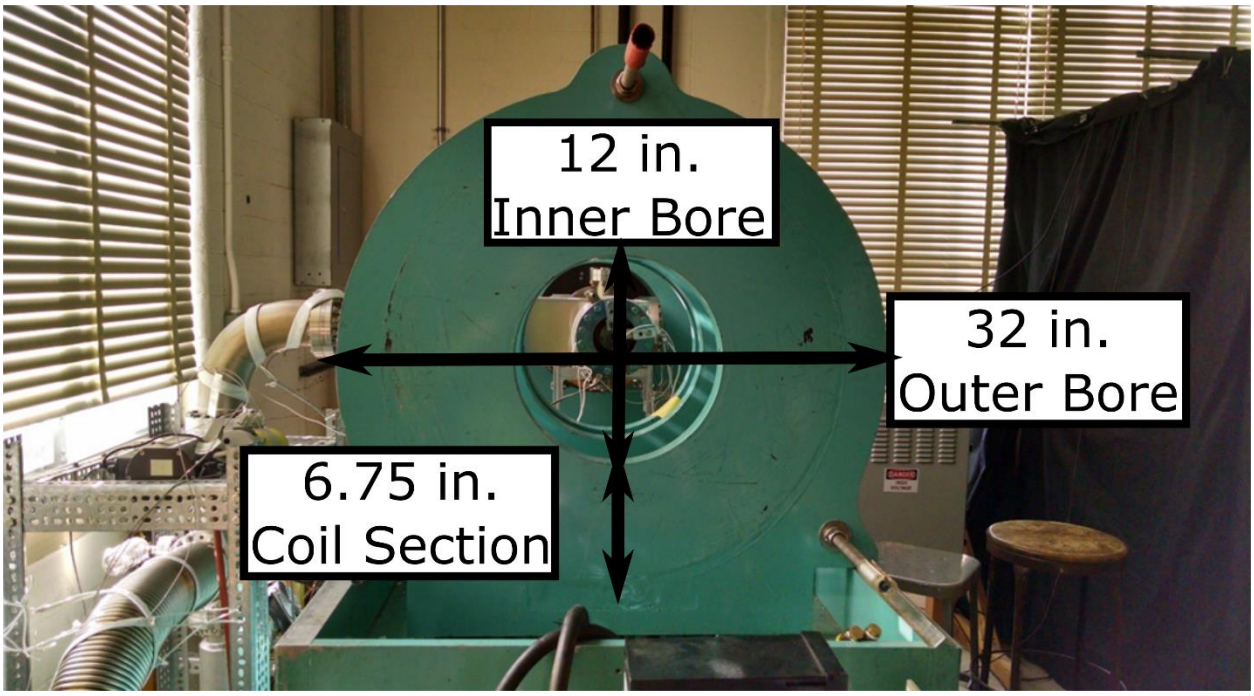

Fig. 66: Side view of the electromagnet coils with physical dimensions.

To verify the magnet's resistance, we applied a fixed current to the winding using a current controlled dc power supply. The current controlled power supply used for this measurement was able to provide up to 40 A of dc current to the winding and displayed the voltage used to supply that current. Using Ohm's law we can calculate the resistance of the coil. The calculated resistance of a single magnet versus the applied current is presented in Fig. 68. The resistance appears to be a function of the current; however, this is simply an artifact of the experimental setup. When the current is low, the voltage supplied by the power supply is also low and within the significant digits displayed. The average resistance value was found to be a resistance of 0.034 Ohms, very close to the expected 0.0359 Ohms. The average presented in Fig. 67 is an average of the when the dc current was greater than 7 A, to remove the error seen at low currents.

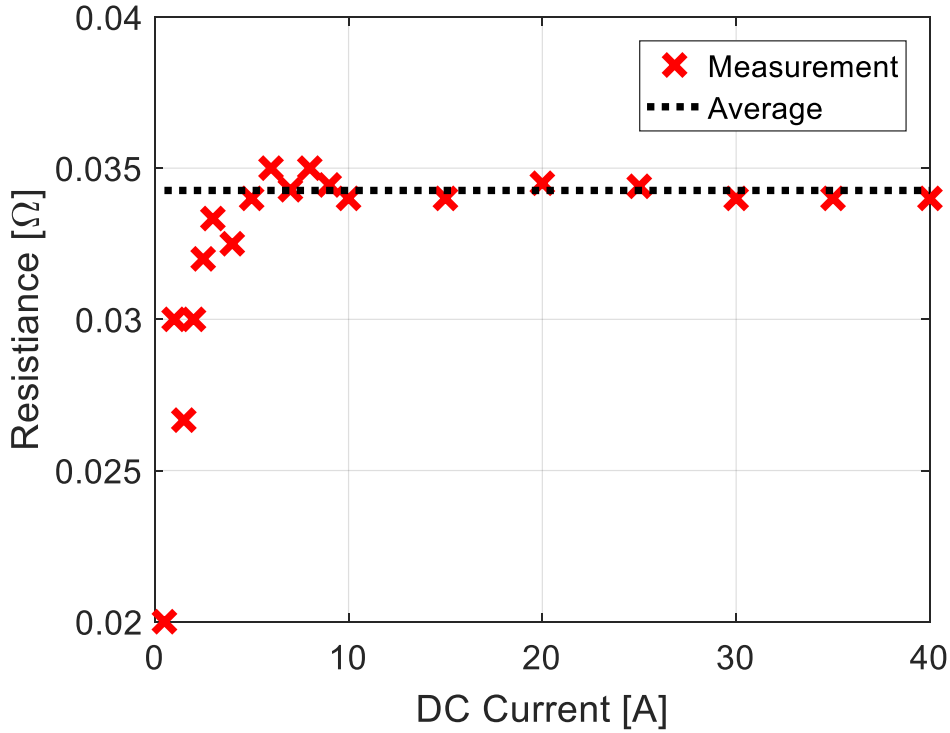

Fig. 67: Measured resistance versus current for a single electromagnet with an average resistance measurement of 0.034 Ω.

Based upon the known dimensions of the coils, we were able to analytically estimate the magnetic field that would be generated by the magnet. To analytically calculate the magnetic field we first assume that only the on-axis magnetic field is desired and that the magnets are rotationally symmetric. For a single loop of wire, the Biot-Savart law can be reduced to [63]

$$B(z) = \frac{\mu_0}{2}\frac{I\,a^2}{(a^2+z^2)^{3/2}}\hat{\boldsymbol{z}} \qquad (119)$$

where μ_0 is the permeability of free space, I is the current in the loop, a is the radius of the loop, and z is the axial distance from the plane of the loop to the point of interest. As indicated by (119), the on-axis magnetic field created by the single loop is in the axial direction. For a magnet, such as the one used in this experiment, where multiple loops of current are present, superposition can be used along with the Biot-Savart law to estimate the on-axis field. Using

superposition is a highly idealized situation and will not be a perfect analytic calculation of the on-axis field but provides a very good estimate. The magnetic field generated by a multi-loop electromagnet can be calculated by

$$B_z(z) = \sum_n \frac{u_0 I_n}{2} \frac{a_n^2}{(h_n^2 + a_n^2)^{3/2}} \qquad (120)$$

where I_n is the current in loop n, a_n is the radius of loop n, and

$$h_n = z - z_n, \qquad (121)$$

with z_n being the axial position of loop n. Since the electromagnets used in this work used a continuous length of wire, the current in each loop was constant. The analytic on-axis magnetic field for a single magnet (at $z = 0$, the center of the magnet) as well as the experimentally measured field are presented in Fig. 68 as a function of the drive dc current. The experimental measurement of the magnetic field was completed using a Sypris Model 6010 Hall Effect Gaussmeter. The probe of the Gaussmeter was aligned along the axis of the magnet. As expected the on-axis magnetic field has a linear relationship with current and matches the analytic theory very well. In addition to measuring the on-axis magnetic field at the center of the magnet, we measured the magnetic field produced by a single magnet as a function of axial position. For this experiment, the magnet was powered with 50 A of dc current. The measured on-axis magnetic field is presented in Fig. 69 where the analytic theory matches the measured values very well. Using a drive current of 50 A, the magnetic field in the center of the magnet is approximately 95 Gauss and falls off to 75 Gauss 0.1 m from the magnet center.

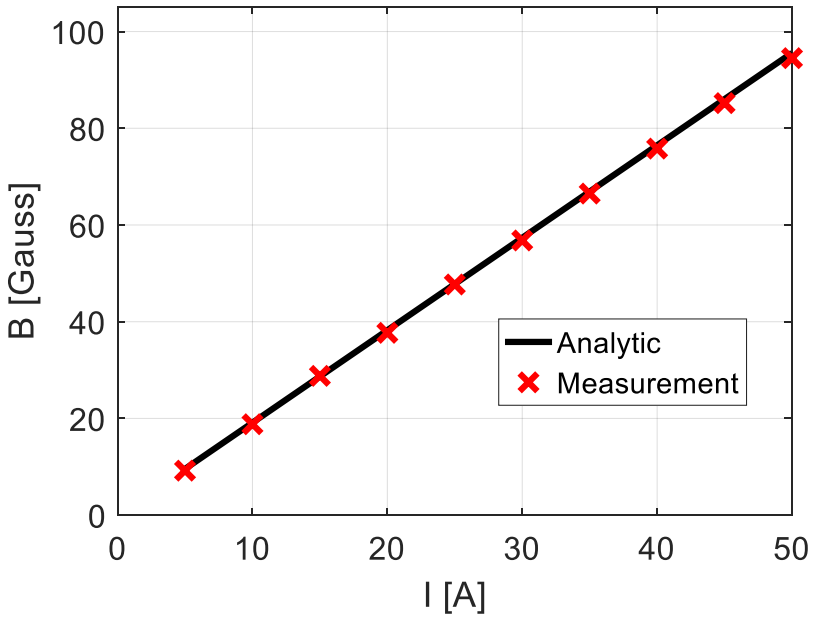

Fig. 68: On-axis axial magnetic field for one magnet coil stack as a function of current measured at a reference position of $z = 0$, at the center of the electromagnet.

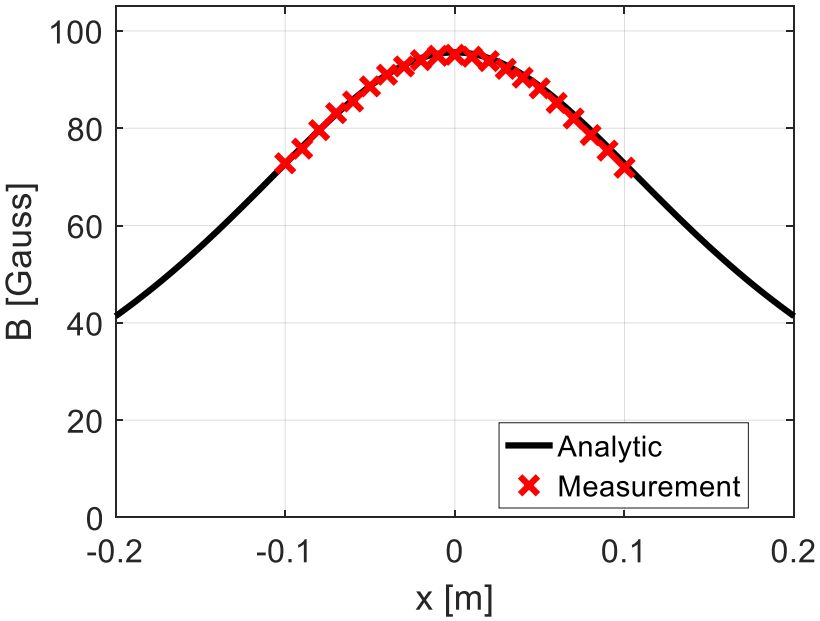

Fig. 69: On-axis axial magnetic field versus axial position for one magnet coil stack driven with 50 A of dc current.

For the MERWA experiment, it was desired to have a magnetic field over a much longer length than the approximately 0.2 m provided by a single magnet. Therefore, the several magnets were aligned with a specific spacing to provide a relatively uniform magnetic field over a longer length. To determine the best magnet spacing, a combination of analytic calculations and magnetics simulations were examined.

When there are multiple magnets, the equation for the on-axis magnetic field is still (120) but it is important to make sure the correct value of z_n is used, taking into account the axial separation of the magnets. The analytic theory was once again verified by experimentally measuring the magnetic field created by a set of three magnets that are separated by a spacing of 0.152 m and each driven with 50 A. The measured magnet field profile along with the analytically computed field are presented in Fig. 70. Once again, the experimental and analytic theory matched very well. Using the confirmed analytic theory, we examined the on-axis field profile of two magnets with a variation in the spacing. Fig. 71 presents the field that is created by two magnets, each driven with 50 A, and spaced with a separation of 0.2 m, 0.23 m, 0.25 m, and 0.28 m. It is possible to see in Fig. 71 that as the spacing between the magnets is increased from 0.2 m to 0.25 m, the peak magnetic field is reduced, but maintains the peak over a longer distance. When the magnet separation is made wider to 0.28 m the uniformity of the field between the magnets begins to decrease and creates a region with lower field in between the magnets. The ideal separation between two magnets is equal to the radius of the magnet. The configuration where the separation is equal to the magnet radius is known as the Helmholtz coil [64] and is known to provide a very uniform field between the magnets.

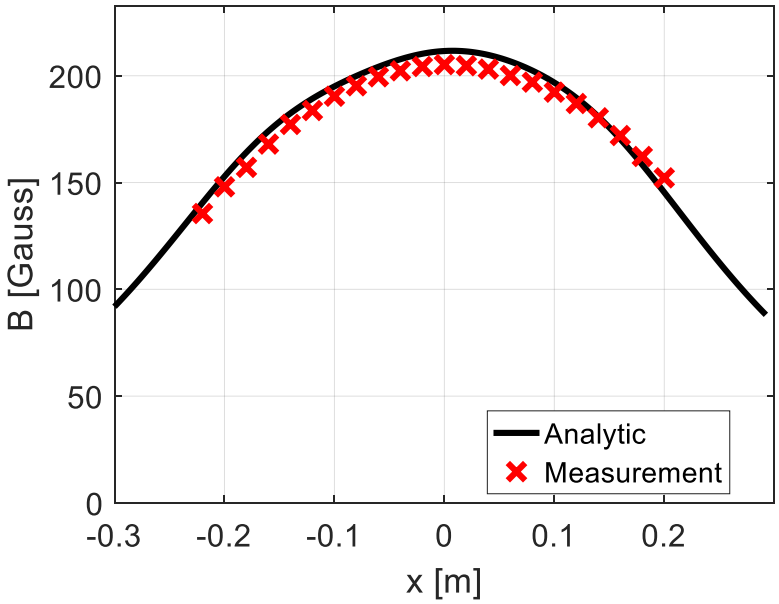

Fig. 70: Analytic and experimentally measured on-axis axial magnetic field versus axial position for three magnets separated by 0.152 m and each driven with 50 A of current.

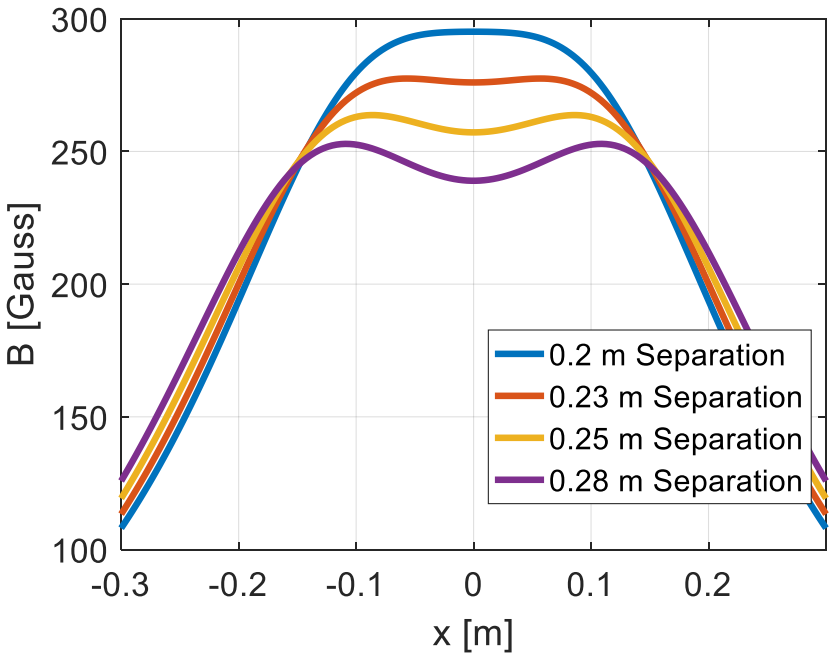

Fig. 71: Analytically estimated on-axis axial magnetic field versus axial position for two magnets with various separation distances. Each magnet is driven with 50 A of current.

The variation of peak field and field uniformity with magnet separation provides an engineering trade-off. Wider magnet separation obviously comes at the cost of reduced magnetic field uniformity, but has the benefit of covering a larger volume. To maximize the 1.5 m axial length of our vacuum chamber we ended up using an average magnet separation of 0.28 m. The 0.28 m separation provided a good compromise between field uniformity and maximum volume of axial magnetic field. To determine this optimal configuration, we used various analytic calculations of the magnetic configurations using all 6 of the magnets we had available. In addition, we had to take into account several physical constraints of the vacuum chamber that prevented using a magnet separation much less than 0.28 m.

To power all six of the magnets, a Sorensen power supply, model DCR 40-500A, was used. The DCR power supply can provide a dc voltage up to 40 V and dc current of up to 500 A. The magnets are connected in series. Based upon the resistance of the magnets calculated above, the dc supply operates in the voltage limited regime at approximately 40 V and 200 A. Fig. 71 presents the measured magnetic field along the length of the entire vacuum chamber when all six magnets are used. The measurement of the magnetic field was completed twice, for accuracy, and both measurements are shown in Fig. 71. The drop in the magnetic field at around z =1000 mm is due to the placement of a pneumatic gate valve that is used to seal the cathode when bringing the chamber up to air. The magnetic field configuration maintains a field of > 500 Gauss over a > 1 m axial range. It will be shown in the next section of the report that a field of 500 Gauss is more than sufficient to confine the electron beam we are interested in using for this work.

One note about the magnet configuration shown in Fig. 64. The last magnet on the right hand side is not connected electrically but was left in place due to a difficult removal process. In addition, to keep the magnets from overheating from long operation the magnets are all water cooled.

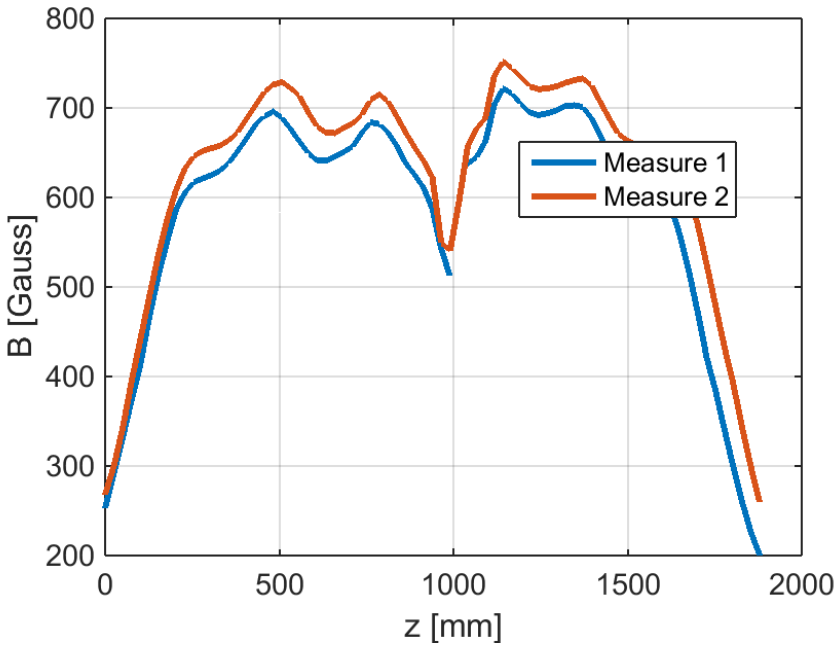

Fig. 72: Two separate measurements of the experimental magnetic field configuration using a Gauss probe

If, in the future, it is determined that the 500 Gauss field is not sufficient to confine the electron beam (for example, if a higher current beam was used) there are several methods that could be applied to increase the magnetic field. First, would be to remove the gate valve that creates the large dip in magnetic field at 1000 mm. Removal of the gate valve should bring the average magnetic field to approximately 700 Gauss. Another method to increase field would be to modify how the magnets are powered. Unfortunately, in the configuration described above, the power supply is being operated in the voltage limited configuration. If a higher field strength was required it would be necessary to reduce the effective resistance of the electromagnet

configuration to allow for higher drive current. This could be achieved by removing one or more of the coils and therefore reducing the overall length of the structure but allowing for a larger peak field.

7.4.3 Electron Beam Optics and Design

This section of the report discusses the procedure followed to design the electron gun that was used for the hot test experiments of the MERWA. It was known that a 10 kV pencil beam with a current of up to 0.3 A was desired, as these were the limits of the HV supplies available. We began the electron gun design by determining the necessary properties of the cathode and finding commercial cathode vendors. After selecting an acceptable cathode we were able to design an anode structure and determine an anode to cathode gap spacing. The electron gun was then simulated in CST Particle Studio, assembled, and electrically connected. The full electron gun was then aligned and evaluated by measuring the current at three different locations inside the chamber. The details of each of these steps of the electron gun design are outlined here.

7.4.3a Cathode specifications

For the prototype MERWA, a pencil electron beam that had a relatively large cross section (5 mm diameter for easier alignment) at a high current density of up to 30 A/cm^2 was desired. To minimize development time, a commercially available cathode was used. In particular, we purchased a high brightness, single-crystal Lanthanum hexaboride (LaB_6) cathode from Kimball Physics Inc. The use of a commercially available cathode came at the cost of customizability. In particular, the cathode option that was available to us had a significantly smaller beam cross section (1.78 mm diameter) and a lower current density (recommended to stay much below 30A/cm^2 to increase lifetime). Nevertheless, the use of a commercial cathode allowed us to

quickly obtain the cathode. The operational specifications of the cathode that was obtained are provided in Table 4.

Table 4: Cathode Specifications

Specification	**Value**
Type	Lanthanum Hexaboride (LaB_6) single crystal
Shape	Flat Cylinder
Size	1.78 mm diameter x 0.25 mm thick
Heater	Refractory Metal
Beam Cross Section	0.0249 cm^2
Beam Radius	0.89 mm
Current Density	Up to 30 A/cm^2, limited to 10 A/cm^2 to improve lifetime
Work Function	2.69 eV
Operating Temperature	1700 K to 1900 K
Energy Spread	Approximately: 0.4 eV
Required Vacuum Level	10^{-7} Torr
Typical Heater Voltage	1 V
Typical Heater Current	10 A
Beam Voltage	10 kV
Beam Current	50 – 250 mA (to maintain 10 A/cm^2 limit)

7.4.3b Anode Design

For an anode, it was desired to use a simple conductive plate with a hole in the center for the electron beam to pass. Therefore, the only important parameter to determine was the separation distance between the anode and cathode. To control the current emitted from the cathode surface, and stay below the current density limit of the cathode, the gun was configured to operate in a space charge limited (SCL) regime. By operating in the SCL regime, the anode-cathode gap set the maximum beam current. To determine this gap, we can examine the SCL configuration and determine the separation we need to set keep the maximum beam current below the limits of the cathode. The derivation of the SCL for a 1-D anode to cathode gap is provided in Appendix 3. The derived Child-Langmuir law [65-67] for a parallel-plane diode is

$$J_{limit} = \frac{4\varepsilon_0}{9d^2}\sqrt{\frac{2e}{m}}V_0^{3/2} = 2.33x10^{-6}\frac{V_0^{3/2}}{d^2}. \quad (122)$$

A more thorough derivation of the Child-Langmuir law can be found in various texts, such as [40] or [68].

Using (122), Fig. 73 presents the Child-Langmuir space charge limited current for a parallel-plane diode with a potential of 10 kV and a separation distance of d. For the MERWA experiments, a current density of 1 – 10 A/cm^2 was desired, corresponding to a range of 15.26 - 5 mm for d. These separation values were reasonable and within the capabilities of our experiment (too small could result in arcing and too large could be difficult to align). The anode was constructed from oxygen-free high conductivity (OFHC) copper and was simply a cylinder with a hole in the center. The specific anode design and anode-cathode separation distance were

verified through particle tracking simulations that incorporated the physical dimensions of the Kimball Physics cathode and are discussed below.

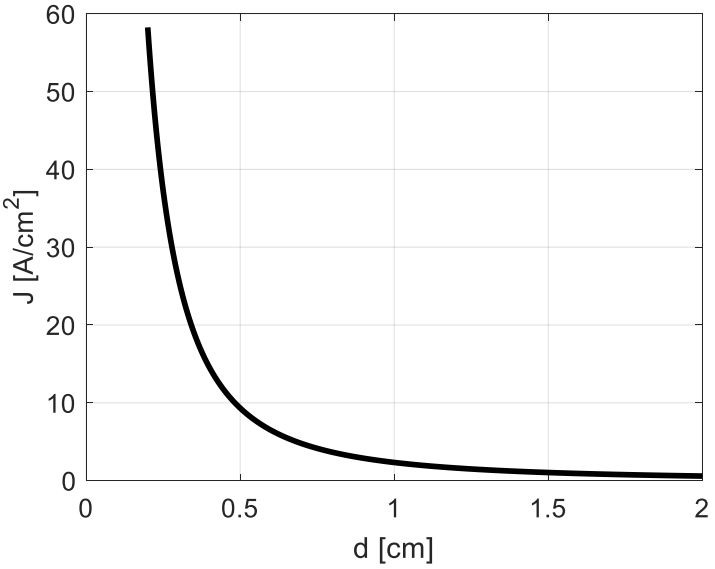

Fig. 73: Child-Langmuir current limit for a parallel-plane diode biased at 10 kV and with separation of d

7.4.3c Magnetic focusing

To focus the electron beam, a confined flow or immersed flow focusing type was used. Under this focusing, the magnetic flux lines pass through both the cathode and the MERWA structure of interest. Immersed flow was used to allow for the use of magnetic fields larger than the Brillouin value without causing excessive scalloping of the beam [40]. As discussed in the previous section, this was accomplished by using large electromagnets.

For the immersed flow beam, we need a field that is strong enough to keep the electron beam confined. To confirm that the magnetic field presented in the previous section (approximately

500 Gauss) is sufficient for confinement we can examine a baseline value, the Brillouin field [40]

$$B_B = 0.83x10^{-3}\left(\frac{I^{1/2}}{r_b V^{1/4}}\right)[Tesla], \qquad (123)$$

where B_B is the magnetic field required for Brillouin flow, I is the beam current, V is the beam voltage, and r_b is the radius of the beam. Fig. 74 presents the required Brillouin flux density required for the beam created by the Kimball Physics cathode, a 10 kV electron beam with a 1.78 mm diameter. For initial experiments, we have operated the beam at a currents less than 0.3 A. The corresponding Brillouin flux density for a 0.3 A beam is 550 Gauss. As long as the magnetic field created by the electromagnets is greater than the Brillouin field value, the beam will be confined.

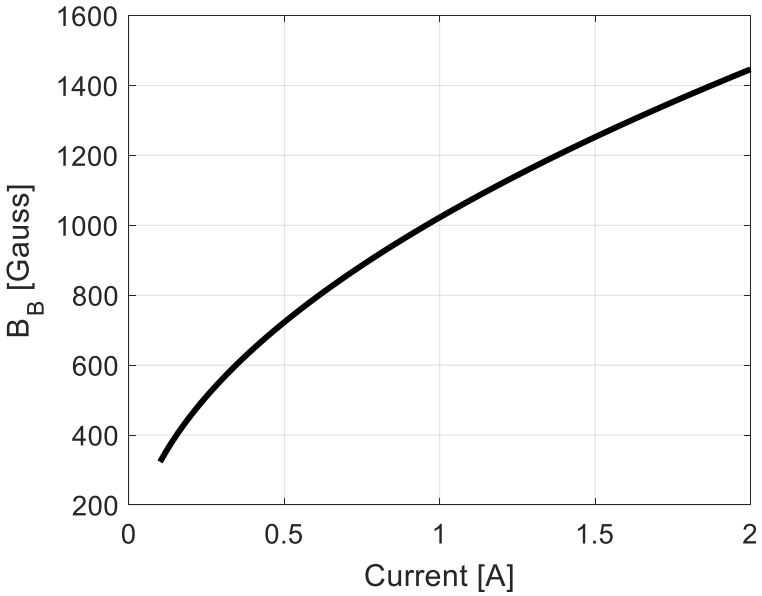

Fig. 74: Brillouin field requirement for various beam currents for a 10 kV electron beam with a 1.78 mm diameter.

Referring back to Fig. 72, the measured magnetic field is greater than 500 Gauss over a longer than 1 m axial distance. This magnetic field is almost just below the Brillouin flux density required for the beam current of 0.3 A, the anticipated maximum beam current that will be used for the foreseeable future of this experimental configuration; therefore, beam currents below approximately 0.3 A should be well confined.

7.4.3d Particle tracking simulations of electron gun

To obtain a more accurate expected beam current value, the anode and cathode were simulated. These simulations were conducted using the particle tracking solver available in the CST Particle Studio software [35]. In the particle tracking model, the physical dimensions of the constructed anode and commercially purchased cathode were taken into account to generate accurate results. These simulations were used to determine the true I-V curve for the SCL electron beam. The one assumption that was made for the particle tracking simulations was the background magnetic field to provide beam confinement. It is possible to implement a full magneto-static simulation that simulates the entire arrangement of the electromagnets; however, since this device will be operated with a magnetic field larger than the Brillouin field, the simulation of the entire magnet configuration would not provide significantly different results than assuming a constant background magnetic field. In addition to a constant field calculation, we ran simulations were we imported magnetic fields obtained from the experimental measurements. The use of an imported field assumes that there is no radial dependency to the field, but was included to demonstrate that not much change occurs, from a constant field, because we are using a magnetic field that is above the Brillouin field. The use of an analytic based background magnetic field can be configured in the CST Particle Studio by selecting the analytic method in the solver setup. If it was desirable to simulate the electromagnets, the solver would have to be changed to a

magneto-static (M-Static) calculation. When using the CST particle tracking algorithm, it is also important for the user to make sure that software is configured to account for space charge effects, as they are not enabled by default.

Fig. 75 presents a zoomed in view of the anode and cathode in the model. In this image, the Kimball physics cathode is to the left, with the emitting portion of the cathode in the center of the cathode structure and encompassed by a conducting plate. The dimensions of the cathode were taken from the data sheet of the Kimball physics cathode, but the primary parameter is the cathode diameter of 1.78 mm. The anode consisted of a copper cylinder of radius 18 mm with a small 3.3 mm radius hole in the center. The spacing between the anode and cathode was a variable of the simulation. For the results presented in Fig. 75 and Fig. 76, the anode to cathode gap was set to 6 mm. Fig. 76 shows the full particle tracking simulation, including the calculated beam result. In Fig. 76, it is possible to see that the entire electron beam traveled from the cathode to the collector without losing any of the beam. In addition, the ripple of the emitted electron beam is very low. The simulation was then ran for various cathode potentials, keeping the anode and collector at zero volts, while measuring the current that strikes the collector structure.

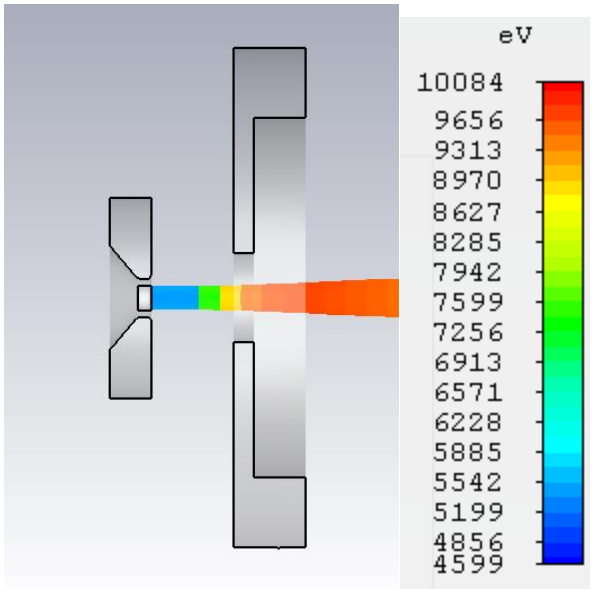

Fig. 75: Zoomed in view of the electron gun in the particle tracking simulation with the cathode on the left and the anode on the right, with the electron beam traveling from the cathode through a hole in the anode.

Fig. 76: Electron gun simulation showing the full simulation showing the full travel distance of the confined electron beam, anode, cathode, and collector. The beam ripple in this simulation is very low.

Although the Kimball Physics cathode can provide a beam with a current density of 30 A/cm^2, lifetime can be significantly improved if the current density is reduced. As a result, the current density of the cathode was limited to 10 A/cm^2. Using the cathode diameter, this limited our current output to approximately 250 mA. Using the desired maximum current density of 10 A/cm^2, the anode cathode spacing could be determined using (122), the Child-Langmuir equation, and a beam voltage of 10 kV. The resulting anode to cathode gap was to be 5 mm or greater. For initial experiments, the anode to cathode separation distance was set to 6 mm to even further limit the current density. Using a 6 mm gap, the particle tracking simulations were conducted for various cathode potentials and measuring the collected current. Fig. 77 presents

the simulated results of the electron beam current for both a simulation that assumed a constant 1 T background magnetic field and one that used the experimentally measured field. At the cathode voltage of -10 kV the collector current was measured to be approximately 210 mA, below our 250 mA limit.

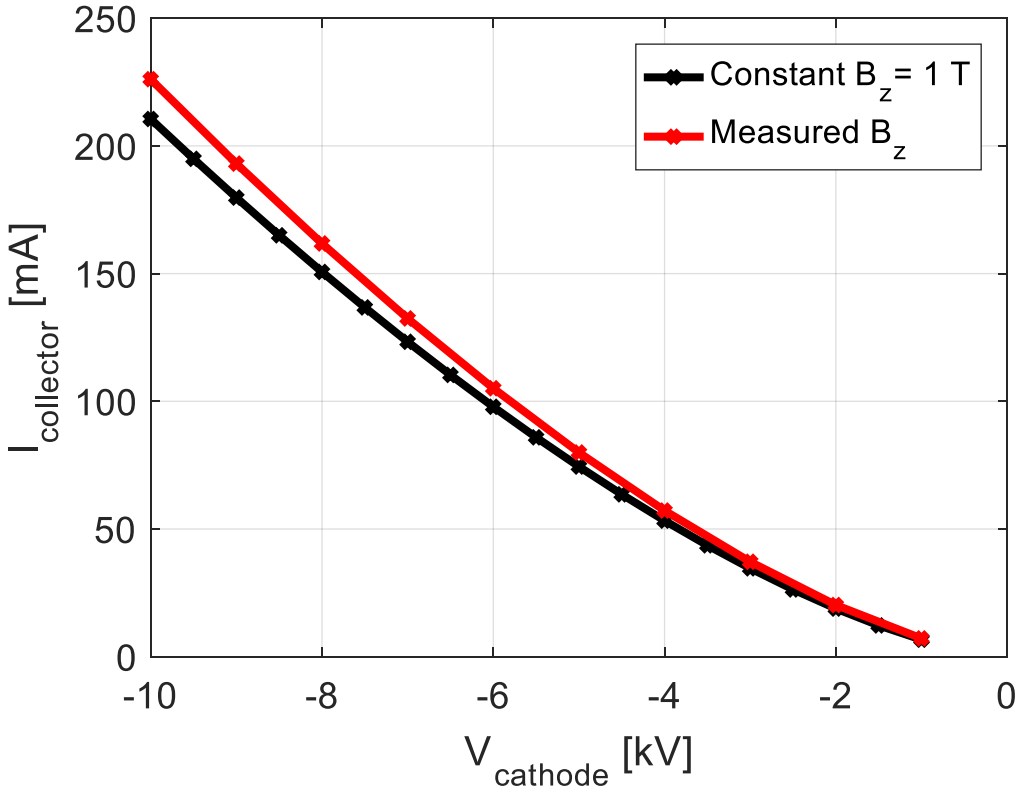

Fig. 77: Simulated beam current collected at the collector for a simulation with a constant 1 T background magnetic field and one that used the experimentally measured magnetic field. In these simulations (shown in Fig. 72), a 6 mm anode to cathode gap was used

7.4.3e Construction of Electron Gun using Kimball Physics Cathode

Using the knowledge of the 6 mm anode cathode gap, it was possible to assemble the electron gun. A track and cart configuration was used to hold and align the anode and cathode. The use of a track system was very beneficial as it maintained alignment between the anode and cathode and allowed for easy modification of the spacing between them. To connect to the track system,

the anode and cathode were both mounted on carts using custom designed support structures. The support structures for both the anode and cathode were constructed out of ceramic, for electrical isolation, and designed to position the beam in the center of the vacuum chamber (on axis) when installed. The support structures, along with the anode and cathode, can be seen in Fig. 78, where each are attached to a cart. In Fig. 78, the left support structure consists of an aluminum cylindrical mounting fixture holding a MACOR tube to which the copper anode is attached to. The right structure of Fig. 78 features the Kimball Physics cathode connected to the MACOR bracket.

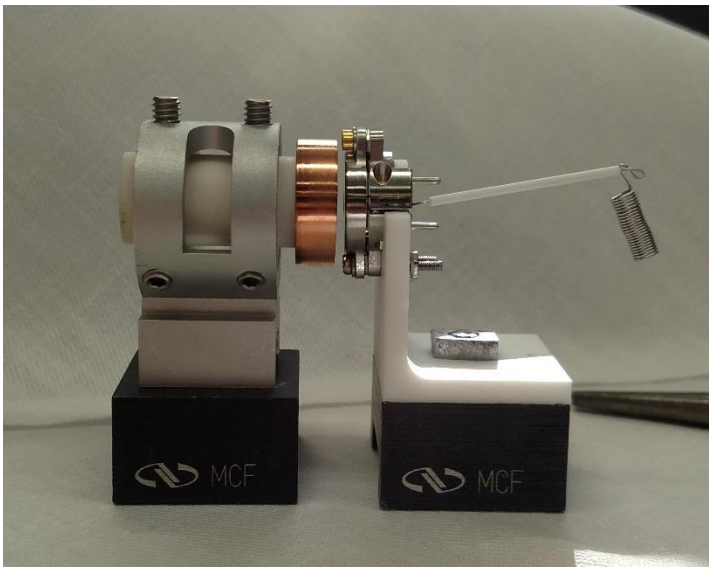

Fig. 78: Kimball Physics LaB6 cathode mounted on MACOR bracket and attached to track cart along with the anode structure

To power the heater and provide the high voltage bias to the cathode, bare copper wire is run from the high voltage feedthroughs on the vacuum chamber to the cathode. The high voltage wires are insulated with ceramic beads. The anode's electrical connection is made using a low voltage insulated wire and is connected to a multi-pin feedthrough. The anode is electrically

connected to ground outside of the vacuum chamber. The fully constructed electron gun assembly on the track system including all wiring is presented in Fig. 79.

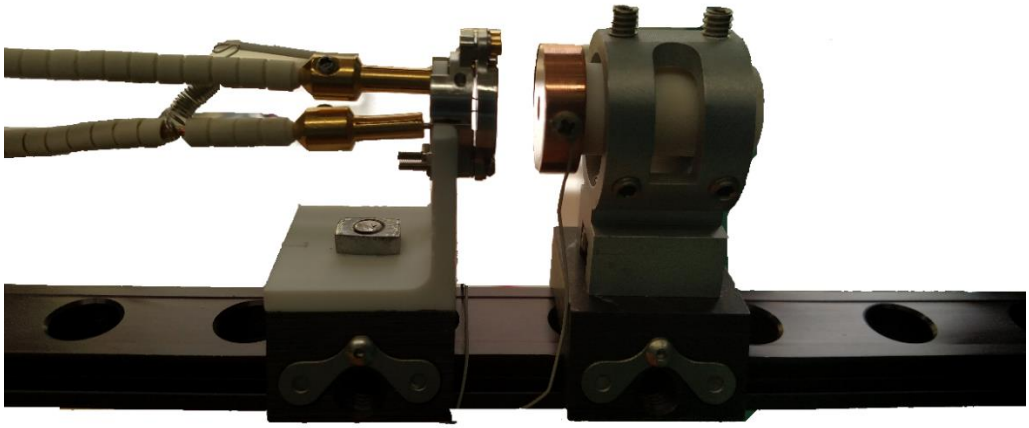

Fig. 79: Electron gun assembly mounted on the positioning track including electrical connections

The track and track carts are manufactured by Newport and are originally created for optical experiments. The track was then connected to a positioning manipulator arm, discussed in previous sections, and connected to the vacuum chamber. The use of the positioning manipulator arm allowed for easy movement and alignment of the electron beam inside of the vacuum chamber. Fig. 80 shows the electron gun on the track connected to the positioner.

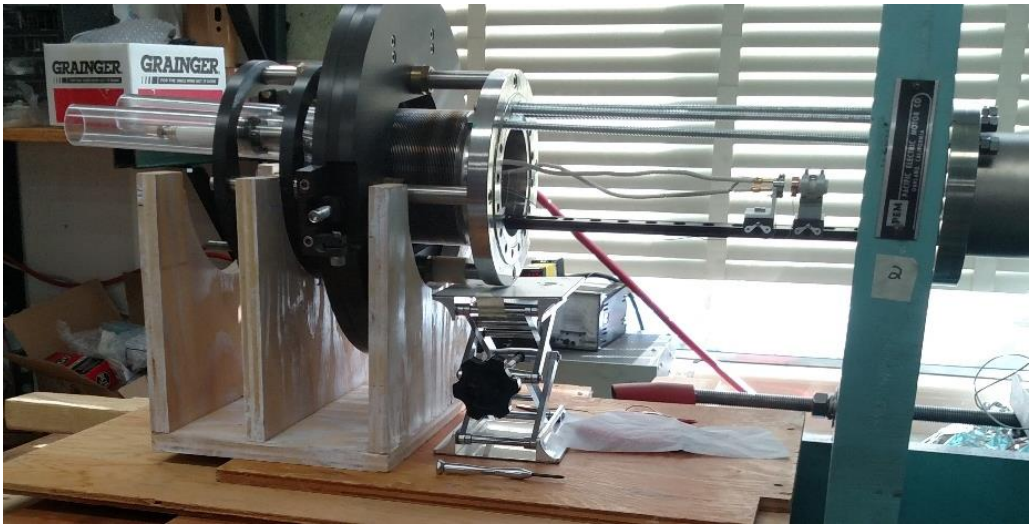

Fig. 80: Electron gun assembly on track connected to the positioner before being connected to the vacuum chamber

7.4.3f Wiring of cathode heater and high voltage pulse

To bias the cathode and power the cathode heater, a custom built heater supply was used. A schematic of the electrical diagram used for the heater is presented in Fig. 81. The heater is powered with a ac voltage though a 10:1 isolation transformer. The primary winding of the transformer is connected to a variable ac power supply connected to a 120 V wall outlet. The secondary side of the transformer is then connected to the cathode heater and floats with respect to the primary side. To prevent the cathode from operating when the chamber pressure is too high (>10^{-7} Torr) a relay was connected in line with the transformer primary line to cut power if the maximum pressure is exceeded.

The desired dc configuration of the device was for the cathode to be biased at a negative potential (-1 kV to-10 kV) and the anode biased at ground. To allow for the negative cathode biasing, the HV negative cathode voltage was connected to the floating secondary of the transformer. In addition, to reduce cooling requirements, it was desired to operate the electron

beam in a pulsed operation. Therefore, the HV negative potential was applied to the cathode using a pulse forming switch. The HV pulsing switch is a PowerMod^{TM} high voltage switch manufactured by Directed Energy Technologies. The switch can handle a current of up to 50 A and hold off a voltage of up to 22 kV. The pulses formed by the switch can have a width of between 2 μS to 200 μS and a pulse repetition frequency of up to 1 kHz. The dc cathode HV is supplied by a Glassman KL010R300 which can provide a positive or negative 10 kV and 0.3 A dc output.

At the other end of the vacuum chamber is a copper collector plate, which is electrically connected to ground. To measure the current emitted from the cathode and the current that strikes the collector, Pearson current monitor coils (model 4100) were used. The use of a current monitor allows for accurate measurement of the pulsed current waveform. The specifics of the electron beam current measurements along with the introduction of beam scrapers which were used along with the collector, are discussed in more detail below.

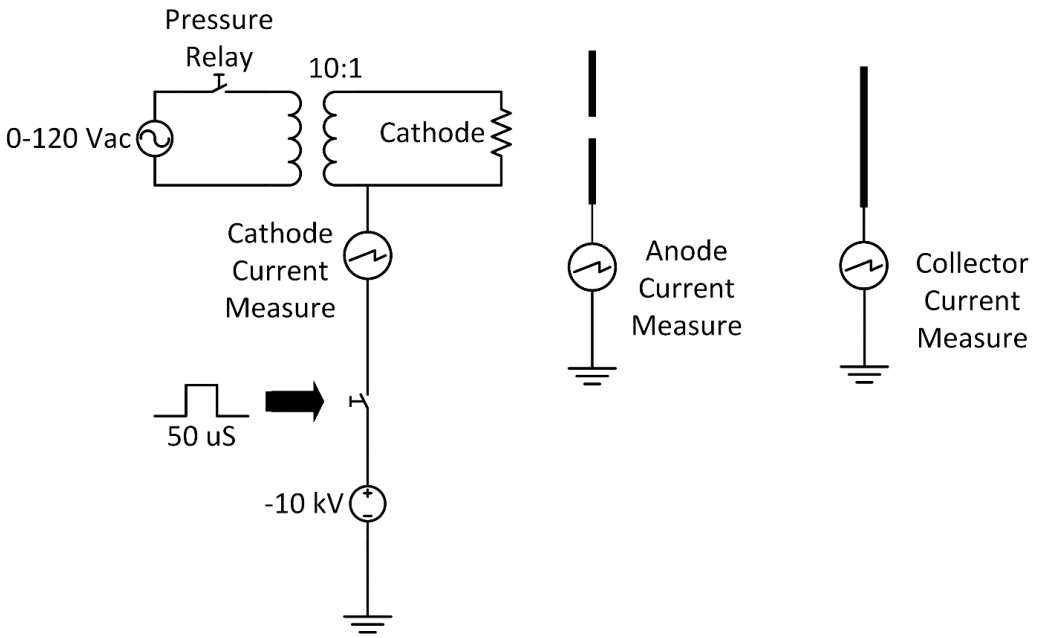

Fig. 81: Electrical wiring diagram of the cathode heater and high voltage supply as well as the anode and collector

7.4.3g Beam scrapers and beam alignment

In addition to the collector at the end of the vacuum chamber, two beam scrapers were constructed. The beam scrapers are simply copper plates that are electrically isolated but attached to manipulator arms allowing physical motion of them inside the vacuum chamber. The two beam scrapers were placed a two different axial positions within the vacuum chamber and were designed to be moveable into and out of the electron beam's path, as shown in Fig. 82. The manipulator arms that hold the beam scrapers have screw gauge micrometers connected to them for precise vertical positioning. By placing the vertically movable beam scrapers at two different axial locations within the vacuum chamber, we could determine the horizontal position of the beam at two locations. The horizontal position of the beam was determined by measuring the current that strikes the beam scraper and slowly lowering the beam scraper until the full amount of the beam current is measured on the scraper. With knowledge of the horizontal position of the

beam at two locations it was very easy to ensure that the beam was traveling straight along the axis of the vacuum chamber. To keep the copper beam scrapers electrically isolated from the manipulator arms, the arm and scraper were attached to each other through the use of a MACOR isolator block. A CAD drawing of the beam scraper, ceramic isolator, and manipulator arm are shown in Fig. 83. A wire was then connected from the beam scraper to ground and ran through a Pearson current monitor coil, identical to the collector configuration, to measure the current. Fig. 84 presents a CAD drawing of the beam scraper assembly connected to the 4" vacuum chamber along with the location of the axially centered beam. The beam scrapers were also designed to have two holes, near the edge closest to the electron beam, to help for alignment of the beam in the transverse direction.

Fig. 82: Two beam scrapers were used with vertical motion capabilities for measurement of the beam's location

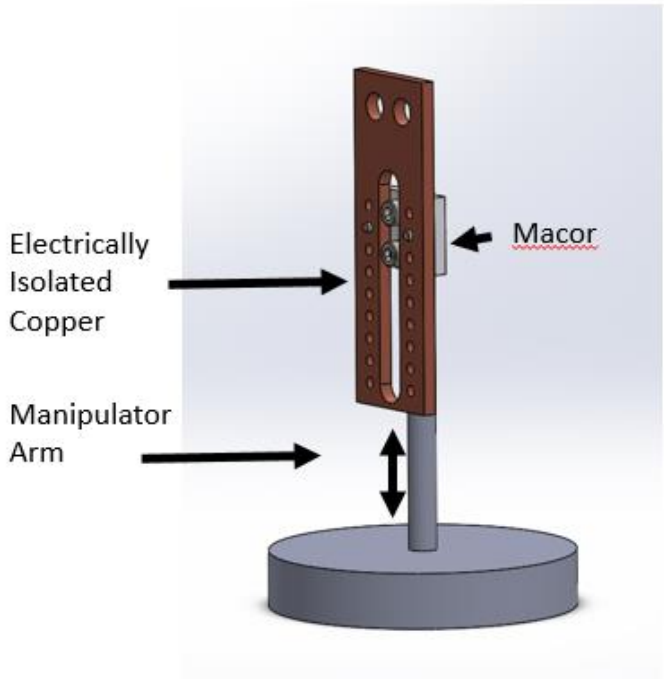

Fig. 83: Copper beam scraper CAD design connected to a one dimensional position manipulator arm

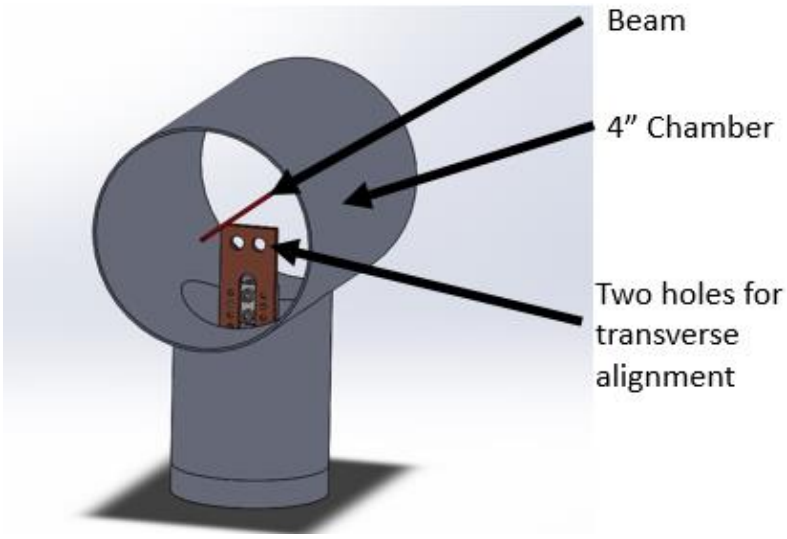

Fig. 84: CAD drawing of the beam scraper connected to a manipulator arm installed in the vacuum chamber with the approximate location of the electron beam

7.4.3h Measured electron beam current

Using the two beam scrapers, we were able to use the beam positioner to create a beam that was centered in the vacuum chamber and traveled on-axis along the length of the chamber. After positioning the beam on-axis, the beam scrapers were moved out of the path of the beam to allow the beam to travel all the way to the collector. The current on the collector was then used to examine the I-V properties of the electron gun. To measure the collected current, the signal from the Pearson current monitor was evaluated using a Keysight high speed oscilloscope, model DSO9404A. For accurate measurement results, the Pearson current monitors are required to be connected to a 50 Ω load. During initial experiments, and conditioning of the electron gun, we experienced several high voltage transient signals due to arcing of the HV. When the HV signal would arc, a large transient current flow would occur, generating a large voltage on the current monitor's output. The 50 Ω inputs of the Keysight oscilloscope have a maximum voltage rating of 5 Vrms. To prevent damaging the inputs of the oscilloscope, 50 Ω passthrough loads were used between the current monitor and the oscilloscope input. A 50 Ω passthrough load is essentially a T-junction with a 50 Ω load as one port of the T. By using a 50 Ω passthrough load, the oscilloscope can be configured to operate in a high impedance configuration (1 MΩ input resistance) while still maintaining a 50 Ω load impedance to the current monitor. The benefit of operating the scope in the high impedance configuration is that the maximum voltage is increased from 5 Vrms to 150 V. The downfall of using a 50 Ω passthrough load is the limited frequency response of the passthrough devices. For this work, we were interested in measuring pulses with a pulse width of 50 μS, corresponding to a frequency of 20 kHz, well within the frequency range of passthrough loads we used.

Using the Pearson current monitors, measurements of the pulsed electron beam's current are similar to the example measurements shown in Fig. 85. In Fig. 85 two curves are presented, the voltage trigger pulse and the current. The pulse is presented only to show the pulse shape, a 50 μS wide pulse starting at time zero, with an arbitrary height. The blue curve represents the measured electron beam current at the collector. The average of the curve within the pulse time is the average current of the electron beam, approximately 47 mA in this case. The slow falloff of the current curve is a result of the cathode potential slowly returning to zero volts when the HV switch is opened.

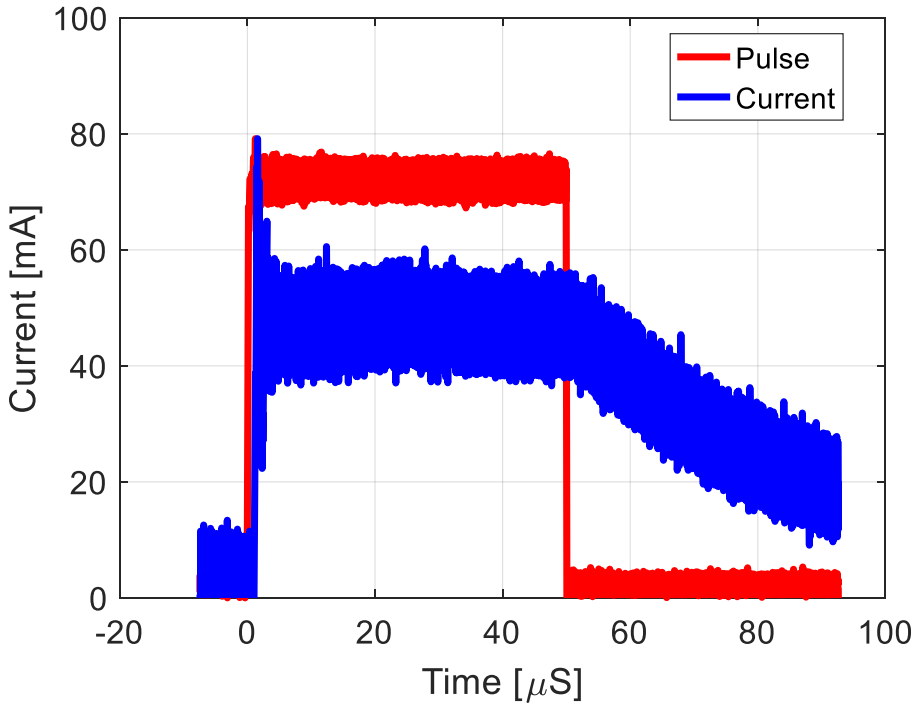

Fig. 85: Results of a pulsed electron beam measured as current striking the collector plate

The HV bias potential of the cathode was varied and the current measured using curves similar to those shown in Fig. 85. The measured current of the electron beam for cathode voltages ranging from -1 kV to -8 kV are presented in Fig. 86. Two experimental curves are presented alongside the simulation results in Fig. 86. The two experimental curves represent two different cathode

heater currents that were used, 7.0 A and 7.8 A. For the 7.0 A heater configuration, it is possible to see that the experimental results match the simulation very well for cathode potentials close to zero. As the cathode potential becomes more negative, the measured electron beam current begins to approach an asymptote value and diverge from the simulation results. When the current supplied to the thermionic heater is reduced, the temperature of the cathode reduces and the emitted current becomes temperature limited. Therefore, to increase the maximum current that can be emitted from the structure, up to the SCL, the temperature of the cathode must be increased. It is possible to see in Fig. 86 that when the heater current is increased from 7.0 A to 7.8 A the cathode temperature is high enough to emit a current of up to 150 mA. By increasing the heater current to 7.8 A the experimental results very accurately match the simulation results, up to a negative cathode potential of -8 kV. If a beam current of greater than approximately 150 mA is desired it would be necessary to further increase the temperature of the cathode by increasing the heater supply current. The particle tracking simulations of the electron gun do not take any temperature limit effects into account, just the space charge limits. Therefore, the simulations will never see a roll off of the current due to temperature limited current.

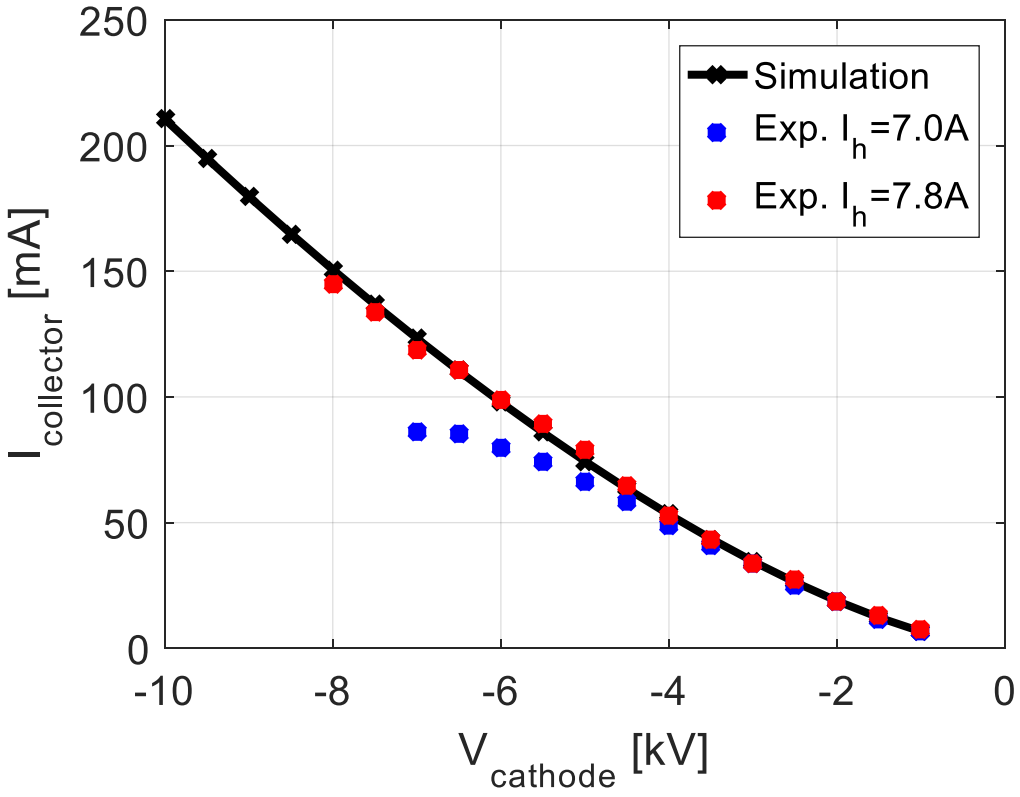

Fig. 86: Beam current measured at the collector versus cathode voltage for two different values of heater current. The reduced heater current reduces the temperature of the cathode.

Electron guns are often referenced through their perveance, defined as [40]

$$P = \frac{I}{V^{3/2}}, \tag{124}$$

where I is the cathode current and V is the cathode voltage. By examining the I-V curve presented in Fig. 86 one can calculate that the perveance of this designed electron gun is approximately 0.2 microperveance. Using this designed and measured electron gun we then moved towards sending the electron beam through the MTM lined rectangular waveguide structure. However, one last piece had to be designed, the velocity modulation structure which is necessary to input and couple out RF signals on the electron beam. The next section discusses the design of the velocity modulation structure.

7.4.4 Velocity Modulation Method

This section discusses the velocity modulation (VM) structure that was created for the hot test experiments. Previous simulations discussed in this dissertation used a resonant cavity or shorted parallel plate waveguide as the method to velocity modulate the electron beam. These two VM methods are not useful for the experimental testing of a prototype device. A parallel plate waveguide is not practical, at the frequencies of interest, as the width of the waveguide would have to be much larger the vacuum chamber available for this work. A resonant cavity configuration is not desirable as it would be a very narrowband structure. Since this is a prototype device, where we do not know the exact frequency of interest for all tests to be done, the use of a resonant structure, even if tunable, would be very cumbersome. Therefore, it was necessary to design a new VM structure.

Initially, it was thought that a small wire loop would be used to cause VM to the electron beam, similar to the one shown in Fig. 87. The wire loop was to be connected to an EM signal generator. We believed that the small wire loop had several advantages in an experimental configuration, over the cavity structure used in simulation, because it has a much wider bandwidth without having to tune the structure. However, the improved bandwidth comes at the cost of reduced efficiency of coupling between the input signal and the beam as the axial electric fields produced by the loop is not as strong as either previous method. Nevertheless, we believed it would provide sufficient VM to examine basic proof of concept. In addition to a wire loop for the input, we initially intended to measure the gain of the space charge wave through the use of several small monopole antennas placed in the MTM liner, along the length of the drift tube. By

adding the monopoles to the MTM liner, the electric fields induced in the liner from the space charge wave would couple to the electric monopoles for measurement. By measuring the magnitude of the electric field on the monopoles we would be able to determine the gain rate of the space charge wave.

To test the concept of using the wire loop as the VM method, we ran initial PIC simulations of the structure with a wire loop as the input method. The initial simulations were successful in modulating the beam we intended to use in experiment (10 kV, 0.3 A) over a relatively wide band. However, the input power required to cause noticeable VM on electron beam was quite large at 100 W. The very large power required was a result of the size of the wire loop, with respect to the wavelength of the signal. The wire loop was electrical small for the frequency range of interest resulting in a very reactive input impedance. A very reactive input impedance causes a very poor match and a significant portion of the signal is simply reflected to the input. 100 W of input power was outside the power capabilities of sources readily available to us for use.

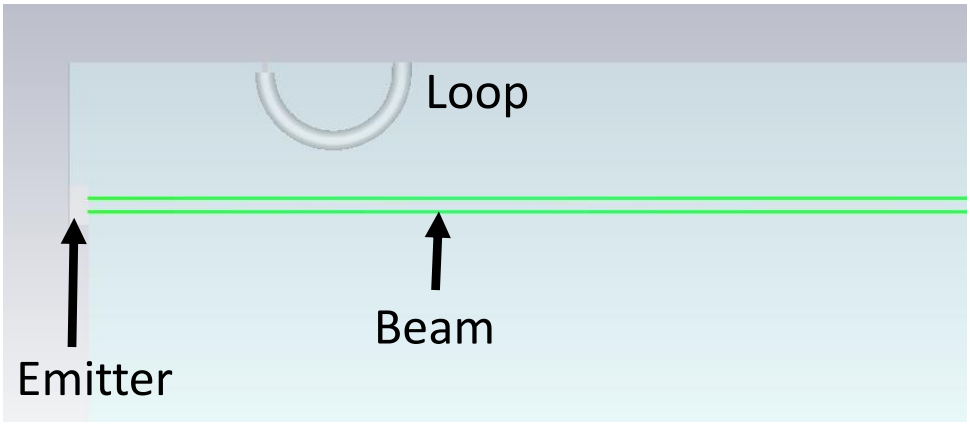

Fig. 87: Pictorial representation of the loop structure that was initially planned to be used to velocity modulate the electron beam. This RF signal applied to the loop was anticipated to generate currents that excite an electric field along the axis of the electron beam. Therefore, if the electron pencil beam was passed near the loop the excited electric fields will cause VM on the beam.

Since the wire loop required a prohibitive amount of input power, we decided to design a new VM structure. In addition, we decided it would be more accurate to use two VM structures, one to create a VM on the beam near the electron gun and the second to measure the VM of the beam before striking the collector rather than the monopoles inside of the liner. Therefore, we created two VM structures. The new VM structure design consisted of two parallel plates of metal separated by a dielectric gap. The parallel plate based VM structure is presented in Fig. 88. In this structure, a 50 Ω input coax is used as connection to the two parallel PEC plates. The two PEC plates are separated and supported by a dielectric spacer. In this work, we used Teflon as the dielectric spacer because Teflon was very easy to work with when constructing the VM structures. The input coaxial cable is connected to the two plates by shorting the center conductor to the back plate and the outer conductor to the front plate. Near the top of the structure, a rectangular hole, presented as a blue color in Fig. 88, is cut into the parallel plates and dielectric. The hole is where the beam will pass through the structure. The basic idea of the parallel plate VM structure was that the input signal from the coaxial cable is converted to a parallel plate mode between the plates which has an electric field vector between the plates parallel with the beam's velocity vector. The electric field vectors, on the center plane of the VM structure, are shown in Fig. 89, where we can see a strong electric field at the location of the beam.

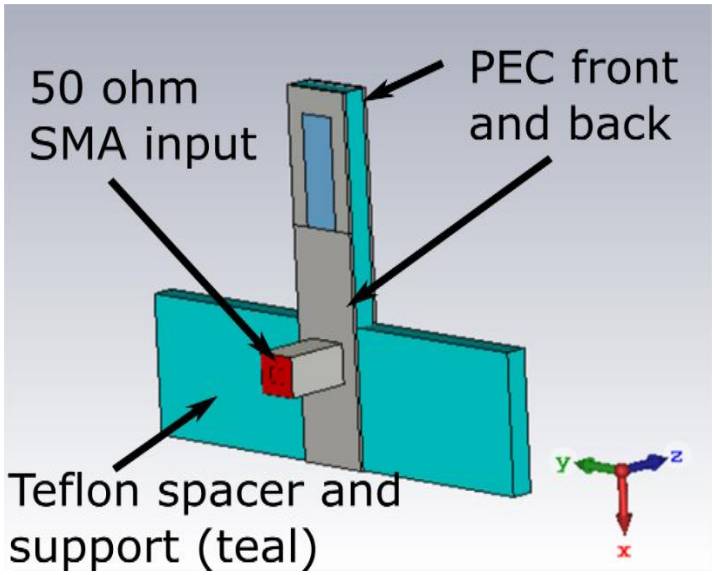

Fig. 88: Simulation model of the VM structure with a square coaxial line input. The teal material represents Teflon while the grey material represents PEC

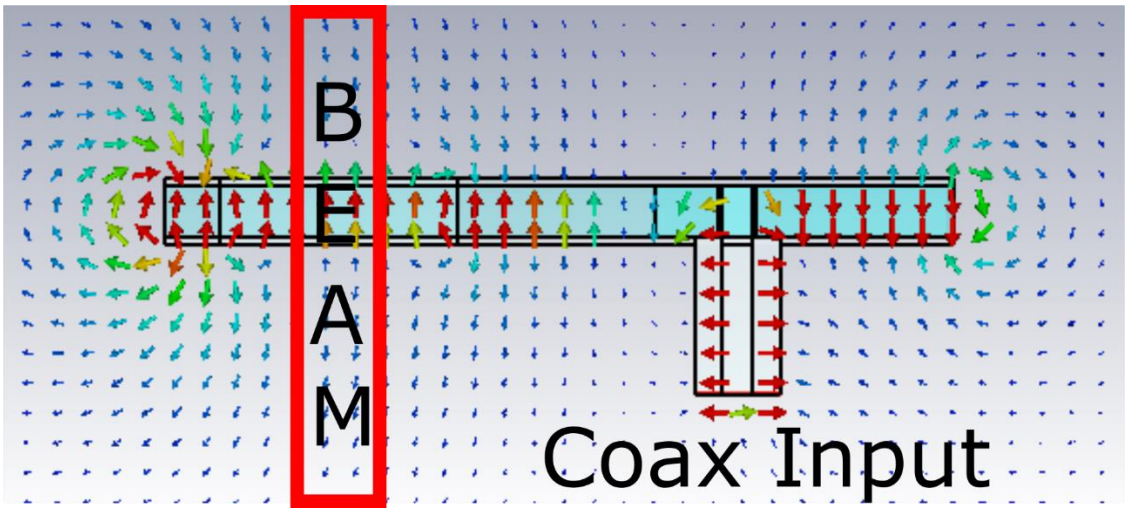

Fig. 89: Electric field profile of the VM grid structure. Input signal from the coaxial cable is converted to an axial electric field between the metal plates with a high strength at the location of where the beam passes

The VM structures would be attached to either end of the MERWA experiment. The VM structure closest to the cathode would modulate the beam before entering the MERWA and the second VM structure would measure the VM of the beam after traveling through the MERWA. A CAD drawing of the full MERWA structure along with one VM structure, all inside of the vacuum chamber, is presented in Fig. 90.

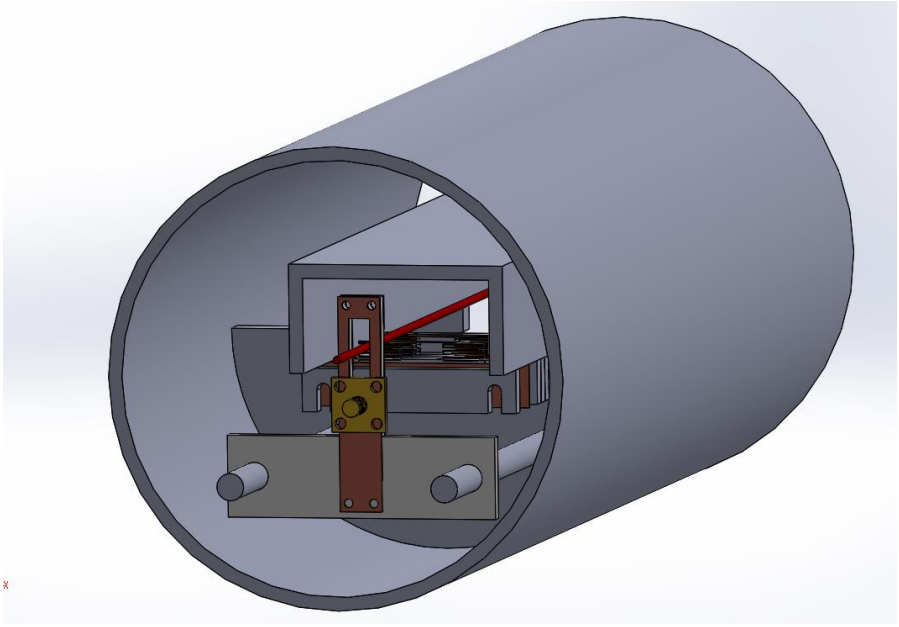

Fig. 90: CAD drawing of full hot test configuration including the MTM assembly, VM structure, and the electron beam

To create the largest VM, the structure needs to maximize the axial electric field at the location where the electron beam will pass through. Numerous simulations were conducted to optimize the electric field strength. One example parameter that was optimized was the width of the electric plates. Fig. 91 presents the electric field strength at the location of where the beam will pass versus the width of the copper PEC plates assuming an input power of 0.5 W and frequency of 2 GHz. As a result, it is desirable to use a plate width that is as narrow as possible. On the other hand it is necessary to keep the hole for the beam as wide as possible, to simplify beam alignment. Therefore, we used a moderate plate width of 10 mm to accommodate a beam hole of approximately 5 mm wide.

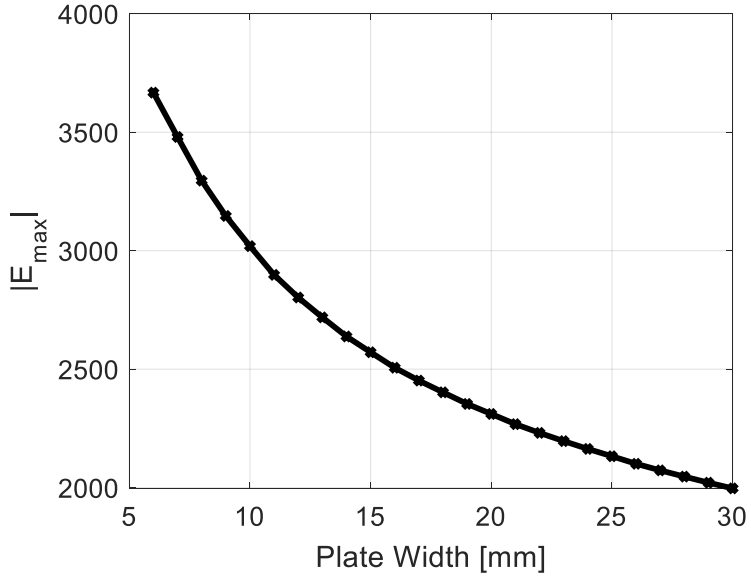

Fig. 91: Simulated electric field strength inside of the beam hole of the VM structure as a function of the plate's width

Using a 10 mm plate width we expect the electric field strength of approximately 3000 V/m at the beam's location. If we compare this to the loop scenario originally investigated, it achieved an axial electric field strength of only 480 V/m. Using this design, the change from the loop structure to the plate based VM structure has increased the electric field strength by a factor of 6.25. Since the electric field vector is proportional to the square root of the input power, the 100 W of input power that was used for the previous loop based simulations should now only require 2.5 W if a plate structure is used. The 2.5 W input power assumption does not include any matching network, which would further reduce the power requirement. Further, the 100 W power input value seen with the loop was not a lower limit, just a value that was found to work; therefore, a power lower than 2.5 W could still definitely work. Simulation and experimental results in section 7.4.5 will examine the input power required to achieve measureable VM.

In addition to creating a large electric field strength, the S-parameters of the structure were examined to determine the structure's response versus frequency. Fig. 92 presents the simulated one port S-parameters for the parallel plate based VM structure. As shown in Fig. 92, the input S_{11} is very high, meaning that, similar to the wire loop, a significant portion of the input signal is reflected. For long term investigations of the MERWA, the frequency response of this structure will need to be improved to reduce the S_{11}. However, for initial experiments we decided to proceed with the design as is. In fact, the poor coupling is slightly advantageous at the early prototype stage of this research. It was not clear how much energy would actually couple to the structure if a backwards wave oscillation was excited. If the coupling was really good, we could possibly couple a very large signal to our measurement equipment and cause damage. Therefore, poor coupling may be better for initial tests with the understanding that it can be improved in the future.

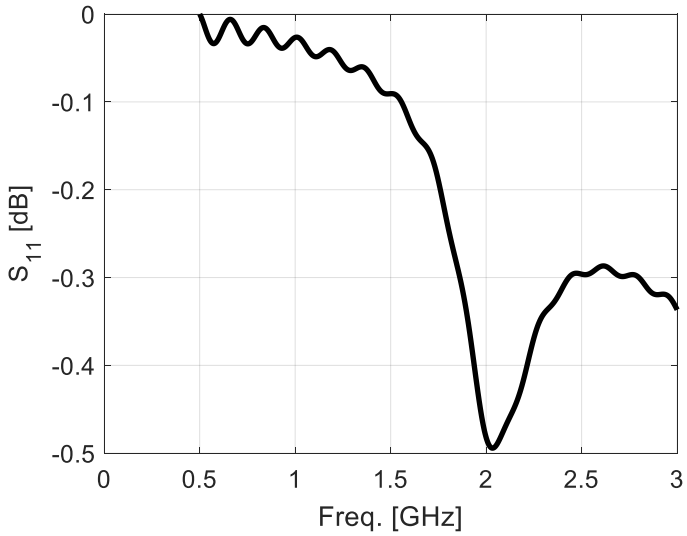

Fig. 92: Simulated one port S-parameter from CST of the plate based VM structure

The plate based VM structures were manufactured in house. They were constructed using 0.125 in. thick sheet Teflon as the insulating center material and 16 oz. copper sheets on either side of the Teflon to act as the plates. A flange mount SMA connector was used to make the coaxial connection with the center conductor of the SMA connector passing through the front grid and Teflon but making electrical contact to the back plate. The center conductor of the SMA connector was soldered to the back plate, while the ground of the connector was soldered to the front plate. The front and back copper plates were held to the Teflon by Kapton adhesive tape and the soldered SMA connections. Fig. 93 shows the two VM structures that were constructed. The two holes in the 'wings' of the Teflon material were used to connect to the MERWA structure.

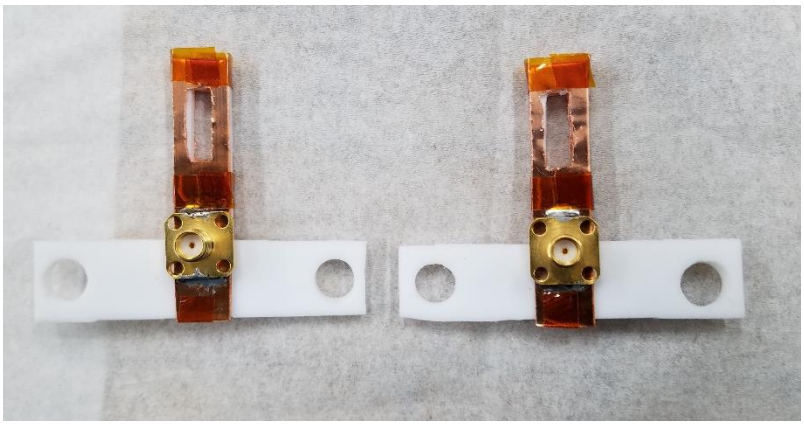

Fig. 93: Constructed parallel plate VM structure where the white material is Teflon and the metal plates are constructed of copper

The frequency response of the constructed VM structures were measured using a VNA and are shown in Fig. 94, compared to the simulation results of Fig. 92. While the two constructed structures both had very similar frequency responses, their agreement with the simulation results was not very good. The disagreement on the plot looks significant, but in reality it is less than one dB. Various system components could cause the shift of a dB in the measurement. In

particular, the losses of the cable and connector used in the experimental measurement could account for some of the error. Several other possible explanations exist to why the experimental measurements disagree with the simulation. First and foremost, the constructed VM structures were constructed by hand with very large tolerances. Secondly, the Teflon used was low cost and a low quality product. As a result, the dielectric constant, and more importantly the loss, of the Teflon sheet may be far from ideal. Finally, the use of thin copper sheet as the plates and Kapton tape to hold the plates to the dielectric did not work as well as envisioned. Since the plates were not completely flat, variation in the spacing between the plates existed.

For initial hot test experiments, our frequency range of interest was intended to be from 1.85 GHz to 2.2 GHz. Conveniently, the agreement between simulation and experiment over a portion of that that frequency band is reasonably good. We also anticipated that original experiments would exhibit oscillation type behavior so the particular magnitude of the S-parameters were not important for initial tests. Therefore, we decided that instead of spending additional time on investigating the source of this discrepancy, we would just try it out as is. Future work will investigate why the experiment disagrees so much with the experimental results and how to improve the agreement. Fig. 95 shows the VM structure mounted to the full MERWA assembly before being moved to the vacuum chamber setup.

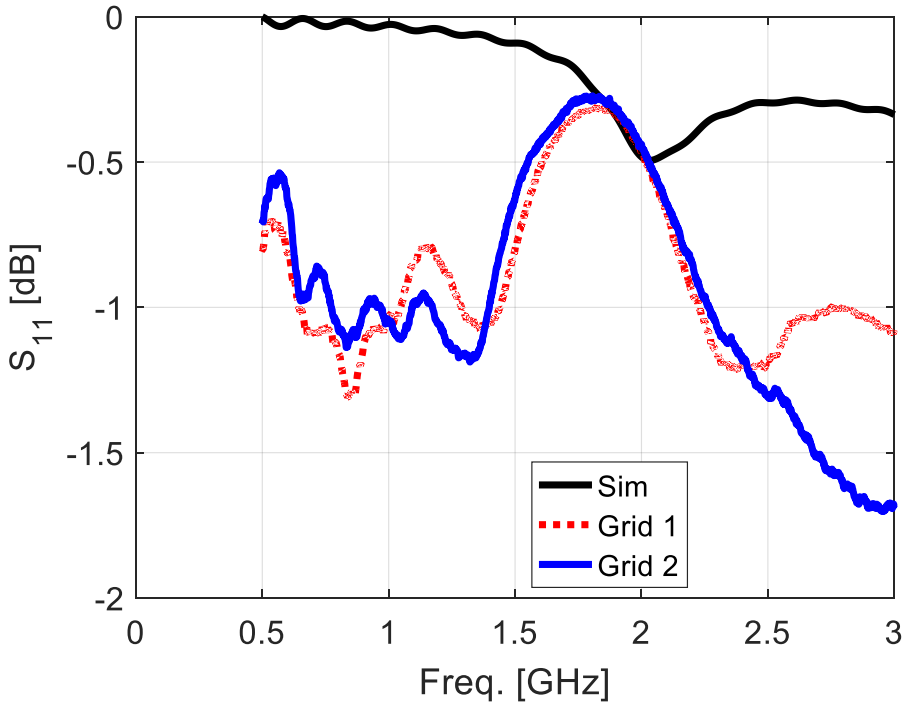

Fig. 94: Simulated and measured S_{11} for the constructed VM structures where Grid 1 and Grid 2 represent the two different constructed structures.

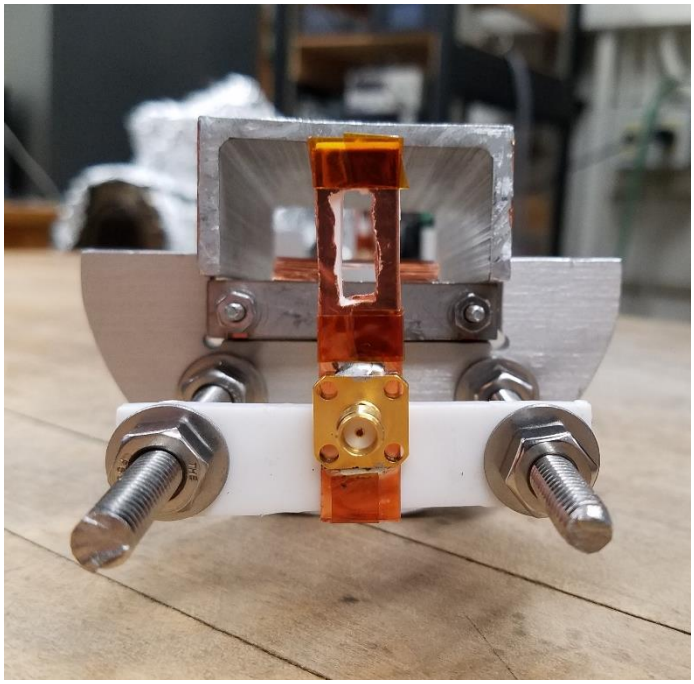

Fig. 95: Constructed VM assembly connected to the experimental MERWA fixture before being moved to the vacuum chamber including the alignment components, copper meander structures, and waveguide assembly.

Long term goals for this research project, as discussed in the final chapter of this dissertation, include the investigation of novel input and output coupling structures that incorporate MTMs. The MTM based coupling structures could potentially have wider bandwidths and improved interaction with the electron beam than conventional coupling structures. As an intermediate step between new novel coupling structures and this VM structure, two initial prospective ideas could be investigated: 1) a matching of this VM structure and 2) a newly constructed VM structure based on a helix. A matching network would improve the VM structure by reducing the S_{11} and increasing the power that reaches the structure. The matching network could be implemented through a series of high and low impedance transmission lines connected directly before the SMA connector of the structure. In addition, one could redesign the plate configuration allowing for variation in the spacing between the plates at different locations to possibly improve the bandwidth. Alternatively, the performance could be improved by completely designing a different VM structure. The most obvious solution, as it is commonly used in other VED projects [40] and is discussed by the original RWA researchers [2] is the use of a helix type structure. A helix is known to have a much wider bandwidth but has a much more complex construction and matching method that must be used. The use of a helix method is anticipated to significantly improve the VM performance. If, in future work, it is decided to create a new VM structure, it would only be necessary to create one instead of the two done for this work. Since this is not a commercial device, the power that is extracted from the beam does not need to be efficient. The second VM structure is simply used for gain type measurements meaning all measurements are relative so an improved VM structure would not be necessarily beneficial at the output.

7.4.5 Hot Test Results

This section discusses the status of the hot tests measurements that have been completed on the MERWA. Three hot tests have been examined and are discussed in this section. First, we measured the presence of the backward wave oscillation that is discussed in Chapter IV. Second, the suppression of the oscillation through the use of physical beam movement and the introduction of lossy elements in the MTM was investigated. Finally, we conducted a preliminary examination of RWA gain using the lossy MERWA structure. All three of these topics are discussed in detail in this section through both experiment and simulation.

7.4.5a Backward Wave Oscillation

The first step towards demonstrating MERWA gain was to first demonstrate the presence of the BWO in the device. Simulations of the full MERWA structure, using the Cu based MTM, demonstrated that in almost all cases the device oscillated and that the oscillation overpowered any form of space charge wave amplification. We demonstrate that this happened in experiment and compare the experimental results to the simulation. In particular, it was of interest to examine the frequency at which the oscillation occurred.

The simulation model of the full MERWA test configuration is presented in Fig. 96. The simulation model consists of the electron beam source at the far left which emits a pencil beam from left to right in the figure. After being emitted from the left, the electron beam first travels through the input VM structure before traveling through the MERWA assembly (rectangular waveguide with MTM liner discussed in section 7.4). The beam then travels through the output

VM structure and finally strikes the simulation boundary, at the right side of the figure. Both the input and output VM structures are connected to 50 Ω ports. To examine the device's oscillation behavior, neither port was driven with any power but only used for measuring output signals. The electron beam emitted from the source had a current of 55 mA and a variable potential. The simulation was run for 62 nS. At the end of the simulation time, an FFT was computed of the signal measured at the coaxial port of the input VM structure. The peak of the FFT was recorded as the frequency of oscillation.

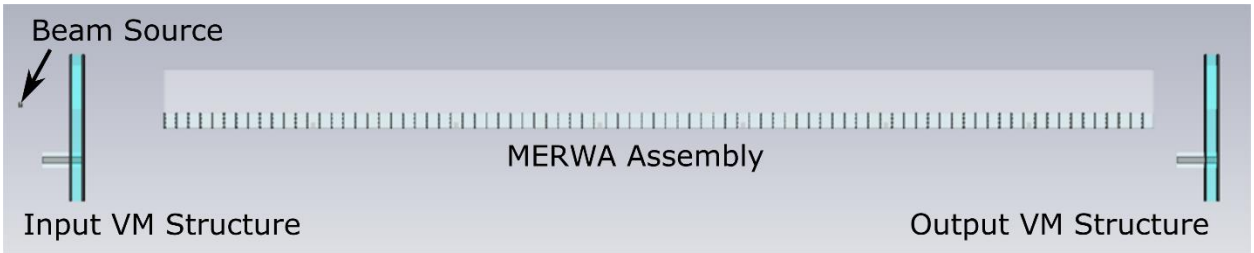

Fig. 96: Full PIC simulation model including the MERWA structure and the input and output VM structures

For the experimental measurements of the oscillation, we connected the output VM structure to a 50 Ω coaxial cable which was connected to a 50 Ω input of an oscilloscope. We used the built in FFT capabilities of the oscilloscope to analyze the spectral content of the signal. In particular, the scope is triggered by the high voltage switch. When the scope is triggered by the switch, it is then configured to calculate the FFT of a portion of the measured signal from the output VM structure. The portion of the full signal consisted of 10 μS from the 50 μS pulse of data, with a 20 μS delay from the start of the pulse. Only a portion of the data was used to remove any transient effects of when the beam starts and stops. We used the automation capabilities of the oscilloscope to automatically record the information about the peak of the FFT calculation

including the magnitude and frequency of the peak. The use of an automatically recording data set allowed for many pulses to be ran and an average of the results could be determined.

To experimentally measure the frequency of oscillation we varied the potential of the electron beam and temperature limited the cathode to maintain a beam current of 50 mA, for all beam potentials. In these experiments, the input VM structure was terminated with a 50 Ω load and no input RF signal was used. A comparison of the experimental measurement results to simulation for beam voltages of 3 to 8 kV is presented in Fig. 97. The experimental measurements match the simulation results very well. An experimental result does not exist at 3 kV as 50 mA of beam current is above the SCL current for the electron gun at 3 kV, but simulation allows for any current to be used. The small variation in the simulation to experimental results can be attributed to experimental measurement errors.

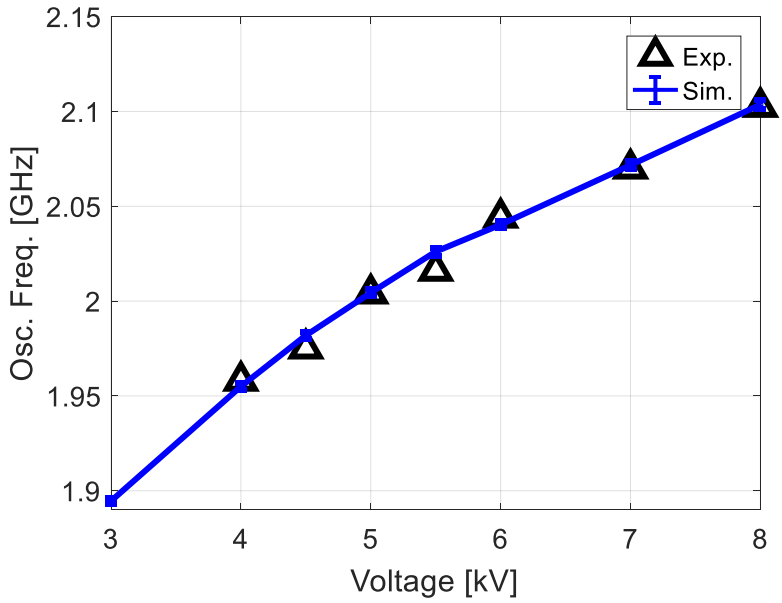

Fig. 97: Measured oscillation frequency versus beam voltage for a 50 mA beam compared to simulation

The other property of the frequency of oscillation to examine and verify was the behavior of the oscillation with a change in the beam current. The change in oscillation frequency with current can be discussed by examining the space charge wave numbers. If we assume the electron beam to be infinitely broad, the space charge waves have wave numbers of

$$\beta = \beta_e \pm \beta_q = \frac{\omega}{u_o} \pm \frac{\omega_p}{u_0}. \qquad (125)$$

If the electron beam is finite, the calculation of the wavenumbers is more complicated as it becomes necessary to compute the reduced, or effective, plasma frequency of the electron beam. Nevertheless, finite beam scenarios have the same behavior with regards to reduced current. An increase in the current increases the plasma frequency and decreases the wavenumber of the 'slow' space charge wave (the wavenumber in (125) using the difference sign), which is the wave that interacts with the backward EM wave [40]. Fig. 98 presents an exaggerated example of this scenario.

Referring to Fig. 98, as the current is increased, the $\beta_e + \beta_p$ curve shifts further to the right of the graph, moving the intersection point of the structure's dispersion curve and the beam line to a lower frequency. The intersection point of the slow beam line ($\beta_e + \beta_p$) and the dispersion of the structure is the frequency of oscillation. Therefore, it should be expected that the frequency of oscillation decreases with an increase in beam current. Fig. 99 presents the experimentally measured frequency of oscillation versus current compared to simulations conducted using CST with a variation in the current. For the results in Fig. 99, the electron beam voltage was fixed at 5 kV and the beam current was varied by temperature limiting the cathode. Several important properties of the results in Fig. 99 should be noted. First, for currents above approximately 20 mA, we see the expected behavior where the frequency of oscillation decreases with an

increase in beam current in both experiment and simulation. Further, the specific frequency at which the device oscillates agrees very well between simulation and experiment. Second, there is a disagreement between the simulation and experiment for beam currents less than 20 mA. Both the simulation and experimental oscillation frequency values require further discussion.

In the simulation, the change in oscillation frequency follows the expected behavior where the frequency increases as the current is dropped to 10 mA. However, it should be noted that the simulated oscillation point at the 10 mA beam current could be argued as incorrect. As mentioned above, the frequency of oscillation was found by examining the FFT of the signal measured on the output VM structure. As the current of the beam is decreased, the magnitude of the signal in the FFT also decreases. The FFT did have a peak at the measured oscillation frequency, but the peak was very small and close to the noise level; therefore, it is possible that this is a false data point and the structure is in fact not oscillating.

For the experimental results below 20 mA, there also appears to be another effect occurring. In the experiment, the frequency of oscillation decreases with current when the current is below 20 mA. Further, the frequency of oscillation appears to be rather random and have much larger variation for low current values. It is not displayed in the data shown in Fig. 99, but there were also several measurements taken at the low currents where the device did not oscillate at all. To demonstrate the inconsistency of the oscillation we ran the experiment with 100 pulses each separated by 200 mS. For each pulse, we recorded the frequency of oscillation. Fig. 100 presents the frequency of oscillation for 100 concurrent pulses. In Fig. 100, it is possible to see that the frequency of oscillation varies wildly with the each pulse. In part (b) of Fig. 100, it appears that

the frequency of oscillation may be stabilizing as more pulses are completed while part (a) does not. However, part (a) and (b) of Fig. 100 are repeats of identical experiments. We would often also not measure an oscillation on the first pulse, but see an oscillation at subsequent pulses. Further, we noticed that the frequency of oscillation appeared to stabilize with a stabilization of the tube pressure. The stabilization of the gas pressure led us to believe that something is occurring with gas discharge effects at low currents. Further research would have to be completed to fully explain the results of the tube at low current. At the current time, we are only interested in higher current beams (>50 mA), so the investigation of low current effects is left for future work.

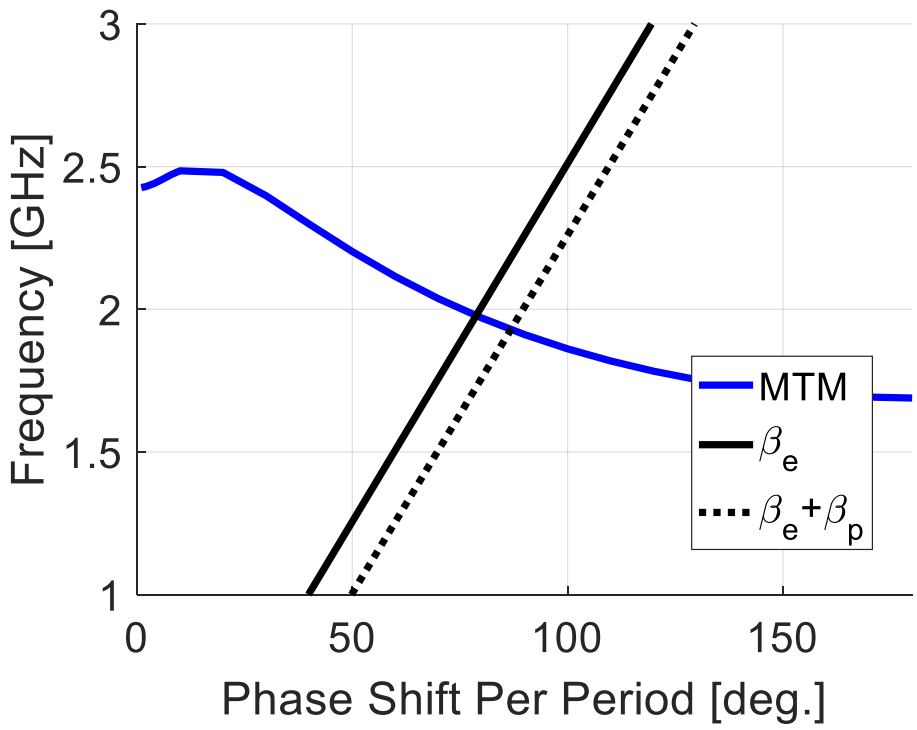

Fig. 98: Dispersion curve of the lowest order hybrid mode in a MTM lined waveguide along with two beam lines, one that includes effect of plasma frequency and one that does not

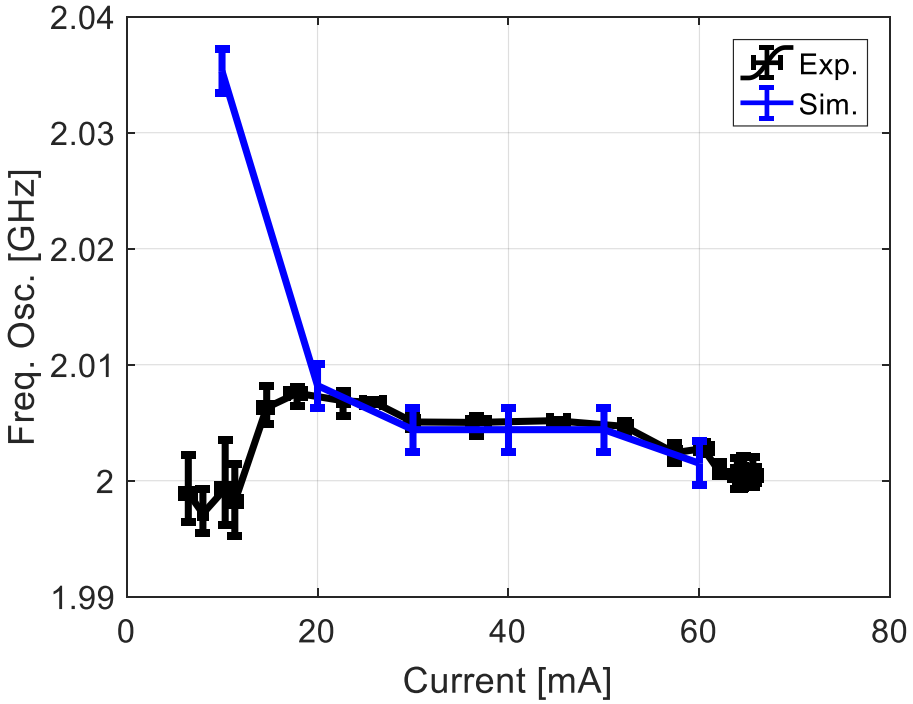

Fig. 99: Measured oscillation frequency using a 5 kV beam versus the beam current.

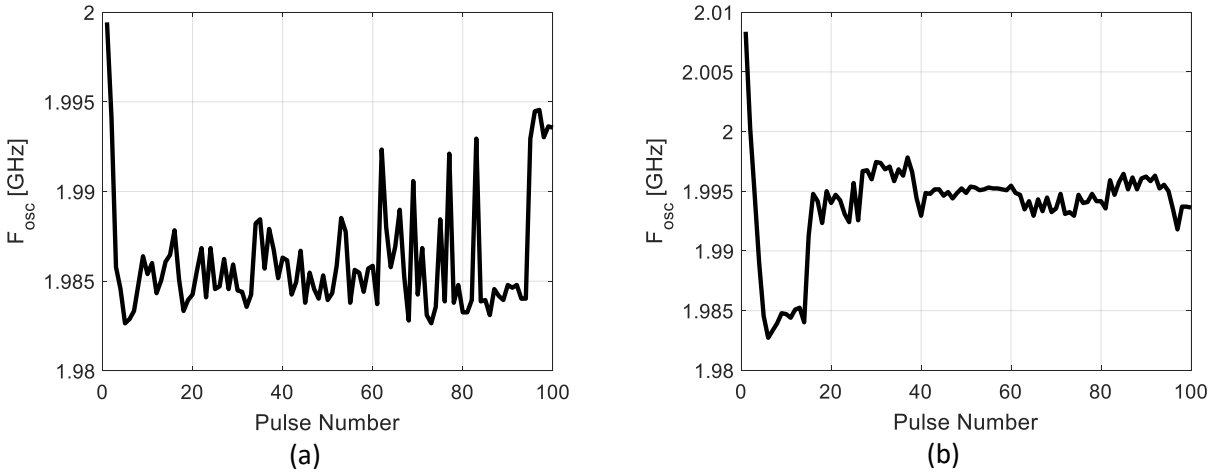

Fig. 100: Measurement of the oscillation frequency for subsequent pulse separated by 200 mS with an 11 mA beam where (a) and (b) are two repetitions of the same experiment

7.4.5b Suppression of BWO through Beam Positioning

For successful MERWA operation, it is necessary to suppress the BWO. One method to suppress the BWO is to move the physical location of where the electron beam travels in the MERWA. In particular, what happens if we move the beam in the vertical direction, away from the MTM structure? Three different vertical positons were examined and are presented in Fig. 101. The original position presented in Fig. 101 (a) is the location of the beam used in all experiments of section 7.4.5a. The other two beam positions are a 1 mm vertical offset and 3.5 mm vertical offset, both referenced from the original beam position. If we examine the eigenmode simulations of the MTM structure we can examine the interaction impedance, discussed in section 4.3, for the three different beam positions. The calculated interaction impedance is presented in Fig. 102. The interaction impedance values presented in Fig. 102 are estimated values of the true interaction impedance as these calculations use the assumption of only using the electric field strength at the center of the beam, not averaged over the cross section of the beam. It is possible to see in Fig. 102 that the interaction impedance of the structure decreases with an increase in the beam's vertical position. If all other parameter of the device remain unchanged, it would be expected that an decrease in the interaction impedance increases the start oscillation current [41].

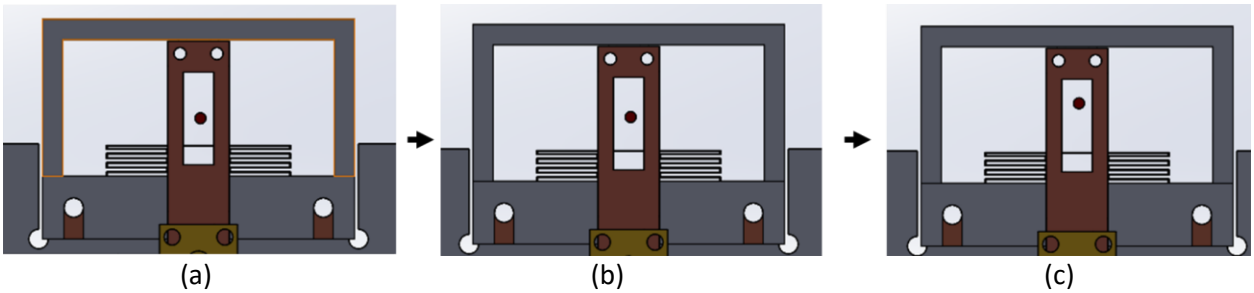

Fig. 101: Three vertical positions of the electron beam in a vacuum chamber: (a) 'original' position, (b) 1 mm vertical offset, and (c) 3.5 mm offset

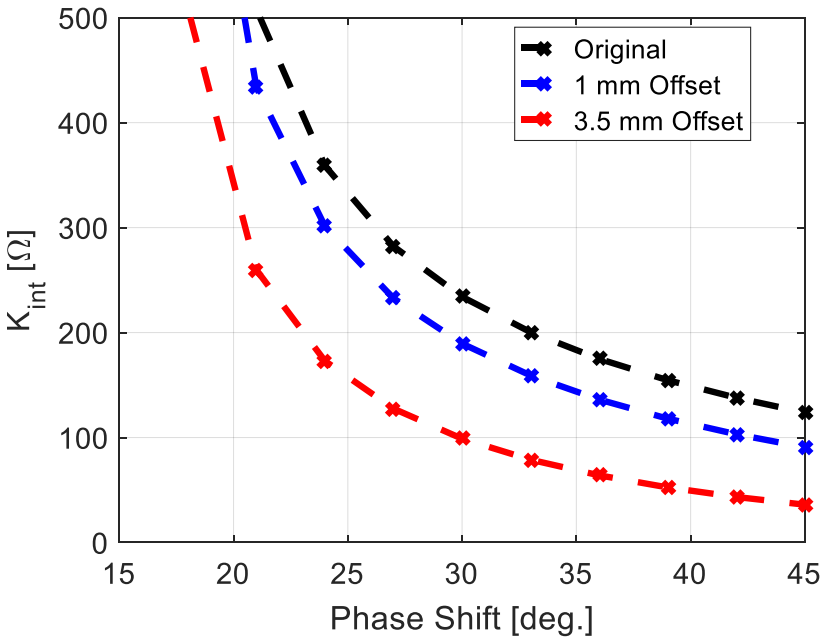

Fig. 102: Simulated interaction impedance versus the phase shift per unit cell for three different beam locations

To experimentally verify the change in start oscillation current, as a function of the beam's vertical position, we measured the start oscillation current at the three beam positions. The beam's position was modified through the use of the position manipulator arm discussed in section 7.4.1 and 7.4.3. To define the start oscillation current we repeated the experimental process discussed in section 7.4.5a but varied the current and measured the frequency of oscillation at each current point. At a sufficiently low beam current, no peaks in the FFT of the signal from the output VM structure would be present. This scenario was defined as 'No Oscillation'. The results of these experiments for the three vertical beam positions are presented in Fig. 103.

Starting with the original position, the device does not oscillate if the current is very low (<5 mA) but oscillates at all currents above approximately 5 mA. When the beam is offset by 1 mm from the original position, the current when the device begins to oscillate is increased to approximately (30 mA). In Fig. 103, one frequency of oscillation occurs for the 1 mm offset scenario at the low current of approximately 10 mA, this is considered an anomaly in the data. When the beam was increased to the 3.5 mm vertical offset position we increased the current up to the SCL current of 60 mA and were still unable to excite the oscillation.

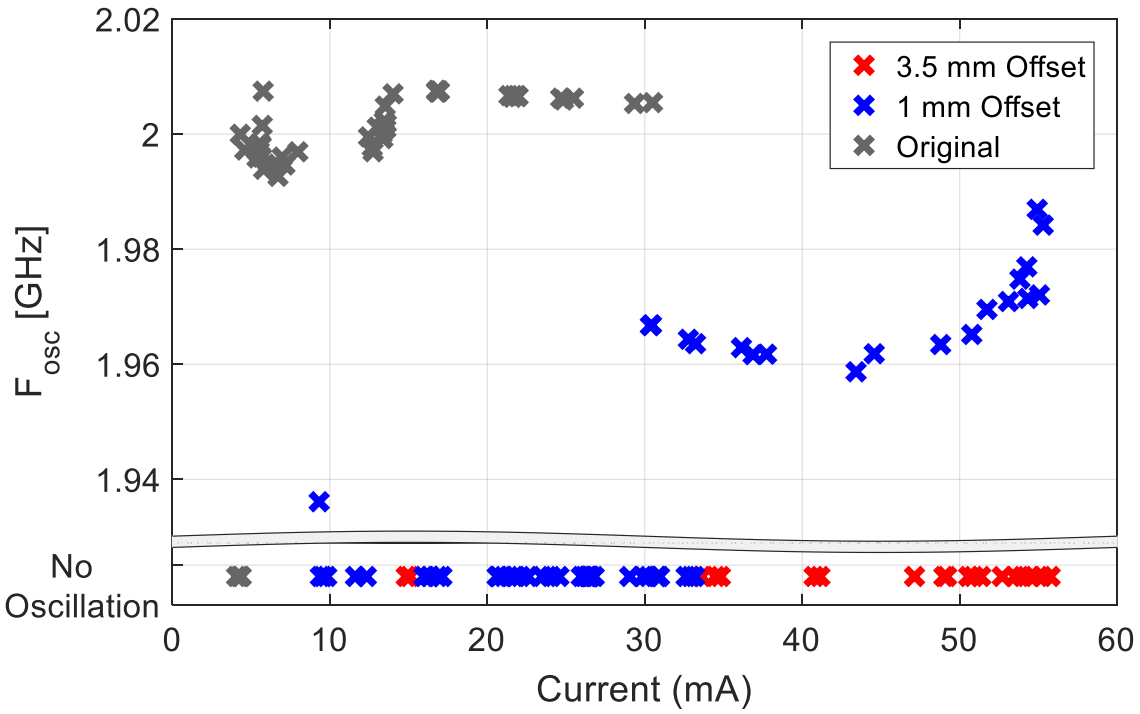

Fig. 103: Measured oscillation frequency versus electron beam current for the three beam positions presented in Fig. 101

From Fig. 103 we can infer that the vertical movement of the beam clearly increases the start oscillation current, a benefit. However, moving the beam away from the MTM also reduces the gain of the resistive wall mechanism. We don't have an analytic theory for the RWA gain inside

a MTM lined rectangular waveguide to accurately determine the reduction in gain as a result of moving the beam. But, based upon the theoretical work of the MERWA in chapter III, moving the beam away from the MTM significantly reduces the RWA gain. The gain reduces because as the gap between the edge of the beam and the location of the MTM liner increases, the admittance of the wall becomes less inductive (the gap adds a capacitive component). Therefore, it is desirable to have a change to the system that reduces the EM mode's propagation but still allows for RWA gain. This implementation is a distributed loss implementation of the BWO suppression techniques discussed in Chapter V.

7.4.5c Suppression of Backwards Wave Oscillation with a Lossy MTM liner

In section 7.3.3, we examined how the use of lossy metal meander elements, specifically SS meanders, increased the attenuation of the EM wave in the structure without significantly effecting the ENG properties. Therefore, it was hypothesized that we could use a SS meander based MTM to create a lossy MERWA structure. The use of a lossy MTM acts as a distributed loss mechanism to the suppression of the BWO, as discussed in section 4.5. The use of SS meander elements as a distributed loss should increase the start oscillation current of the device.

To examine if the use of SS meander elements does increase the start oscillation current of the MERWA structure, we built a new MTM assembly using SS meanders. Using the same measurement procedure discussed in 7.4.5a and 7.4.5b, we varied the current of the electron beam and measured the frequency of oscillation on the output VM structure. Fig. 104 shows the frequency of oscillation of the SS structure versus the Cu structure when the beam was vertically offset by 1 mm from the centered positon. The measurements presented here for the SS MERWA

structure were conducted with a beam voltage of 5 kV. Recall that at the 1 mm offset position, the Cu structure began to oscillate at approximately 30 mA. By changing the Cu meanders to SS we can see in Fig. 104 that the structure does not oscillate for any current up to 60 mA. The beam was moved to its' original position and the experiment was repeated with the results presented in Fig. 105. Once again, the SS MTM structure did not oscillate for any current up to approximately 65 mA while the Cu structure oscillated at 5 mA. From Fig. 104 and Fig. 105 it is possible to see that by using a SS based MTM structure the start oscillation current has been increased to above approximately 65 mA (the SCL current for this 5kV beam).

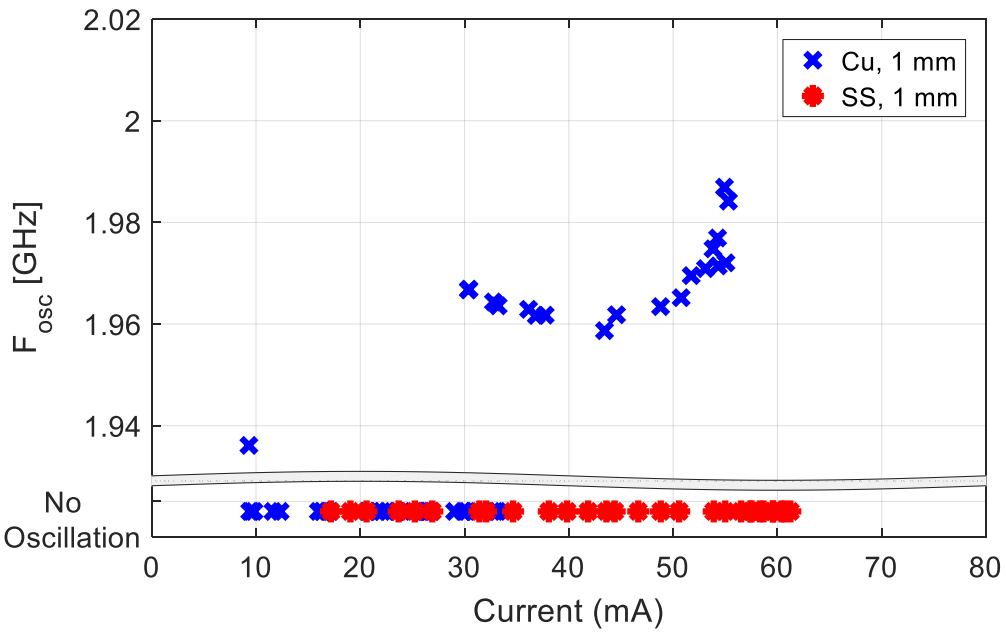

Fig. 104: Oscillation frequency versus current for the copper and stainless steel based MTM structures when the electron beam is vertically offset by 1 mm from the original centered position using a 5 kV beam.

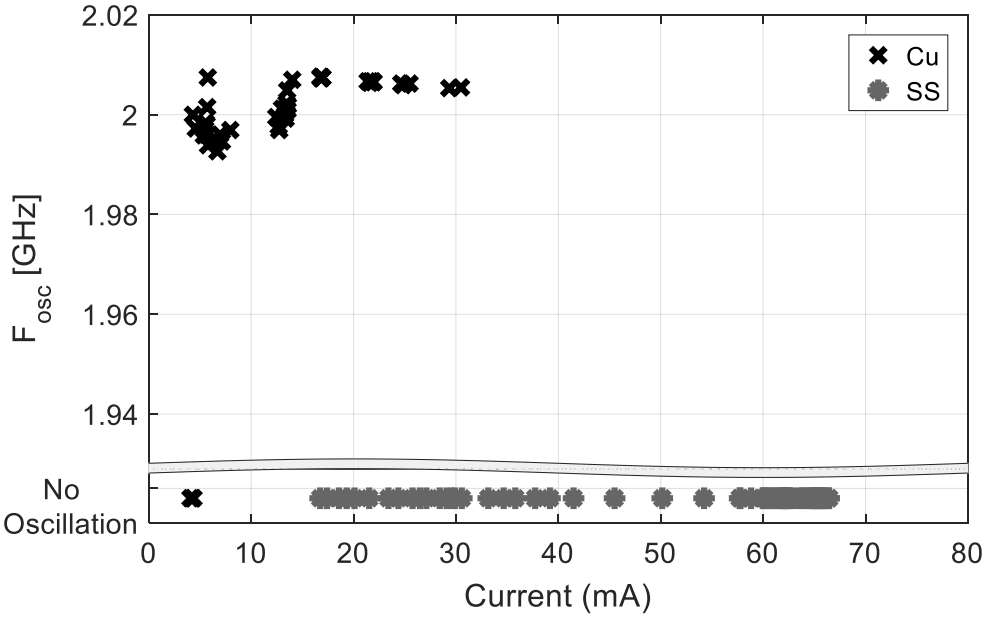

Fig. 105: Oscillation frequency versus current for the copper and stainless steel based MTM structures when the electron beam is in the centered vertical positon using a 5 kV beam.

After demonstrating the presence and suppression of the backwards wave oscillation, the next step was to demonstrate resistive wall amplification. To avoid the backwards wave oscillation, the resistive wall amplification was examined using the SS based MERWA. The progress on demonstration of restive wall gain is discussed in the next section.

7.4.5d Preliminary gain measurements of a MERWA using a lossy MTM

As a result of the VM structure constructed for this work, absolute gain of the device cannot be measured accurately. Poor coupling between the VM structures and the beam as well as the poor match of the VM structures to the 50 Ω feed lines make gain measurements nearly impossible. However, we can compare the output signal of the device with and without the MTM liner, a very accurate relative measurement. This was conducted by inputting a continuous RF signal to the input VM structure and measuring the amplitude of the signal at the output VM structure

during the pulse of an electron beam. The configuration of the device without the MTM liner will simply exhibit classical klystron gain while both klystron and MERWA gain will be present in the experiment with the MTM liner. The difference in the signal from these two experiments can be attributed to MERWA gain.

In addition to not being able to accurately measure true gain of the structure, we have not developed an analytic theory for the MTM lined rectangular waveguide. The absence of a complete analytic theory is due to the very complex solution for a small cylindrical beam in a rectangular structure with a liner on only one side. The resulting space charge gain equation would be extremely complicated and is left for future work. In this work, we focused on the simple demonstration of space charge wave growth that is larger than standard klystron gain as demonstration of the MERWA operation.

After conclusion of the BWO suppression experiments presented in section 7.4.5c, we conducted numerous experiments on the SS based MERWA to demonstrate the resistive wall gain by comparing the output signal with and without the liner. The experiments were conducted at a wide range of frequencies, beam voltages, and beam currents (up to the SCL value). Initial results did not demonstrate measurable gain improvement over the klystron. To fully understand the poor performance, simulations were conducted of the full device using the model shown in Fig. 96.

Through the use of PIC simulations of the full MERWA structure, we determined that it was simply not realistic to get measurable space charge wave growth on the output VM structure with

the beam parameters available. Using current levels below the SCL of the electron gun did not produce a gain substantially larger than the klystron gain. As a result, it became necessary to increase the current of the electron beam. From the BWO experimental results, in Fig. 105, it is possible to see that the maximum current achievable was approximately 65 mA for the 5 kV beam, due to the SCL. To increase the SCL current, the anode to cathode gap of the electron gun was reduced from 6 mm to 3 mm. The SCL current that should be expected from the decreased anode to cathode gap was predicted using particle tracking simulations. The results of the simulations using a 3 mm gap are presented in Fig. 106, compared to the previously presented 6 mm gap results. The reduction of the gap created an increase in the SCL current by almost a factor of 2, as seen in Fig. 106.

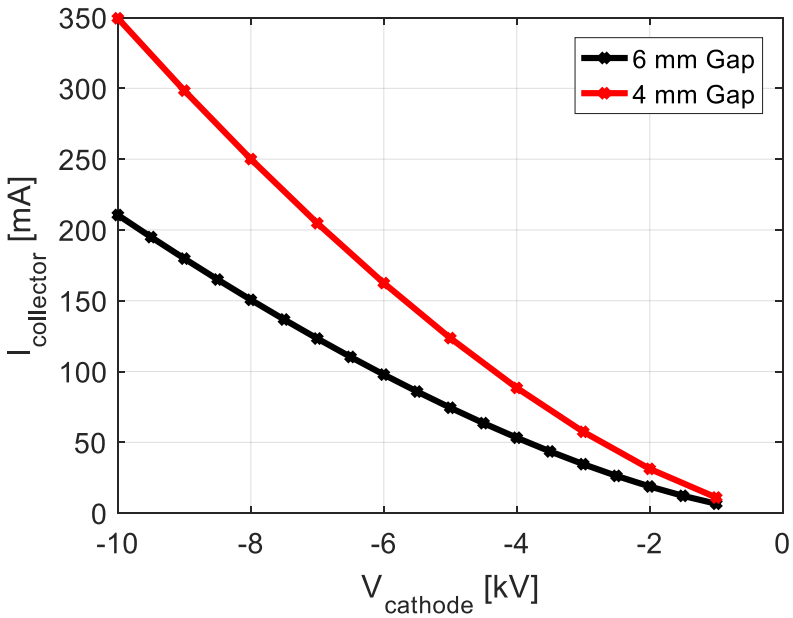

Fig. 106: SCL current from the electron gun versus beam voltage when modifying the anode to cathode gap from 6 mm to 3 mm

We arbitrarily choose to conduct gain experiments with a 5 kV beam voltage. Using a 5 kV electron beam, our SCL current was now 150 mA, from Fig. 106. To predict the performance of the MERWA with a 150 mA beam current, PIC simulations were conducted. The PIC simulations used a 5 kV, 150 mA beam and assumed an input power to the VM structure of 16 dBm. The input power was selected as the maximum output power of our source is 20 dBm and we anticipate a 3 to 4 dB loss from our vacuum compatible coaxial cables. The simulations were run for 65 nS and an FFT of the signal from the output VM structure was computed. The magnitude of the FFT, at the frequency of the drive signal, was used to compare PIC simulations with and without the MTM liner. Fig. 107 presents the simulation results of the structure with and without the MTM liner. The results in Fig. 107 demonstrate a clear improvement in the output signal due to the presence of a growing space charge wave that exists in the structure with a MTM liner. At the low frequency of 1.8 GHz, the improvement in output signal is approximately 7 times and nearly 10 times as high at 1.9 GHz.

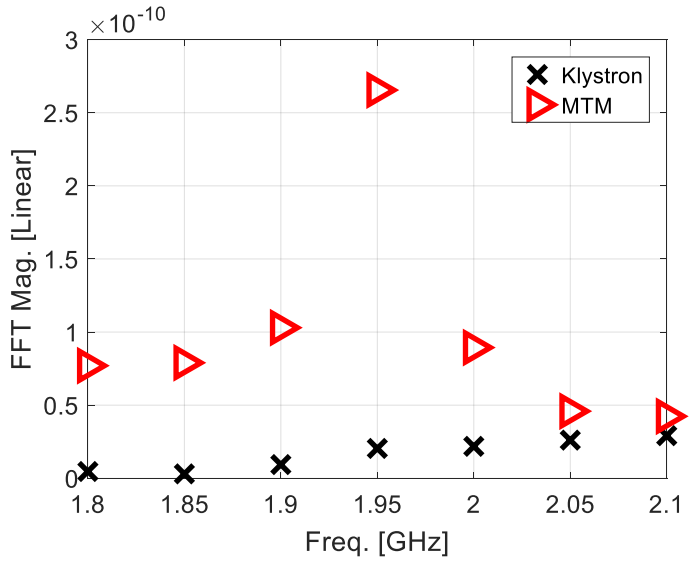

Fig. 107: Simulation results of the SS MTM based MERWA: FFT magnitude from PIC simulations with and without the MTM liner.

The improvement in output signal presented in Fig. 107 may appear low, but the purpose of these simulations was not to optimize the conditions for optimal gain. Rather, the simulations were meant to simply demonstrate that a measureable gain does exist without exciting an unstable oscillation using parameters that are achievable in our experimental setup (beam current below the SCL and input RF signal level from the available source). In addition, the absolute level of the FFT results presented in Fig. 107 may appear low, at approximately 1×10^{-10}; however, the low FFT magnitude is only due the relatively short FFT time frame of 65 nS. The absolute magnitude of the FFT is only important for comparison to other points on the figure. Experimental measurements will produce higher values than those seen in these FFT results as the time frame will be significantly larger. Simulations were not run for longer time due to simulation limitations. The meshing of the meandered line MTM requires a large number of cells (>5M cells). As a result of the large number of cells, the time of simulation is approximately 6 hours even with the use of GPU computing. Simulation times could be reduced through the use of effective medium properties. Effective mediums have not been implemented yet as it is still necessary to develop a method to calculate the attenuation constant of the liner (determine the loss) in addition to the wave number presented in section 7.3. Determination of the attenuation constant and complete verification of the equivalency between the MTM and effective medium in PIC simulations is left for future work.

The high gain point at 1.95 GHz warrants some additional discussion, as this FFT magnitude at this point may be inaccurate. At some drive frequencies, the FFT of the output signal showed two frequency peaks in simulation. Fig. 108 presents an example FFT of the output signal. For

the simulation used to generate the results in Fig. 108, the input signal was a 2 GHz signal; however, another FFT peak occurs at approximately 1.954 GHz.

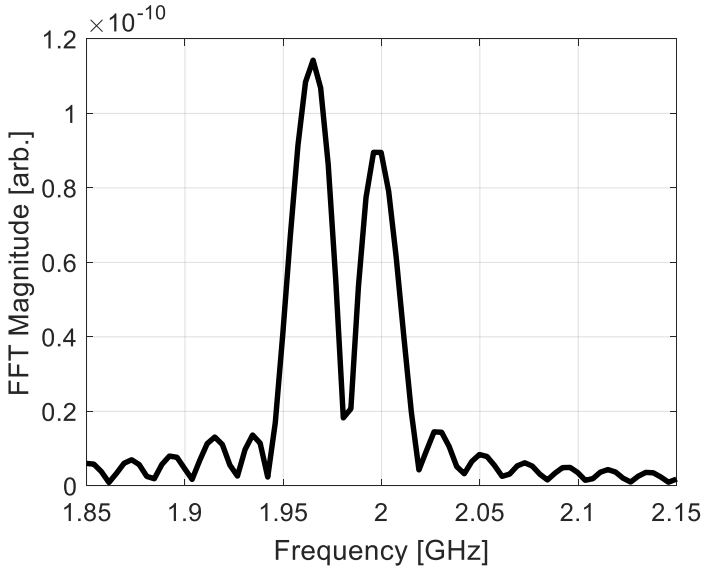

Fig. 108: FFT of the signal at the output VM structure for a simulation that was driven with a 2 GHz signal

The second frequency component at approximately 1.954 GHz is a result of the backwards traveling EM mode. It is believed that the EM mode is excited through a combination of the ramp up of the input signal and the initial pulse of electrons from the beam (both of which have large temporal frequency content). By examining the output signal versus time, there appears to be no growth to the output signal versus time, indicating an oscillation is not forming. To help examine the excitation of the EM mode, and if it turns into an oscillation, the simulation was modified to only provide a pulse type input. In this configuration, the input signal was a 2 GHz driving signal that ramped up over 10 nS, held a constant magnitude for 10 nS, and then ramped down over 10 nS. The simulation ran for an additional 110 nS, with the beam continuing to flow, after shutting off the input signal. The input waveform, in addition to the signal produced at the output, are presented in Fig. 109. The output signal presented in Fig. 109 does not disappear after

30 nS, but rather outputs a signal the entire time of the simulation. However, the output signal is slowly decaying away as time progresses.

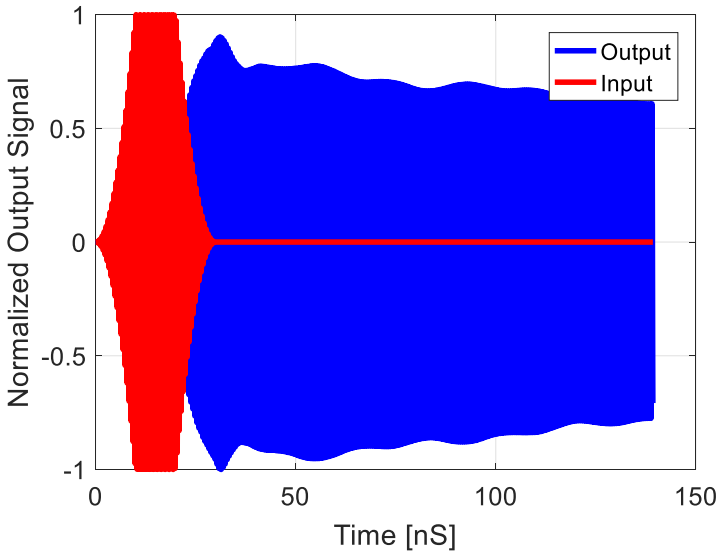

Fig. 109: Input and output signals for a simulation that used a 'pulsed' drive signal

From the results in Fig. 109, the EM mode is clearly excited and has a relatively long decay time. Since the EM mode is not growing, it is possible that if simulations with a continuous input were run for a longer simulation time, the EM mode frequency would eventually decay away. Experimental verification of this process is still in progress; however, initial results indicated that no oscillation was present in the device with a 150 mA electron beam. In addition, if the experiment was driven with an input signal, only one peak on the FFT was observed, not two. The absence of two peaks in the initial experimental results appear to confirm the theory that any EM mode excitation decays away, when using a beam with a current of 150 mA or less.

As a result of the EM mode being excited, the simulated improvement in the output signal very close to the EM mode frequency (where the FFT cannot clearly separate the BWO frequency

from the driving frequency) should not be attributed completely to the growing space charge wave but a combination of the space charge wave and the presence of the EM mode. For this particular structure, the offending EM mode frequency is around 1.95 GHz. At drive frequencies that are far enough away from the BWO frequency, such that the FFT calculation can clearly distinguish between the two frequencies, the improvement in gain at the drive frequency should be attributed completely to the growing space charge wave. Further, the growing space charge is only present because of the addition of the MTM liner, demonstrating the MERWA theory.

Regardless of the excitation of the EM mode, the results in Fig. 107 demonstrate the presence of a growing space charge due to the addition of the MTM, at all points except 1.95 GHz. Based upon the simulation-verified measurable difference in the output using achievable beam parameters, the experiment was modified to increase to the beam current. After decreasing the anode to cathode spacing experimentally, we were able to successfully achieve a beam current of 150 mA. However, the decrease of the anode-cathode gap gave rise to some additional problems. When sending the beam though the entire MTM structure and VM structures we experienced an increase in the amount of beam loss (cathode current minus anode current versus the collector current) and a ‘ripple’ of the current measurement when the current went above approximately 100 mA. An example of the measured current and ripple (seen on the collector current after approximately 20 μS) is presented in Fig. 110. Based on previous experiments with this electron beam, a ripple in the collector current is usually an indicator that the electron beam is traveling/scrapping near a conductive surface or interacting with ions. Re-alignment of the electron beam along the axis of the chamber was attempted, but was unable to decrease the beam loss. We also conducted experiments where the collector was biased positive (30 V) to collect

secondary electrons emitted from the collector but did not observe any change in the behavior. It may be possible that a much higher potential is required on the collector to collect higher energy secondary electrons (<1kV); the investigation of high energy secondary electrons is left for future work. Running particle tracking simulations on the electron gun determined that, due to the decrease in the anode to cathode gap, the optics of the electron beam were modified allowing for a larger beam diameter. Fig. 111 shows the emitted beam from the particle tracking results. The particle tracking results were run with two beam configurations: (a) where all particles are emitted normal from the surface of the cathode and (b) where some particles are emitted slightly off normal from the cathode surface.

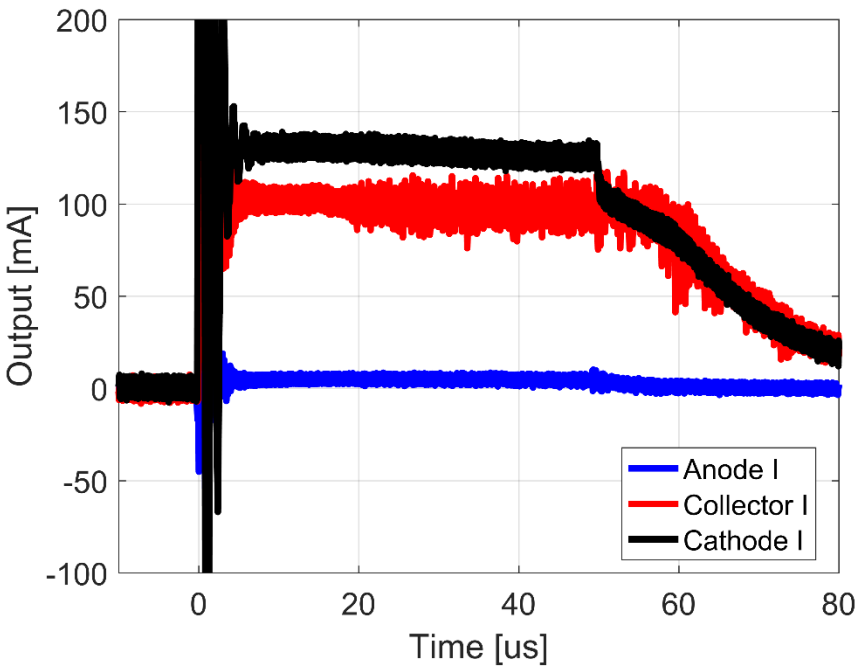

Fig. 110: Experimentally measured of the electron beam current at the collector after traveling though the VM and MTM structures

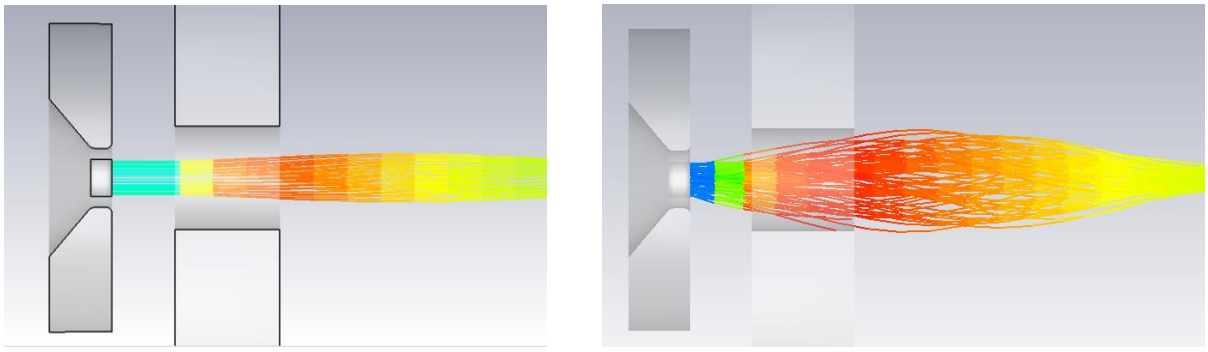

(a) (b)

Fig. 111: Beam emitted off of the cathode with (a) no angular distribution on the emitted beam and (b) a 20 angular distribution on the emitted beam.

The increase in the beam diameter is a consequence of the decreased anode to cathode spacing. When the anode is significantly closer to the cathode, a larger defocusing effect is present. The defocusing effect can be seen in Fig. 111 (a) where the diameter of the electron beam becomes larger than the cathode shortly after passing through the anode. This defocusing effect is even more substantial for electrons that are emitted with velocity vectors that are not completely normal from the cathode surface (electrons have some transverse velocity when emitted). Fig. 111 (b) presents a simulation of the emitted beam when the particles emitted from the cathode are given a transverse velocity as well. In this particular case, a distribution of emission angles is used, with the maximum emitted angle being 20° from normal. It is possible to see in Fig. 111 (a) that adding a little bit of transverse velocity to the particles emitted from the cathode surface (introducing an angular distribution to the initial velocity vectors) greatly increased the diameter of the emitted beam.

It is unknown what the specific angular distribution is of electrons emitted from the Kimball Physics cathode, but we know that there is some angular distribution to the emitted beam because anode current is measured in experiment. An anode current can only be present if the

electrons emitted have a transverse velocity component (unless the current is coming from an unknown secondary electron source, such as the collector). Using the 20° angular distribution on the emitted beam, Fig. 112 shows the travel of the electron beam as viewed from the collector's position. The beam is shown to be significantly larger than the beam as it comes off of the cathode. In addition, the beam appears to have a spiral type effect as it travels to the collector. It is hypothesized that because of the larger beam diameter and the small spiral to the beam's motion, the beam is striking the sides of the VM structure. The square holes cut in the copper plates of the VM structures, to allow for beam travel through the structure, were only constructed to be 5 mm wide. The larger beam diameter and a small spiral effect explains both the lost beam (collection on the ground plates of the VM structure) and the ripple in the current (part of the beam is passing very closely to the edges of the conductive plates and/or interacting with ions).

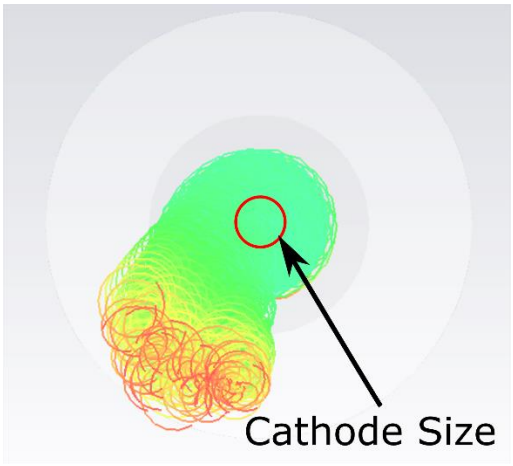

Fig. 112: View of the electron beam, from the position of the collector showing a beam diameter much larger than the cathode dimension as well as a spiral affect that is occuring.

The issue of increased beam diameter and spiraling effect can be improved through two methods. First, using knowledge of the 3 mm anode to cathode gap, the anode should be redesigned to prevent the diverging and/or have a focusing effect. This could be accomplished by changing the

anode hole diameter and creating an anode hole with a taper. In addition, the spiraling effect could possibly be improved with an increase in the magnetic confinement or a reduction in beam current. Both possible improvements to the electron beam, in addition to confirming that CST is correctly modeling the SCL with a smaller anode to cathode gap, are left for future work. As a result of the increased beam loss, we experimentally limited the beam current to about 75 mA instead of 150 mA. A beam current of 75 mA appeared to have a relatively low beam loss.

Experimental verification of the MERWA gain at 75 mA and 125 mA is an on-going process. In addition to the beam loss issues, EM coupling issues are currently being overcome to ensure accurate measurements of the output signal level. To ensure that the lower current measurements will still have measureable gain improvement, over the klystron case, additional simulations were conducted with a beam current of 75 mA and 125 mA. The simulation results of the two lower current cases, comparing the un-lined configuration to the MTM lined configuration, are presented in Fig. 113. The lower current cases still demonstrate an improvement to the output signal when the MTM liner is present. As expected, the amount of improvement is clearly a function of the current, where more current produces a larger improvement. The lower current simulations were also plagued by the EM mode excitation issue; therefore, the 2 GHz point for the 75 mA case and 1.95 GHz for the 125 mA case should be ignored. The frequency is higher for the 75 mA case because the frequency of the excited EM mode is inversely proportional to the beam current. Experimental hot tests, to be completed as part of the future work, should easily measure an improvement in the output signal in addition to the existence or absence of two frequency points in the output signal.

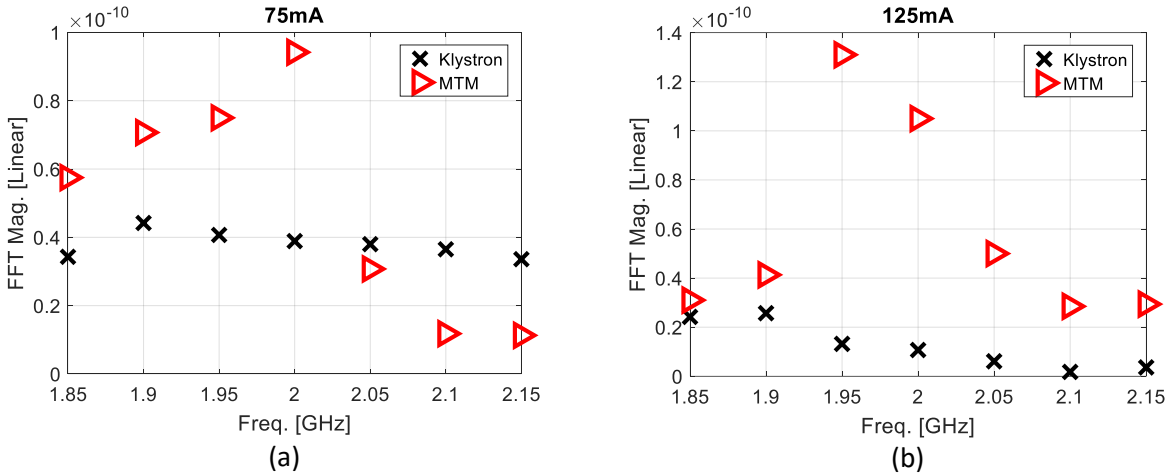

Fig. 113: Simulated gain of the SS based MERWA using lower electron beams currents of: (a) 75 mA and (b) 125 mA.

7.4.6 Experimental Hot Test Conclusions

Several very important hot test results were examined and verified as a result of this work. First, we have demonstrated the presence of the BWO, successfully matching simulation to experiment. Second, we successfully suppressed the BWO through movement of the beam's location, with respect to the MTM, and with a lossy SS based MTM. Finally, we have conducted preliminary measurements of the MERWA space charge wave gain. While we have not demonstrated the gain experimentally, we have identified the limitations of the experimental setup that has hindered the verification of the MERWA gain. Modifications to the experimental setup and retesting of the MERWA growing space charge wave are on-going work.

Chapter VIII: Conclusions and Future Work

8.1 Conclusions

In this dissertation, we introduced the concept of a metamaterial-enhanced resistive wall amplifier, or MERWA. We examined the MERWA through a combination of theoretical, computational, and experimental studies. We demonstrated, both theoretically and through the use of PIC simulations, that using ENG metamaterial shells in a MERWA can address major shortcomings that have hampered the use of RWAs as practical HPM amplifiers. We also examined the effect of the dielectric constant and beam fill factor on the device's performance. We demonstrated that MERWAs can offer significant gain rate values over wide bandwidths. In addition, we simulated this MERWA using the PIC technique in CST Particle Studio and observed a large numerical gain rate, which was demonstrated to be clearly due to the presence of the MTM shell in the amplifier.

In addition to demonstrating gain in the structure, we examined the requirements that the liner must possess to produce a high gain of the space charge wave. We determined that the liner may exhibit an anisotropic permittivity, but requires an ENG property in the direction perpendicular to the beam and along the direction of the liner's thickness. Our investigation of the liner's properties also identified the presence of a hybrid TM mode in ENG lined wave guiding structures. The dispersion of the hybrid TM mode was examined as well as the possibility of the mode supporting a BWO. An examination of the BWO included the calculation of the start oscillation current and length for the Drude-lined scenario and proposing several methods to suppress the oscillation.

To determine the capabilities of the MERWA to function as a HPM amplifier, we examined the modifications required to the analytic theory, originally presented by Birdsall and Whineery [1], to account for relativistic electron beams. The modification of the theory to allow for relativistic beams was verified through simulation and will allow for future investigations of MW level high power MERWAs.

This work demonstrated that a practical MERWA is realizable. We examined the periodic meander lines as an improvement of the wire array in a parallel plate configuration and demonstrated that the array of meanders has Lorentz-Drude effective medium properties. A periodic array of meanders was constructed and used as a rectangular waveguide liner. The ENG properties of the rectangular waveguide liner were then verified though measurement of the electromagnetic properties. The use of the periodically spaced inductive meandered lines MTM in a MERWA was verified computationally through PIC simulations for a planar structure and demonstrated gain that matched theory.

A prototype MERWA was constructed using the periodic, inductive meandered line array in a rectangular waveguide and demonstrated that the MTM exhibits a Drude-Lorentz type permittivity through both transmission and dispersion measurements that agree well with simulation. In addition, this work investigated how the material choice affects the performance of this MTM implementation by demonstrating that using less conductive metals does not have a large effect on the structure’s dispersion but significantly increases the absorption.

Finally, we constructed all of the facilities necessary to perform hot test measurements of the MERWA and conducted initial hot tests. Hot test measurements of the device examined several important qualities of the MERWA to confirm the analytic and computationally predicted theory. First, the presence of BWO was successfully demonstrated and the frequency of oscillation agreed well with simulation. Second, two methods were examined to successfully suppress the BWO. Finally, a preliminary examination of the device's gain was examined and generated the requirements of the experiment necessary to demonstrate growth of the space charge wave.

The work completed as part of the dissertation creates the foundation necessary for research to continue on the wideband, high power capable, high-gain MERWA. The theory, simulation, and experimental investigations all provide verification of the capabilities of this device. To create a complete device, numerous challenges must be investigated and overcome. A summary of immediate topics for future research are listed below.

8.2 Future Work

8.2.1 HPM Compatible Metamaterial Investigation

In Chapter VI, we presented the results of a theoretical and computational investigation of the relativistic HPM MERWA, where we assumed the liner was a homogenous dielectric with Drude dispersion properties. In the experimental part of this work we investigated the periodic, meandered line array as the ENG liner. The meandered line elements are not expected to have extremely high power capabilities; therefore, a new MTM liner structure will have to be designed that is high power compatible. The investigation of the alternative MTM structures will primarily be an investigation of planar structures and an examination of the cold tube dispersion.

Depending on the complexity of the designed structures, this work will also include PIC simulations.

8.2.2: Wideband input and output structures

In the prototype investigation of this work, simple VM structures were used to create and extract VM on the electron beam. To create a usable amplifier, it is necessary to create more efficient structures for VM. In particular, the structures need to be able to produce and extract an axial electric field to interact with the beam for a wide range of frequencies. The structure also needs to be matched over a wide frequency band for high efficiency. As mentioned in section 7.4.4, immediate next steps of improved VM structures may be to implement a helix type structure, as commonly used in TWT devices. For long term research, we would like to investigate the possibility of using a MTM structure to function as the input and output VM structures.

8.2.3: Intentional MTM randomization for bandwidth enhancement and backward wave suppression

In section 7.4.5a, we demonstrated the presence of the BWO present in MERWA. In section 7.4.5b and c, we demonstrated that the BWO could be suppressed by either moving the beam away from the MTM liner or by increasing the loss of the MTM liner. Both of these solutions to suppress the BWO are not ideal. As previously mentioned, physically moving the beam away from the MTM liner does suppress the BWO but also causes a reduction in the forward space charge gain as well. Increasing the loss of the liner also suppressed the BWO, but precise control over the liner's loss can be very difficult to achieve. As a result, the liner may be overly lossy

which would also reduce the resistive wall gain. An alternative method for BWO suppression, suggested in section 4.5d, is to intentionally randomize the MTM elements. This future work will investigate the effects on forward space charge gain and BWO if we create random variation of the individual elements of the MTM liner. The randomization of the MTM liner could be achieved by either changing the material or design of individual meander elements, or as simple as intentionally slightly randomizing the periodicity of the MTM. By randomizing the MTM, it should be possible to suppress the BWO and possibly increase the bandwidth of the structure as well.

8.2.4: Increased beam current using a reservoir type cathode

As noted in section 7.4.5d, hot test experiments would benefit from a higher current beam. When using the Kimball Physics Cathode, we were using a beam with a current density of approximately 30 A/cm^2. It should not be expected to easily obtain a cathode that can produce a larger current density; therefore, we explored obtaining a cathode with a larger beam diameter. Specifically, we are working with Calabazas Creek Research, Inc. to obtain a new cathode assembly. The cathode was manufactured by Ceradyne, Inc., a 3M Company. The cathode is a reservoir type cathode which was selected to allow for the ability to recharge the reservoir as necessary, even though the rated lifetime is > 10,000 hours and to allow for replaceable emission pellets if they become contaminated. In addition, the cathode was designed to have a controlled porosity to allow for accurate estimations of expected current emission, lifetime, etc. Most importantly, the cathode was designed to be compatible with a reusable electron gun structure that was being provided to us by Calabazas Creek Research, Inc. for use in these experiments. The operational specifications of the cathode are provided in Table 5. Future work will

incorporate the higher current cathode into the experimental setup and measure MERWA performance with a higher current beam.

Table 5: Cathode Specifications

Specification	Value
Type	Controlled Porosity Reservoir
Beam Cross Section	0.1 cm^2
Beam Radius	1.75 mm
Current Density	1 – 20 A/cm^2
Lifetime	>10,000 @ 20 A/cm^2, 50,000 @ 5 A/cm^2
Beam Voltage	10 kV
Beam Current	0.1 – 2 A

References

[1] C. K. Birdsall and J. R. Whinnery, "Waves in an electron stream with general admittance walls," *Journal of Applied Physics,* vol. 24, no. 3, pp. 314-323, 1953.

[2] C. K. Birdsall, G. R. Brewer, and A. V. Haeff, "The resistive-wall amplifier," *Proc. I.R.E,* Article vol. 41, no. 7, pp. 865-875, 1953.

[3] L. Solymar, "Note on Plasma, Resistive Wall, and Acoustic Amplifiers," *Journal of Applied Physics,* vol. 35, no. 11, pp. 3420-3421, 1964.

[4] V. K. Neil and A. M. Sessler, "Longitudinal Resistive Instabilities of Intense Coasting Beams in Particle Accelerators," *Review of Scientific Instruments,* vol. 36, no. 4, pp. 429-436, 1965.

[5] B. Vural and S. Bloom, "Streaming instabilities in solids and the role of collisions," *Electron Devices, IEEE Transactions on,* vol. 13, no. 1, pp. 57-63, 1966.

[6] H. Suk, J. G. Wang, and M. Reiser, "Resistive-wall instability experiment in space-charge dominated electron beams," in *1995 Particle Accelerator Conference*, 1995, vol. 5, pp. 2974-2976.

[7] H. Suk, J. G. Wang, Y. Zou, S. Bernal, and M. Reiser, "Preliminary measurement of energy-spread change resulting from the resistive-wall instability," in *1997 Particle Accelerator Conference*, 1997, vol. 2, pp. 1650-1652.

[8] H. Suk, J. G. Wang, M. Reiser, and Y. Zou, "Experiments on space-charge waves in electron beams propagating through a resistive-wall channel," *Journal of Applied Physics,* vol. 86, no. 3, pp. 1699-1709, 1999.

[9] H. S. Uhm, "Self-consistent nonlinear theory of the resistive-wall klystron," in *SPIE*, 1994, vol. 2154, pp. 39-48.

[10] J. Welter *et al.*, "MEMS-microfabricated components for millimeter-wave and THz TWTs," in *2004 IEEE International Vacuum Electronics Conference (IVEC)*, 2004, p. 258.

[11] T. Rowe, J. H. Booske, and N. Behdad, "Metamaterial-Enhanced Resistive Wall Amplifiers: Theory and Particle-in-Cell Simulations," *IEEE Transactions on Plasma Science,* vol. 43, no. 7, pp. 2123-2131, 2015.

[12] R. J. Barker, et al., *Modern microwave and millimeter-wave power electronics*. Hoboken, N.J.: IEEE Press : Wiley-Interscience, 2005, p. 827.

[13] A. S. Gilmour, *Klystrons, traveling wave tubes, magnetrons, crossed-field amplifiers, and gyrotrons*. Norwood, MA: Artech House.

[14] J. R. Pierce, "The wave picture of microwave tubes," *Bell System Technical Journal,* vol. 33, no. 6, pp. 1343-1372, 1954.

[15] S. Y. Liao, *Microwave electron-tube devices*. Prentice-Hall, 1988.

[16] J. R. Pierce, "Waves in electron streams and circuits," *Bell System Technical Journal,* vol. 30, no. 3, pp. 626-651, 1951.

[17] H. S. Uhm, "Space charge waves in a cylindrical waveguide with arbitrary wall impedance," *Physics of Fluids,* vol. 25, no. 4, pp. 690-696, 1982.

[18] W. H. Press, *Numerical recipes in FORTRAN : the art of scientific computing*. Cambridge [England] ; New York, NY, USA: Cambridge University Press, 1992.

[19] N. Engheta, *Metamaterials Physics and Engineering Explorations*. Hoboken : Wiley, 2006., 2006.

[20] D. P. Starinshak, J. D. Wilson, and C. T. Chevalier, "Investigating holey metamaterial effects in terahertz traveling-wave tube amplifier," NASA2007.

[21] A. Rashidi and N. Behdad, "Metamaterial-enhanced traveling wave tubes," pp. 199-200: IEEE.

[22] A. R. Tarhani and N. Behdad, "Epsilon negative loaded traveling wave tube," ed: US Patent 20,150,256,139, 2015.

[23] Z. Duan, J. S. Hummelt, M. A. Shapiro, and R. J. Temkin, "Sub-wavelength waveguide loaded by a complementary electric metamaterial for vacuum electron devices," *Physics of Plasmas,* vol. 21, no. 10, p. 103301, 2014.

[24] Y. Wang *et al.*, "All-metal metamaterial slow-wave structure for high-power sources with high efficiency," *Applied Physics Letters,* vol. 107, no. 15, p. 153502, 2015.

[25] D. Shiffler, J. Luginsland, D. M. French, and J. Watrous, "A Cerenkov-like maser based on a metamaterial structure," *IEEE Trans. Plasma Sci.,* vol. 38, no. 6, pp. 1462-1465, Jun 2010.

[26] Z. Duan, B.-I. Wu, J. Lu, J. A. Kong, and M. Chen, "Cherenkov radiation in anisotropic double-negative metamaterials," *Optics Express,* vol. 16, no. 22, pp. 18479-18484, Oct 27 2008.

[27] Z. Duan, B.-I. Wu, J. Lu, J. A. Kong, and M. Chen, "Reversed Cherenkov radiation in unbounded anisotropic double-negative metamaterials," *Journal of Physics D-Applied Physics,* vol. 42, no. 18, Sep 21 2009, Art. no. 185102.

[28] D. M. French, D. Shiffler, and K. Cartwright, "Electron beam coupling to a metamaterial structure," *Physics of Plasmas,* Article vol. 20, no. 8, p. 8, Aug 2013, Art. no. 083116.

[29] Y. X. Zhang, M. Hu, Y. Yang, R. B. Zhong, and S. G. Liu, "Terahertz radiation of electron beam-cylindrical mimicking surface plasmon wave interaction," *Journal of Physics D-Applied Physics,* vol. 42, no. 4, Feb 2009, Art. no. 045211.

[30] J. S. Hummelt, S. M. Lewis, M. Shapiro, and R. J. Temkin, "Design of a metamaterial-based backward-wave oscillator," *IEEE Transactions on Plasma Science,* vol. 42, no. 4, pp. 930-936, 2014.

[31] Y. Wang *et al.*, "Metamaterial-based high-power microwave radiation sources," pp. 1-2: IEEE.

[32] J. B. Pendry, A. J. Holden, W. J. Stewart, and I. Youngs, "Extremely Low Frequency Plasmons in Metallic Mesostructures," (in English), *Physical Review Letters,* vol. 76, no. 25, pp. 4773-4776, 1996.

[33] J. B. Pendry, A. J. Holden, D. J. Robbins, and W. J. Stewart, "Low frequency plasmons in thin-wire structures," *Journal of Physics-Condensed Matter,* vol. 10, no. 22, pp. 4785-4809, Jun 8 1998.

[34] W. Rotman, "Plasma simulation by artificial dielectrics and parallel-plate media," *IRE Transactions on Antennas and Propagation,* vol. 10, no. 1, pp. 82-95, 1962.

[35] "Computer Simulation Technology (CST) Particle Studio," ed. www.cst.de.

[36] J. G. Pollock and A. K. Iyer, "Below-Cutoff Propagation in Metamaterial-Lined Circular Waveguides," *IEEE Transactions on Microwave Theory and Techniques,* vol. 61, no. 9, pp. 3169-3178, 2013.

[37] J. R. Pierce, "Traveling-Wave Tubes," *Bell System Technical Journal,* vol. 29, no. 3, pp. 390-460, 1950.

[38] J. H. Booske *et al.*, "Accurate parametric modeling of folded waveguide circuits for millimeter-wave traveling wave tubes," *IEEE Transactions on Electron Devices,* vol. 52, no. 5, pp. 685-694, 2005.

[39] C. T. Chevalier, K. A. Herrmann, C. L. Kory, J. D. Wilson, A. W. Cross, and S. Santana, "Three-Dimensional Simulation of Traveling-Wave Tube Cold-Test Characteristics Using CST MICROWAVE STUDIO," 2003.

[40] A. S. Gilmour, *Principles of traveling wave tubes*. Artech House, 1994.

[41] R. G. E. Hutter, *Beam and wave electronics in microwave tubes*. Boston Technical Pub., 1965.

[42] S. Sengele, M. L. Barsanti, T. A. Hargreaves, C. M. Armstrong, J. H. Booske, and Y.-Y. Lau, "Backward-Wave Suppression Analysis, and Design and Fabrication of a Prototype Millimeter-Wave Ring-Bar Slow-Wave Structure," *Plasma Science, IEEE Transactions on,* vol. 42, no. 12, pp. 3949-3960, 2014.

[43] S. Sengele, M. L. Barsanti, T. A. Hargreaves, C. M. Armstrong, J. H. Booske, and Y. Y. Lau, "Impact of random fabrication errors on backward-wave small-signal gain in traveling wave tubes with finite space charge electron beams," *Journal of Applied Physics,* vol. 113, no. 7, p. 074905, 2013.

[44] D. R. Smith, D. C. Vier, W. Padilla, S. C. Nemat-Nasser, and S. Schultz, "Loop-wire medium for investigating plasmons at microwave frequencies," *Applied Physics Letters,* vol. 75, no. 10, pp. 1425-1427, 1999.

[45] S. Tretyakov, *Analytical modeling in applied electromagnetics*. Artech House, 2003.

[46] D. R. Smith, S. Schultz, P. Markos, and C. M. Soukoulis, "Determination of effective permittivity and permeability of metamaterials from reflection and transmission coefficients," *Physical Review B,* Article vol. 65, no. 19, p. 5, May 2002, Art. no. 195104.

[47] C. A. Balanis, *Advanced engineering electromagnetics*. Hoboken, N.J.: John Wiley & Sons.

[48] J. H. Booske *et al.*, "Periodic magnetic focusing of sheet electron beams," *Physics of plasmas,* vol. 1, no. 5, pp. 1714-1720, 1994.

[49] A. Taflove and S. C. Hagness, *Computational electrodynamics*. Artech house, 2005.

[50] B. B. Godfrey, "Numerical Cherenkov instabilities in electromagnetic particle codes," *Journal of Computational Physics,* vol. 15, no. 4, pp. 504-521, 1974.

[51] P. A. Cherenkov, "Visible emission of clean liquids by action of γ radiation," *Doklady Akademii Nauk SSSR,* vol. 2, p. 451, 1934.

[52] A. D. Greenwood, K. L. Cartwright, J. W. Luginsland, and E. A. Baca, "On the elimination of numerical Cerenkov radiation in PIC simulations," *Journal of Computational Physics,* vol. 201, no. 2, pp. 665-684, 12/10/ 2004.

[53] J. D. Blahovec, L. A. Bowers, J. W. Luginsland, G. E. Sasser, and J. J. Watrous, "3-D ICEPIC simulations of the relativistic klystron oscillator," *IEEE transactions on plasma science,* vol. 28, no. 3, pp. 821-829, 2000.

[54] G. E. Sasser, J. D. Blahovec, L. A. Bowers, J. W. Luginsland, J. J. Watrous, and S. Colella, "Current emission, resistive losses, and other challenging problems in the simulation of high power microwave components."

[55] S.-F. Chang, J. E. Scharer, and J. H. Booske, "Wave dispersion, growth rates, and mode converter analysis for a sheet beam, hybrid-mode Cerenkov amplifier," *IEEE transactions on plasma science,* vol. 20, no. 3, pp. 293-304, 1992.

[56] M. G. Silveirinha, C. A. Fernandes, and J. R. Costa, "Electromagnetic characterization of textured surfaces formed by metallic pins," *IEEE Transactions on Antennas and Propagation,* vol. 56, no. 2, pp. 405-415, 2008.

[57] T. Rowe, N. Behdad, and J. H. Booske, "Metamaterial-Enhanced Resistive Wall Amplifier Design Using Periodically Spaced Inductive Meandered Lines," *IEEE Transactions on Plasma Science,* vol. 44, no. 10, pp. 2476-2484, 2016.

[58] Q. Gang, W. Jia-Fu, Y. Ming-Bao, C. Wei, C. Hong-Ya, and L. Yong-Feng, "Lowering plasma frequency by enhancing the effective mass of electrons: A route to deep sub-wavelength metamaterials," *Chinese Physics B,* vol. 22, no. 8, p. 087302, 2013.

[59] P. W. Kolb, T. S. Salter, J. A. McGee, H. D. Drew, and W. J. Padilla, "Extreme subwavelength electric GHz metamaterials," *Journal of Applied Physics,* vol. 110, no. 5, p. 054906, 2011.

[60] J. Joe, L. J. Louis, J. E. Scharer, J. H. Booske, and M. A. Basten, "Experimental and theoretical investigations of a rectangular grating structure for low-voltage traveling wave tube amplifiers," *Physics of Plasmas,* vol. 4, no. 7, pp. 2707-2715, 1997.

[61] S. Maslovski, S. Tretyakov, and P. Belov, "Wire media with negative effective permittivity: A quasi-static model," *Microwave and Optical Technology Letters,* vol. 35, no. 1, pp. 47-51, 2002.

[62] L. R. Industries. (2017). *Bonderite L-GP Aquadag E Acheson*. Available: http://www.laddresearch.com/aquadag-e

[63] K. E. Lonngren, S. V. Savov, and R. J. Jost, *Fundamentals of Electromagnetics with MATLAB*. Scitech publishing, 2007.

[64] E. Ramsden, *Hall-effect sensors: theory and application*. Newnes, 2011.

[65] C. D. Child, "Discharge From Hot CaO," *Physical Review (Series I),* vol. 32, no. 5, pp. 492-511, 1911.

[66] I. Langmuir, "The Effect of Space Charge and Residual Gases on Thermionic Currents in High Vacuum," *Physical Review,* vol. 2, no. 6, pp. 450-486, 1913.

[67] I. Langmuir, "The Effect of Space Charge and Initial Velocities on the Potential Distribution and Thermionic Current between Parallel Plane Electrodes," *Physical Review,* vol. 21, no. 4, pp. 419-435, 1923.

[68] Y. Y. Lau, "Simple theory for the two-dimensional Child-Langmuir law," *Physical review letters,* vol. 87, no. 27, pp. 278-301, 2001.

[69] M. Reiser, *Theory and design of charged particle beams*. John Wiley & Sons, 2008.

Work Published by the Author

Published Articles

[1] T. Rowe, T. Shih, and N. Behdad, “On the Power Handling Capability of Non-Foster Impedance Matching Network Using Gridded Vacuum Tubes and Power Transistors,” submitted to *IEEE Antennas and Propagation Magazine*, 2017.

[2] T. Rowe, J. H. Booske, and N. Behdad, "Inductive Meandered Metal Line Metamaterial for Rectangular Waveguide Linings" *Plasma Science, IEEE Transactions on,* in Press.

[3] T. Rowe, N. Behdad, and J. H. Booske, "Metmaterial-Enhanced Resistive Wall Amplifier Design Using Periodically Spaced Inductive Meandered Lines," *Plasma Science, IEEE Transactions on,* vol. 44, pp. 2476-2484, 2016.

[4] T. Rowe, J. H. Booske, and N. Behdad, "Metamaterial-Enhanced Resistive Wall Amplifiers: Theory and Particle-in-Cell Simulations," *Plasma Science, IEEE Transactions on,* vol. 43, pp. 2123-2131, 2015.

[5] T. Rowe, M. Pearlman, and J. Browning, "Simulation of Electron Hop Funnels Using Version 9.2 of Lorentz-2E," *Plasma Science, IEEE Transactions on,* vol. 42, pp. 84-90, 2014.

[6] M. Pearlman, T. Rowe, and J. Browning, "Simulation of Electron Hop Funnel Hysteresis," *Plasma Science, IEEE Transactions on*, vol. 41, pp. 2291-2298, Aug. 2013.

[7] T. Rowe, P. M., and B. J., "Hysteresis in experimental IV curves of electron hop funnels," *J. Vac. Sci. Technol. B Journal of Vacuum Science & Technology B: Microelectronics and Nanometer Structures*, vol. 31, p. 042204, 2013.

[8] R. T. Rowe, "Geometry and Material Effects on Electron Transport in Hop Funnels," M.S. Thesis, 2013.

Conference Proceedings

[1] T. Rowe, P. Forbes, N. Behdad, and J. H. Booske, “Inductive Meandered Line Metamaterial for Metamaterial-Enhanced Resistive Wall Amplifiers,” submitted to the International Vacuum Electronics Conference, London, UK, 2017.

[2] T. Rowe, P. Forbes, J. H. Booske, and N. Behdad, “Material Selection for the Periodic Elements of a Metamaterial-Enhanced Resistive Wall Amplifier,” submitted to the International Conference on Plasma Science, Atlantic City, New Jersey, USA, 2017.

[3] T. Rowe, P. Forbes, N. Behdad, and J. H. Booske, “Metamaterial-Enhanced Resistive Wall Amplifier,” at the Nineteenth Annual Directed Energy Symposium, Huntsville, AL, USA, 2017.

[4] T. Rowe, N. Behdad, and J. Booske, “Metamaterial design for a metamaterial-enhanced resistive wall amplifier,” at the International Vacuum Electronics Conference, Monterey, California, USA, 2016.

[5] T. Rowe, N. Behdad, and J. H. Booske, “Theory and simulation of a relativistic high power microwave metamaterial-enhanced resistive wall amplifier,” at the International Conference on Plasma Science, Banff, Alberta, Canada, 2016.

[6] T. Rowe, T.Y. Shih, and N. Behdad, “Power and bandwidth limitations of non-foster electrically-small antennas for ultra-wideband transmit applications,” at the International Union of Radio Science Conference, Puerto Rico, 2016.

[7] T.Y. Shih, T. Rowe, and N. Behdad, “Efficiency enhancement of ultra-wideband, non-foster matched electrically small HF antennas,” at the International Union of Radio Science Conference, Puerto Rico, 2016.

[8] T. Rowe, N. Behdad, and J. Booske, “Metamaterial design for a metamaterial-enhanced resistive wall amplifier,” at the International Vacuum Electronics Conference, Monterey, California, USA, 2016.

[9] T. Rowe, T.Y. Shih, J. Booske, and N. Behdad, “Gridded vacuum tube use in transmitting wideband non-foster electrically small antennas,” at the International Vacuum Electronics Conference, Monterey, California, USA, 2016.

[10] T. Rowe, T.Y. Shih, and N. Behdad, “Transmitting power handling limitations of a wideband, non-foster electrically-small antenna,” at the IEEE International Conference on Wireless Information Technology and Systems,” 2016.

[11] T. Rowe, N. Behdad, and J. Booske, "Metamaterial-enhanced resistive wall amplifiers," at the International Vacuum Electronics Conference, Beijing, China, 2015.

[12] J. Browning, E. Wright, T. Rowe, B. McMillon, B. Garner, and D. Plumlee, "A microplasma discharge using a plasma reservoir source," at the Plasma Science (ICOPS), 2013 Abstracts IEEE International Conference on, 2013, pp. 1-1.

[13] T. Rowe, M. Pearlman, and J. Browning, "Investigation of current transmission through insulating funnels via secondary electron emission," at the 2012 IEEE 39th International Conference on Plasma Sciences (ICOPS), 2012.

[14] M. Pearlman, T. Rowe, and J. Browning, "Hop structure optimization," at the International Conference on Plasma Science (ICOPS), 2011.

Appendix 1: Calculating the Interaction Impedance

The interaction impedance is the ratio of the axial electric field squared to that of the power traveling through the cross section of the device. The interaction impedance for a given radius is equal to

$$K(r) = \frac{|E_z(r)|^2}{2\beta^2 P_z}, \qquad \text{(A1.1)}$$

where P_z is the Poynting power in the axial direction and β is the wavenumber.

To determine P_z we began by examining P_w, the power in the wave,

$$P_W = \int\int E \times H^* dA, \qquad \text{(A1.2)}$$

where A is the cross section of the device. Since we want the power in the z direction

$$P_z = \int\int E \times H^* \cdot dA\, \hat{z}. \qquad \text{(A1.3)}$$

For a TM field in an infinitely wide parallel plate waveguide configuration ($E_y = H_z = 0$)

$$E \times H^* = \begin{vmatrix} \hat{x} & \hat{y} & \hat{z} \\ E_x & 0 & E_z \\ H_x^* & H_y^* & 0 \end{vmatrix} = \hat{x}E_z H_Y^* - \hat{y}E_z H_x^* + \hat{z}\, E_x H_Y^*, \qquad \text{(A1.4)}$$

so the axial power will be

$$P_z = \int\int E_x\, H_y^*\, dA. \qquad \text{(A1.5)}$$

For the planar MERWA, using Fig. 15 as a reference for structure dimensions, and assuming a unit width in the y-direction of W the power becomes:

$$P_z = \int_{-W/2}^{W/2} \int_{-d2}^{d2} E_x H_y^* \, dx \, dy. \qquad \text{(A1.6)}$$

*A*ll fields are independent of y, therefore:

$$P_z = 2W \int_{-d_2}^{d2} E_x \, H_y^* \, dx. \qquad \text{(A1.7)}$$

For a TM field the x-directed electric field is (more details in Appendix 2),

$$E_x = \frac{k}{\omega \varepsilon_x} H_y, \qquad \text{(A1.8)}$$

so

$$P_z = 2W \int_{-d2}^{d2} \frac{k}{\omega \varepsilon_x} H_y \left(H_y^*\right) dx, \qquad \text{(A1.9)}$$

or

$$P_z = 2W \int_{-d2}^{d2} \frac{k}{\omega \varepsilon_x} \left|H_y\right|^2 dx. \qquad \text{(A1.10)}$$

Now there are two separate sections of fields, region 1: 0 to d_1, and region 2: d_1 to d_2.

$$P_z = 2W \left[\int_{-d2}^{-d1} \frac{k}{\omega \varepsilon_x} \left|H_{y,2}\right|^2 \, dx + \int_{-d1}^{d1} \frac{k}{\omega \varepsilon_x} \left|H_{y,1}\right|^2 \, dx + \int_{d1}^{d2} \frac{k}{\omega \varepsilon_x} \left|H_{y,2}\right|^2 \, dx \right] \qquad \text{(A1.11)}$$

To solve the integral of (A1.11), we need to determine the magnetic field profiles. We knew that the magnetic fields must solve the equation (discussed in more detail in Appendix 2):

$$\frac{\partial^2 H_y}{\partial x^2} + H_y\left(\omega^2 \epsilon_{zz}\mu_{yy} - \beta_z^2 \frac{\epsilon_{zz}}{\epsilon_{xx}}\right) = 0. \qquad \text{(A1.12)}$$

For a planar configuration, the solution of (A1.12) will have cosine and sine basis functions. Therefore, the general solution of (A1.12) for the two separate regions, the vacuum space and the liner, respectively, will be:

$$H_{y,1}(x) = A_1 \cos(\beta_{x,1} x) + B_1 \sin(\beta_{x,1} x), \qquad \text{(A1.13)}$$

and

$$H_{y,2}(x) = A_2 \cos(\beta_{x,2} x) + B_2 \sin(\beta_{x,2} x), \qquad \text{(A1.14)}$$

where

$$\beta_{x,1}^2 = \left(\frac{\omega^2}{c^2} - \beta_z^2\right), \qquad \text{(A1.15)}$$

and

$$\beta_{x,2}^2 = \frac{\epsilon_{zz}}{\epsilon_{xx}}\left(\omega^2 \epsilon_{xx}\mu_{yy} - \beta_z^2\right). \qquad \text{(A1.16)}$$

We can also knew that (from Appendix 2)

$$E_z = -\frac{j}{\omega \varepsilon_0}\frac{\partial H_y}{\partial x}; \qquad \text{(A1.17)}$$

Therefore,

$$E_{z,1}(x) = \left(-\frac{j}{\omega\varepsilon_0}\right)\left[-A_1\beta_{x,1}\sin\left(\beta_{x,1}x\right) + B_1\beta_{x,1}\cos\left(\beta_{x,1}x\right)\right] \qquad \text{(A1.18)}$$

and

$$E_{z,2}(x) = \left(-\frac{j}{\omega\varepsilon_0}\right)\left[-A_2\beta_{x,2}\sin\left(\beta_{x,2}x\right) + B_2\beta_{x,2}\cos\left(\beta_{x,2}x\right)\right] \qquad \text{(A1.19)}$$

We were then able to use boundary conditions to reduce these equations. First, since E_x is symmetric about x=0,

$$E_{x,1}(x=0) = \frac{k}{\omega\varepsilon_x}H_{y,1}(x=0) = 0 \qquad \text{(A1.20)}$$

or

$$H_{y,1}(x=0) = 0. \qquad \text{(A1.21)}$$

Therefore,

$$A_1 = 0, \qquad \text{(A1.22)}$$

$$H_{y,1} = B_1\sin\left(\beta_{x,1}x\right), \qquad \text{(A1.23)}$$

and

$$E_{z,1} = \frac{k}{\omega\varepsilon_x}B_1\sin\left(\beta_{x,1}x\right). \qquad \text{(A1.24)}$$

Secondly, the boundary condition at the PEC wall

$$E_{z,2}(x = d_2) = 0, \qquad \text{(A1.25)}$$

gave

$$A_2 = B_2 \cot(\beta_{x,2} d_2). \qquad \text{(A1.26)}$$

Therefore, the magnetic field in the region 2, the liner, is

$$H_{y,2}(x) = B_2 \cot(\beta_{x,2} d_2) \cos(\beta_{x,2} x) + B_2 \sin(\beta_{x,2} x) \qquad \text{(A1.27)}$$

To determine the magnetic field in region 1 it was necessary to apply a third boundary condition, for continuity of fields across the boundary,

$$\varepsilon_0 E_{x,1}(d_1) = \varepsilon_{xx} E_{x,2}(d_1), \qquad \text{(A1.28)}$$

or

$$H_{y,1}(d_1) = H_{y,2}(d_1). \qquad \text{(A1.29)}$$

Therefore,

$$B_1 = B_2 \csc(\beta_{x,1} d_1) \left[\cot(\beta_{x,2} d_2) \cos(\beta_{x,2} d_1) + \sin(\beta_{x,2} d_1)\right] \qquad \text{(A1.30)}$$

We were down to only one unknown (B_2) which is dependent on initial conditions

$$H_{y,1} = B_2 \csc(\beta_{x,1} d_1) \left[\cot(\beta_{x,2} d_2) \cos(\beta_{x,2} d_1) + \sin(\beta_{x,2} d_1)\right] \sin(\beta_{x,1} x), \qquad \text{(A1.31)}$$

and

$$H_{y,2}(x) = B_2\left[\cot\left(\beta_{x,2}d_2\right)\cos\left(\beta_{x,2}x\right) + \sin\left(\beta_{x,2}x\right)\right]. \tag{A1.32}$$

We were then able to determine the axial power

$$P_z = 2W\left[\int_{-d2}^{-d1}\frac{k}{\omega\varepsilon_x}\left|H_{y,2}\right|^2\,dx + \int_{-d1}^{d1}\frac{k}{\omega\varepsilon_0}\left|H_{y,1}\right|^2\,dx + \int_{d1}^{d2}\frac{k}{\omega\varepsilon_x}\left|H_{y,2}\right|^2\,dx\right]. \tag{A1.33}$$

to be

$$\begin{aligned} P_z = 2W\frac{k}{\omega\varepsilon_x}B_2^2\Bigg[&\int_{-d2}^{-d1}\left[\cot\left(\beta_{x,2}d_2\right)\cos\left(\beta_{x,2}x\right) + \sin\left(\beta_{x,2}x\right)\right]^2\,dx \\ &+ \int_{-d1}^{d1}\Big[\csc\left(\beta_{x,1}d_1\right)\left[\cot\left(\beta_{x,2}d_2\right)\cos\left(\beta_{x,2}d_1\right)\right. \\ &\left.+ \sin\left(\beta_{x,2}d_1\right)\right]\sin\left(\beta_{x,1}x\right)\Big]^2\,dx \\ &+ \int_{d1}^{d2}\left[\cot\left(\beta_{x,2}d_2\right)\cos\left(\beta_{x,2}x\right) + \sin\left(\beta_{x,2}x\right)\right]^2\,dx\Bigg]. \end{aligned} \tag{A1.34}$$

Finally, to calculate the interaction impedance we solved (A1.1) using (A1.24) a numerical solution of (A1.34).

Appendix 2: Wall Admittance for a Planar Parallel Plate Waveguide Lined with an Anisotropic Metamaterial

To determine the gain of an MERWA with an anisotropic liner, it was important to evaluate the admittance of the liner, as seen by the electron beam. To evaluate the admittance of the liner we examined the field profile. The admittance at the edge of the wall, in a parallel plate scenario, is the negative ratio of the transverse magnetic field to the axial electric field at the location of the wall. Mathematically, the admittance of the wall is,

$$Y_{wall} = -\frac{H_{y,liner}(d_1)}{E_{z,liner}(d_1)}. \qquad \text{(A2.1)}$$

To determine the field profiles we started from Maxwell's equations and, assuming exponential dependence of $e^{j(\omega t - kz)}$, we split the equations using the permittivity tensor of

$$\varepsilon_r = \begin{bmatrix} \varepsilon_x & 0 & 0 \\ 0 & \varepsilon_y & 0 \\ 0 & 0 & \varepsilon_z \end{bmatrix}. \qquad \text{(A2.2)}$$

The resulting Maxwell's equations are

$$\frac{\partial E_z}{\partial y} + jkE_y = -j\omega\mu_{xx}H_x, \qquad \text{(A2.3)}$$

$$\frac{\partial E_z}{\partial x} + jkE_x = j\omega\mu_{yy}H_y, \qquad \text{(A2.4)}$$

$$\frac{\partial E_y}{\partial x} - \frac{\partial E_x}{\partial y} = -j\omega\mu_{zz}H_z, \qquad \text{(A2.5)}$$

and

$$\frac{\partial H_z}{\partial y} + jkH_y = j\omega\epsilon_{xx}E_x, \qquad \text{(A2.6)}$$

$$\frac{\partial H_z}{\partial t} + jkH_x = -j\omega\epsilon_{yy}E_y, \qquad \text{(A2.7)}$$

$$\frac{\partial H_y}{\partial x} - \frac{\partial H_x}{\partial y} = j\omega\epsilon_{zz}E_z. \qquad \text{(A2.8)}$$

We then assumed a TM mode ($H_z = 0$) and since the structure is infinite in the y-dimension we also assume $\partial/\partial y = 0$. Therefore, we were able to solve everything in terms of H_y which reduces the six Maxwell's equations down to three:

$$E_x = \frac{k}{\omega\epsilon_{xx}}H_y, \qquad \text{(A2.9)}$$

$$E_z = -\frac{j}{\omega\epsilon_{zz}}\frac{\partial H_y}{\partial x}, \qquad \text{(A2.10)}$$

and

$$\frac{\partial^2 H_y}{\partial x^2} + H_y\left(\omega^2\epsilon_{zz}\mu_{yy} - \beta_z^2\frac{\epsilon_{zz}}{\epsilon_{xx}}\right) = 0. \qquad \text{(A2.11)}$$

For a lined parallel plate, the fields in the liner have cosine and sine basis functions. Therefore, the general solution of (A2.11) give the magnetic field in the liner as

$$H_{y,liner}(x) = A\cos\left(\beta_{x,liner}x\right) + B\sin\left(\beta_{x,liner}x\right), \qquad \text{(A2.12)}$$

using the coordinate system shown in Fig. 28, where

$$\beta_{x,liner}^2 = \beta_{x,l}^2 = \frac{\epsilon_{zz}}{\epsilon_{xx}}\left(\omega^2\epsilon_{xx}\mu_{yy} - \beta_z^2\right). \qquad \text{(A2.13)}$$

We then calculated the axial electric field based upon (A2.10) to be

$$E_{z,liner}(x) = -\frac{j}{\omega\epsilon_{z,liner}}\frac{\partial}{\partial x}\left[H_{y,liner}(x)\right]. \quad \text{(A2.14)}$$

Combining (A2.12) and (A2.14), we can re-write the wall admittance, (A2.1), as

$$Y_{wall} = -\frac{A\cos(\beta_{x,l}d_1) + B\sin(\beta_{x,l}d_1)}{\frac{j\beta_{x,l}}{\omega\epsilon_{z,l}}\left[A\sin(\beta_{x,l}d_1) - Bcos(\beta_{x,l}d_1)\right]}. \quad \text{(A2.15)}$$

It is then possible to use the boundary condition of the problem (tangential electric field must go to zero at the outer perfect electric conductor (PEC), d_2) to simplify the wall admittance. Specifically,

$$E_{z,l}(d_2) = 0, \quad \text{(A2.16)}$$

gives

$$A = B\cot(\beta_{x,l}d_2). \quad \text{(A2.17)}$$

Therefore, the wall admittance can be finally written as

$$Y_{wall} = \left(\frac{j\omega\epsilon_{z,l}}{\beta_{x,l}}\right)\frac{\cot(\beta_{x,l}d_2)\cos(\beta_{x,l}d_1) + \sin(\beta_{x,l}d_1)}{\left[\cot(\beta_{x,l}d_2)\sin(\beta_{x,l}\mathrm{d}_1) - cos(\beta_{x,l}d_1)\right]} \quad \text{(126)}$$

Finally to obtain the admittance at the edge of the beam, we must transform the wall admittance using equations for a cutoff transmission line (hyperbolic sines and cosines). The input admittance is then

$$Y_{input} = Y_0\frac{Y_{wall} + Y_0\tanh(\psi(d_1 - \mathrm{b}))}{Y_0 + Y_{wall}\tanh(\psi(d_1 - \mathrm{b}))}, \quad \text{(A2.18)}$$

where

$$Y_0 = \frac{j\omega\varepsilon_0}{\psi}, \qquad \text{(A2.19)}$$

and

$$\psi^2 = \beta_z^2 - \omega^2\varepsilon_0\mu_0. \qquad \text{(A2.20)}$$

Appendix 3: Derivation of Relevant Electron Beam Equations

Space Charge Limited Current in a Conducting Tube

Fig. 114 (a) shows a representation of the scenario where an electron beam is emitted from the cathode and is then passed through an anode tube. The anode is biased at Φ_b and the cathode is biased at ground. Fig. 114 (b) presents the electric potential inside of the conducting anode as a function of radius for a given beam current. Since the anode is electrically connected to the beam potential Φ_b, the edges of the parabola in Fig. 114 (b) are always equal to Φ_b. As the current of the beam is increased the depth of the parabola increases. If the current becomes sufficiently large that the potential at the center of the beam becomes less than zero (the potential of the cathode), the current traveling in the tube becomes space charge limited. A thorough analysis of the current limit of beams in conducting tubes is presented in [69]; a simplified version is presented here for clarity.

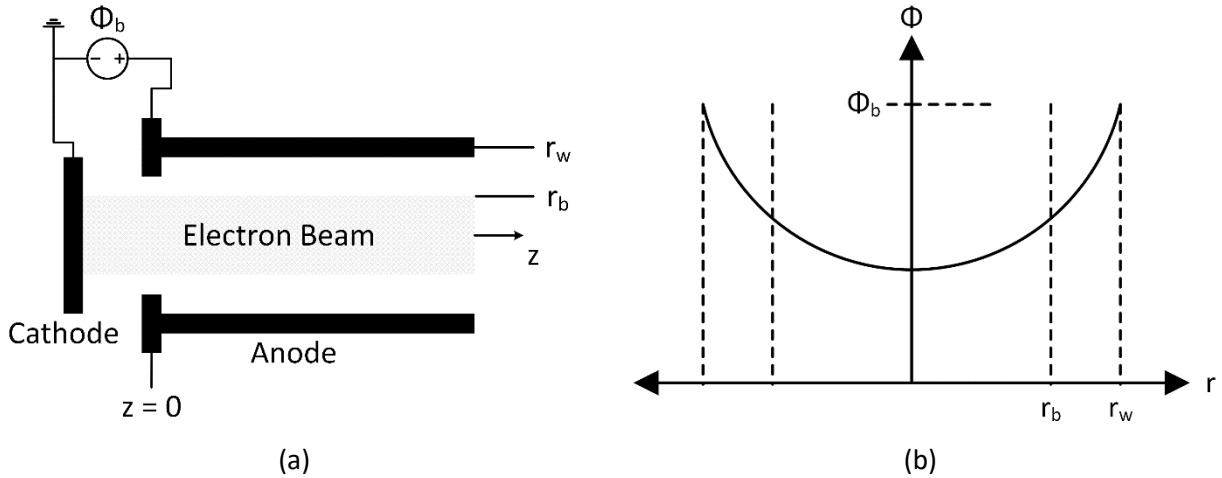

Fig. 114: (a) Pictoral representation of the biasing of a conducting wall which the electron beam is passed through and (b) the electric potential as a function of radius inside of the conducting tube

To determine the electric potential inside of the beam and conducting tube we examine the cylindrical version of Poisson's equation:

$$\nabla^2\Phi(r) = \frac{en(r)}{\varepsilon_0}, \qquad \text{(A3.1)}$$

where Φ is the electric potential, e is the charge of an electron, n is the electron density, and ε_0 is the permittivity of free space. We assume that the kinetic energy of the electron, T, at z=0 is, $T(z=0) = T_b = e\Phi_b$, while at $z > \sim r_w, T(r) = e\Phi_b(r)$. Therefore, for positions $z > \sim r_w$ Poisson's equation can be rewritten to the form

$$\frac{1}{r}\frac{d}{dr}\left(r\frac{dT(r)}{dr}\right) = \frac{en(r)}{\varepsilon_0} = \frac{I_0}{\varepsilon_0\pi r_b^2 u(r)}, \qquad \text{(A3.2)}$$

or

$$\frac{1}{r}\frac{d}{dr}\left(r\frac{dT}{dr}\right) = \frac{I_0}{\varepsilon_0\pi r_b^2\sqrt{2e/m}}T^{-1/2}, \qquad \text{(A3.3)}$$

where I_0 is the current of the electron beam, r_b is the radius of the electron beam, and m is the mass of the electron. To solve for the maximum current that can travel through the conducting tube, we numerically solve (A3.3) as a function of the radius and beam current, $T(r, I_0)$. We solve this numerically multiple times using different boundary conditions of $0 \leq T(r=0) \leq e\Phi_b$. Fig. 115 show the numerical solution, plotting the on-axis beam energy, $T(r=0)$ versus I_0, the current in the electron beam. In Fig. 115, it is possible to see that the current is maximized when the on axis beam energy is relatively low. The maximum of the curve in Fig. 115 occurs when $T(r=0) = 0.174\ e\Phi_b$ and $I_0/\left(\pi\varepsilon_0\sqrt{2e/m}\Phi_b^{3/2}\right) = 1.963$. Therefore, if we assume that $r_b = r_w$ we can find that

$$I_{max} = 1.963\pi\varepsilon_0\sqrt{2e/m}\Phi_b^{3/2} = 32.4\times10^{-6}\Phi_b^{3/2}\ [A]. \qquad \text{(A3.4)}$$

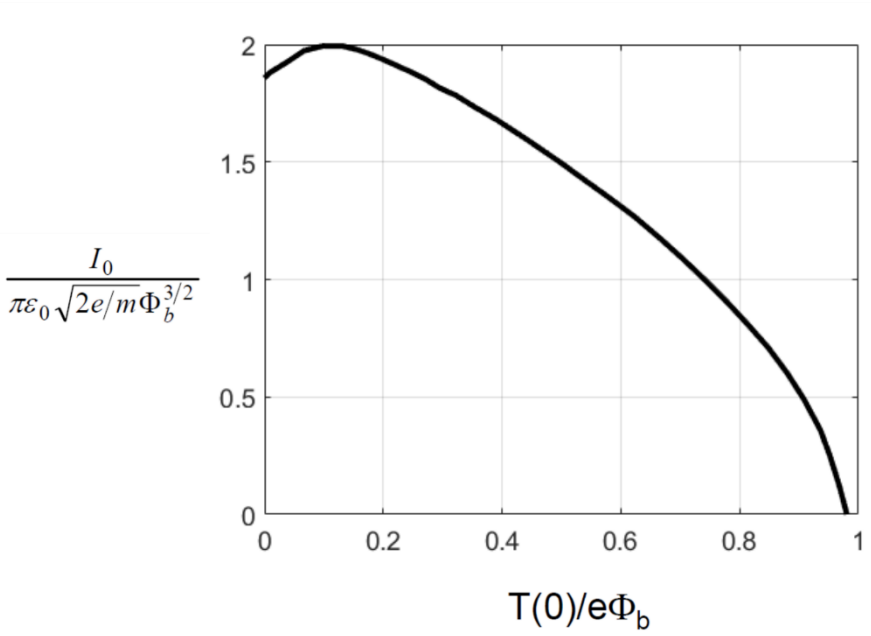

Fig. 115: On-axis kinetic energy of the electron beam versus the beam current

Using (A3.4), the limiting current is $I_{max} = 11$ kA for a 500 kV beam. If the current of the beam is higher than this I_{max} value then the potential on-axis will go to zero, the potential of the cathode. If the on-axis potential is equal to the cathode, the on-axis electrons will be reflected by this virtual cathode. This leads to an instability due to the oscillation of current. We can further refine this calculation for a system that has a fill factor of 50%. Without replotting T, it can be shown that if $r_b < r_w$ then I_{max} is modified by $[1 + 2\ln(r_w/r_b)]$ [69]. Therefore, for any scenario where $r_b < r_w$ the maximum current that can be used will be higher than a 100% fill factor. Therefore, our calculated limit of 11 kA will be more than sufficient. For reference, we can calculate the limiting current if $r_b = 0.5r_w$,

$$I_{max} = [1 + 2\ln(2)](32.4\times10^{-6})\Phi_b^{3/2}. \qquad \text{(A3.5)}$$

Using (A3.5) it can be determined that for a 50% fill factor 500 keV beam, the limiting current is 27.33 kA. This limit is orders of magnitude greater than our anticipated beam current indicating that our tube size is sufficient for an electron beam of this voltage and current.

Relativistic Brillouin Field Requirement

To determine the Brillouin field required to confine the electron beam we can examine the space charge expansion of a relativistic cylindrical electron beam. The force from space charge for a relativistic particle is:

$$\frac{d}{dt}(\gamma m_0 \boldsymbol{v}) = q\boldsymbol{E} + q\boldsymbol{v} \times \boldsymbol{B}. \qquad \text{(A3.6)}$$

For the space charge forces, the electric field can be defined as

$$\boldsymbol{E}(r) = \frac{\rho r}{2\varepsilon_0}\hat{\boldsymbol{r}}, \qquad \text{(A3.7)}$$

and the self magnetic field

$$\boldsymbol{B}(r) = \frac{\mu_0 \rho u_0}{2} r\hat{\boldsymbol{\varphi}} = \left(\mu_0 \varepsilon_0 u_0 \frac{\rho r}{2\varepsilon_0}\right)\hat{\boldsymbol{\varphi}} = \left(\frac{u_0}{c^2}E_r\right)\hat{\boldsymbol{\varphi}}. \qquad \text{(A3.8)}$$

where r is the radial location, u_0 is the beam velocity, ε_0 is the permittivity of free space, and ρ is the charge density. The equation for the radial force from space charge can then be rewritten in the form

$$\frac{d}{dt}(p_r) = \frac{d}{dt}\gamma m_0 v_r = qE_r + qv_z \times B_\varphi \qquad \text{(A3.9)}$$

where p_r is the radial momentum. Since the beam is traveling primarily in the axial direction, we assume $v_z \approx u_0$, reducing the equation for the space charge force to

$$\frac{d}{dt}(p_r) = q\left(E_r + \frac{u_0^2}{c^2}E_r\right) = \frac{qE_r}{\gamma^2}. \qquad \text{(A3.10)}$$

If we compare this to a non-relativistic beam, the space charge expansion is actually reduced by $1/\gamma^2$. Since the space charge expansion is reduced, the magnetic field required to confine the beam is reduced by the same factor. For a non-relativistic electron beam, the Brillouin equilibrium field [40] is

$$B_B = \left(\frac{1}{r_b}\right)\sqrt{\frac{2\, I_{beam}\, m}{\pi\, \epsilon_0\, u_0\, e}}, \qquad \text{(A3.11)}$$

where I_{beam} is the beam current and r_b is the beam radius. Since the space charge expansion is reduced by a factor of $1/\gamma^2$, the Brillouin equilibrium field is also reduced resulting in a field requirement of

$$B_B = \left(\frac{1}{r_b\gamma^2}\right)\sqrt{\frac{2\, I_{beam}\, m}{\pi\, \epsilon_0\, u_0\, e}}, \qquad \text{(A3.12)}$$

or approximately

$$B_B \approx 0.83 \times 10^{-3}\left(\frac{I^{1/2}}{r_b\, \gamma^2\, V^{1/4}}\right)\ [Tesla]. \qquad \text{(A3.13)}$$

Space Charge Limited Emission Current

The 1-D space charge limited configuration can be derived from Poisson's equation:

$$\nabla^2 V(z) = \frac{\rho(z)}{\varepsilon_0}, \qquad \text{(A3.14)}$$

where ε_0 is the permittivity of free space, ρ is the charge density, and $V$is the potential between the two plates. Knowing that the current density is

$$J(z) = \rho(z)u(z) \qquad \text{(A3.15)}$$

with, the electron velocity, u, equal to

$$u(z) = \sqrt{2\eta V(z)}, \qquad \text{(A3.16)}$$

where η is the electron charge to mass ratio, for non-relativistic beams. Poisson's equation can then be re-written in the form

$$\nabla^2 V(z) = \frac{J_{limit}}{\varepsilon_0 \sqrt{2\eta} V(z)}. \qquad \text{(A3.17)}$$

To solve Poisson's equation for the space charge limited current, we integrate both sides of the equation and then assume the boundary conditions of the potential at the cathode, $V(z = 0) = 0$, and the electric field at the cathode is also zero, $E(0) = -dV(0)/dz = 0$. A second integration of the equation can then be completed to determine the voltage

$$V(z) = \left(\frac{3}{2}\right)^{4/3} \left(\frac{J_{limit}}{\varepsilon_o}\right)^{2/3} \left(\frac{1}{2\eta}\right)^{1/3} z^{4/3} + C_1 \,. \qquad \text{(A3.18)}$$

The final boundary condition is then applied as the potential at the anode $V(z = d) = V_0$. The equation is then re-arranged for the SCL current

$$J_{limit} = \frac{4\varepsilon_0}{9d^2} \sqrt{\frac{2e}{m}} V_0^{3/2} = 2.33x10^{-6} \frac{V_0^{3/2}}{d^2}, \qquad \text{(A3.19)}$$

which is the Child-Langmuir law [65-67] for a parallel-plane diode. A more thorough derivation of the Child-Langmuir law can be found in various texts, such as [40] or [68].